University of Wisconsin Milwaukee

UWM Digital Commons

August 2019

Study of the Long-Term Shaft Resistance of Energy Piles in Saturated Clays

saeed yazdani kachooie
University of Wisconsin-Milwaukee

Follow this and additional works at: https://dc.uwm.edu/etd

Part of the Civil Engineering Commons

STUDY OF THE LONG-TERM SHAFT RESISTANCE OF ENERGY

PILES IN SATURATED CLAYS

by

Saeed Yazdani

A Dissertation Submitted in

Partial Fulfillment of the

Requirements for the Degree of

Doctor of Philosophy

in Engineering

at

The University of Wisconsin-Milwaukee

August 2019

ABSTRACT

STUDY OF THE LONG-TERM SHAFT RESISTANCE OF ENERGY PILES IN
SATURATED CLAYS

by

Saeed Yazdani

The University of Wisconsin-Milwaukee, 2019
Under the Supervision of Professor Sam Helwany

This research aims to qualitatively/quantitively assess the effect of temperature variation on the energy pile shaft resistance. The important mechanisms by which heating can change the shear strength of clay and clay-concrete interface are evaluated using experimental and numerical methods. As for experimental method, temperature-controlled triaxial tests, constant normal load (CNL) direct shear tests and small-scale pile tests were conducted. As for numerical approach, a fully coupled thermo-hydro-mechanical (THM) analysis was performed to simulate the experimental test results so that the capability of such analysis to predict thermo-mechanical behavior of energy piles is evaluated. Reconstituted (HC-77) kaolin clay, one-dimensionally consolidated from slurry, was used in all the studies. Cyclic and monotonic heat ranging between 24° C and 34°C were applied to the clay specimen and interface. The interface was sheared under two stiffness boundary conditions; Constant Normal Load (CNL) and Constant Normal Stiffness (CNS), where the applied normal stresses varied between 100 kPa and 300 kPa. The results of experimental tests indicate that heating improves the shear strength of normally consolidated (NC) clay and NC clay-concrete interface. However, a decrease in strength of over-consolidated (OC) clays was observed, which is thought to be linked to the heat-induced change in the contact stress

between clay particles. It was also found out that the increase in the strength of interface under CNL condition, which was about 10%, is exclusively attributed to heat strengthening of clay at the interface. However, the increase in shaft resistance under CNS condition (96% and 49% due to non-cyclic heating and cyclic heating-cooling, respectively) is primarily attributed to the heat-induced increase of effective lateral stress (81% and 35% due to non-cyclic heating and cyclic heating-cooling, respectively). The heat-induced increase in the shear strength of clay (8-10%) also partially contribute to the overall increase of the shaft resistance under CNS condition. It was also observed that there is very good agreement between the results experimentally measured and those numerically predicted. Therefore, fully coupled THM analysis can effectively be used to predict the thermo-mechanical behavior of real energy piles in clays.

To
my parents,
my sister,
and my brothers

TABLE OF CONTENTS

LIST OF FIGURES

LIST OF TABLES

ACKNOWLEDGEMENTS

I would like to express my sincere gratitude to my advisor Prof. Helwany for providing me this great opportunity to study and learn in his lab, and his support of my PhD study. Without his trust in me and my capabilities it would not possible to conduct this research.

Besides my advisor, I would like to thank the rest of my thesis committee: Prof. Dsouza, Prof. Rahman, Prof. Sobolev, and Prof. Yu for their comments and encouragement.

My sincere thanks also go to Mr. Rahim Reshadi and Mr. John Condon who provided me an opportunity to have access to the laboratory and research facilities. I am extremely thankful and indebted to them for sharing expertise, and sincere and valuable guidance and encouragement extended to me.

Last but not the least, I would like to thank my family: my parents, my sister and brothers for supporting me spiritually throughout conducting this research

Chapter 1

Energy Consumption (Statistics and Facts), Geothermal Energy and Energy Piles

1-1- **Introduction**:

World energy statistics

Exhaustion of natural sources of energy and negative environmental effects (CO_2 emissions, global warming, climate change, etc.) are two main concerns that have been raised as result of the rapid grow in world energy use. This section provides a globally/locally overview of building energy consumption gathered and presented by the International Energy Agency (IEA)[1]. These statistics providing a deep understanding of energy consumption and its possible environmental impacts may help countries/governments to make wise decision on producing and consuming energy in secure and sustainable manner. Figure 1-1 provides some statistics on final total energy consumption[2] (FTC) (including different types of energy) and CO_2 emissions by fuel combustion during 1971-2015. During this period the energy consumption has grown by 120% and CO_2 emissions by 133%. It is worth noting that total energy consumption and CO_2 emissions in 1971 have been recorded as 4333 Mtoe (million tonnes of oil equivalent) and 13334 Mt (million tones), respectively [2].

According to the EIA (in its International Energy Outlook) In 2030, energy consumption attributed to the residential and non-residential building sectors will approximately be 67% and 33%, respectively, which is mainly because of population growth and living conditions enhancement [3].

---

[1] The International Energy Agency (IEA), an autonomous agency, was established in November 1974. Its primary mandate was – and is – two-fold: to promote energy security amongst its member countries through collective response to physical disruptions in oil supply and provide authoritative research and analysis on ways to ensure reliable, affordable and clean energy for its 28-member countries and beyond [1].

2 Total final consumption (TFC) is the sum of consumption by the different end-use sectors and includes non-energy use.
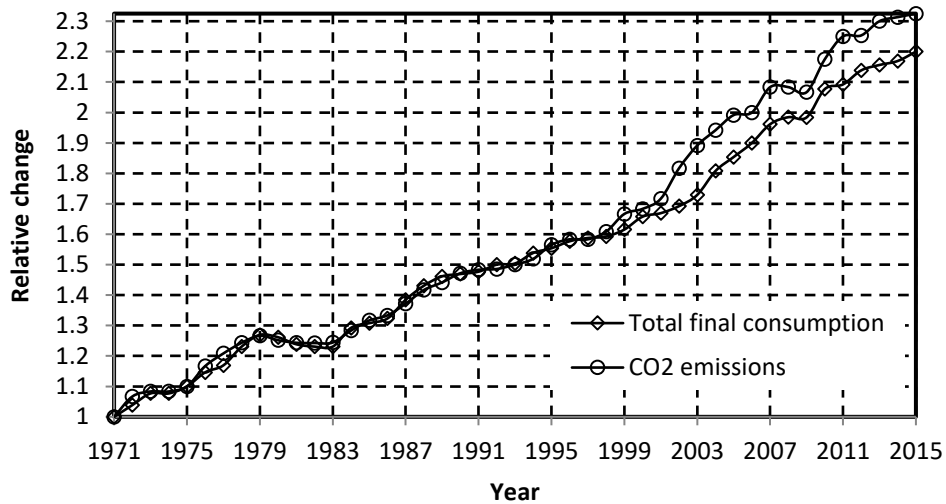
Figure 1-1- Total final energy consumption (TFC) and CO2 emissions (gathered and presented by International Energy Agency (IEA)) [2].

According to supplementary information provided by IEA, the share of three fossil fuels including oil, natural gas, and coal has been more than 70% of the world energy consumption during this period. It has also been reported by IEA that fossil fuels continue to account for much of increased energy demand to 2035, contributing 75% of global energy demand. This trend will obviously lead to rapid depletion of natural energy sources (mainly fossil fuels) and will seriously impact the environment. International policy attempts are required to create positive change in this trend by increasing energy efficiency (including renewable and green technologies) [2].

Figure 1-2 shows the world energy consumption by two important sectors: residential, and commercial and public buildings. The building energy consumption shown in Figure 1-2 was only provided by fossil fuels. It should be noted that the energy consumption in the both sectors has been reported 541.58 and 494.54 Mtoe in 1971, respectively. Although the overall change in energy use has been positive for both sectors during the entire period 1971-2015,

commercial/public buildings showed a reduction in energy consumption during 1988 and 1994 followed by a growth in energy use.
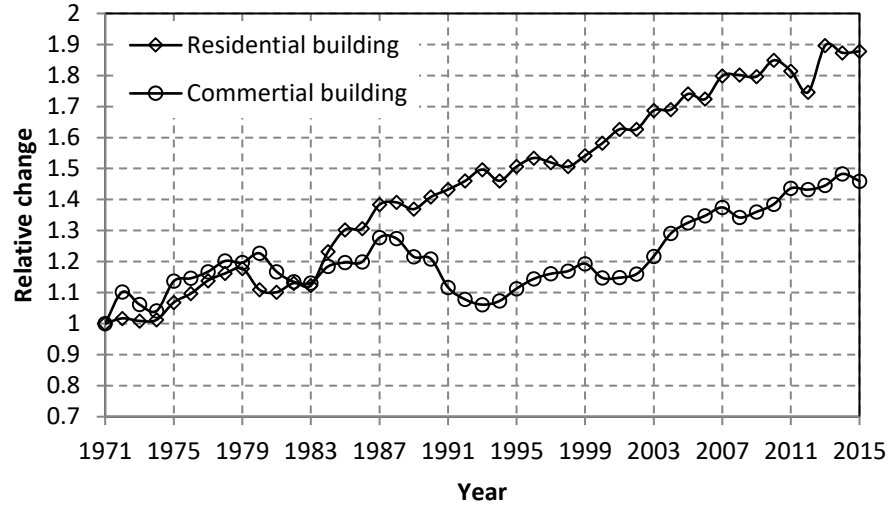
Figure 1-2- Energy consumption of buildings (gathered and presented by International Energy Agency (IEA)) [2].

Figure 1-3 compares the fossil-fuel-generated energy consumption in the building sector and the global fossil-fuel-generated energy consumption between 1971 and 2015. Figure 1-3(a) indicates that the overall fossil fuel generated energy use has increased at a low rate during those years. This could be associated with this fact that in the recent years an important part of buildings energy needs has been met by other type of energy such as renewable energy and hydro. According to Figure 1-3(b) buildings account for about 30% of the global fossil-fuel-generated energy use, which implies that they have made critical contribution to fossil fuel burning and global carbon emission. In the countries extremely dependent on fossil fuels for their energy needs, the average energy use in buildings may rise as high as 80% of total final energy use [1].
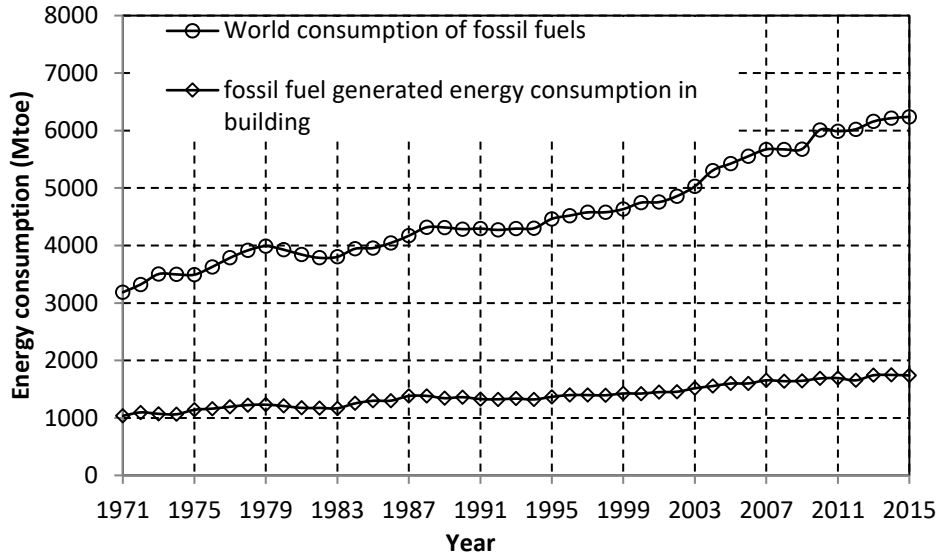
(a)
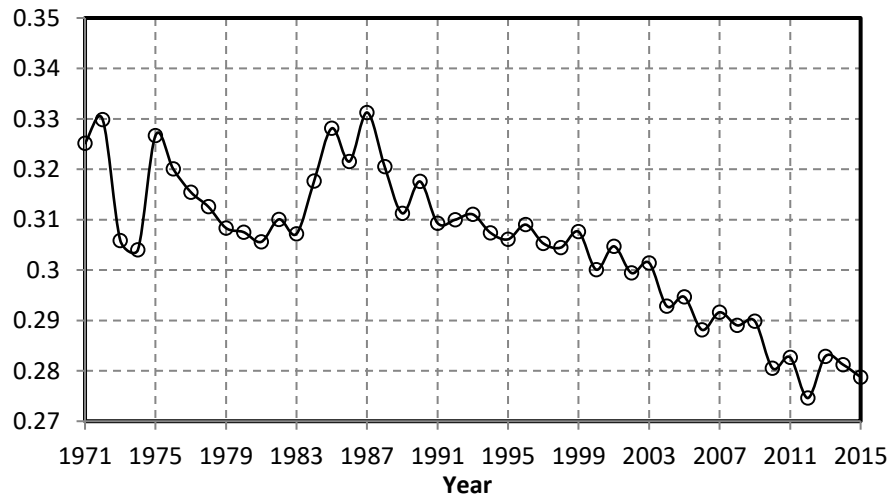
(b)

Figure 1-3- Fossil-fuel-generated energy consumption (a) a comparison between energy use in the building sector and global energy use, and (b)

However, it has not been shown how different building services make contribution to building energy consumption presented above. The main areas of energy consumption in buildings are heating, ventilation and air conditioning (HVAC), lighting, major appliances (water heating, refrigerators, freezers and dryers) and miscellaneous areas including electronics [1]. Among these

5

building services, HVAC is the largest energy end use. In developed countries HVAC accounts for 50% of the total energy use in buildings and 20% of the total national energy use [4].

USA energy statistics

U.S. building energy use in 2014 has been illustrated in Figure 1-4 [5]. It can be seen that total energy use in residential/commercial buildings was 38.5 quads[3], which is more than 40% of all U.S energy use and associated CO2 emissions. It is worth noting that the United States gets 81% of its total energy from fossil fuels, which are the major source of CO2 emissions. Figure 1-4 also indicates that HVAC accounts for about 35% of all U.S building energy, which represents as much as 12.2% of total U.S energy produced in 2014. HVAC demand of buildings is mainly supplied by both electricity and burning natural gas. Most electricity, however, is also produced from burning of fossil fuels, which indicates fossil fuels mainly supply building with heating/cooling/ventilation. For instance, the combustion of fossil fuels made contribution to providing about 70% of total U.S. electricity need in 2015.

Therefore, HAVC demand has made buildings sector in charge for a considerable share of global and U.S. fossil fuel burning and equally important source of CO2 emissions. CO2 emissions contribute to climate change having serious impact for humans and the environment. According to the U.S. Environmental Protection Agency, CO2 emissions account for more than 80 percent of the greenhouse gases emitted in the United States.

---

[3] Quad = Quadrillion Btu; Btu = British thermal unit

(a)

(b)
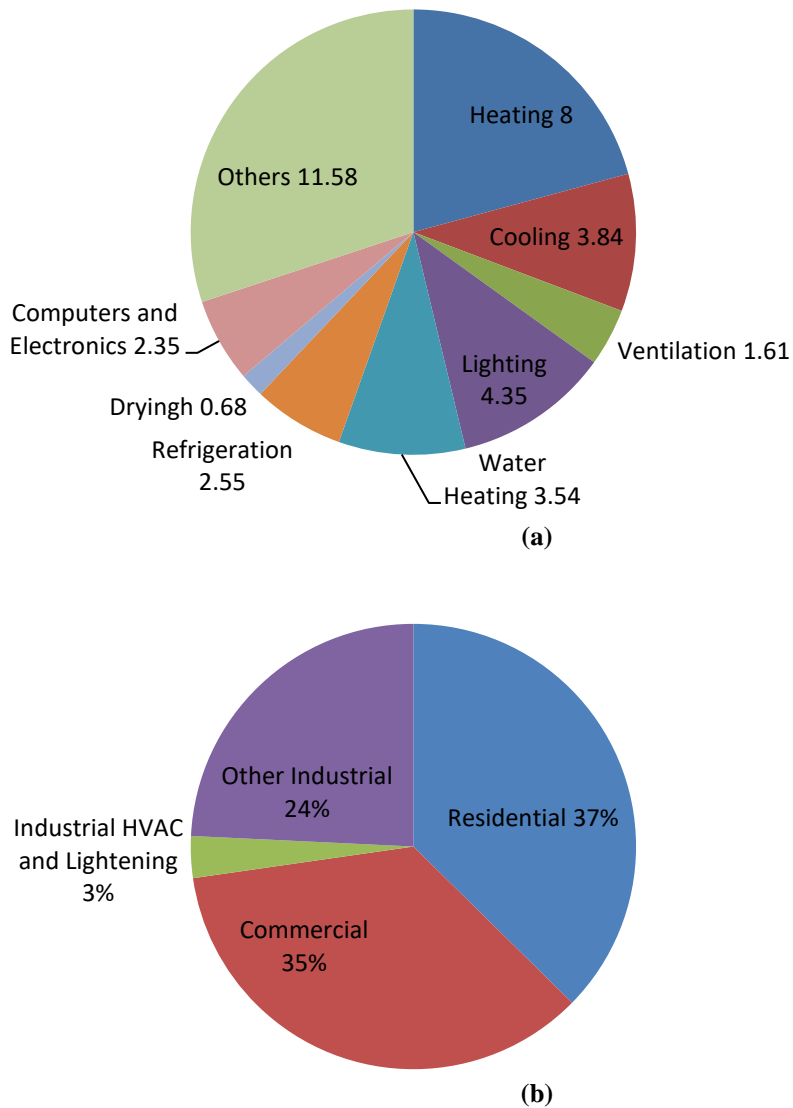
Figure 1-4- U.S. Energy use in 2014: (a) by different building services, and (b) by different sectors [5].

Generally, the increase in energy use in buildings has significant potential to raise global temperatures, to change water supplies and weather patterns, and to threaten coastal community with increasing sea levels, and will exhaust fossil fuels in the next decades. These serious negative consequences for human societies and the environment have made it essential to reduce energy consumption in buildings to meet energy and environmental challenges.

Among different building services, HAVC represents an important opportunity to decrease energy used by buildings sector and reduce CO2 emissions as it is provided by fossil fuels to an appreciable extent. This is basically can be met by instituting energy policies promoting building efficiency, new technologies for generating renewable energy and social awareness on the serious consequences of irrational use of energy. Opportunities for improving building efficiency are enormous including: high-performance windows, optimal levels of insulation, reflective surfaces, energy efficient appliances and equipment and efficient cook stoves and solid-state lighting (SSL), among others. The major and traditional renewable energy sources available for buildings are solar energy, wind energy, geothermal energy and bio energy. A combination of energy efficiency with utilizing renewable energy would cause major reduction in energy needs in buildings in the next coming years [1].

On the other hand, an increase of about 50% is in global energy demand expected by 2050 if no attempt made to improve energy efficiency in the buildings sector [1]. Moreover, 77% decrease in total CO2 emissions in building sectors by 2050 is approximately required to keep global temperature rise below 2 °C [1].

1-2- Geothermal energy and Energy piles:

Geothermal energy:

Geothermal energy refers to heat stored in ground. The heat stored in shallow depth, within 100 m below the surface, comes from sun radiation every day, while the thermal energy in greater depths is generated due to radioactivity in the earth core. Large amount of thermal energy is stored in greater depth, which makes deep geothermal energy suited for power generation in large scale [6 & 7]. However, the associated cost with making use this energy is substantial. On the other hand,

thermal energy stored in shallow depths is lower, but almost stable throughout the year. This stability refers to the fact that the temperature in the lower deep zone is not affected by the seasonal changes. Figure 1-5 displays ground temperature distribution measured at shallow depths in Atlanta, USA.
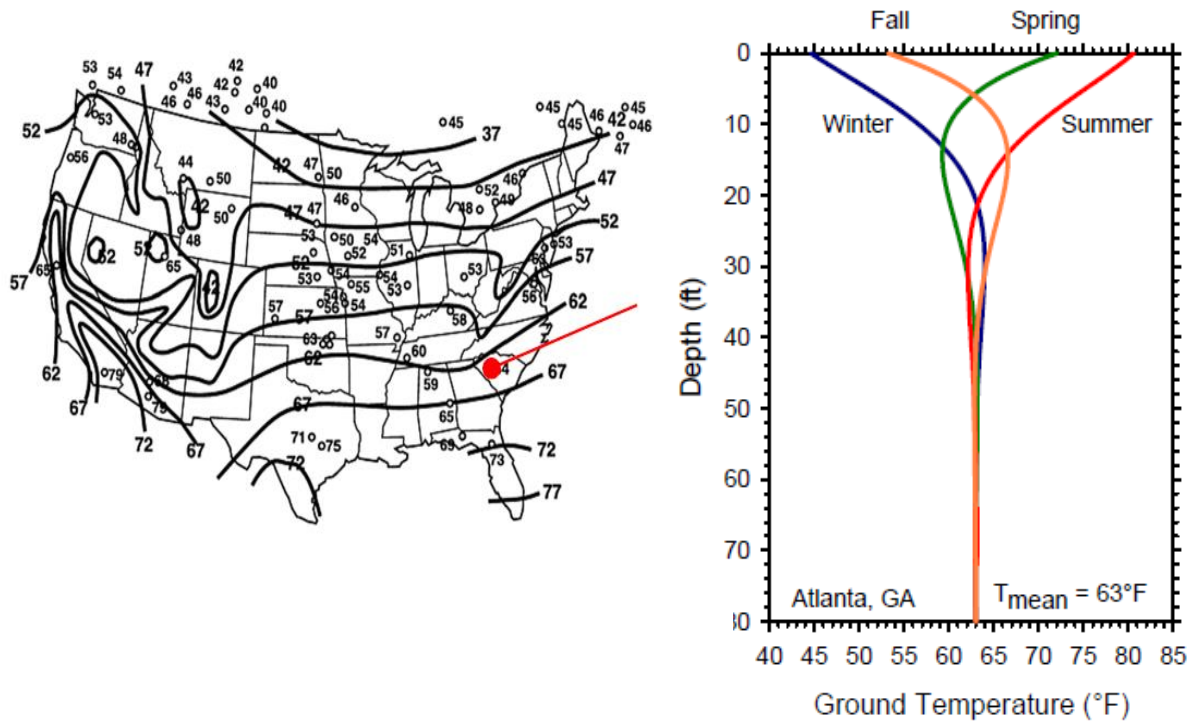
Figure 1-5- Ground temperature change with depth [8].

Figure 1-5 shows that there is seasonal fluctuation of ground temperature to a depth of 30 ft. The temperature fluctuation is less important below 30 ft and becomes zero at depth of 50 ft, where mean annual temperature is constant 63 °F. This makes shallow geothermal energy appropriate to be used as a heat source and heat sink during winter and summer, respectively. As another example, in most Europe countries the ground temperature varies between 10 °C and 15 °C in depths 10-50 m below the ground surface, while the ground surface temperature is lower. On the other hand, in the tropical regions the ground temperature is almost constant in depths of 10-50 m

9

and usually varies between 10 °C and 15 °C, while the ground surface temperature is greater (possible higher than 40 °C). This range of temperature can basically make the shallow depth to behave like a heat storage for cooling purposes during the year [14]. The variation of the mean daily ground surface temperature can be estimated using a sinusoidal function (Equation (1-1)):

$$T_{gs} = T_{m,out} + \Delta T_{out} \cos(\frac{2\pi}{\bar{P}}(t - \varepsilon_t)) \qquad (1-1)$$

T_{gs} is the ground surface temperature, t is time, $T_{m,out}$ is the average yearly temperature, ΔT_{out} is the temperature amplitude, $\bar{P}$ is the duration period, and ε_t is the phase displacement [14].

Energy piles

One of the main methodologies to make use the shallow geothermal energy is Energy Foundation or Energy Pile. Energy piles are dual-function technology, where simultaneously performs as a rigid foundation to support the top building and a heat exchanger unit for heating/cooling purposes. This section provides an overview of this technology, its application and its advantages and disadvantages. Energy piles system contains of two principal circuits: the primary circuit below ground and the secondary circuit in the building (Figure 1-6). The primary circuit consists of closed pipe work installed in the concrete pile. A heat carrier fluid is circulated through the pipes that exchanges energy from the building with the ground. The secondary circuit is also a network of closed fluid-based pipes placed in the floors and walls of the structure, bridges, beneath roads and other infrastructure requiring heating/cooling (Figure 1-6). Primary and secondary circuits are connected via a heat pump that increases the temperature level, typically from 10–15°C to a level between 25°C and 35°C [9 & 10].
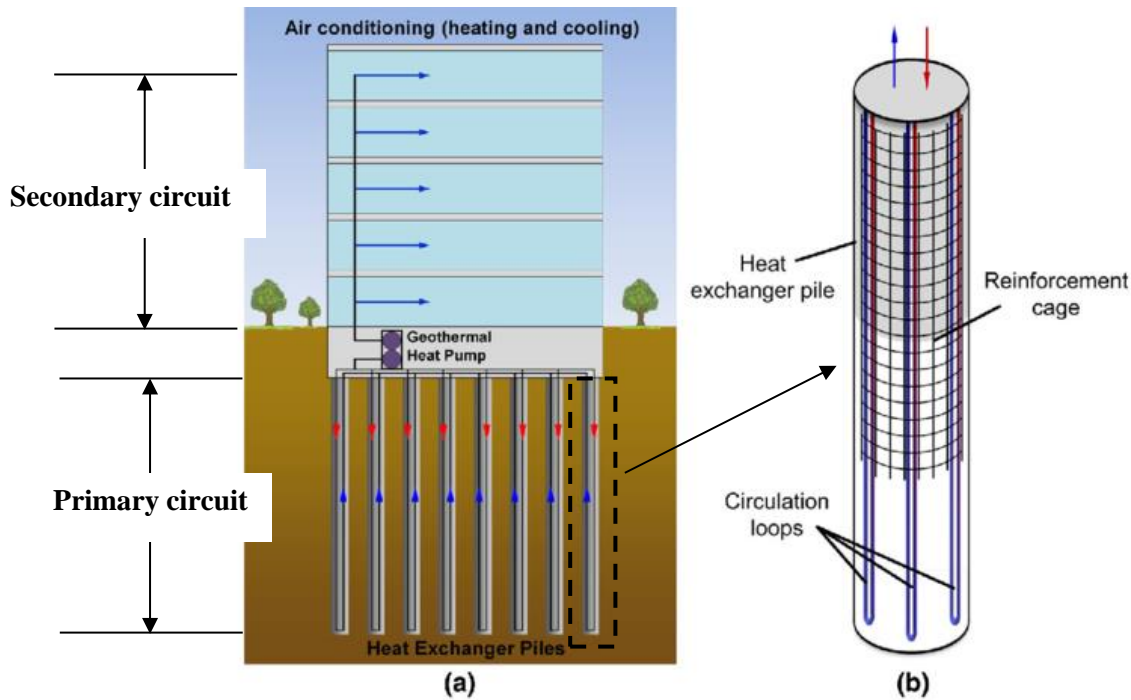
Figure 1-6- Energy pile system.

This technology provides the heating demand in buildings during winter by extracting energy from the ground. On the other hand, the cooling energy demand can be satisfied by transferring heating collected during summer and storing it into the ground for cooling purposes [6]. However, the main difference from conventional ground-source heat pump (GSHP) systems is that the pile elements that serve as heat exchangers are already required for structural purposes and need not be constructed separately [11].

Energy piles are prefabricated (driven pile) and cast-in-place reinforced concrete (drilled shafts) [12]. Nowadays, however, drilled shafts are favorable to driven piles as driving procedure may be harmful to the integrated heat exchanger system. Figure 1-7 schematically illustrates the construction sequence of energy (cast-in-place) pile: *Phase 1 and 2*: drilling a hole, *Phase 3*: placing reinforcement cage into the hole and *Phase 4 and 5*: pouring concrete. It should be noted

that other material like steel is no longer of any interest due to low heat thermal capacity as compared to concrete.
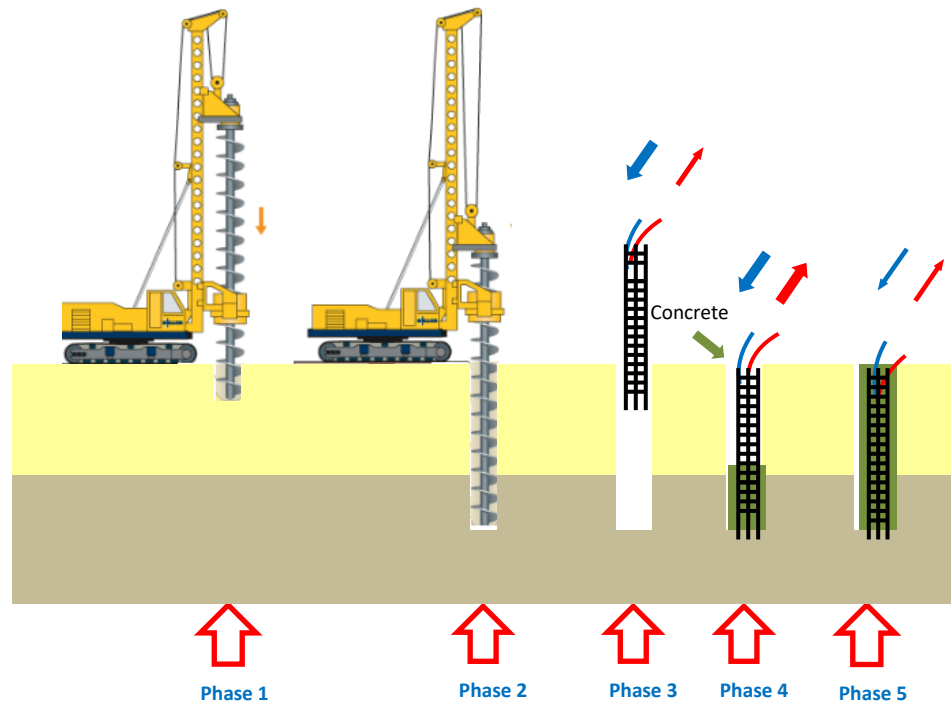
Figure 1-7- Energy (cast-in-place) pile Construction sequence.

As mentioned earlier, the fluid-carrying pipes are mounted along the reinforcement cage in both cases of driven piles and drilled shaft (Figure 1-8). The pile depth is generally determined by the mechanical load imposed by the superstructure rather than the thermal energy required [9]. However, the thermal energy transferred between the ground and energy pile increases with the pile depth that thus makes deeper energy piles more beneficial as a heat exchanger. The economically minimum depth of energy piles is about 6 m [13]. The usual diameters of cast-in-place concrete pile foundations are from 1.5-4.0 m.

Figure 1-8- Reinforcement cages with the attached fluid-carrying pipes.

The integrated heat-carrying liquid (absorber) pipes are generally made of high-grade polyethylene or Cross-linked polyethylene. Their diameter varies between 20 and 25 mm with Pipe diameters range from 20 to 25 mm, with 2.0 or 2.3 mm wall thickness respectively [10]. The pipes length mainly depends on pile depth and the thermal energy required. Continuous loops of pipes (heat exchange loop) with different configuration are installed in energy piles. The configuration is generally chosen based on the required thermal energy and overall efficiency of the system. Common configurations practically used are single/double/multi U-tube, single/double/multi W-tube (Figure 1-9). The pipes are generally pressurized prior to concrete pouring to avoid any potential damage to the pipes due to confining pressure imposed by the wet concrete. The pressure is relieved once the concrete has hardened after a few days [10].

Heat transfer liquid circulated in the integrated pipes is generally water in places with warm weather, while antifreeze solutions such as water and glycol mixtures, saline solutions, brine, potassium acetate are commonly used in cooler climates [10]. However, Kavanaugh recommended no to use antifreeze fluid as a part of heat transfer liquid. Generally lower flowrate of the fluid is more preferred as the circulated fluid has more time to exchange heat with the surrounding ground [10].

W-shaped pipes

U-shaped pipes

(single, double or triple)
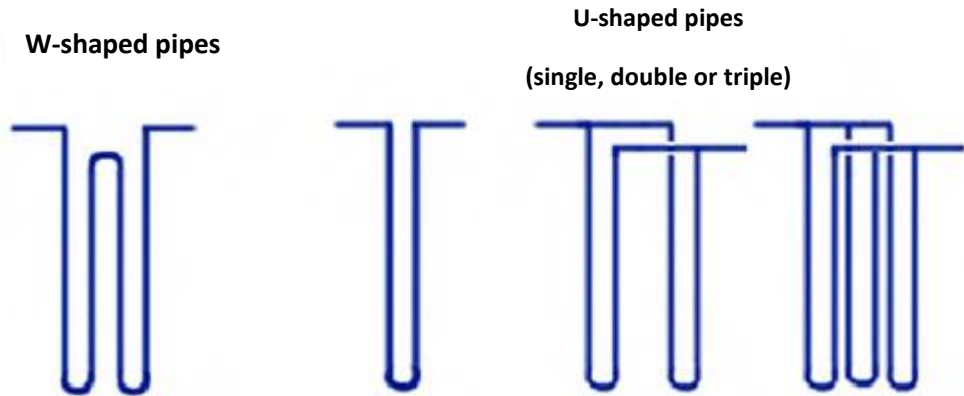
Figure 1-9- Heat exchange loop configuration [10].

The heat pump connecting the primary circuit to the secondary circuit has responsibility of circulating the heat-transfer-fluid through the absorber pipes. As shown in Figure 1-10, in winter, the cooler fluid (from the secondary circuit) is transferred to the primary unit (by the heat pump) to extract energy from the ground with higher temperature.
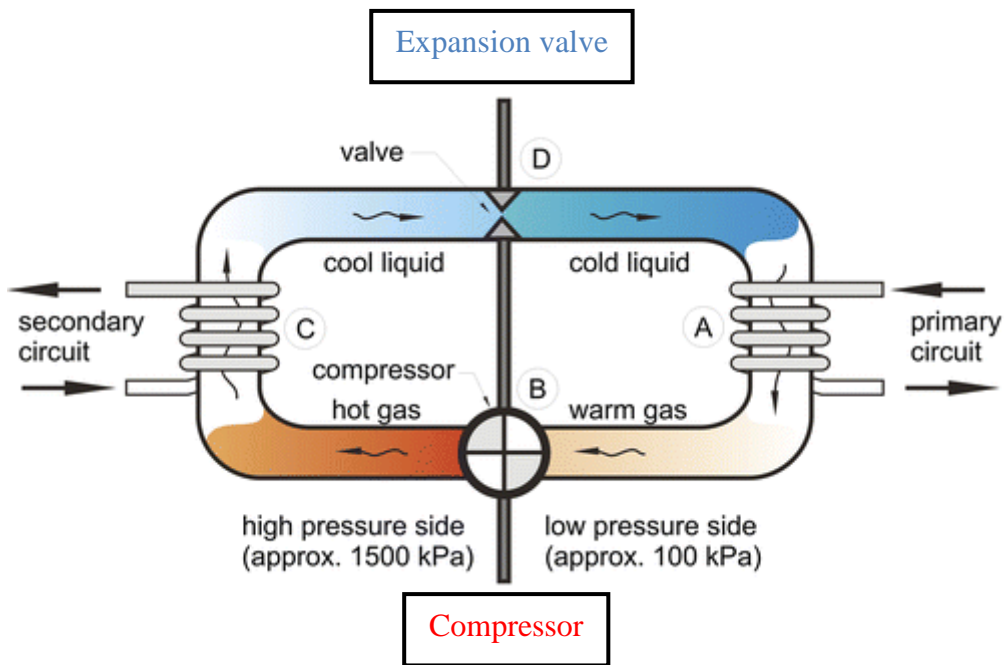
Figure 1-10- Heat exchange process in a heat pump.

The extracted thermal energy is raised by a compressor to higher, usable temperature to provide warmth to the interior of the building (Figure 1-10). In summers, however, the heat generated in building transfers to the ground with lower temperature to provide cooling demand. Therefore, heat is cyclically exchanged in each circuit during the heat pump operation. It also cyclically changes the temperature along the pile and the surrounding soil.

Figure 1-11 shows the temperature fluctuations in soil around energy piles supporting a rehabilitation center in Vienna [14]. The temperature fluctuations were recorded between February 2003 and December 2005. As it can be seen the ground temperature rose up to 16 °C (in summer) and dropped down to about 6 °C and a cyclic trend was created. Note that each number (along the horizontal axis) presents a month plotted in chronical order.
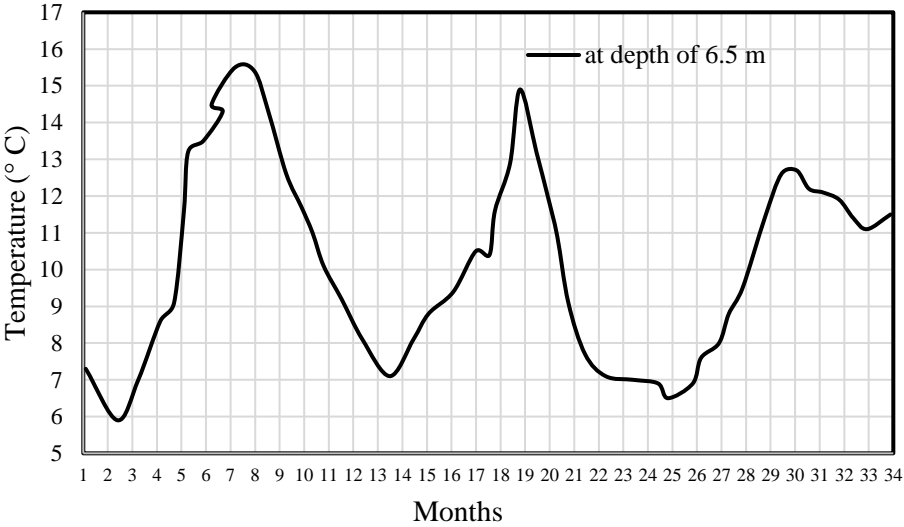
Figure 1-11- mean daily ground temperature variation due to energy pile operation (rehabilitation center in Vienna) [14].

Figure 1-12 also illustrates the temperature variations in the surrounding soil of a group of energy piles (with pile spacing of 1.4 m) supporting a raft foundation beneath a paper-processing plant in Vienna [14]. The date shown in the figure is only presented for depths of 5.0 m, 10.0 m and
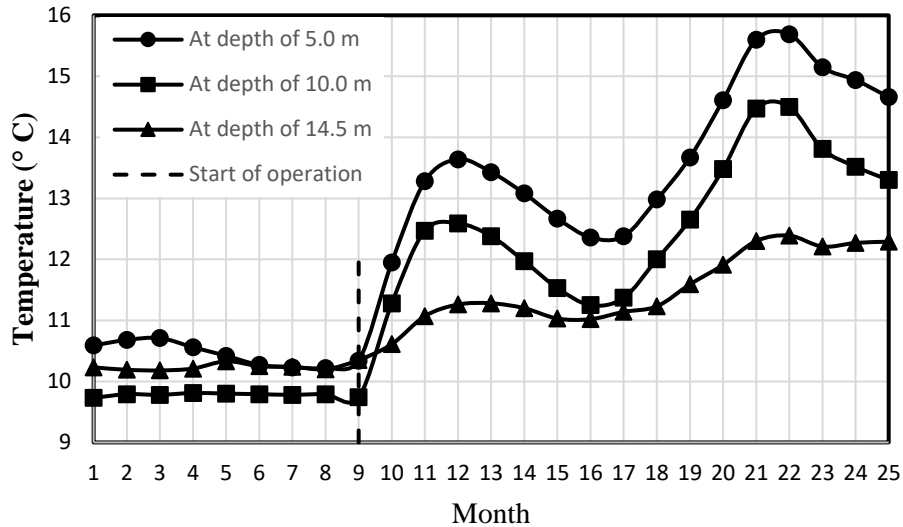
Figure 1-12- mean daily ground temperature variation due to energy pile operation (paper processing plant in Vienna) [14].

14.5 m during a 2-year period starting from Nov 1994 and ending Nov 1996. Note each number (along the horizontal axis) presents a month sorted in chronical order. It is clearly seen that the amount of temperature variation due to energy pile operation, starting in July 1995, never exceeded 5 °C. It is obviously a smaller change in temperature as compared with that shown in Figure 1-11. Generally, the change in soil temperature due to pile energy operation depends on many factors including the ground temperature and energy demand of the building.

Continuous or intermittent operation of an energy pile system can generate different trend of temperature variation in the pile and surrounding soil, as shown by Faizal et al (2016) [23]. Intermittent operation is more common in residential buildings, where the heat pump operates for a part of day, while continuous operation may be more appropriate for other types of buildings such as commercial and industrial buildings. Figure 1-13 shows the temperature variations in an actual energy pile, working in heating mode, due to three operational modes: 24 h continuous operation (24 h mode), 16 h operation with 8 h rest (16 h mode), and 8 h operation with 16 h rest (8 h mode) [23]. Intermittent operation causes a cyclic temperature variation in the pile, while in

16

continuous operation the pile temperature degrades continuously with a decreasing rate with time. Higher heat transfer between energy pile and the ground is expected in intermittent operation compared to continuous operation due to temperature recovery occurring in the ground during the stoppage (resting) time. Moreover, as shown by Faizal et al (2016) [23], induced thermal stress/strain in pile due to intermittent operation is lower than those developing during continuous operation, due to lower pile temperature change.
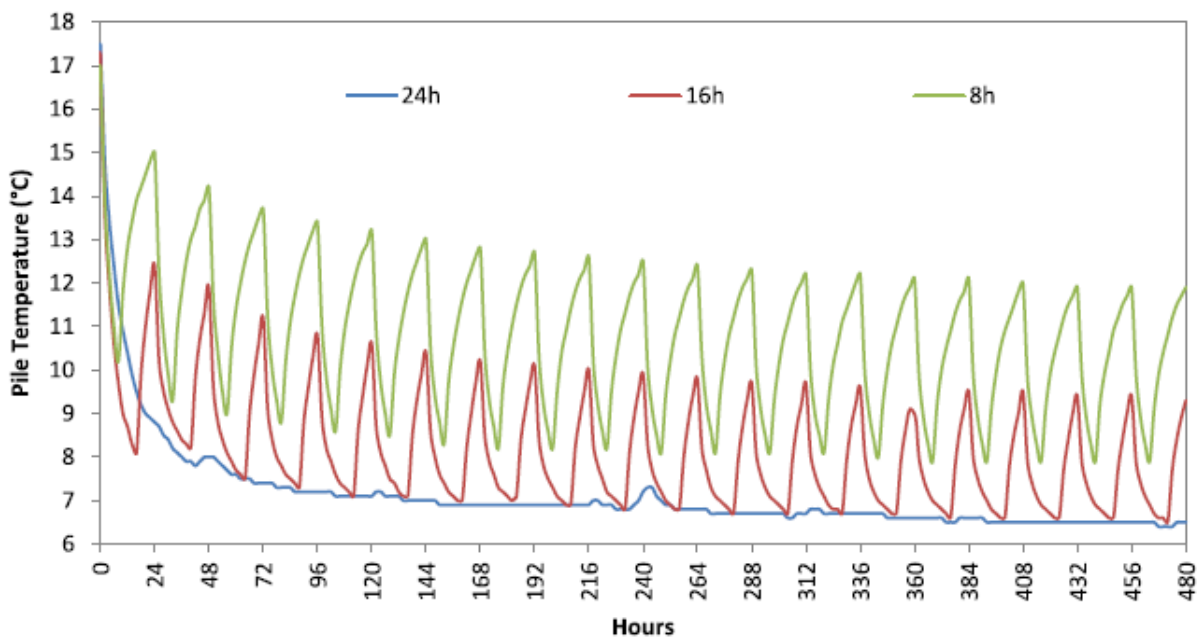
Figure 1-13- pile temperature variation during three different operation modes [23].

The soil temperature around an energy pile also can change due to hydration of cast-in-place energy piles. Brandl [14] reported that the ground temperature can rise to 70 °C due to the pile hydration (within 24 hours after concrete pouring) that may significantly affect the soil properties. It should be noted, however, thermal energy provided by this technology does not completely satisfy all heating/cooling energy demand, but electrical energy is still required to drive the heat pump [10]. According to Brandl [12], a well-designed energy foundation system generally extracts

75% of total energy required from the ground, while electrical energy is responsible for 25% of total energy required.

The efficiency of heat pumps and the entire geothermal foundation system is evaluated using the coefficients of performance (COP), and the seasonal performance factor (SPF), respectively. COP is a heat pump parameter, which is defined as the ratio of the output energy (usable energy derived) and the input energy (electrical energy consumed to derive the heat pump) [14]:

$$COP = \frac{\text{Output energy after heat pump}}{\text{input energy for heat pump opertaion}} \qquad (1-2)$$

COP generally varies between 3 and 6 [14]. However, for economic reasons a value of COP $\geq$ 4 is usually required to be achieved, as mentioned by Brandl (2006) [14]. It should be mentioned, COP=4 means that a heat pump requires 3 portions of geothermal energy and 1 portion of electrical energy to generate 4 portions of usable energy. Basically, the amount of usable energy generated from a certain amount of geothermal energy is greater by a heat pump with higher COP, implying that the energy loose between primary and secondary circuits is lower. In other word, higher temperature required in the secondary circuit along with low temperature of the shallow depths decreases the efficiency of the system operating in winter mode [13]. For this reason, the usable temperature in the secondary circuit should vary between 35°C and 45°C, and the temperature of fluid circulating in the primary circuit should be above 0-5°C [13]. In summer mode, however, lower use temperature (inflow temperature to the cooling system of the secondary circuit) and high temperature of the ground reduces the efficiency. Therefore, this technology is appropriately applicable to conditions where low temperature heating/cooling is required.

In addition to the thermal efficiency of heat pump, the following factors also affect the overall efficiency of the system [15]:

(1) thermal and hydrogeological characteristics of the ground including: thermal conductivity and thermal capacity of the subsoil layers, ground temperature in shallow depths, ground water level (moisture content), and direction and velocity of groundwater flow (hydraulic gradient of ground water).

(2) Properties of energy piles, including: energy pile spacing and length, thermal conductivity and heat capacity of pile material and integrated tubes, and pile and tubes diameters.

(3) Properties of heat-transfer fluid including: flow rate and thermal and physical properties.

(4) Cycles of heating and cooling, energy demand and climate condition.

SPF of a thermo-active system with a heat pump is the ratio of the usable energy output of the entire system to the electrical energy required to generate it, which accounts for all factors mentioned above. Therefore, SPF is a more appropriate parameter for evaluating the performance efficiency of entire system as compared to COP, as it accounts for all components (including the primary/secondary circuits and the heat pump) contributing to energy production. Currently, typical values of SPF vary between 3.8 and 4.8 [14].

Due to larger thermal conductivity, saturated soils (like saturated clay) enhance the efficiency of a thermo-active system as compared with dry soil (like dry sand and gravel). Moreover, for a certain heating/cooling demand deeper and larger piles are required if the pile installation occur in dry soils. Generally, producing 1 kw heating requires a pile shaft area of 20-50 m^2, where the lower limit occurs when the pile is installed in saturated soils, while the upper limit is valid for dry soils [12].

The energy pile operation can be classified into two categories: single mode operation and seasonal mode operation [16]. In single mode operation the energy pile is responsible of providing either heating (in winter) or cooling (in summer) (as shown in Figure 1-14), which implies that heat flow takes place in one direction (i.e. either from the ground into the pile or from the pile into the ground). This mode of operation may not be environmentally friendly as the heat extracted/recharged from/into the ground is not recovered/discharged during pile operation. This, in turn, causes an imbalance in the surrounding soil's energy that may change the ground temperature with time and reduce the long-term efficiency of the system. However, in soils where heat convection makes important contribution to heat transfer (i.e. highly permeable soils with high hydraulic gradient of groundwater (greater than 0.5 m/day)) the induced energy imbalance can be relatively fixed [13]. In this case recharge/discharge naturally occurs during winter/summer due to groundwater flow (heat convection)

On the other hand, a two-way heat transfer takes place when seasonal operation occurs, where earth's energy equilibrium is annually achieved during heating/cooling periods in a year. Thus, it is unlikely that this mode impacts the long-term efficiency of a geothermal system. Furthermore, it is preferred by the ecologist due to its environmentally friendly for the sustainability of groundwater [13]. Ground with low permeability and a low hydraulic gradient of the groundwater are preferable for the seasonal mode [14].
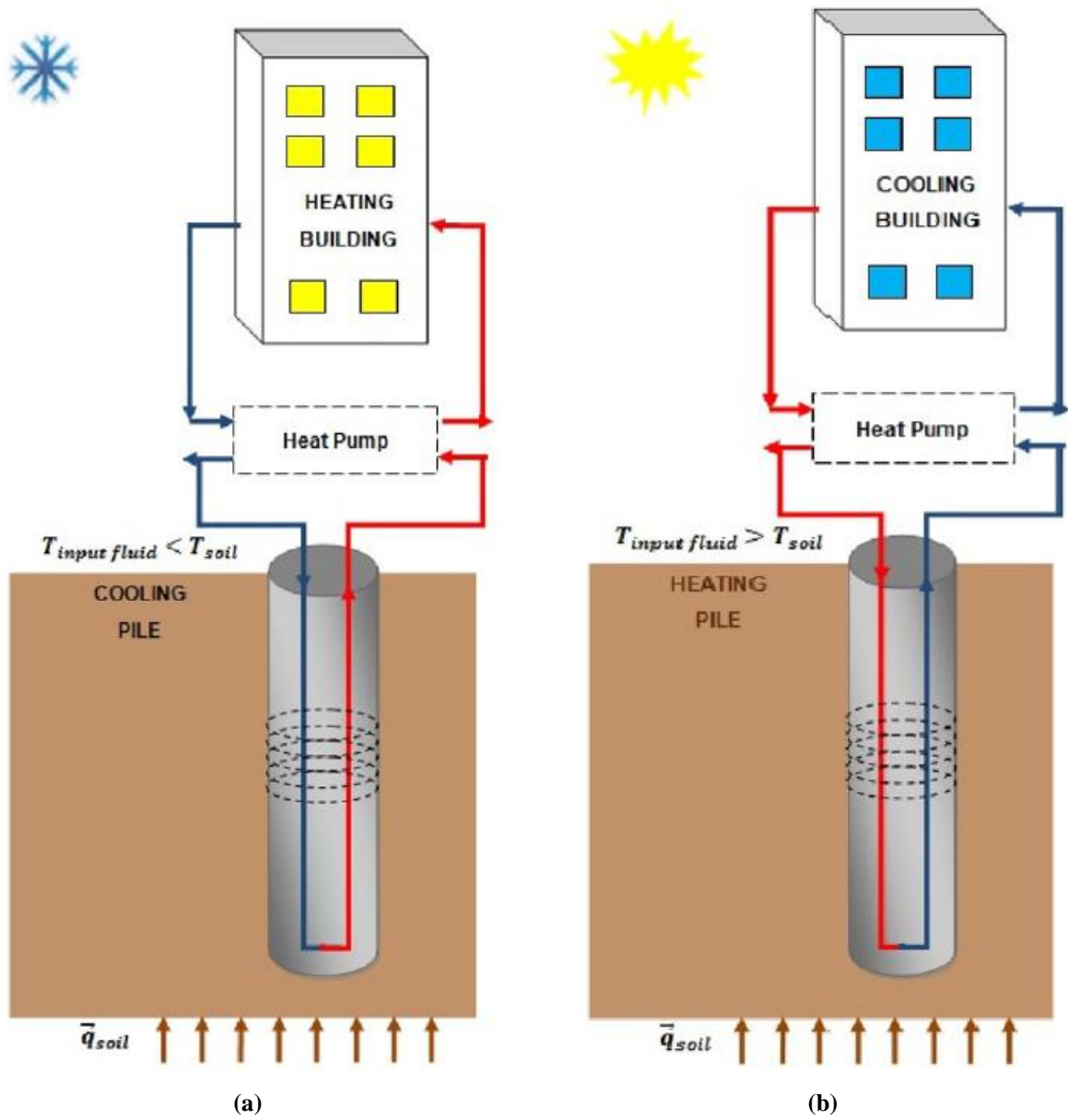
Figure 1-14- Scheme of energy piles system operation: (a) energy extraction and (b) energy storage.

Well-designed energy piles can importantly reduce the heating/cooling cost. Additionally, they effectively contribute to environment protection through using clean and renewable energy know as geothermal energy. Austria, Switzerland and Germany are known as the first countries that have investigated and utilized geothermal energy using different approaches including energy pile application. Currently, however, the energy pile application is globally growing for heating/cooling purposes [10]. Figure 1-15 shows the number of energy piles employed in Austria between 1984 and 2004 [13]. Brandl (2013) reported that during 2005-2013 energy piles installed per year was higher than 6000 [13].
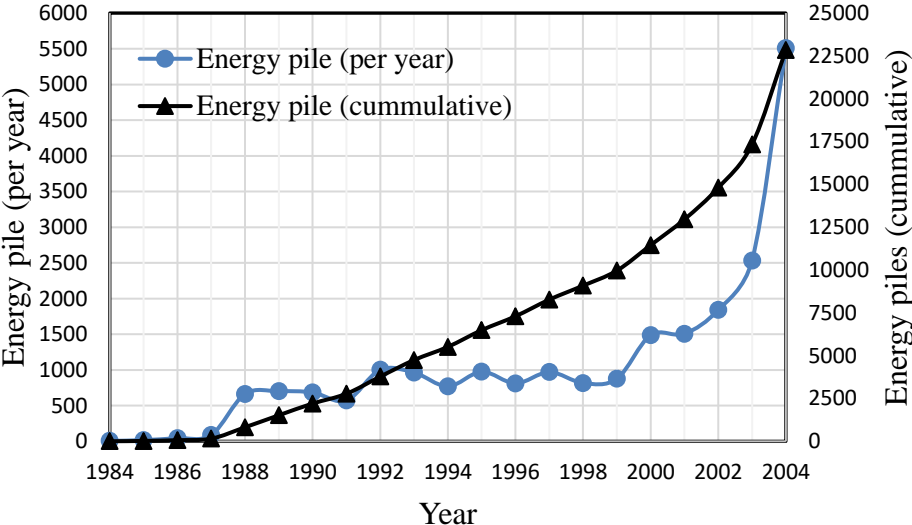
Figure 1-15- Number of energy piles employed in Austria between 1984 and 2004 [13].

Figure 1-16 also shows the trend of energy pile use in UK between during 2005-2015 and the resultant decrease in CO2 emissions. As it can be seen, annually increasing use of energy pile was associated with annual decline in the energy-related CO2 emission.
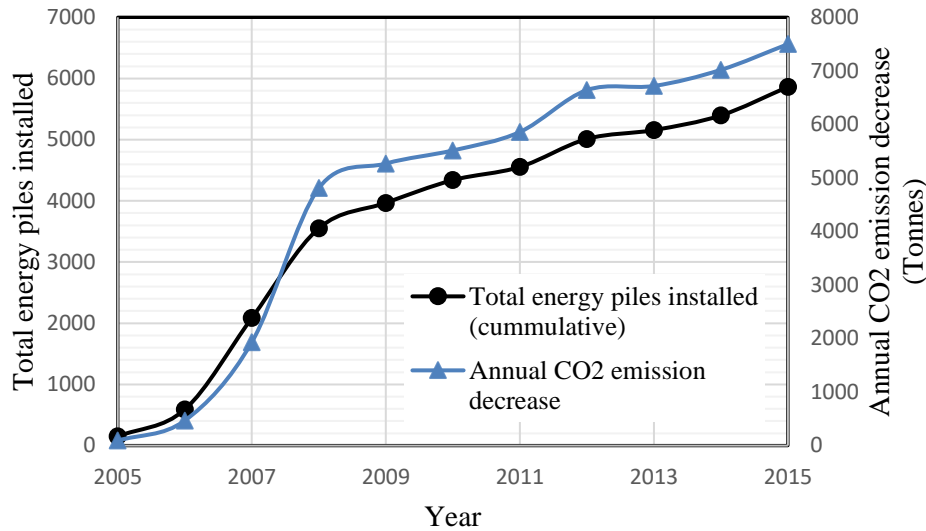
Figure 1-16- Number of energy piles employed in UK between 2005 and 2015 and the resultant reduction of CO2 emission [17].

Some successful utilization of geothermal power using different technologies, including: energy piles, diaphragm wall and conventional heat exchangers, is presented in Table 1. These technologies can be employed by residential/commercial/industrial buildings, roads, (underground subway) tunnels and bridges for providing heating/cooling demand. However, energy piles are more feasible for buildings that structurally require piles, while diaphragm walls and horizontal loops are more suitable for other structures like underground subway tunnels, carparks, and the buildings supported by shallow foundations [10]. However, the installation cost is usually compensated in the first years of building operation through significant energy saving and reduced energy cost.

Table 1-1- Case histories of geothermal energy utilization using different technologies.

Case study	Characteristics of the thermo-active system
Lainzer Tunnel, Austria (Vienna)	(1) The tunnel was a part of a railway station, which uses energy piles (bored pile) in its side walls (lot LT24). Energy piles operation started in spring 2004 to provide heating/cooling demand of the administrative buildings [9]. (2) The thermo-active system consists of 59 energy piles with a diameter of 1.2 m and an average length of 17.1 m. It should be noted that every third structural piles were converted to an energy pile [9]. (3) About 50% of the total required heat was provided by geothermal energy [9].
Uniqa Tower, Austria (Vienna)	(1) It is a high-rise building with a surrounding diaphragm wall reaching down to a depth of 35 m below the ground surface [9]. (2) In this project diaphragm walls served as heat exchanger (by placing absorber pipes inside them). 7800 m^2 of diaphragm walls made contribution to energy absorption from the ground to produce a heating capacity of 420 kW and a cooling capacity of 240 kW [9]. (3) Ground water was at shallow depth making the surrounding ground ideal for geothermal utilization [9]. (4) The annual heating output reaches up to 818 MWh and the annual cooling output up to 646 MWh [9].
EA Generali Centre, Austria (Vienna)	(1) It is a high-rise building with a surrounding diaphragm wall used as heat exchanger. (2) 4200 m^2 of the diaphragm wall was used for energy absorption from the surrounding ground. (3) The annual heating output reaches up to 630 MWh and the annual cooling output up to 220 MWh [9].
Columbus Centre, Austria (Vienna)	(1) It is a high-rise building. The energy absorber system consists of diaphragm wall (12400 m^2) and 300 energy piles [9]. (2) The energy absorption can produce a heating capacity of 1428 kW and a cooling capacity of 370 kW [9]. (3) The annual heating output reaches up to 1677 MWh and the annual cooling output up to 660 MWh [9].
Euros Office Centre, Austria (Vienna)	(1) It is a high-rise building. The energy absorber system consists of 242 energy piles and mat foundation (6000 m^2) [9]. (2) The energy absorption can produce a heating capacity of 2026 kW and a cooling capacity of 1680 kW [9]. (3) The annual heating output reaches up to 1450 MWh and the annual cooling output up to 840 MWh [9].

Table 1-1 (continued)

Project	Characteristics of Energy foundation
Swiss Federal Institute of Technology in Lausanne	**(1)** Energy foundation in this project was energy pile that was extensively used for study the thermo-hydro-mechanical response of energy pile and the surrounding soil [9].
Dock Midfield terminal at Zurich airport, Switzerland	**(1)** 300 energy piles (of total 440 structural piles) were employed as energy absorber (energy foundation) to satisfy heating/cooling demand of the terminal [9]. **(2)** 85% of annual heat demand (approximately 2700 MWh/year) was reported to be met by the geothermal energy (through the energy piles), while annual cooling demand (approximately 1200 MWh/year) was provided by the geothermal energy [9]. **(3)** 25% saving was reported to be achieved by this system and the energy pile installation cost was compensated in almost 8 years [9].
The 200 m high Frankfurt Main tower, Frankfurt, Germany	**(1)** The energy foundation of this building was 112 energy piles having a length of 30 m. The total piles supporting the structural loads are 213 end-bearing piles with length of 30-50 m [9].
Berlin's International Solar Center, Berlin, Germany	**(1)** The heat exchanger system consists of 200 energy piles designated to provide 20% and 100% of heating and cooling demand, respectively [9].
Lambeth College's new sixth form center, UK	**(1)** Heating/cooling demand of the building was met by employing 146 energy piles having a length of 25 m [9].
Stockton College, New Jersey, United States	**(1)** It employs the conventional ground heat exchanger which consists of heat exchanger wells and a water source heat pump [9]. **(2)** The implementation of this system resulted in a reduction of 25% in electricity and 70% in natural gas consumption. Overall the system was found to significantly contribute to a confirmed 13% overall reduction in CO_2 emissions at the College [9].

As mentioned earlier, this technology could also be used in bridge decks by placing the secondary circuit (absorber pipes) inside the deck, as shown in Figure 1-17. This way bridge decks can benefit in many ways such as [14]:

(1) by keeping the deck temperature positive ($\geq 2\ °C$) the pavement will be free from ice and snow, that thus the possibility of car accident will significantly reduce,

25

(2) the heating provided can be used instead of using de-icing salt, which generally makes roads unclean,

(3) cyclic expansion/contraction of the pavement and the effects of freeze-thaw cycles can be considerably minimized by keeping the pavement temperature constant during the year. This, in turn, minimizes the relevant structural damages to the pavement, and

(4) maintenance cost will be decreased.
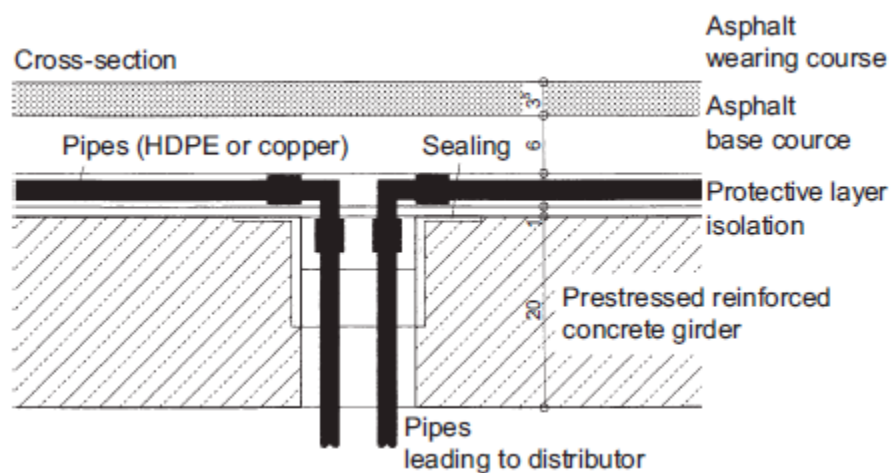
Figure 1-17- Ground source heat exchanger utilized for heating/cooling purposes in bridge deck [14].

As for road pavements, similar benefits can be counted due to application of energy piles. However, as mentioned by Brandl [14], the negative impacts of the use of snow chains (such as mechanical aberration of the road surface) can be avoided by keeping the pavement temperature above 2 °C. Figure 1-18 illustrates a schematic view of road pavement employed absorber pipes for heating/cooling purposes.
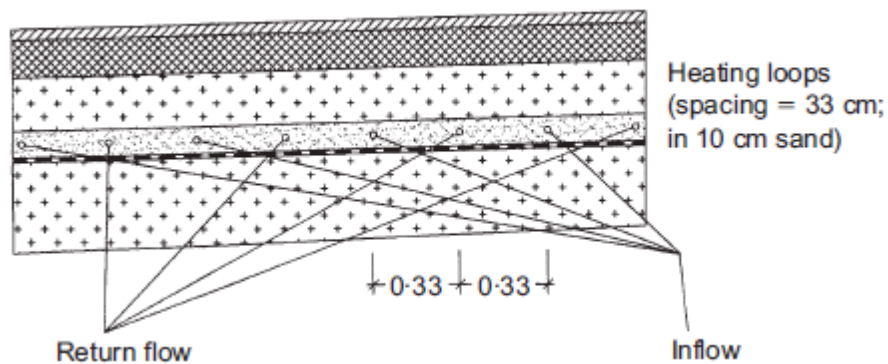
Figure 1-18- Schematic view of road pavement equipped with integrated heat exchange (absorber) pipes [14].

Energy tunnels incorporating supporting elements (including anchors, rock/soil nails and secondary concrete lining) and heat exchanger (absorber) pipes can be used for heating/cooling of underground structures such as transportation tunnels, car parks, and basements of high-rise buildings. Anchors and soil nails are able to utilize significant amount of geothermal energy as they are usually inserted deeply into the surrounding ground [14]. Interestingly, nearby structures (including residential/commercial/public buildings) can also benefit by using the extracted geothermal energy by the tunnel with geothermal equipment. For instance, Branld reported [14] that heating/cooling demand of about 1200 adjacent private buildings as well as large public buildings can partially be met by a railway tunnel in Vienna with geothermal equipment.

Unlike the energy piles, tunnels are usually located at depths with almost constant ground temperature, that thus can utilize larger amount of geothermal energy. Furthermore, the heat generated by transportation (in the tunnel) is another source of energy that exchanges heat with the absorber pipes.

Design of energy piles:

The German VDI 4640 design standard and International Ground Source Heat Pump Association (IGSHPA) guidelines are the two most famous standard which have been used since the early 80's [10]. An appropriate design approach allows us to choose an energy pile system with high thermal efficiency. The thermal efficiency could be assessed before and after construction through numerical analyses and field tests. The COP and SPF, as mentioned earlier, are two factors employed as quantitative indices of thermal efficiency assessment. Both the primary and secondary circuits (and their components) and the heat pump should be taken into account in analysis and design of the system.

Numerical solutions to heat transfer in energy pile system are based on cylindrical heat source theory indicating that the heat transfer along the heat exchange (energy pile) only occurs in radial direction and is constant [10]. Input data for a computer software package employing a numerical solution basically includes building heating/cooling demand, air temperature, ground temperature distribution, geothermal properties of soil and primary/secondary circuits, while the output could be mean daily COP/SPF [10].

The thermal response test (TRT) is a field test widely used to assess the thermal efficiency of energy pile system before and after construction [18-21]. The test consists of circulating a fluid (with known inlet temperature) into the absorber pipes and measuring the outlet temperature with time. It allows us to estimate the ground thermal conductivity, pile thermal resistance and thermal efficiency of the energy pile system, which are important parameters for an accurate design. The soil thermal properties such as thermal conductivity may also be measured using laboratory tests. However, laboratory tests should be conducted under real field conditions by inclusion fluid flow and field mechanical stresses.

Generally, the following steps should be taken when analyzing and designing an energy pile system:

Obviously the *first step* is to estimate the amount of heating/cooling energy demand of the building. Knowledge of types of the building- generally classified based on the size, use, construction type/material, nature of occupancy- and temperature of outdoor and primary/secondary circuits is necessary in this step. Based upon this information from this step the operation mode of the system (i.e. single mode or seasonal mode) and the required thermal ground properties required to achieve an optimum performance is determined [10].

The *second step* consists of geotechnical/geothermal/hydrological properties determination. The geotechnical properties determination generally includes physical/hydraulic/strength parameters estimation. The geothermal properties determination mainly involves estimation of thermal conductivity/capacity of ground, in-situ ground temperature and ground thermal gradient. The hydrological properties include groundwater level, groundwater level fluctuations, groundwater flow direction and velocities, etc. [10 and 14].

In the *third step* an initial guess for the foundation details is made based upon the data from steps 1 and 2. The foundation details include type and size of energy foundation (length, width, thickness and diameter), depth of energy foundation, pattern of energy foundation installation (position and spacing), installation method and construction material used and its thermal/mechanical properties. Furthermore, details of primary/secondary circuits (including all integrated absorber pipes), heat pump and type and velocity of circulating fluid within absorber pipes should be determined in this step [10 and 14]. Brandl [14] suggested the following information, including the geometrical characteristics of energy foundation and the corresponding extracted geothermal energy, that could be used in pre-design phase of energy foundation:

- Energy piles with diameter, D = 0.3–0.5 m: 40–60 W/m.

- Energy piles with diameter, D ≥ 0.6 m: 35 W per 1 m2 of shaft area.

- Diaphragm walls: 30 W/m2.

- Base slabs: 10–30 W/ m2.

However, this pre-design information should be approved in the following design steps using numerical analyses and field test investigation.

1-3- Heat transfer between energy pile and soil

Figure 1-19 illustrates the heat exchange process in an energy pile. According to the figure, in heating mode, heat flows from the circulating fluid in the absorber pipes to the surrounding concrete and soil, while it flows in the opposite direction in cooling mode. The heat transfer generally occurs through several processes including convective heat transfer at the fluid-pipe interface, and conductive heat transfer through the tube wall, concrete and surrounding soil. Other heat transfer mechanisms such as convection and radiation in the solid phase of the geothermal pile system are ignored.

The conductive heat transfer in the tube walls, concrete and surrounding soil is generally three-dimensional transient process that can be presented by the following equation in cylindrical coordinates with radius r, azimuth φ and axis z [14]:

$$\frac{\partial T}{\partial t} = \frac{\lambda}{\rho c}\left(\frac{\partial^2 T}{\partial r^2} + \frac{1}{r}\frac{\partial T}{\partial r} + \frac{1}{r^2}\frac{\partial^2 T}{\partial \varphi^2} + \frac{\partial^2 T}{\partial z^2}\right) \tag{1-3}$$
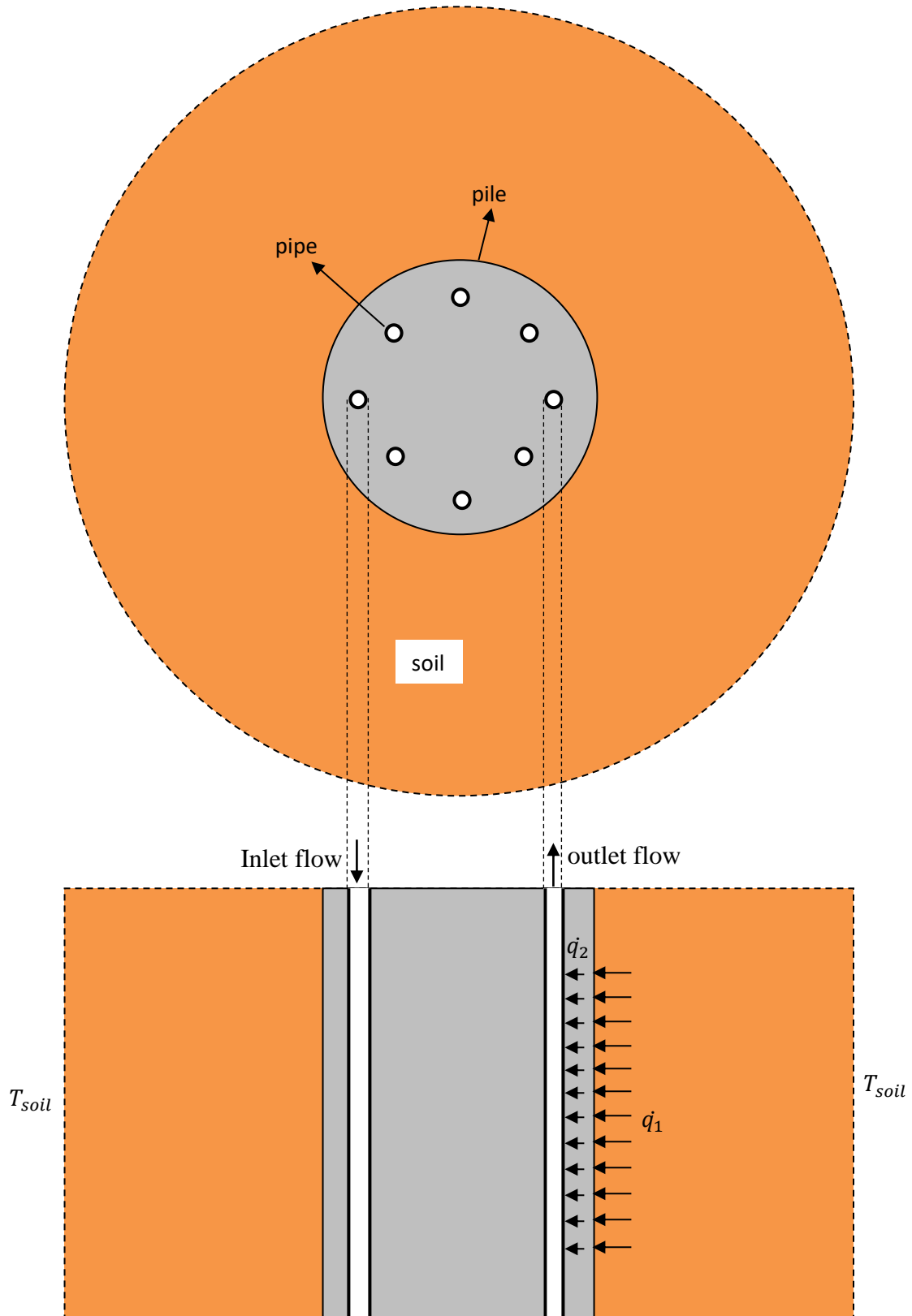
Figure 1-19- Schematic of heat transfer in energy pile.

Where, λ is thermal conduction coefficient, ρ is the unit weight and c is specific heat capacity.

Thermal conduction coefficient λ (W/m °C) is a measure of the ability of a material to transfer heat by conduction and defined as heat energy (Watt) transferred per unit time and area per unit temperature gradient $(= \frac{\Delta T}{L})$. It is also a temperature-dependent parameter. In porous media such as rock and soil, λ is influenced by porosity, density, moisture content, the chemical properties pore fluid, and soil particles mineralogy. The thermal conduction coefficient od soil can be approximated using the following equation:

$$\lambda_{soil} = \lambda_{solid}^{(1-n)} \cdot \lambda_{pore-fluid}^{n} \qquad (1-4)$$

Where, n is soil porosity and λ_{solid} and $\lambda_{pore-fluid}$ are thermal conductivity coefficients of solid particles and pore fluid, respectively. Soil thermal conductivity is commonly measured using a thermal response test (TRT) or alternatively using laboratory testing.

The heat capacity c (J/kg K) defines the amount of energy stored in a material per unit mass per unit change in temperature [14]. This material property must be considered in calculations of transient conductive heat transfer. The specific heat capacity of soil can be estimated (Equation 1-3) by taking into account the specific heat capacities of different components of soil mass.

$$c_{soil} = \left(c_{solid} \cdot (1-n) \cdot \rho_{solid} + c_{pore-fluid} \cdot n \cdot S_w \cdot \rho_{pore-fluid} + c_{air} \cdot n \cdot (1-S_w) \cdot \rho_{air} \right) \Big/ \rho_{soil} \qquad (1-5)$$

Where, c, n, ρ and S_w are specific heat capacity, porosity, density and degree of saturation, respectively.

λ, ρ and c of the soil and concrete are temperature-dependent parameters and can been combined into a single parameter known as thermal diffusivity a ($\frac{\lambda}{\rho c}$), which has physical significance in the context of conductive heat transfer. It determines the rate of conductive heat transfer in a substance with respect to its volumetric heat storage capacity. Values of thermal diffusivity can be estimated either indirectly using available data on are often calculated from the widely available data on λ, ρ and c, or directly using laboratory tests.

Solution to the conductive heat transfer at the pipe-fluid interface requires considering different thermal and hydrodynamics conditions. It is internal forced convection as the fluid is forced by the heat pump to flow through the pipes. It is generally satisfactory to assume that the fluid flow in pipes only occur in the direction of flow. Thus, it is usually assumed the flow and thermal properties at any cross section normal to the flow direction are uniform. However, these properties may change with time in transient condition unless the flow occurs under steady-state condition [22]. It is convenient to use an average value (v_m) for the flow velocity at any cross section (having a normal vector in the flow direction), although it varies from zero at the tube wall to a peak value at the tube center. When the tube outer surface is subjected to a temperature variation, a mean value (T_m) is usually considered for temperature of the fluid at any cross-section, while it varies from T_s (outer surface temperature) at the wall-fluid interface to a peak (or minimum in the case of heating) at the tube center. The properties of the fluid flowing in the pipe is usually estimated at a temperature equivalent the arithmetic average of the mean temperature at the inlet (T_{inlet}) and outlet (T_{outlet}) ($\frac{T_{inlet} + T_{outlet}}{2}$) [22].

In energy pile application, hydrodynamic entry length along which the velocity profile develops is negligible and the fluid flow is usually explained as hydromechanically fully developed flow, where the velocity profile of the fluid at any cross section remain unchanged. Thus, it is convenient

33

to assume a steady-state flow along the absorber pipes. It should be noted that the velocity profile is generally parabolic in laminar condition, while it is rather flatter in turbulent flow [22].

Like the velocity profile, the temperature profile, due to heat exchange between the fluid and the surrounding soil and concrete, develops along a very short length of the pipe (thermal entrance region) and remains approximately unchanged along the entire length of pipe, which is known as thermally fully developed region. In a thermally fully developed region, the dimensionless temperature profile ($\frac{T_s - T(r,x)}{T_s - T_m}$) at any cross section is constant and does not change with x. Note that T(r,x) may change with x (flow direction). However, the dimensionless temperature remains unchanged as x increases as long as the temperature of pipe outer surface (Ts) remains constant, which is assumed to be the case in the energy pile application.

The region along which both flow and heat transfer occur under hydrodynamically and thermally developed conditions is called fully developed flow, where:

Hydrodynamically fully developed: $\qquad \dfrac{\partial v(r,x)}{\partial x} = 0 \ \rightarrow v = v(r)$

Thermally fully developed: $\qquad \dfrac{\partial}{\partial x}\left(\dfrac{T_s(x) - T(r,x)}{T_s(x) - T_m(x)}\right) = 0$

Note x and r are the distances measured from the pipe entrance and the pipe center, respectively, as shown in Figure 1-20.

Temperature profile   Velocity profile
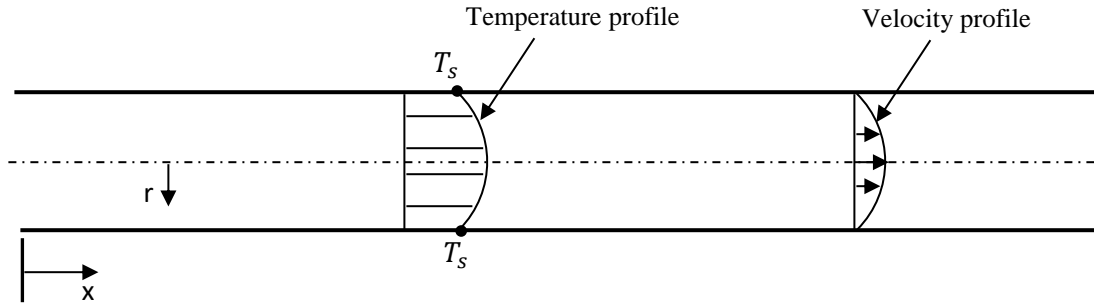
Figure 1-20- Fluid flow in an absorber pipe (in the case of cooling).

For laminar flow, hydrodynamic entry length $(L_{h-laminar})$ and thermal entrance region $(L_{t-laminar})$ can be approximated using the following equations [22]:

$$L_{h-laminar} \approx 0.05. Re. D \qquad (1-6)$$

$$L_{t-laminar} \approx 0.05. Re. Pr. D = Pr. L_{h-laminar} \qquad (1-7)$$

For turbulent flow, however, they are approximately equal [22]:

$$L_{h-turbulent} \approx L_{t-turbulent} \approx 10\ D \qquad (1-8)$$

Re is the Reynolds number defined as [22]:

$$Re = \frac{\rho v_m D}{\mu} \qquad (1-9)$$

Where v_m is the mean fluid velocity, D is the diameter of the pipe, and μ is the viscosity of the fluid. It is already known that for [22]:

Laminar flow: Re < 2300,

Transient flow: 2300 < Re < 10000, and

Turbulent flow: Re > 10000

35

Pr is a dimensionless parameter, which is known as Prandtl number [22]:

$$\text{Pr} = \frac{\mu c_{fluid}}{\lambda} \qquad (1-10)$$

Where c_{fluid} is the fluid heat specific capacity.

Pr descries the relative thickness of the velocity and the thermal boundary layers and it is usually larger than 1 for liquids.

Heat transfer analysis between the fluid and the surrounding concrete and soil

The energy balance for a steady-state flow in absorber pipes can be expressed as (Figure 1-21):

$$\dot{Q} = \dot{m}.c_{fluid}.(T_{exit} - T_{inlet}) \qquad (1-11)$$

Where T_{exit} and T_{inlet} are the mean fluid temperature at the inlet and exit of the pipe, respectively, $\dot{m}$ is the mass flow rate and $\dot{Q}$ is the rate of heat transfer rate to or from the fluid.
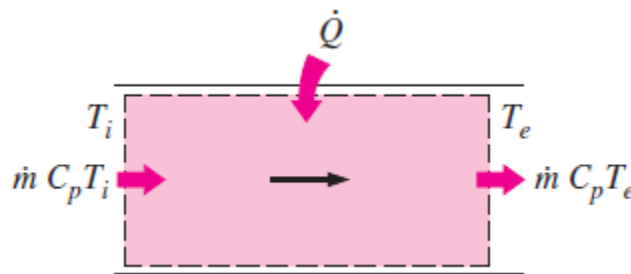
Figure 1-21- Heat transfer between the pipe wall and the flowing flow [22].

$\dot{Q}$ is usually evaluated under two common boundary conditions: constant surface temperature (T_s = constant) or constant surface heat flux ($\dot{q}_s$ = constant). Constant surface temperature condition is more representative for an energy pile application. Furthermore, the heat transfer

between the fluid and the pipe wall at any cross section can be expressed using the following equation:

$$\dot{q}_s = h_x(T_s - T_m) \tag{1-12}$$

Where h_x is the heat transfer coefficient at x, and T_s and T_m are the surface and the mean fluid temperature at x. In the above equation, h_x is constant along the pipe, T_m varies with x and T_s can be either constant (in the case of constant surface temperature) or vary with x (in the case of constant surface heat flux). Note the above statement is valid for fully developed flow in the pipe which is a reasonable assumption in energy pile application due to very small hydrodynamic/thermal entry lengths.

For energy pile application, it may be required to assess an average heat flux for the entire length of the absorber pipe. To do so, Equation (1-12) can be rewritten as:

$$\dot{q}_s = h_x(T_s - T_m)_{ave} \tag{1-13}$$

$$(T_s - T_m)_{ave} = T_s - (\frac{T_{inlet} + T_{exit}}{2}) \tag{1-13a}$$

In fact, T_m is expressed approximately by an arithmetic average of the mean temperature at the inlet (T_{inlet}) and the exit (T_{exit}) of the pipe. This expression of the mean temperature is based on this assumption that the fluid velocity varies linearly along the pipe, which is not necessarily the case when the surface temperature is constant. Generally, the following relationship between the inlet and exit temperature can be presented when the pipe surface temperature is constant:

$$T_{exit} = T_s - (T_s - T_{inlet}) \exp\left(-\frac{hA_s}{\dot{m}c_{fluid}}\right) \tag{1-14}$$

Where $A_s = PL$ is the surface area of the pipe.

However, it has been observed that the arithmetic average approach gives acceptable results if the ration of $\frac{(T_{exit} - T_s)}{(T_{inlet} - T_s)}$ is less than 40%, which is the case in some engineering application such as energy pile application [22].

Based on the type of flow (i.e. laminar or turbulent) and thermal condition at the pipe surface (i.e. constant surface temperature or constant surface heat flux) the heat transfer coefficient (h) can be approximated as:

Laminar flow- constant surface temperature: $\qquad h = 4.36\frac{\lambda}{D}$

Laminar flow- constant surface heat flux: $\qquad h = 3.66\frac{\lambda}{D}$

Where λ and D are the fluid thermal conduction coefficient and pipe diameter, respectively.

Unlike the laminar flow, for turbulent flow the heat transfer coefficient (h) may not be sensitive to the thermal conditions at the pipe surface and can be expressed as:

$$h = Nu.\lambda.D = \left[\frac{\left(\frac{f}{8}\right)(Re - 1000)Pr}{1 + 12.7\left(\frac{f}{8}\right)^{0.5}(Pr^{\frac{2}{3}} - 1)}\right].\lambda.D \qquad 0.5 \leq Pr \leq 2000 \text{ and } 3000 < Re < 5 \times 10^6$$

$$f = (0.79.Ln(Re) - 1.64)^{-2} \qquad\qquad 10^4 \leq Re \leq 10^6$$

In the above equation Nu is a dimensionless parameter called Nusselt number. It is defined as the ratio of the heat transferred through a layer of fluid by convection and the heat transferred by conduction the same fluid layer. f is the friction factor in turbulent flow in a pipe with smooth walls.

According to the above discussion, heat exchange in geothermal foundations involves different three-dimensional unsteady conductive/convective heat transfers through multiple non-finite homogeneous material (i.e. soil and concrete). Furthermore, the thermal properties of soil, liquid and concrete are temperature-dependent and non-isotropic making heat transfer in geothermal foundation more difficult to model. Therefore, a complex numerical solution is generally required to obtain solutions to this, considering appropriates thermal properties and boundary conditions. However, some simplifying assumptions are usually made to make the problem more amenable to solution:

(a) Thermal properties of the soil, concrete and liquid are isotropic and temperature-independent.

(b) Heat transfer in concrete/soil/liquid is steady state.

(c) Heat flow and temperature variations are neglected along the pile (in z-direction), so that one dimensional heat transfer (in radial direction-normal to the pipes surfaces) is considered in analytical/numerical solutions.

(d) The heat exchange between the ground and pile equally distributes heat flux at the surface of all integrated tubes.

(e) The concrete thermal (conductive) resistance between the ground and fluid is negligible. Thus, it is assumed the tube surface is surrounded by soil approximated as an infinite homogenous medium.

(f) There is no thermal interference from adjacent piles.

Accordingly, the heat transfer in geothermal piles can be estimated by replacing the pile and tubes with a cylindrical heat source (with diameter of zero or equal to the pile diameter) of infinite (or

finite) length at the center of infinite (semi- finite) cylinder representing the surrounding soil. The Line source and the hollow cylindrical source models are two widely used models that account for the above simplifications. In the line source model, the diameter of the cylinder is assumed to be zero, while it is the same as pile diameter. The models can be used in one-dimensional analytical solutions, where the temperature in the surrounding soil in radial direction (normal to the cylinder axis) at a given time can be calculated. Figure 1-22 shows the hollow cylindrical source model.
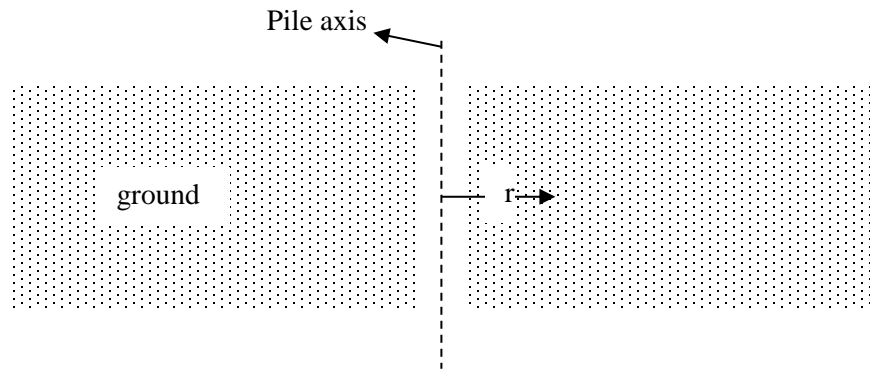
Figure 1-22- Cylindrical source model: Infinite cylindrical medium with a cylindrical gap.

For this model Equation (1-3) reduces to the following equations for two heat flow conditions:

$$\frac{\partial T}{\partial t} = \frac{\lambda}{\rho c}\left(\frac{\partial^2 T}{\partial r^2} + \frac{1}{r}\frac{\partial T}{\partial r}\right) \qquad \leftrightarrow \qquad \text{unsteady} - \text{state heat transfer} \qquad (1 - 15a)$$

$$0 = \frac{\lambda}{\rho c}\left(\frac{\partial^2 T}{\partial r^2} + \frac{1}{r}\frac{\partial T}{\partial r}\right) \qquad \leftrightarrow \qquad \text{steady} - \text{state heat transfer} \qquad (1 - 15b)$$

To find a solution to the above differential equations, the following initial (t = 0) and boundary conditions are assumed:

Boundary conditions:

At r = 0
$$\frac{\partial T(r,t)}{\partial r} = 0 \text{ (due to symmetry of heat transfer)}$$

At r = R
$$-\lambda_{soil} \frac{\partial T(r,t)}{\partial r} = h_x(T_s - T_m)_{ave}$$

$$T_s = T(R,t) = \text{soil temperature at } r = R$$

$$T_m = \frac{T_{inlet} + T_{exit}}{2}$$

r → ∞
$$T(r,t) = T_{ground}$$

Initial condition

t = 0
$$T(r,0) = T_{ground}$$

Note that the thermal condition on the ground surface is not considered. T_{inlet} is usually a given parameter estimated based on the air temperature on the ground surface. T_{exit} may also be a given parameter approximated by mechanical engineer based on the heating/cooling demand of the building. If both T_{inlet} and T_{exit} is assumed to remain unchanged during a period of time (like winter season) then the heat transfer becomes a steady state problem, where T(r, t)=T(r). T_{ground} is another known parameter which is equal to the temperature of the ground surrounding the pile and it is assumed to be constant along the pile length. The heat flux ($\dot{Q}_t$) extracted/injected from/to the ground by an energy pile can be estimated by the following equation:

$$\dot{Q}_t = \left(\int \dot{q}\,(R,t).p.\,dl \right).n_{pipe} \tag{1-16}$$

$$\int_{t_1}^{t_2} \dot{q}\,(R,t) = -\lambda_{soil} \frac{\partial T(r,t)}{\partial r} = h_x(T_s - T_m)_{ave}$$

$\dot{q}(R,t)$ is the heat flux density at the pile-ground interface at time t, p is the pipe premier and dl is differential length of the pipe (assuming the length and diameter of the pipes are given) and n_{pipe}

is the number of absorber pipes in the pile. The heat flux ($\dot{Q}_{primary}$) transferred by the flowing fluid in the absorber pipes (the primary circuit) can be determined as:

$$\dot{Q}_{primary} = n_{pile}.\dot{Q}_t = n_{pile}.n_{pipe}.\dot{m}.c_{fluid}.(T_{exit} - T_{inlet}) \qquad (1-17)$$

Where n_{pile} is the number of energy piles in the primary circuit. $\dot{m}$, c_{fluid}, T_{exit} and T_{inlet} are assumed to the same in all pipes.

On the other hand, If the electrical power of the heat pump (P_{hp}) is known the heat flux provided in the second circuit ($\dot{Q}_{secondary}$) is calculated as:

$$\dot{Q}_{primary} + P_{hp} = \dot{Q}_{secondary} = \dot{m}.c_{fluid}.(T_{exit} - T_{inlet}) \qquad (1-18)$$

$\dot{m}$, c_{fluid}, T_{exit} and T_{inlet} are the mass flow rate, specific heat capacity, fluid temperature at the exit and inlet in the secondary circuit, respectively.

In the design process, the pile/pipe geometry and their quantity are initially guessed followed by estimation of $\dot{Q}_{secondary}$ using equations (11-15 to 11-18). The estimated $\dot{Q}_{secondary}$ then is compared with the energy required for heating/cooling purposes in the building whereby the initial guess of geometry and quantity is confirmed or updated.

1-4- Problems (concerns) associated with energy piles

Despite successful implementations of energy piles reported in the literature ([9-14]), their important contribution to the annual saving of energy cost in buildings sector as well as decrease in the global fossil fuels burning and its associated CO_2 emissions, there are still some concern and uncertainties associated with their application. From environmental point of view, significant decrease in the groundwater temperature (during winter mode) increases the pH value, reduces calcium solubility, and raises the solubility of gaseous substances

such as CO_2, while significant rise in the ground water temperature (during summer mode) may cause relatively large reduction in oxygen solubility, that thus make the groundwater unfit for drinking [14]. Furthermore, long-term thermal efficiency of energy pile may decrease due to frequent temperature fluctuations and imbalance between the heat extracted and injected [14].

From geotechnical point of view, ultimate geotechnical bearing capacity, serviceability and pile structural capacity may be jeopardized due to repeated temperature variation in the pile and surrounding soil. In the next chapter the potential impact of energy pile operation on the above-mentioned limit states will be discussed in detail. Moreover, there is still no comprehensive guidelines available for design practice [14].

References:

[1] International Energy Agency (IEA), (2013). *Transition to Sustainable Buildings: Strategies and Opportunities to 2050 (Executive summary).*

[2] International Energy Agency (IEA),. (2017). *Key World Energy Statistics*.

[3] Pérez-Lombard, L., Ortiz, J., and Pout, C. (2008). A Review on Buildings Energy Consumption Information. *Energy and Buildings*, 40(3), 394-398.

[4] Cao, X., Xilei, D., & Liu, J. (2016). Building energy-consumption status worldwide and the state-of-the-art technologies for zero-energy buildings during the past decade. *Energy and Buildings*, 128, 198-213.

[5] U.S. Department of Energy, (2015). *Quadrennial Technology Review- An Assessment of Energy Technologies and Research Opportunities, Chapter 5: Increasing Efficiency of Building Systems and Technologies*.

[6] Bouazza, A., Singh, R.M., Wang, B., Barry-Macaulay, D., Haberfield, C., Chapman, G., Baycan, S., & Carden, Y. (2011). Harnessing on site renewable energy through pile foundations. *Australian Geomechanics Journal*, 46(4), 79-90.

[7] Singh, R.M., Bouazza, A., Wang, B., Barry-Macaulay, D., Haberfield, C., Baycan, S., & Carden, Y. (2011). Geothermal Energy Pile: Thermal cum Static Load Testing. In *Australian Geothermal Energy Conference* (p. 245-248). Sebel Albert Park, Melbourne.

[8] Olgun, G. (2013). *Energy Piles: Background and Geotechnical Engineering Concepts.* Lecture, Atlanta, GA.

[9] Adam, D., & Markiewicz, R. (2009). Energy from earth-coupled structures, foundations, tunnels and sewers. *Geotechnique*, 59(3), 29-236.

[10] Moel, M., Bach, P.M., Bouazza, A., Singh, R.M., & Sun, J.O. (2010). Technological Advances and Applications of Geothermal Energy Pile Foundations and their Feasibility in Australia. *Renewable and Sustainable Energy Reviews*. 14(9), 2683-2696.

[11] Laloui, L., & Di Donna, Alice. (2011). Understanding the behavior of energy geo-structures. In *Proceedings of the Institution of Civil Engineers.* (pp. 184-191).

[12] Brandl, H. (1998). Energy piles and diaphragm walls for heat transfer from and into the ground. In *Proceedings of the 3rd International Geotechnical Seminar on Deep Foundations on Bored and Auger Piles* (pp. 37-60). Ghent, Belgium.

[13] Brandl, H. (2013). Thermo-Active Ground-Source Structures for Heating and Cooling. In *11th International Conference on Modern Building Materials, Structures and Techniques* (pp. 9-18). Vienna, Austria.

[14] Brandl, H. (2006). Energy foundations and other thermo-active ground structures. *Ge´otechnique*. 56 (2), 81-122.

[15] Ennigkeit, A., & Katzenbach, R. (2001). The double use of piles as foundation and heat exchanging elements. *In Proceedings of the Fifteenth International Conference on Soil Mechanics and Geotechnical Engineering (ICSMGE)* (pp. 893-896). Istanbul, Turkey.

[16] Suryatriyastuti, M., Mroueh, H., & Burlon, S. (2012). Understanding the temperature-induced mechanical behavior of energy pile foundations. *Renewable and Sustainable Energy Reviews*. 16(5), 3344-54.

[17] Amis, A., & Loveridge, F.A. (2014). Energy piles and other thermal foundations for GSHP – developments in UK practice and research. *REHVA Journal*, 2014 (1), 32-35.

[18] Fadejev, J., Simson, R., Kurnitski, J., & Haghighat, F. (2017). A review on energy piles design, sizing and modelling. *Energy*, 122, 390−407.

[19] Mehrizi, A., Porkhial, S., Bezyan B., & Lotfizadeh, H. (2016). Energy pile foundation simulation for different configurations of ground source heat exchanger. *International Communications in Heat and Mass Transfer,* 70, 105-114.

[20] Park, H., Lee, S.R., Yoon, S., & Choi, J.C. (2013). Evaluation of thermal response and performance of PHC energy pile: Field experiments and numerical simulation. *Applied Energy*, 103, 12-24.
[21] Hamada, Y., et al. (2007). Field performance of an energy pile system for space heating. *Energy and Buildings*, 39(5), 517-524.

[22] Cengel, Y. A. (2003). Heat Transfer: A Practical Approach (2nd edition). McGraw-Hill.

[23] Faizal, M., Bouazza, A., & Singh, R.M. (2016). An experimental investigation of the influence of intermittent and continuous operating modes on the thermal behavior of a full-scale geothermal energy pile. *Geomechan. Energy. Environ*, 8, 8-29.

Chapter 2

Thermo-Mechanical Behavior of Energy

Piles and Research Plan

2-1- Introduction:

Deep foundation design process consists of checking for two main limit states: Serviceability limit state (SLS) and Ultimate limit state (ULS), that must not be reached. Serviceability limit state refers to conditions under which the building fails to perform its intended function. Some common problems arose when this state is reached include access difficulties, drainage problems and damage to architectural finishing, as mentioned by Salgado (2006) [1]. SLS is generally achieved because of excessive pile head settlement and is prevented by limiting the amount of settlement. The ULS, however, refers to conditions under which the stability (or safety) of the supported building or the pile structure are jeopardized [1]. These conditions include the classical geotechnical bearing capacity failure and structural collapse of the pile [1]. To prevent ULS the mechanical load applied to the pile must be kept smaller than its geotechnical/structural bearing capacity.

Energy piles, which serve as heat exchanger in addition to a rigid foundation, may thermally induce additional settlement or load, that thus jeopardize both the serviceability and stability (safety) of the supported building. There have been many researches done to study the effect of temperature variations on the above-mentioned parameters: pile heat settlement, pile axial stress (force) and geotechnical bearing capacity. In the following, a summary of the output of these studies will be presented.

2-2- Pile head settlement:

To examine the effects of temperature on the pile head settlement it is necessary to define a reference value, which is the free (unrestrained) pile deformation (ΔL_{free}) because of temperature change (ΔT):

$$\Delta L_{free} = \alpha_{pile} L_{pile} \Delta T \qquad (2-1)$$

Figure 2-1 illustrates temperature-induced pile deformation under some simplifications and end constraints.
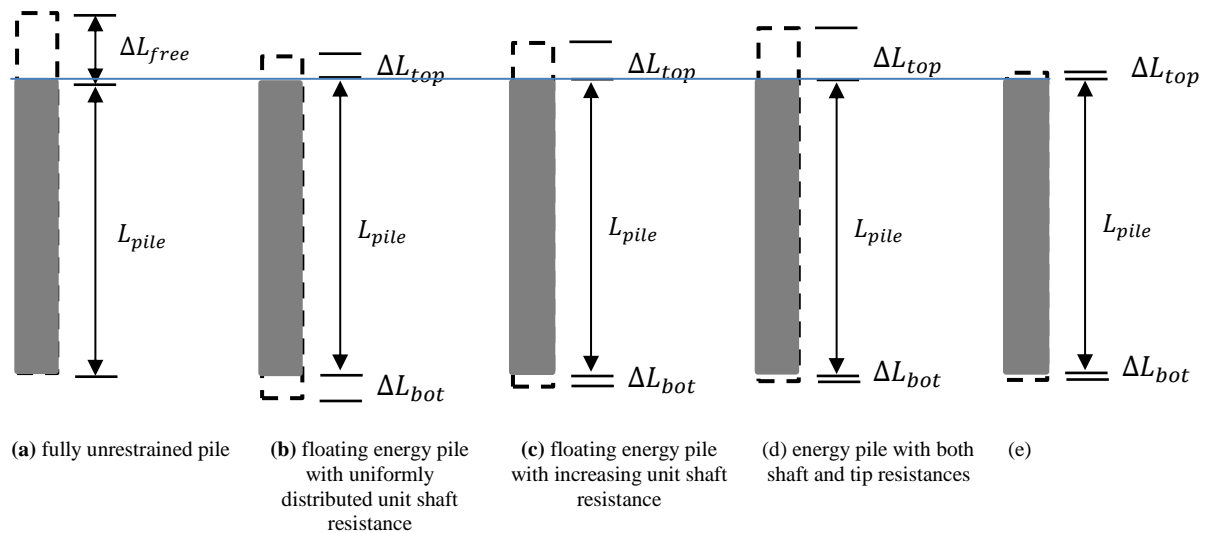
Figure 2-1- Simplified illustration of thermal deformation of energy piles under different end constraints.

Figure 2-1(a) shows free (unrestrained) deformation of a pile without shaft and base resistance. For simplicity it is assumed that the thermal deformation is zero at the base.

Figure 2-1(b) depicts the thermal deformation of a floating energy pile with uniformly distributed unit shaft resistance and negligible tip resistance. The neutral point at which the relative motion between the pile and soil is zero is located at the mid-depth of pile ($L_{np} = 0.5\ L_{pile}$) due to equally

distributed shaft resistance about the middle point. Note that L_{np} is the depth of neutral point from the ground surface. Therefore, the temperature-induced deformation equally occurs at the two ends ($\Delta L_{top} = \Delta L_{bot} < 0.5 \, \Delta L_{free}$). The magnitude of thermal deformation depends on the frictional resistance provided by the soil along the shaft. The above explanation is valid for both heating and cooling operations.

Figure 2-1(c) shows the thermal deformation of a floating energy pile with increasing unit shaft resistance with depth and negligible tip resistance. In this case, the neutral point moves toward the base ($L_{np} > 0.5L_{pile}$) as the shaft resistance developing in the lower part of pile is larger than that in the upper part. Thus, the thermal deformation at the top end (ΔL_{top}) tends to be higher than that at the base (ΔL_{bot}) (i.e. $\Delta L_{bot} < \Delta L_{top} < \Delta L_{free}$). This simplified explanation is also valid for both heating and cooling operations.

Figure 2-1(d) explains the thermal behavior of an energy pile with both shaft and tip resistances. Assuming the same distribution of shaft resistance, the neutral point is located at a larger depth compared to the previous case, due to the presence of the tip resistance in addition to the shaft resistance. As a result, ΔL_{bot} tends to be smaller than that in the previous case, while ΔL_{top} is larger. This explanation is applicable for heating operation (summer mode), while in heating mode (winter mode) the thermal deformation of pile can be examined by 1(b).

Figure 2-1(e) presents an energy pile under more realistic condition where it is constrained at two ends and shaft. Due to restraints at the top by the superstructure ΔL_{top} is smaller than that in the other cases illustrated above. However, depending on the restraint condition at the two ends and the unit shaft resistance distribution, the neutral point depth could be either above the mid-depth or below it. For instance, if the pile is confined between a heavy supersaturate (at the top) and a

relatively soft/loose soil at the base, the neutral point tends to be above the mid-depth, whereas it moves toward the pile base if there is a stiff soil located at the base with a light overlying superstructure. In the earlier case, ΔL_{top} approaches zero, while in the latter case it approaches ΔL_{free} if the shaft resistance is insignificant. In the above simplified explanation, it is assumed that the soil thermal expansion/contraction due to temperature variation is negligible. Based on the analysis of the available outcomes of several lab/full scale [2-30] and numerical [31-44]- studies, Bourne-Webb and Freitas (2018) [45] and Bourne-Webb et al. (2019) [46] reported that under monotonic heating/cooling the average value of ΔL_{top}, is approximately 0.6 ΔL_{free}, based on the full-scale testing, while it is about 0.8 ΔL_{free}, based on small-scale testing. However, irrespective of the testing scale, they showed that the average value of ΔL_{top} is about 0.5 ΔL_{free} and 0.9 ΔL_{free}, during monotonic heating and cooling, respectively. They also indicated that under some conditions ΔL_{top} may exceed ΔL_{free} during cooling [45-46]. Based on their analysis, the temperature-induced pile head settlement estimated by numerical methods is slightly higher than that observed in full-scale tests [45-46].

It was also shown that the pile head settlement under seasonally cyclic temperature variation (or during intermittent operation) continuously increases over thermal cycles, with a significant decreasing rate over cycles following the first one [34]. The increasing accumulated settlement with thermal cycles is attributed to the interaction between base/shaft resistances during heating/cooling cycles, as illustrated by Bourne-Webb and Freitas (2018) [45]. Based on their analysis of full/small scale testing results, they [45-46] stated that if the frictional resistance mobilizing under existing mechanical load is less than the ultimate shaft capacity, additional thermal load will generate a thermo-elastic pile deformation, meaning that thermal strains induced during heating (or cooling) phase of a cycle is approximately recovered during the subsequent

cooling (or heating). For instance, an energy pile with a light overlying structure may experience thermo-elastic strains during its operation, while heat exchange process in a pile carrying a heavy superstructure may cause irrecoverable thermal strains.

2-3- Pile axial stress (force)

Like pile head settlement, to better examine the temperature-induced axial stress, it is necessary to define a reference stress value, which is theoretically the largest temperature-induced stress value developing in the pile. This reference stress value corresponds to conditions where perfect restraints available at the pile ends and the axial deformation is not allowed to occur:

$$\Delta\sigma_{fixed} = \alpha_{pile}\Delta TE_{pile} \qquad\qquad (2-2)$$

Where $\Delta\sigma_{fixed}$ is the reference stress value and E_{pile} is the modulus of elasticity of pile.

Furthermore, the following simplified illustration can be used to qualitatively describe the thermally induced axial stress in pile [45]. Figure 2-2 illustrates thermo-mechanical axial stress developing in a floating energy pile with uniform unit shaft resistance and negligible base resistance (Figure 2-2a). The thermal expansion/contraction of the surrounding soil and the axial load are also assumed to be negligible.

(a) Floating pile with zero base resistance   (b) under mechanical loading   (c) under thermal loading   (d) under thermo-mechanical loading
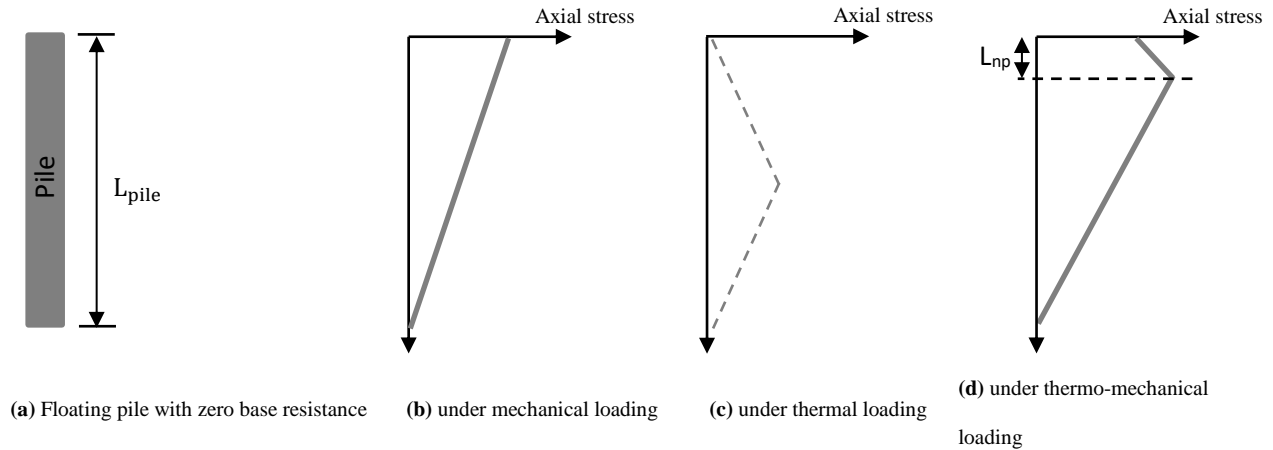
Figure 2-2- Thermo-mechanical stress in energy pile – under application of heating.

Figure 2-2b shows mechanical axial stress developing in the pile, assuming a uniform unit shaft resistance developing along the pile. Note that under downward mechanical loads the mobilized shaft resistance acts in upward direction. Figure 2-2c shows the axial stress distribution due to thermal loading. As previously mentioned in Figure 2-1b, the neutral point is at the mid-depth ($L_{np} = 0.5\,L_{pile}$), at which the relative motion between pile and soil is zero, the sign of mobilized shaft resistance reverses and the highest axial stress ($\Delta\sigma_{th-max} \leq \Delta\sigma_{fixed}$) occurs. Assuming linearly increasing unit shaft resistance, the neutral point level is theoretically $0.67\,L_{pile}$. Figure 2-2d combines the effects of both mechanical and thermal loading. Obviously, under thermo-mechanical loading the neutral point level rises ($0 < L_{np} < 0.5\,L_{pile}$) to provide force equilibrium along the pile axis. The highest axial stress induced by thermo-mechanical loading is compressive and greater than that induced by mechanical loading. If further restraints available at the two ends (i.e. in the presence of external load and base resistance), the neutral point moves to another depth different than that shown in Figure 2-2d. Moreover, the highest thermo-mechanical stress could significantly increase depending on the restraint degree.

Figure 2-3, on the other hand, illustrates the thermal stress developing during application of cooling. Similar assumptions to those made in Figure 2-2 are considered to describe Figure 2-3. Unlike heating, cooling induces negative axial stress along the pile (Figure 2-3c). Therefore, different distribution of axial stress develops under thermo-mechanical loading, as shown in Figure 2-3d. In this instance, the neutral point tends to be located at larger depth and the corresponding stress is the greatest tensile stress. Similarly, the presence of restraints at the pile ends will change the neutral point location and the corresponding tensile stress.

(a) Floating pile with zero base resistance   **(b)** under mechanical loading   **(c)** under thermal loading   **(d)** under thermo-mechanical loading
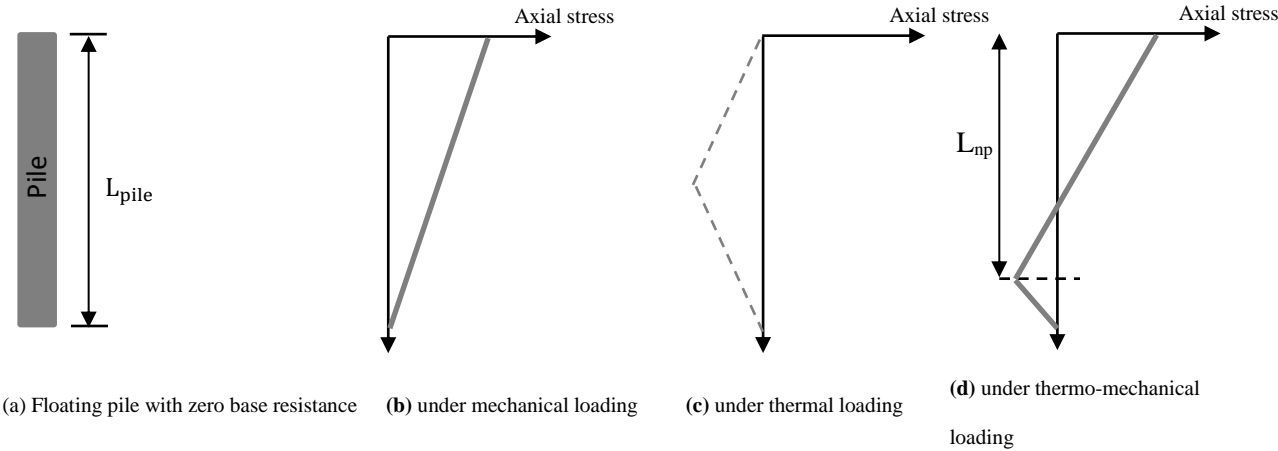
Figure 2-3- Thermo-mechanical stress in energy pile – under application of cooling.

Based on the full-scale test results reported in literature, the ratio of the thermal stress ($\Delta\sigma_{th}$) and the reference stress value ($\Delta\sigma_{fixed}$) is found to be about 0.6, while it is less than 0.2 from the small-scale results [45-46]. The latter was interpreted on the basis of this fact that there is limited shaft resistance mobilized due to the small confining pressure around a small-scale pile [45-46]. Regarding cyclic thermal loading, the greatest thermal stress occurs in the first cycle, which is upper-bounded by $\Delta\sigma_{fixed}$, while in the following cycles the change in thermal stress is negligible [19 & 45-46].

2-4- Geotechnical bearing capacity

The effect of temperature on the shaft resistance has received more attention comparing to the base resistance, possibly due to more complexity associated with the shaft resistance. It is believed, however, that the unit base resistance increases during thermal loading possibly due to soil stiffening at the base. This part mainly discusses the potential thermal changes in the shaft resistance. The unit shaft resistance q_s at isothermal condition is proportional to the drained friction angle available at the pile-clay interface δ and the effective normal stress acting on the pile surface σ_h', which can mathematically be presented in the following equation:

$$q_s = \sigma_h' \tan(\delta) \tag{2-3}$$

δ is dependent on varying parameters including the pile surface roughness, the particle size/shape and the strength/deformability characteristics of the surrounding clay [47]. When the pile-soil interface is heated, it is very unlikely that the geometrical properties mentioned above (the roughness and particle size/shape) are impacted under the low temperature variations typically induced at the energy pile interface. Therefore, the change in clay strength/deformability characteristics is possibly responsible for causing any variation in the interface friction angle δ during heat application. It can be described with direct temperature effects on the clay microscopic structure and/or its indirect effects through thermal consolidation occurring within clay mass. It is already known that temperature effects on clay behavior is greater than that on sand behavior, which is usually ignored for the temperature range typically observed in an energy pile [54-55]. Shaft friction degradation may also occur due to the thermally cyclic displacement along the interface, similar to that observed by several researchers for the piles cyclically loaded ([48-52]). This is primarily attributed to the fact that soils (particularly sands) near the pile surface tend to

show a contractive behavior under cyclic shearing, causing a progressive decrease in the normal force acting at the interface, thus reducing the interface frictional resistance. This degradation phenomenon has mainly been observed for the interface between sandy soils and different construction material ([48-53]), while the response of clay-concrete interface under cyclic shearing has not been investigated well. Nevertheless, a progressive volume decrease in clay is also expected due to this phenomenon that will cause a reduction in the normal stress (lateral effective stress) σ'_h, an increment in the PWP at interface (due to progressive contraction in clay), as well as the shaft friction degradation. However, the shaft degradation is less significant at the clay-concrete interface since clays volumetric reduction toward cyclic shearing forces is generally lower than that in sandy soils. Furthermore, depending on the amount of contraction accumulated at the end of heat cycles, the "post-heat cycling" interface strength can be altered, that should be taken into account in energy pile design.

As for pile-clay interface, σ'_h can also vary due to the heat-induced excess pore water pressure (PWP), which is strongly dependent on the rate of heating/cooling as well as the clay permeability [54]. The induced excess PWP is due to differential expansion between clay particles and pore water. If drainage is allowed (even at a slow rate), the excess PWP generated during heating will dissipate with time, leading to a thermal consolidation in clay. Conversely, when the interface is cooled down to the initial temperature, development of a negative PWP (suction) primarily occurs in clay followed by restoration if there is enough time. The earlier case can lead to a reduction in σ'_h and the short-term shaft resistance, while the latter can enhance both.

Table 1 summarizes the results of researches considering the effects of temperature on the shaft/base resistances of energy piles in different soils. According to Table 1 and the earlier discussion, the temperature influence on the pile-clay interface behavior is more important

comparing to that of pile-sand interface, that deserves more attention on all sides. The interaction between the mechanical stresses/PWP/mechanical properties available at the interface, the unit shaft resistance and the heating/cooling cycles can be expressed in the following mathematical form;

$$q_s = (\sigma'_{h0} + \Delta\sigma'_{h-th})tan(\delta + \Delta\delta_{th}) \qquad (2-4a)$$

$$\Delta\sigma'_{h-th} = \Delta\sigma_{h-th} - \Delta u_{th} \qquad (2-4b)$$

Where, σ'_{h0} is the effective lateral stress before heat application, and $\Delta\sigma'_{h-th}$ and $\Delta\delta_{th}$ are the heat-induced changes in the lateral effective stress and the interface friction angle, respectively, with a sign, either positive or negative. $\Delta\sigma_{h-th}$ and Δu_{th} are the thermally induced changes in the total lateral stress and the excess PWP, respectively.

2-5- Research plan

A well-designed experimental/numerical research program aiming to assess the shaft resistance of an energy pile in saturated clays should be able to tackle the questions arising from the above discussion, which are: how the clay strength is affected under low-amplitude temperature cycles and how the normal effective stress is redistributed at the interface on account of the thermally developed PWP as well as the thermal consolidation of clay.

The current study aims to address the above-mentioned questions using 3 series of thermo-mechanical experimental tests and numerical simulations. In the next chapters the results from a series of temperature-controlled consolidated drained (CD) triaxial tests on saturated kaolin are discussed first. It allows for observing the heat-induced changes in the shear strength of clay, and the subsequent effects on the friction angle at interface (δ), as discussed previously. Afterward,

the results from the second and the third series of tests focusing on the thermo-mechanical behavior of concrete-clay interface will be discussed in relation to the findings in the first series of tests and equation (4). It should be noted that the second and the third tests were conducted by two different apparatuses of temperature-controlled constant normal load (CNL) direct shear box and lab-scale pile. Finally, the results obtained from experimental tests will be reproduced using a fully coupled thermo-hydro-mechanical analysis to analyze the capability of such analysis to predict the response of real energy piles in clays.

Table 2-1- A summary of previous studies on the temperature effects on shaft/base resistances.

	Authors	Testing approach	Thermal loading	Findings
(1)	Goode III et al. (2015) [13]	Centrifuge-scale energy foundations (under centrifuge acceleration of 24g), with semi-floating and end-bearing toe boundary conditions and free- expansion and restrained-expansion head boundary conditions, in dry sand and unsaturated silt layers.	Non-cyclic temperature variation of 7-18 °C	(1) The effects of temperature on the ultimate bearing capacity of the semi-floating foundations embedded in dry sand was negligible, while the ultimate bearing capacity of the semi-floating foundations in unsaturated silt was clearly improved. (2) The above finding was proposed to be due to a combination of radial stress changes and thermally induced water flow in the unsaturated the unsaturated silt. The change in radial stress of the dry sand was assumed to be small due to lower initial confining pressure. (3) The ultimate bearing capacity of the end-bearing pile in silt, however, shows temperature independency. This may be attributed to this fact that the tip resistance is the major resistance component.
(2)	Wang et al. (2014) [56]	Full-scale test on a 16.1-m-long energy pile (with a diameter of 0.6 m) embedded in very dense sandy material-	Short/Long-term heating/cooling cycle. Short/long term heating involved applying continuous heating for 9/52 days. Short/Long-term cooling involved returning the pile temperature to the initial temperature after short/long-term cooling.	(1) Post long-term heating shaft capacity showed an increment of at least 14% compared to initial shaft resistance (isothermal shaft resistance). (2) Post long-term cooling shaft resistance is almost equal to the initial shaft capacity. (3) The displacement required to achieve the ultimate shaft resistance is less when the pile is heated.
(3)	Ng et al. (2014) [14]	4 centrifuge model tests on aluminum energy piles in medium dense saturated sand were performed at 40g to study the effects of heating on the bearing capacity.	The reference pile (RP) was loaded at 22 °C (isothermal condition). One energy pile (EP1) was loaded at 37 °C without initial mechanical loading. Two more energy piles were loaded at 52 °C with (EP2) and without (EP3) initial mechanical loading.	(1) According to the failure criterion of 10%Dpile, the ultimate bearing capacity increased by 19% (EP1), 42% (EP2) and 46% (EP3). (2) The ultimate bearing capacity of EP1 and EP2/EP3 increased by 13% and 30%, based on the failure criterion proposed by Ng et al. (2004). (3) The thermal improvement of ultimate bearing capacity was related to an increase in shaft resistance by 19.6% (EP1) and 15.4% (EP2) and an increase in base resistance by 6.4% (EP1) and 38.5% (EP2). (4) Based on the above observation, it was concluded that under lower temperature variation (i.e. 15 °C for EP1) the shaft resistance increase makes more important contribution to the ultimate bearing capacity, while under higher temperature variation (i.e. 30 °C for EP2) the base resistance improvement is more important. (5) The shaft resistance increase was attributed to the heat-induced increase in the contact effective pressure due to differential thermal expansion between the model pile and soil. The base resistance enhancement, on the other hand, was related to larger mobilized base resistance due to larger downward thermal expansion of the pile. (6) Due to high sand permeability the heat induced excess pore water pressure in the surrounding sand is negligible.
(4)	Ghaaowd and McCartney (2018) [57]		Two model pile were loaded at elevated temperature of 44 °C and 63 °C.	(1) Significant increase in pull-out capacity was observed for model piles loaded at elevated temperature. The pull-out capacity of model piles loaded at 44 °C and 63 °C is 45% and 95%, respectively, greater than that of the model pile loaded at ambient. (2) There is an approximately linear relationship between pullout capacity increment and temperature increment (with a slope of about 9 kN/° C).

Table 2-1 (continued)

	Authors	Testing approach	Thermal loading		Findings
(5)	Rosenberg (2010) [58] and McCartney & Rosenberg (2011) [59]	The effects of temperature on the ultimate bearing capacity was investigated using centrifuge testing approach (at g-level of 24). The contribution of shaft resistance to the ultimate bearing capacity was also estimated using a modified load transfer T-Z analysis. The scale model concrete piles having a diameter of 76.2 mm and length of 381 mm, were embedded in Bonny silt with plasticity limit of 4.	Three sets of thermal loading were applied: non-cyclic heating with and without building load and one heating-cooling cycle with building load.	(1) (2) (3) (4)	Piles loaded at elevated temperature showed significant increase in the ultimate bearing capacity, based on the Davisson's failure criterion. Thermally increased change in almost linearly change with temperature change with slop of approximately 10 kN/° C. According to T-Z analysis (using a modified unit shaft resistance accounting for temperature effects), the corresponding shaft resistance of energy piles loaded at elevated temperature increased with temperature variation with a rate of almost 10 kN/° C. The ultimate bearing capacity loaded at ambient temperature, after it was subjected to one heating-cooling cycle, also increases but with lower rate than that observed for that piles loaded at elevated temperature.
(6)	Szymkiewicz et al. (2015) [21]	3 full-scale tests were carried out to understand impact of temperature variations on the ultimate bearing capacity and the shaft resistance. The piles were bored pile (CFA) with a length of 12 m and 0.52 diameter installed in soil profile consisting of a layer of silt (3.0 m) on the top and a saturated sand layer.	Heating-cooling cycles (each heating/cooling phase last 7 days) were applied for 150 days. The first pile was loaded at the ambient temperature. The 2nd and 3rd piles were loaded after they were subjected to thermal cycles.	(1) (2) (3)	Piles loaded after they were subjected to thermal cycles showed at least 30% increase in their ultimate capacity, based on the failure criterion of 10%D. It was concluded that the ultimate bearing capacity improvement is mainly attributed to thermal improvement of the corresponding shaft capacity. Shaft capacity improvement was mentioned to be as a result of thermal densification of the sand.
(7)	Wang et al. (2016) [16]	1g lab scale modeling was utilized to study the effects of heating-cooling cycles on the energy pile behavior. The piles were 1600mm long with a diameter of 104mm, which were embedded in dry sand.		(1)	The contact pressure at the pile-soil interface increased during heating (up to 7.8 kPa) and decreased (down to -3.4 kPa). Thus, the shaft resistance can be influenced by heating-cooling cycles.
(8)	Maghsoodi et al. (2018) [60]	Direct shear test under CNL and CNS conditions were utilized to understand the temperature effects on the shearing strength of soil and soil-concrete interface. Fontainebleau sand, in a dense condition, and NC kaolin clay were used in the study. The shear strength of soil-soil was only evaluated under CNL condition, while the shear strength of corresponding interface was evacuated under both CNL and CNS conditions.	Non-cyclic thermal loading was used, i.e. 5, 22 and 60 °C.	(1) (2) (3)	Shear strength of sand and sand-concrete interface was reported to be temperature independent. Peak shear strength of clay increased with temperature due to cohesion improvement. Cohesion was reported to be 11, 17 and 23 kPa at 5, 22 and 60 °C (rate of ≈ 0.23 kPa/°C). the shear strength improvement was mentioned to be related to thermal contraction (stiffening). The internal friction angle was found temperature -independent. Temperature effects on the critical shear strength was insignificant. Peak shear strength of the clay-concrete interface was also thermally increased but with lower rate. Critical interface shear strength showed thermal independency.
(9)	Yavari et al. (2016) [61]	CNL direct shear test was utilized to study the effect of temperature on the peak/critical shear strength of sand-sand, clay-clay and clay-concrete interface. the sand specimen was at loose state with a relative density of 46% and the clay was prepared under NC condition. The tests were conducted at low normal stress (5-100 kPa).	The tests were conducted at 5, 20 and 40 °C.	(1)	Both soil-soil and soil-concrete interface was reported to be almost temperature independent.

Table 2-1 (continued)

	Authors	Testing approach	Thermal loading	Findings
(10)	Di Donna et al. (2016) [62]	The clay/sand-concrete interface response to temperature was investigated using direct shear test under both CNL and CNS conditions. Dry and saturated sand (with a dry density of 1.55 to 1.65 g/cm^3) were used, in addition to NC clays. Tests were carried out under different normal stress, normal stiffness, temperature (20 to 60 °C), roughness and monotonic and cyclic loading. 500 or 1000 kPa/mm was used as normal stiffness for the sand-concrete interface, while for the clay-concrete interface 200 kPa/mm was considered.	Three elevated temperature (monotonic thermal loading) were considered: 20, 50 and 60 °C.	(1) The effects of elevated temperature (20 and 60 °C) on shear strength of sand-concrete interface under both monotonic (CNL condition) and cyclic (CNS condition) loading was found to be insignificant. (2) The interface shear strength of interface shows a reduction under cyclic loading with respect to non-cyclic loading. It occurs due to reduction in effective normal stress at the interface. The shear strength parameters including adhesion and friction angle at the interface remained unchanged. (3) As for clay-concrete interface, shear strength showed an increase at elevated temperature (under CNL condition) presumably due to thermal consolidation of clay. (4) The shear strength improvement was associated with a rise in adhesion (form 7 kPa at 20 °C to 20 kPa at 50 °C) and a decrease in friction angle (form 25 ° at 20 °C to 23 ° at 50 °C). (5) The interface shear strength of interface was not affected under cyclic loading due to insignificant clay tendency to volume contraction during shearing.
(11)	Wang et al. (2011) [63]	3 small-scale energy piles embedded in silica sand were tested to estimate the effects of temperature on loading/shaft capacities of piles. One Sand specimen was dry with a dry density of 1.37 gr/cm3, while other samples had moisture content/ dry density of 24%/1.12gr/cm3 and 21.5%/1.21gr/cm3, respectively.	The results were interpreted based on the temperature 10 mm away from the pile surface, which were about 28 °C.	(1) The effect of temperature on the shaft resistance of pile in silica sand was found minor.
(12)	Xiao et al. (2014) [64]	A modified direct shear test (under CNL condition) was used to investigate the effect of temperature on soil and soil-concrete interface. The soil was unsaturated compacted silt with low plasticity.	Tests were conducted at temperatures of 6 and 21 °C.	(1) The interface showed thermal strengthening mainly due to thermal strengthening of silt itself. (2) As for shear strength parameters, cohesion increased up to 29%, while insignificant changes occur in friction angle.
(13)	Murphy and McCartney (2014) [65]	Borehole shear tests were conducted on soil layers at small (laboratory) and full (field) scale to estimate the effects of temperature on shear strength of soil-concrete interface. the small-scale tests were carried out in Boulder clay, compacted 15% to reach a dry density of 15.6 kN/m^3, at interface normal stresses of 12.4, 24.8, 37.2 and 49.6 kPa. The field tests were done in medium dense silty sand under interface normal stresses of 13.6, 18.1 and 22.6 kPa.	Small scale interfaces were sheared at elevated temperatures of 10 and 35 °C. Field tests were done at elevated temperatures of 10, 25 and 45 °C.	(1) For small-scale testing, both peak shear strength and friction angle insignificantly increases with temperature. Furthermore, the normalized T-z curve was not thermally affected. Inconsistent interface response to temperature was observed for full-scale testing. While interface shear strength increases from 10 to 25 °C, it decreases from 25 to 45 °C. it was indicated that the time considered for fully dissipation of temperature-induced PWP at temperature of 45 °C is not sufficient. This in turn decrease the effective normal stress at the interface and thus the shear strength with respect to that at 25 °C.

References:

[1] Salgado, R. (2007). The engineering of foundations. Boston: McGraw-Hill.

[2] Bourne-Webb, P.J. et al. (2009). Energy pile test at Lambeth College, London: geotechnical and thermo-dynamic aspects of pile response to heat cycles. *Geotechnique,* 59 (3), 237-248.

[3] Murphy, K.D., & McCartney, J.S. (2015). Seasonal response of energy foundations during building operation. *Geotech. Geol. Eng*, 33(2), 343-356.

[4] Murphy, K.D., McCartney, J.S., & Henry, K.S. (2015). Evaluation of thermo-mechanical and thermal behavior of full-scale energy foundations. *Acta Geotechnica,* 10 (2), 179-195.

[5] Santiago, C.de., et al. (2016). Thermo-mechanical behavior of a thermo-active precast pile. *Bulg. Chem. Commun*, 48 (Special Issue E), 41-54.

[6] You, S., Cheng, X., Guo, H., & Yao, Z. (2016). Experimental study on structural response of CFG energy piles. *Appl. Therm. Eng*, 96, 640-651.

[7] Sutman, M., Olgun, G., Laloui, L., & Brettmann, T. (2017). Effect of end-restraint conditions on energy pile behavior. *Geotech. Front. 2017 Geotech. Mater. Model. Test. ASCE GSP,* 280, 165-174.

[8] Allani, M., Van Lysebetten, G., & Huybrechts, N. (2017). Experimental and numerical study of the thermo-mechanical behaviour of energy piles for Belgian practice. in: *A. Ferrari, L. Laloui (Eds.), Advances in Laboratory Testing and Modelling of Soils and Shales (ATMSS), 2017, pp. 405e412,* https://doi.org/ *10.1007/978-3-319-52773-4_48.*

[9] Kalantidou, A., Tang, A.M., Pereira, J.-M., & Hassen, G. (2012). Preliminary study on the mechanical behavior of heat exchanger pile in physical model. *Geotechnique*, 62 (11), 1047-1051.

[10] Yavari, N., Tang, A.-M., Pereira, J.-M., & Hassen, G. (2014). Experimental study on the mechanical behavior of a heat exchanger pile using physical modelling. *Acta Geotecnica,* 9 (3), 385-398.

[11] Ng, C.W.W., Shi, C., Gunawan, A., & Laloui, L. (2014). Centrifuge modelling of energy piles subjected to heating and cooling cycles in clay. *Geotech. Lett*, 4 (4), 310-316.

[12] Stewart, M.A., & McCartney, J.S. (2014). Centrifuge modeling of soil-structure interaction in energy foundations. *ASCE J. Geotech. Geoenviron. Eng*, 140 (4), https://doi.org/10.1061/(ASCE)GT.1943-5606.0001061.

[13] Goode III, J.C., & McCartney, J.S. (2015). Centrifuge modeling of boundary restraint effects in energy foundations. *ASCE J. Geotech. Geoenviron. Eng,* 141 (8), https://doi.org/10.1061/(ASCE)GT.1943-5606.0001333.

[14] Ng, C.W.W., Shi, C., Gunawan, A., Laloui, L., & Liu, H.-L. (2015). Centrifuge modelling of heating effects on energy pile performance in saturated sand. *Can. Geotech. J.,* 52 (8), 1045-1057.

[15] Liu, H.-L., Wang, C.-L., Kong, G.-Q., Ng, C.W.W., Che, P. (2016). Model tests on thermomechanical
behavior of an improved energy pile. *Eur. J. Environ. Civil Eng*, 16.
[16] Wang, C.-L., Liu, H.-L., Kong, G.-Q., Ng, C.W.W., Wu, D. (2016). Model tests of energy piles with and without a vertical load, *Environ. Geotech*, 3 (4), 203-213.

[17] Huang X., Wu, J., Peng, H., Hao, Y., & Lu, C. (2018). Thermomechanical behavior of energy pile embedded in sandy soil. *Math. Probl Eng*, 5341642, 11, https://doi. org/10.1155/2018/5341642.

[18] Suryatriyastuti, M.E., Mroueh, H., & Burlon, S. (2012). Understanding the temperature induced mechanical behavior of energy pile foundations. *Renewable and Sustainable Energy Reviews*, 16 (5), 3344-3354.

[19] Freitas, T.M., Cruz Silva, F., & Bourne-Webb, P.J. (2013). The response of energy foundations under thermo-mechanical loading. in: *Proc. of the 18th Intl. Conf. on Soil Mech. and Geot. Eng'g, Paris*, 3347-3350.

[20] Murphy, K.D., & McCartney, J.S. (2015). Seasonal response of energy foundations during building operation. *Geotech. Geol. Eng*. 33 (2), 343-356.

[21] Szymkiewicz, F., Burlon, S., Guirado, F., Minatchy, C., & Vinceslas, G. (2015). Experimental study of heating-cooling cycles on the bearing capacity of CFA piles in sandy soils. in: *Proc. XVI ECSMFE: Geotechnical Engineering for Infrastructure and Development, Edinburgh*, 2647-2652.

[22] Habert, J., El'Mejahed, M., & Bernard, J.B. (2016). Lessons Learned from Mechanical Monitoring of a Thermo-active Pile. in: *Energy Geotechnics, in: F. Wuttke, S. Bauer, M. S_anchez (Eds.), CRC Press*, 551-556.

[23] Faizal, M., Bouazza, A., & Singh, R.M. (2016). An experimental investigation of the influence of intermittent and continuous operating modes on the thermal behavior of a full-scale geothermal energy pile. *Geomechan. Energy. Environ*, 8, 8-29.

[24] McCartney, J.S., & Murphy, K.D. (2017). Investigation of potential drag down/uplift effects on energy piles, *Geomechan. Energy. Environ*. 10, 21-28.

[25] Yavari, N., Tang, A.-M., Pereira, J.-M., & Hassen, G. (2014). Experimental study on the mechanical behavior of a heat exchanger pile using physical modelling. *Acta Geotecnica*, 9 (3), 385-398.

[26] C.W.W. Ng, C. Shi, A. Gunawan, L. Laloui, (2014). Centrifuge modelling of energy piles subjected to heating and cooling cycles in clay, G_eotech. Lett. 4 (4), 310-316.

[27] Ng, C.W.W., Gunawan, A., Shi, C., Ma, Q.J., & Liu, H.L. (2016). Centrifuge modelling of displacement and replacement energy piles constructed in saturated sand: a comparative study. *G_eotech. Lett*. 6 (1), 34-38.

[28] Nguyen, V.T., Tang, A.M., & Pereira, J.-M.. (2017). Long-term thermo-mechanical behavior of energy pile in dry sand. *Acta Geotech* 12 (4), 729-737.

[29] Wang, C.-L., Liu, H.-L., Kong, G.-Q., Ng, C.W.W. (2017). Different types of energy piles with heating-cooling cycles. in: *Proceedings of the Institution of Civil Engineers - Geotechnical Engineering*, 170, 220-231, 3.

[30] Wang, C.-L., Liu, H.-L., Kong, G.-Q., Ng, C.W.W., Wu, D. (2016). Model tests of energy piles with and without a vertical load. *Environm. Geotechn,* 3 (4), 203-213.

[31] Dupray, F., Laloui, L., & Kazangba, A. (2014). Numerical analysis of seasonal heat storage in an energy pile foundation. *Comput. Geotech*, 55, 67-7.

[32] Ozudogru, T.Y., Olgun, C.G., & Senol, A. (2014). 3D numerical modeling of vertical geothermal heat exchangers. *Geothermics*, 51, 312-324.

[33] Rotta Loira, A.F., Gunawan, A., Shi, C., Laloui, L., Ng, C.W.W. (2015). Numerical modelling of energy piles in saturated sand subjected to thermo-mechanical loads. *Geomechan. Energy Environ*. 1, 1-15.

[34] Khosravi, A., Moradshahi, A., McCartney, J.S., & Kabiri, M. (2016). Numerical analysis of energy piles under different boundary conditions and thermal loading cycles. in: *Proc. 3rd European Conference on Unsaturated Soils, "E-UNSAT 2016", p. 6*.

[35] Tsetoulidis, C., Naskos, A., & Georgiadis, K. (2016). Numerical investigation of the mechanical behaviour of single energy piles and energy pile groups. in: *F. Wuttke, S. Bauer, M. S_anchez (Eds.), Energy Geotechnics, CRC Press*, 569-575.

[36] Gawecka, K.A. et al. (2017). Numerical modelling of thermo-active piles in London Clay. in: *Proc. Insti. Civil Eng. Geotechn. Eng.*, 170, 201-219. GE3.

[37] Alberdi-Pagola, M., Madsen, S., Lund Jensen, R., & Erbs Poulsen, S. (2017). Numerical investigation on the thermo-mechanical behavior of a quadratic cross section pile heat exchanger, in: *IGSHPA Technical/Research Conference and Expo*, Denver, 134-143.

[38] Dupray, F., Laloui, L., & Kazangba, A. (2014). Numerical analysis of seasonal heat storage in an energy pile foundation. *Comput. Geotech,* 55, 67-7.

[39] Suryatriyastuti, M., Mroueh, H., & Burlon, S. (2013). Numerical analysis of a thermoactive pile under cyclic thermal loads. in: *Proc. European Geothermal Congress, Pisa, Italy*, p. 8.

[40] Suryatriyastuti, M.E., Mroueh, H., & Burlon, S. (2014). A load transfer approach for studying the cyclic behavior of thermo-active piles. *Comput. Geotech*. 55, 378-391.

[41] Pasten, C., & Santamarina, J.C. (2014). Thermally induced long-term displacement of thermoactive piles. *ASCE J. Geotechn. Geoenviron. Eng,* 140 (5), 5p.

[42] Olgun, C.G., Ozudogru, T.Y., Abdelaziz, S.L., & Senol, A. (2015). Long-term performance of heat exchanger piles. *Acta Geotechnica*, 10 (5), 553-569.

[43] Di Donna, A., & Laloui, L. (2015). Numerical analysis of the geotechnical behavior of energy piles. *Int. J. Numer. Anal. Methods GeoMech*, 39 (8), 861-888.

[44] Ng, C.W.W., Ma, Q.J., & Gunawan, A. (2016). Horizontal stress change of energy piles subjected to thermal cycles in sand. *Comput. Geotech,* 78, 54-61.

[45] Bourne-Webb, P.J., & Freitas, T.M. (2018). Thermally-activated piles and pile groups under monotonic and cyclic thermal loading-A review. *Renewable Energy, https://doi.org/10.1016/j.renene.2018.11.025*.

[46] Bourne-Webb, P.J., Freitas, T.M., & Assuncao, R.M. (2019). A review of pile-soil interactions in isolated, thermally-activated piles. *Computers and Geotechnics*, 108, 61-74.

[47] Lemos, LJL., & Vaughan PR. (2004). Clay-interface shearing resistance. *Geotechnique*, 50(1), 55-64.

[48] Mortara, G., Mangiola, A., & Ghionna, V. (2007). Cyclic shear stress degradation and post-cyclic behavior from sand-steel interface direct shear tests. *Canadian Geotechnical Journal,* 44(7), 739-752.

[49] Tabucanon, TJ., Airey, DW, & Poulos, HG. (1995). Pile skin friction in sands from constant normal stiffness tests. *Geotechnical Testing Journal,* 18(3), 350-364.

[50] Uesugi, M., Kishida, H., & Tsubakihara, Y. (1989). Friction between sand and steel under repeated loading. *Japanese Society of Soil Mechanics and Foundation Engineering,* 29(3), 127-137.

[51] Uesugi, M., Kishida, H., & Uchikawa, Y. (1990). Friction between dry sand and concrete under monotonic and repeated loading. *Soils and Foundations*, 30(1), 115–128.

[52] Zhang, G., & Zhang, JM. (2006). Monotonic and cyclic tests of interface between structure and gravelly soil. *Soils and Foundations Journal*, 46(4), 505–518.

[53] Di Donna, A., Ferrari, A., & Laloui, L. (2016). Experimental investigation of the soil concrete interface: physical mechanisms, cyclic mobilization and behavior at different temperatures. *Canadian Geotechnical Journal*, 43(4), 659-672.

[54] Fuentes, R., Pinyol, N., & Alonso, E. (2016). Effect of temperature induced excess porewater pressures on the shaft bearing capacity of geothermal piles. *Geomechanics for Energy and the Environment*, 8, 30–37.

[55] Yavari, N., Tang, AM., Pereira, JM., & Hassen, G. (2016). Effect of temperature on the shear strength of soils and soil/structure interface. *Canadian geotechnical journal*, 53(7), 1186-1194.

[56] Wang et al. (2014). Posttemperature Effects on Shaft Capacity of a Full-Scale Geothermal Energy Pile. *J. Geotech. Geoenviron. Eng.*, 141(4). DOI: 10.1061/(ASCE)GT.1943-5606.0001266.

[57] Ghaaowd, I. and McCartney, J.S. (2018). Centrifuge modeling of temperature effects on the pullout capacity of energy piles in clay. DFI 43rd Annual Conference on Deep Foundations, Anaheim, CA., Oct 24-27. 1-7.

[58] Rosenberg, J.E. (2010). Centrifuge Modeling of Soil Structure Interaction in Thermo-Active Foundations. M.S. Thesis. University of Colorado at Boulder.

[59] McCartney, J.S., & Rosenberg J.E. (2011). Impact of Heat Exchange on Side Shear in Thermo-Active Foundations. *Geo-Frontiers 2011- ASCE 2011*, pp. 488-498.

[60] Maghsoodi, S., Cuisinier, O., & Masrouri, F. (2018). Thermal effects on the mechanical behavior of the soil-structure interface. *Canadian geotechnical journal*.

[61] Yavari, N., Tang, AM., Pereira, J-M., & Hassen, G. (2016). Effect of temperature on the shear strength of soils and soil/structure interface. *Canadian geotechnical journal*, 53(7), 1186-1194.

[62] Di Donna, A., Ferrari, A., & Laloui, L. (2016). Experimental investigation of the soil concrete interface: physical mechanisms, cyclic mobilization and behavior at different temperatures. *Canadian Geotechnical Journal*, 43(4), 659-672.

[63] Wang, B., Bouazza, A., Haberfield, C. (2011). Preliminary observations from laboratory scale model geothermal pile subjected to thermo-mechanical loading. *Geo-Frontiers 2011 advances in geotechnical engineering*, 430-439.

[64] Xiao, S., Suleiman, M.T., McCartney, J.S. (2014). Shear Behavior of Silty Soil and Soil-Structure Interface under Temperature Effects. In: *Geo-Congress GSP 234 © ASCE*, 4105-4114.

[65] Murphy, K.D., & McCartney, J.S. (2014). Thermal Borehole Shear Device. *ASTM geotechnical testing journal*, 37(6), 1040-1055.

Chapter 3

Effect of Temperature on the Drained Shear Strength of Clay

3-1- Introduction

As mentioned earlier, temperature variations can occur in the soil around an energy pile during its operation. During warm seasons when the energy pile exchanges heat with the soil because of air conditioning, the temperature of the soil in the vicinity of the pile may reach temperatures up to 40°C (Brandl 2006 [8]). Temperature can influence many engineering aspects of soil behavior including deformability and strength (Yilmaz 2009 [43]; Yilmaz 2011 [42]; Khalili et al. 2010 [25]). Reduction in soil strength and stiffness due to temperature increase may cause additional settlement and axial forces in energy piles. The thermo-mechanical behavior of single and group of energy piles has been investigated by many researchers through in-situ and laboratory tests and numerical analysis (Bourne-Webb et al. (2009) [7]; Stewart and McCartney (2014) [35]; Mimouni and Laloui (2014) [30]; Abdelaziz and Ozudogru (2016) [1]; McCartney and Murphy (2017) [29]). The thermal-mechanical behavior of soil was initially taken into consideration during soil sampling and transportation to the laboratory (Campanella and Mitchell 1968 [11]; Virdi and Keedwell 1988 [41]). As a result, the response of soil was studied under temperature increase up to 50°C (Abuel-Naga et al. 2007 [2]). The effect of even higher temperatures (up to 100°C) on the thermo-mechanical response of clays for radioactive waste storage applications has been investigated (Abuel-Naga et al. 2007 [2]). The following summarizes the current knowledge (available in the published literature) about the thermo-mechanical response of soil.

Drained thermal volumetric change of unsaturated/saturated soil can be described mainly by the secondary compression behavior following the most recent loading or unloading increment prior to heating. For positive increment of secondary compression, the induced thermal volumetric change is positive (contractive), while it is expansive if the rate of secondary compression is negative (expansion). The thermal volumetric change is insignificant if the secondary compression

is negligible (Coccia and McCartney 2016a [13] and b [14]; Towhata et al. 1993 [38]; and Burghignoli et al. 2011 [10]). Accordingly, heating causes volumetric contraction in NC clay and OC clays with the recent history of loading, while it generates dilative volumetric change in OC clays with the recent history of unloading. In addition, the observed volumetric contraction during heating was found to be irreversible, while thermally induced expansive response was found to be reversible (Demars and Charles1982 [16]; Towhata et al. 1993 [38]; Baldi et al. 1988 [5]; Hueckel and Baldi 1990 [21]; Laloui and Cekerevac 2003 [26]; Abuel-Naga et al. 2007b [3]; Sultan et al. 2002 [34]; Coccia and McCartney 2016a [13] and b [14]; and Burghignoli et al. 2011 [10]).

Jaradat et al. (2017) indicated that clay particle orientation and pore size distribution, as two main parameters describing clay microstructure, can be thermally influenced. Their study has shown that thermally induced reorientation of kaolin clay particles was mainly determined by their relative orientation (in the initial configuration) with respect to thermal gradient. The thermally induced reorientation for kaolin clay particles, initially oriented perpendicular to the thermal gradient, was more important as compared to that for kaolin clay particles initially oriented parallel to the thermal gradient. Darbari et al. (2017) [15] indicated that heating decreases the size of larger pores in kaolin clay, while it causes an increase in the size of smaller pores. This behavior is attributed to the anisotropic thermal expansion coefficient of clay particles that can explain the thermally induced contraction in clays.

Campanella and Mitchell (1968) [11] have shown that undrained heating causes pore pressure increase in soil. Cycles of undrained heating/cooling will result in accumulation of excess pore water pressure, which in turn causes a reduction in mean effective stress and even shear failure. On the other hand, no clear relationship between temperature changes and shear strength has been observed yet. Several researchers indicated that heating causes soil stiffening (Cekerevac and

Laloui 2004 [12]; Abuel-Naga et al. 2006 [4]; Laguros 1969; Houston et al. 1985 [19]; Trani et al. 2010 [39]), while a strength decrease has been reported by others (Noble and Demirel 1969 [31]; Bruyn and Thimus 1996 [9]; Hueckel and Baldi 1990 [21]). Several other studies, however, observed no appreciable influence on the shear strength (Burghignoli et al. 2011 [10]; Hueckel and Pellegrini 1989 [23]). As a final point, the residual shear strength (at large strains) was shown to be independent of temperature (Cekerevac and Laloui 2004 [12]; Trani et al. 2010 [39]).

Even though there is a vast amount of literature on the soil thermo-mechanical behavior, most of research has been carried out for the range of temperatures corresponding to conditions of nuclear waste disposal in clays (15° C to 115° C). Furthermore, more attention has been paid to the effects of elevated temperature on soil behavior, rather than the effects of cyclic variations of temperature. Cyclic thermal loading is relevant to energy piles since they cause cyclical temperature variations in the surrounding soil on daily and seasonal basis. In this type of thermal loading the maximum temperature experienced by the soil is usually less than 40 °C (Di Donna and Laloui 2015 [18]).

This chapter presents the results of compressive triaxial tests carried out on HC-77 kaolin clay under different thermal loading. Tests were performed at different stress states and histories to understand their effects on the thermo-mechanical behavior of clay. These tests are relevant to energy piles operating in summer mode where the surrounding soil is used as a heat sink, thus a temperature rise in the soil is expected. In the following sections, the soil, the test apparatus, the experimental plan, and test results are described in detail.

3-2- Thermo-mechanical behavior of clay

Salgado (2007) [33] hypothesized that porosity and effective stress are the two properties that control the shear strength of a soil. Thus, the soil shearing response to temperature variations may be examined through thermal changes in these two properties. A theoretical framework, through

which the effect of temperature on porosity and shear strength is described, will be established herein.

Thermal volumetric changes of soil
The theoretical relationships between temperature increment and induced thermal volumetric change in a soil were proposed and explained by Campanella and Mitchell (1968) [11], which is basically a "pore water volume"-based technique. Assuming fully saturated condition, the thermal volumetric changes of clay will occur through changes in the volume of solid particles and pore water. The evolution of solid particles volume, $(\Delta V_s)_{\Delta T}$, and pore water volume, $(\Delta V_w)_{\Delta T}$, due to temperature increment (ΔT) can be expressed as follows:

$$(\Delta V_s)_{\Delta T} = \alpha_s V_s \Delta T \qquad\qquad (3-1)$$
$$(\Delta V_w)_{\Delta T} = \alpha_w V_w \Delta T \qquad\qquad (3-2)$$

Where V_s and V_w are solid particles and pore water volumes, respectively. α_s and α_w are the coefficients of thermal expansion of solid particles and pore water, respectively. The study by Campanella and Mitchell (1968) [11] suggested using 3.5×10^{-5} $(\frac{1}{{}^\circ C})$ for α_s, and 2.1×10^{-4} $(\frac{1}{{}^\circ C})$ for α_w.

In drained thermal loading, the excess pore pressure induced by thermal expansion discrepancy between pore fluid and solid particles is allowed to be dissipated. This may possibly produce reduction in porosity as indicated in the literature (Baldi et al. 1988 [5]; Campanella and Mitchell 1968 [11]; Burghignoli et al. 2011 [10]). However, Darbari et al. (2017) [15] have recently shown that thermally induced reduction in porosity should be interpreted in terms of the anisotropic thermal expansion coefficient of clay particles. Conversely, during cooling, the change in pore pressure is negative thus causing the water to be absorbed by the soil.

If the volume of water exiting/entering is given by $(\Delta V)_{wdr}$, the total volume changes, $(\Delta V)_{\Delta T}$, during a drained thermal loading may be expressed by (Baldi et al. 1988 [5]):

$$(\Delta V)_{\Delta T} = (\Delta V)_{wdr} - (\Delta V_s)_{\Delta T} - (\Delta V_w)_{\Delta T} \quad (3-3)$$

By substituting equations (3-1) and (3-2) into equation (3-3), the equation can be rewritten as follows:

$$(\Delta V)_{\Delta T} = (\Delta V)_{wdr} - (\alpha_s V_s + \alpha_w V_w)\Delta T \quad (3-4)$$

Since the coefficient of thermal expansion and the volumes of solid particles and pore water are positive, the second term in Equation (3-4) has the same sign as ΔT. $(\Delta V)_{\Delta T}$, however, may have either the same or opposite sign as ΔT, depending on the magnitude of $(\Delta V)_{wdr}$. It is to be noted that $(\Delta V)_{wdr}$ is positive when the pore water is allowed to drain out of the sample. With the same temperature increment, the amount of water exiting/entering over equal period of time is mainly controlled by the initial porosity of clay; the higher the soil porosity, the larger $(\Delta V)_{wdr}$. It is noteworthy that the thermal volumetric change is associated with changes in both void ratio and particle arrangement. The latter is important in fine-grained soil because it may yield different structures and fabrics such as dispersed or flocculated fabrics. As discussed later, different structures and fabrics may affect the effective stress distribution in fine-grained soils.

Thermally-induced change in effective stress
This section describes the effects of temperature variations on effective stress through two theoretical models: Sridharan and Rao's model and Lambe-Bolt's model. These models were used by Hueckel (1992b) [20] to examine the concept of effective stress and deformation in clays. According to Hueckel (1992b) [20], there are three internal stress components that contribute in carrying external loads: stress in solid skeleton σ_c, bulk water pressure u, and physico-chemical interaction between solid particles σ_{R-A}. The physico-chemical interaction of two clay platelets is

a combination of repulsive interaction due to negatively charged clay surfaces and attractive interaction related to Van der Waals forces. For parallel clay platelets of constant surface charge, σ_{R-A} is defined as follows:

$$\sigma_{R-A} = \sigma_R - \sigma_A \qquad (3-5)$$

Where σ_R is the repulsive force and σ_A is Van Der Waals attraction force that is mainly dependent on the inter-particle distance, δ. Figure 1 illustrates the model by Sridharan and Rao. In this model, the effective stress is defined as a difference between total stress, and the sum of pore water pressure and physico-chemical interaction. In terms of stress increment, it can be written as follows (Hueckel (1992b) [20]):

$$\Delta\sigma' = \Delta\sigma_c = \Delta\sigma - \Delta u - \Delta\sigma_{R-A} \qquad (3-6)$$

For a drained loading condition with a constant total stress, Equation (3-6) yields:

$$\Delta\sigma' = \Delta\sigma_c = -\Delta\sigma_{R-A} \qquad (3-7)$$

Sridharan and Rao's model can be used to assess the behavior of clay with flocculated arrangement of particles as indicated in Figure 3-1(b).
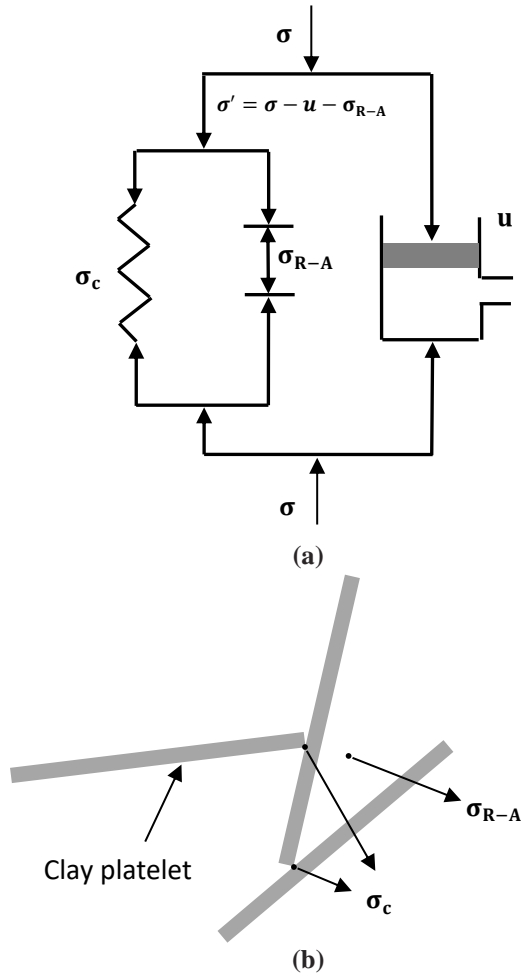
Figure 3-1-(a) Model 1: Sridharan and Rao's model, **(b)** Corresponding clay particles arrangement (Hueckel (1992b) [20]).
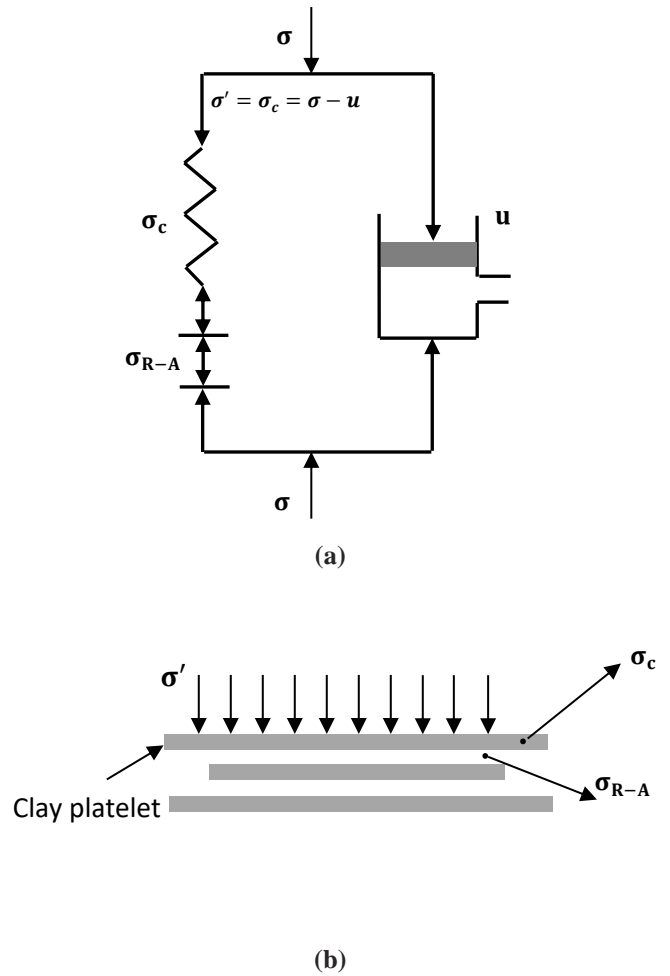
Figure 3-2- (a) Model 2: Lambe-Bolt's model, **(b)** Corresponding clay particles arrangement (Hueckel (1992b) [20]).

The Lambe-Bolt model assumes that the effective stress is equal to the physico-chemical interaction. This model is schematically illustrated in Figure 2. In terms of stress increments, the relations between stress components are given by equations 3-8(a) and 3-8(b), which comply with the effective stress principle by Terzaghi (1936) [37].

$$\Delta\sigma' = \Delta\sigma_c = \Delta\sigma_{R-A} \qquad\qquad (3-8a)$$

$$\Delta\sigma = \Delta\sigma' + \Delta u \qquad\qquad (3-8b)$$

In a drained loading condition with a constant total stress, these equations yield:

$$\Delta\sigma' = \Delta\sigma_{R-A} = \Delta\sigma = 0 \qquad\qquad (3-9)$$

This model is appropriate for the clay having a predominant population of face-to-face contacts (parallel arrangement) as illustrated in Figure 3-2(b). The one-dimensional consolidation process can be understood as a progressive conversion of model 1 into model 2. Hueckel (1992(b)) [20] suggested that the increment of physico-chemical interaction may be expressed in terms of rates of inter-particles distance $d\delta$, change of dieletric coefficient dD, ionic concentration change dC, and temperature change, dT:

$$\Delta\sigma_{R-A} = \xi_\delta d\delta + \xi_D dD - \xi_c dc + \xi_T dT \quad (3-10)$$

Using macroscopic experiments, Lambe (1960) [28] suggested that coefficients ξ_δ, ξ_D and ξ_c are always positive. However, the coefficient ξ_T can be negative for dense clays with a dry unit weights greater than 1.8 g/cm3. Assuming constant magnitudes for dielectric coefficient and ionic concentration, the increment of physico-chemical interaction can be explained as follows:

$$\Delta\sigma_{R-A} = \xi_\delta d\delta + \xi_T dT \qquad\qquad (3-11)$$

From this equation, physico-chemical interaction can directly be altered by temperature through $\xi_T dT$, while it may indirectly be influenced through $\xi_\delta d\delta$ due to reorientation and relative movement of clay particles during thermal deformation (consolidation). Kaolin particles can be heavily reoriented during heating if they are initially oriented perpendicular to the thermal gradient, while the thermal reorientation is less important if kaolin particles are oriented parallel to the thermal gradient as suggested by Jaradat et al. (2017). At constant total stress in drained loading conditions, however, Lambe-Bolt series model implies that the effective stress is independent of variation in physico-chemical interaction, according to Equation (3-9). Whereas, in the Sridharan and Rao's model, following Equation (3-7), the effective stress appears to be

directly influenced by $\Delta\sigma_{R-A}$. The two models described above are used to gain insight into the experimental study presented below.

3-3- Description of soil, test apparatus, and testing program

Kaolin clay HC-77, is classified as CL (lean clay) using the Unified Soil Classification System and commercially available in powder, was used in this study. The liquid and plastic limits are 45% and 25%, respectively. Figure 3-3 presents the particle size distribution curve of the clay.

All test specimens were prepared by one-dimensionally consolidating a slurry obtained by mixing kaolin powder with de-aired distilled water at a moisture content two times the liquid limit of the clay. One-dimensional consolidation was performed on the slurry in a rigid cylinder subjected to a vertical pressure of 100 kPa applied in small increments. At the end of consolidation, a specimen measuring 50 mm in diameter and 100 mm in height was trimmed in preparation for triaxial testing.
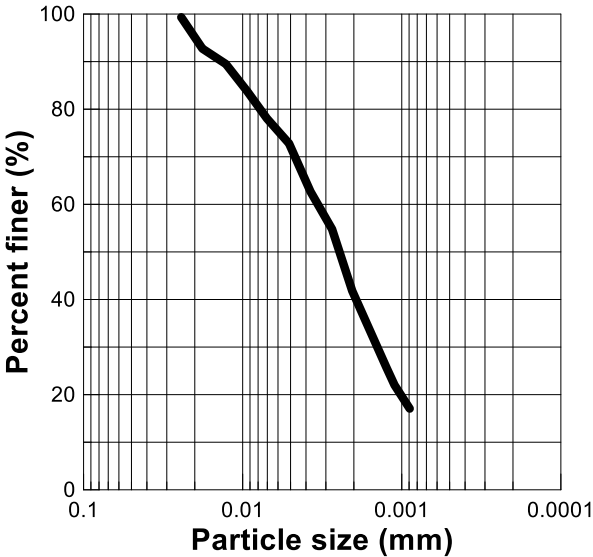
Figure 3-3- Particle size distribution of Kaolin HC-77.
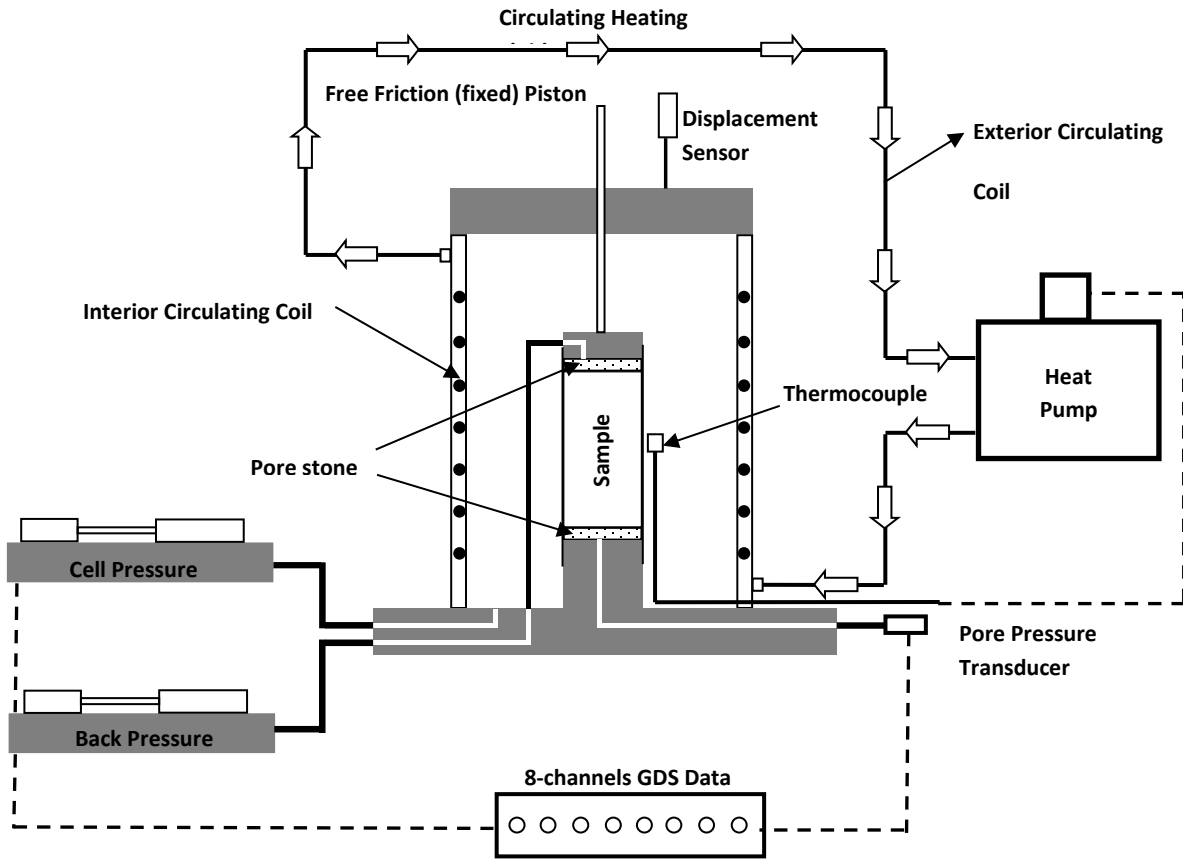
Figure 3-4- Temperature controlled triaxial apparatus.

A GDS temperature controlled triaxial testing apparatus (Figure 4) was used to perform all triaxial tests. The GDS controllers precisely measure and adjust both back and cell pressure within ± 1 kPa accuracy. The displacement sensor is attached to the top surface of the chamber. Note that the axial loading (deviatoric stress) is applied by moving the triaxial cell (and the specimen fixed inside the cell) upward against the fixed piston. Correspondingly, the cell upward movement measured by the sensor is essentially equal to the clay axial deformation created by the piston. The thermal loading system consisted of a heat pump, a thermocouple, and a data logger. The sample temperature was controlled by circulating heating fluid from the heat pump through a hollow metal coil placed within the triaxial cell wall. To avoid any disturbances, the K-type thermocouple was

placed on the side of sample (not inside the sample) to measure the cell water temperature adjacent to the soil sample. The temperature inside the sample, however, was estimated by preliminary calibration tests, where sample and water temperatures were recorded simultaneously. Figure 3-5 shows the reference temperature profile and the measured specimen temperature during one heating/cooling cycle (24-34-24 °C). As the figure shows, each heating/cooling cycle lasts 292 minutes; during which the specimen temperature was raised from 24°C to 34°C in 252 minutes and reduced back to ambient temperature (24°C) in 40 minutes.
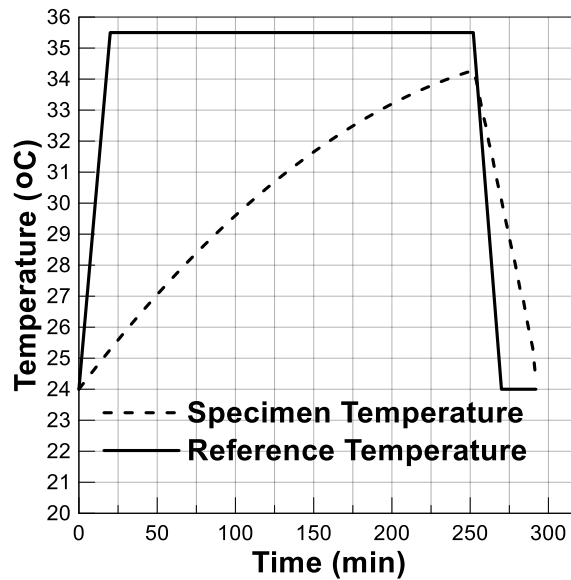
Figure 3-5- Applied temperature variations with time.

Another primarily calibration test was performed to estimate the effect of temperature variation on the thermal expansion/contraction of the drainage system. A perfectly non-porous rubber cylinder having the same dimension as that of the clay specimen was installed in the cell with a saturated pore stone/filter paper at each end. All drainage lines were fully saturated with de-aired water. The test was conducted under cell/back pressures of 150 kPa and 50 kPa, respectively, similar to the mechanical loading used in the actual tests. The test was repeated two times under 10 and 20 cycles

of the reference temperature variation (24-34-24 °C), shown in Figure 3-5, and the thermally induced change in volume of water expelled/absorbed was recorded. For instance, the thermally-induced volume change of the drainage system with the reference temperature is depicted in Figure 3-6 (for 3 heat cycles). Very similar variation was noted during heat cycles. Furthermore, the average volume change within each heating/cooling phase was found to be nearly 0.05 cm3.The amount of water thermally expelled/absorbed during actual tests were carefully corrected based on the results obtained in the calibration test and presented in Figures (3-8) -(3-13).
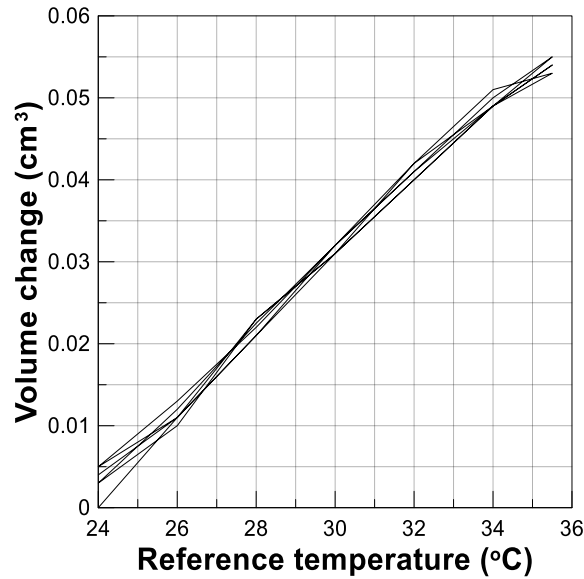
Figure 3-6- Thermally induced-volume change of the drainage system during 3 heat cycles.

To investigate the clay shearing response to temperature, 19 consolidated drained triaxial tests were performed. The triaxial testing program is summarized in Table 3-1. The following describes a step-by-step procedure of the thermal triaxial tests.

Step 1: Primary consolidation
To investigate the dependence of clay thermal behavior on stress state and history, different initial confining pressures and histories were considered. With respect to Normally Consolidated (NC) clays, the specimens were primarily consolidated under effective confining pressures of 100kPa,

200 kPa and 300kPa to study the effect of stress state. Whereas Over-Consolidated (OC) clays were initially consolidated under confining pressures of 200 kPa, 500 kPa and 900 kPa, and then unloaded in order to obtain over consolidation ratios of 2 (lightly OC clay), 5 (intermediate OC clay), and 9 (heavily OC clay), respectively. The 50-kPa back pressure was used in all tests to ensure saturation of the clay specimen and to avoid any evaporation during heating.

Step 2: Drained thermal loading
In this stage the soil specimen was subjected to either non-cyclic or cyclic heating. As for non-cyclic heating, the specimen temperature was slowly raised to 34°C (in 252 minutes) from its initial temperature of ≈24° C. For cyclic heating, each thermal cycle (24-34-24° C) shown in figure 3-5 was repeated 10 or 20 times to examine the potential effect of heat cycles on shear strength of clay. As reported by Laloui et al. (2014) [27], 3.33°C/hour is the heating rate, at which heating can occur under drained condition, where thermally induced excess pore pressure is kept close to zero. In this study the reference temperature profile (Figure 5), which was determined through primary calibration tests, was used to produce drained condition during thermal loading. From Figure 3-5, the rate of specimen temperature changes was slightly higher than 3.33°C/hour in the first 20 minutes, but it dropped below 3.33°C/hour over the rest of heating period. Pore water pressure was also measured during heat cycles to ensure that thermally induced pore pressure within the specimen is minor. As shown in Figure 3-7, some pore pressure was generated in the beginning of each cycle because of higher rate of heating, which was 1- 2% of the effective isotropic pressure in all cases. At the end of the heating phase, however, almost no excess PWP was observed at the boundary of the clay specimen. At the end of the step, the specimen was left for 3 hours to ensure that any thermally-induced PWP at the center of the sample is also dissipated prior to shearing.
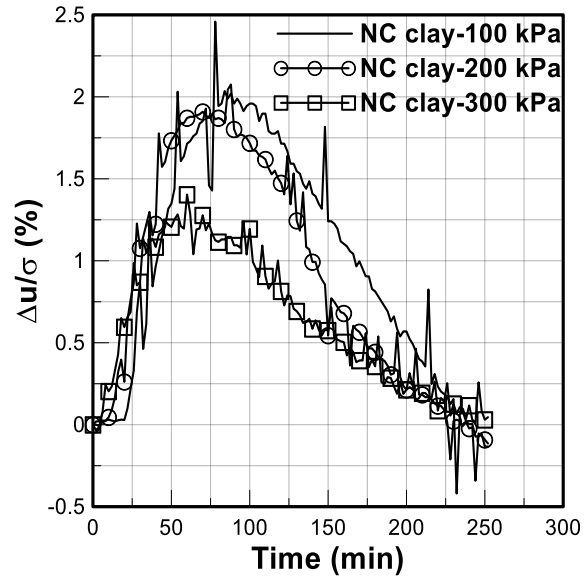
Figure 3-7- The ratio of thermally induced PWP and effective confining pressure (Δu/σ) during heating phase within a thermal cycle.

Step 3: shearing

To ensure drained condition during shearing, the strain-controlled axial load was applied at a strain rate of 0.005 %/min in accordance with ASTM D7181- 11. The specimens subjected to cyclic thermal loading were sheared at a constant 24°C, while those heated monotonically up to 34°C, were sheared at 34°C.

It should be noted that the tests were carried out at least twice (3-4 times in some cases) to ensure that the results are repeatable

Table 3-1- Tests details performed in this study.

Test #	h_0 (cm)	D_0 (cm)	σ_0'(kPa)	OCR	Thermal loading	ΔV_C(cm3)	ΔV_T(cm3)	$\Delta \sigma_d$ (kPa)
1	10	5	100	1	24°C	6.03	0	165.82
2	10	5	100	1	34°C	6.733	0.227	154.67
3	10	5	100	1	(24°C-34°C)-10 cycles	5.75	0.488	150.11
4	10	5	100	1	(24°C-34°C)-20 cycles	5.09	-0.274	158.2
5	10	5	200	1	24°C	8.06	0	306.71
6	10	5	200	1	34°C	-	-	303.44
7	10	5	200	1	(24°C-34°C)-10 cycles	10.83	0.299	318
8	10	5	300	1	24°C	11.45	0	449.56
9	10	5	300	1	34°C	14.314	0.257	455.75
10	10	5	300	1	(24°C-34°C)-10 cycles	14.046	0.108	481.63
11	10	5	100	2	24°C	11.46	0	169.7
12	10	5	100	2	34°C	10.42	0.469	163.63
13	10	5	100	2	(24°C-34°C)-10 cycles	10.28	0.125	162.89
14	10	5	100	5	24°C	15.2	0	186.56
15	10	5	100	5	34°C	14.7	0.258	170.65
16	10	5	100	5	(24°C-34°C)-10 cycles	14.61	0.0469	175
17	10	5	100	9	24°C	16.87	0	198.53
18	10	5	100	9	34°C	14.8	0.39	190.8
19	10	5	100	9	(24°C-34°C)-10 cycles	18.03	0.191	171.5

h_0:Initial Height, D_0: Initial Diameter, σ_0: Cell Pressure, ΔV_C:Volume Change during Consolidation, ΔV_T: Volume Change during Thermal Loading
$\Delta \sigma_d$: Deviator Stress

3-4- Experimental results

Thermal volumetric change

The evolution of specimen's volume during thermal loading is presented herein. It was calculated based on the theoretical relationship proposed by Campanella and Mitchell (1968) [11] as discussed earlier (Equation 3-4). According to this theoretical relationship, the volumetric change in clay in non-isothermal condition can be obtained by integration of equation (3-4) over thermal loading duration, $\int_0^t (\Delta V)_{\Delta T}$. The volumetric thermal strain ε_{v-th} is therefore defined as the ratio of $\int_0^t (\Delta V)_{\Delta T}$ and the specimen's volume,V_c, at the beginning of thermal loading:

$$\varepsilon_{v-th} = \frac{\int_0^t (\Delta V)_{\Delta T}}{V_c} \qquad (3-12)$$

A simple numerical code was developed to plot the volumetric thermal strain as a function of time using equation (3-12). The contractive and dilative volumetric strains were considered to be positive and negative, respectively.

Figure 3-8 shows the thermal evolution of volume of NC clays (at 100 kPa) with respect to time. Figures 3-8(a) indicates that pore water drains out of the clay specimen during non-cyclic heating causing a contractive behavior of clay. As for cyclic heating, Figure 3-8(b), the pore water drainage also occurs during the heating phase, while it is absorbed into the specimen during the cooling period of each cycle. The volume of water drained out of the specimen during the first cycle is greater as compared with that in subsequent cycles. The variations of volumetric thermal strain are very similar to that of thermally expelled pore water, where the largest change occurs in the first cycle, and in the subsequent cycles the clay specimen contracts during heating and expands during cooling. Similar thermal evolution of the volume can also be noted during applying 20 thermal cycles, although its magnitudes are different within the first 10 cycles comparing to those observed during applying 10 thermal cycles. It may be attributed to varying initial soil conditions including moisture content, degree of saturation, density, or variations in the heating rate or conditions of the testing device. Nevertheless, $|\varepsilon_{v-\text{th}}|$ generated during the cyclic heating is less than 0.25% for all tests, which is deemed insignificant.

The thermal volumetric change behavior of NC clays at confining effective pressures of 200 kPa and 300 kPa is illustrated in Figures 3-9 and 13-10, respectively. It can be noted that the variation of thermally expelled water volume and the corresponding thermal strain with respect to time is similar to that shown in Figure 3-8. Figures 3-9 and 3-10 also show the variations of volumetric strain (during 10 cycles of heating) as function of temperature. Figure 3-9(b) clearly indicates that the volume change is relatively larger during the initial heat cycle ($\approx 0.17\%$), while it is very small in the subsequent heat cycles (less than 0.04% in each cycle). After the initial heat cycle, similar to that explained in Figure 3-8, the thermally induced volumetric strain decreases progressively in the subsequent cycles and reaches almost 0.1% at the end of 10th cycle. This may be attributed to

the relatively faster cooling rate used in each cycle as compared with the heating rate (Figure 3-5). In fact, during a rapid cooling, relatively larger changes in excess PWP is likely to generate as compared with those induced during the heating phase, which occurs at a lower rate. Thus, the amount of water absorbed during cooling is expected to be relatively larger than that drained out of the sample during heating. It can also be noted in Figures 3-9a and 3-10a, where the amount of water absorbed during the cooling phase of each cycle is larger (approximately 0.02-0.07 cm3) than that drained out in the preceding heating phase. Therefore, according to Equation 3-4, the resulting total volume change $((\Delta V)_{\Delta T})$ and strain will be larger during the cooling phases as opposed to those during the heating phases, under similar temperature increment. The cummulative strain hence tends to gradually decrease with heat cycles.

The data presented in Figure 3-10(b) illustrate the same trend of volumetric strain with temperature for a specimen with 300-kPa confining pressure. It is noted that the volumetric strain decrease (dilative behavior) in subsequent heat cycles is greater than that observed for the specimen with 200-kPa confining pressure. Figure 3-10(b) shows that the largest volumetric strain occuring in the first cycle of about 0.15% has reduced to 0.025% at the end of 8th heat cycle.
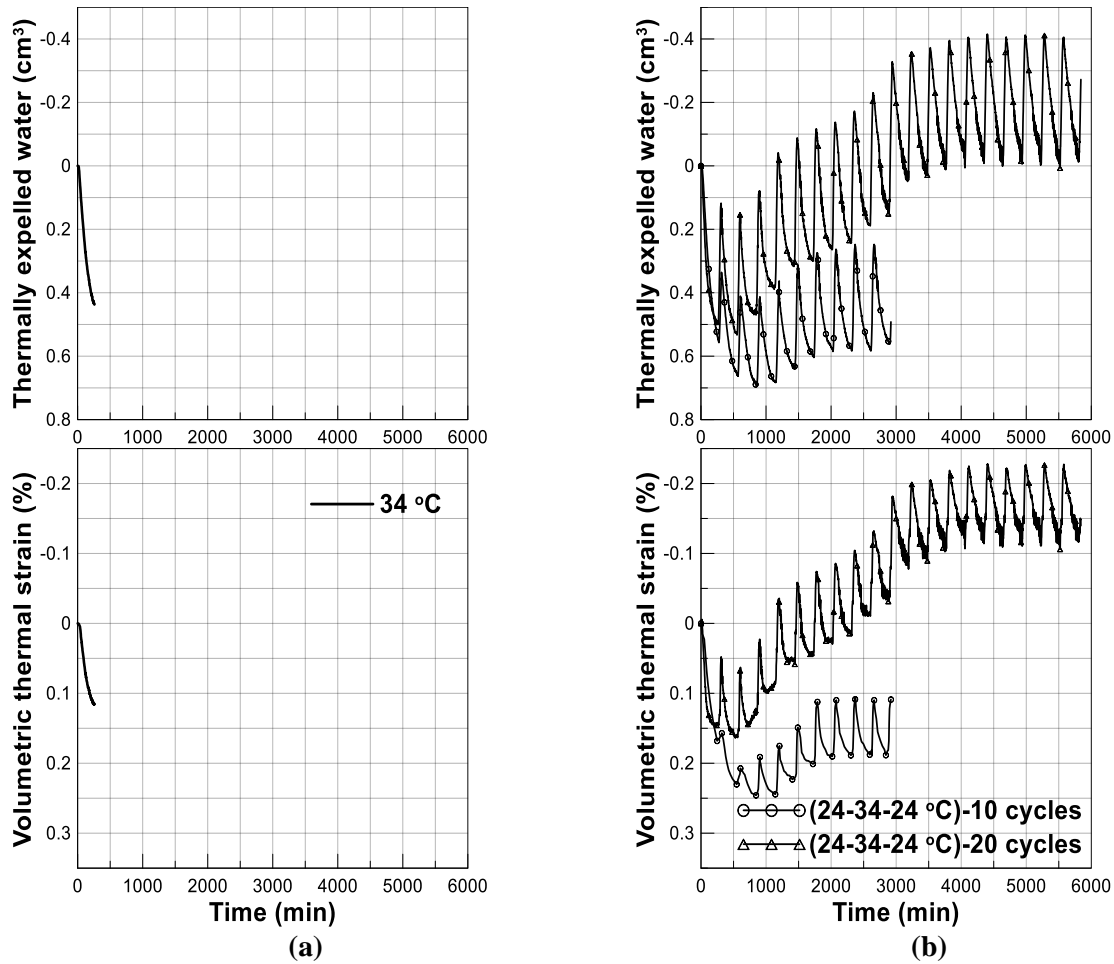
Figure 3-8- Thermal volumetric behavior of NC clay at 100 kPa (a) during non-cyclic heating and (b) during cyclic heating.

Several observations are noted from Figures (3-8)-(3-10): (1) the thermal evolution of volumetric strain is consistent with the evolution of expelled pore water, (2) clay contracts during heating phase and expands during cooling, (3) the maximum volume change occurs in the first cycle, which is also largely irreversible, (4) in subsequent cycles, volume changes are smaller and nearly reversible, (5) total volumetric strain tends to decrease with heating cycles (perhaps because of relatively rapid cooling) and this tendency becomes more pronounced as confining effective stress increases, and (6) there is no important change in NC clay porosity during temperature variations. With respect to the volumetric behavior during heating, similar results have been reported by Campanella and Mitchell (1968) [11], Demars and Charles (1981) [16], Hueckel and Baldi 1990

[21], Towhata et al. 1993 [38], Delage et al. (2000) [17], Cekerevac and Laloui (2004) [12], Abuel-Naga et al. (2006) [4], Burghignoli et al. (2011) [10], Bing et al. (2014) [6], Di Donna and Laloui (2015) [18], and Coccia and McCartney 2016(a) [13] & (b) [14]. Regarding the volumetric behavior during cooling phase, although Campanella and Mitchell (1968) [11] and Hueckel and Baldi (1990) [21] reported an expansive behavior during cooling period, Di Donna and Laloui (2015) [18] and Burghignoli et al. (2011) [10] observed that clays contract during cooling phase, after it is initially heated up. The cooling-induced expansive response observed here may be related to the relatively rapid cooling causing relatively high negative PWP within the clay. It, in turn, could lead to absorbing relatively large quantities of water and thus the clay expansion, according to Equation 3-4.

Similar observations to (3) and (4) have been reported by Campanella and Mitchell (1968) [11], Demars and Charles (1981) [16], Burghignoli et al. (2011) [10], Bing et al. (2014) [6], Vega and McCartney (2015) [40] and Di Donna and laloui (2015) [18]. However, there is some controversy in the literature about (5). Campanella and Mitchell (1968) [11] observed a progressive increase (with slow rate in subsequent cycles) in volumetric strain with heating cycles, while Burghignoli et al. (2011) [10] reported an ever-contracting behavior with gradually decreasing values of volumetric strain with thermal cycles. Demars and Charles (1981) [16], Abuel-Naga et al. (2006) [4] and Burghignoli et al. (2011) [10] found that thermally induced volumetric strains were independent of confining pressures. Bing et al. (2014) [6] showed that clay specimens at high confining pressures tend to have smaller thermally induced volumetric strains.
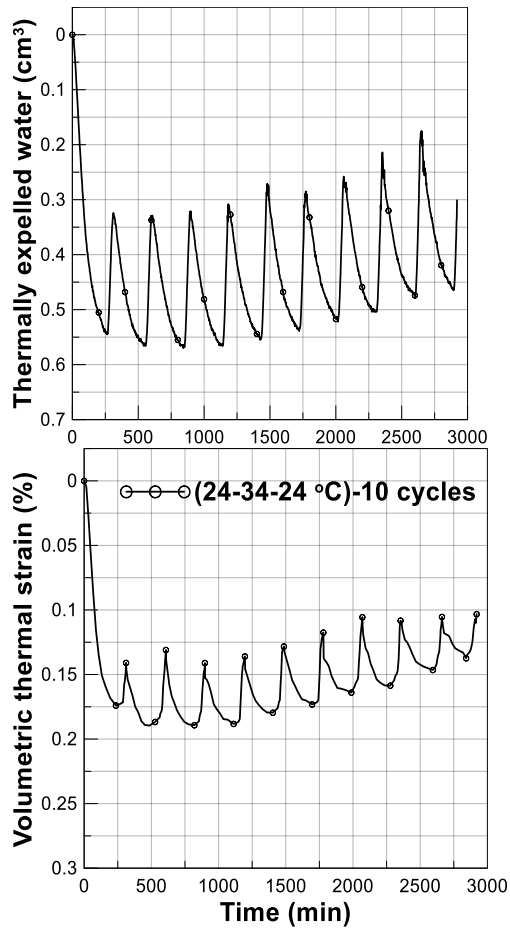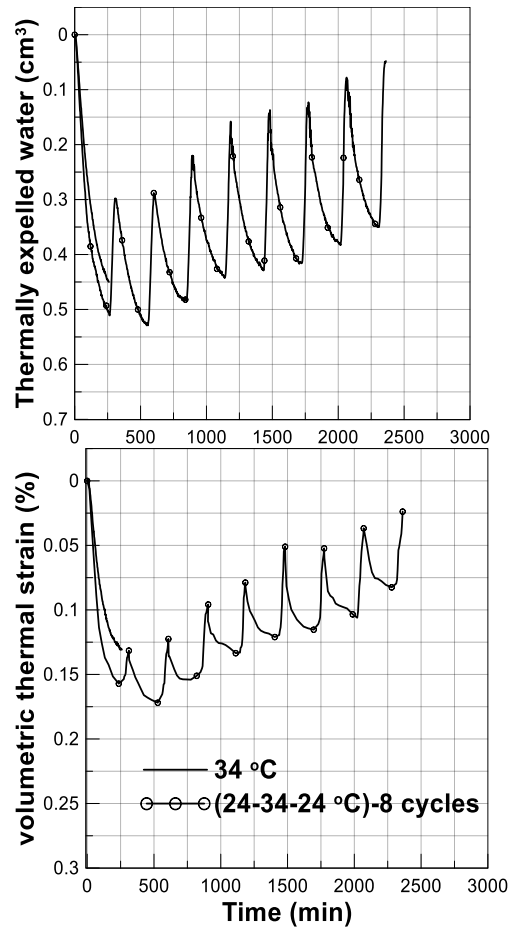
Figure 3-9- Thermal volume behavior of NC clay at 200 kPa (a) versus time, and (b) versus temperature.

Figure 3-10- Thermal volume behavior of NC clay at 300 kPa (a) versus time, and (b) versus temperature.

Temperature induced volume changes of OC clays are shown in Figures (3-11) -(3-13). Similar pattern of thermally induced volume changes with time and temperature can be observed for OC clays. OC clays, however, tend to have less drained pore water and volumetric strains during heat cycles as compared with NC clays. Figure 3-11(c) indicates that the largest contractive volumetric strain for lightly OC clay (OCR=2), which occurs in the first cycle, is about 0.225%, while for intermediate and heavily OC clays, Figures 3-12(b) and 3-13(b), it is estimated to be $\approx 0.11\%$ and $\approx 0.125\%$, respectively, which are clearly less than those observed for NC clays. In subsequent cycles, similar to NC clays, smaller volumetric strains are generated, which are less than 0.04% for all OC clays. At the end of heat cycles, the total volumetric strains were nearly 0%, -0.025% and 0.04% for lightly, intermediate and heavily OC clays, respectively. It is noteworthy that at high OCR values, Figures 3-12(b) and 3-13(b), the specimens initially exhibit expansive behavior at 24°C-25°C, followed by a contractive behavior between 25°C and 34°C.

The volumetric behavior of the clay (shown in Figures (3-8)-(3-13)) can also be described with respect to the thermal cycles for both the NC and OC clays, as presented in Figure 3-14. Only the thermal strain corresponding to the end of each thermal cycle has been considered. Form Figure 3-14, it can be noted that the greatest change in the thermal strain happens at the end of the first cycle (except for the NC clay at 100 kPa, which occurs at the end of the second cycle) followed by a gradual decrease in the total volumetric stain in the next cycles. However, the strain changes tend to stabilize over the last 3-4 cycles.
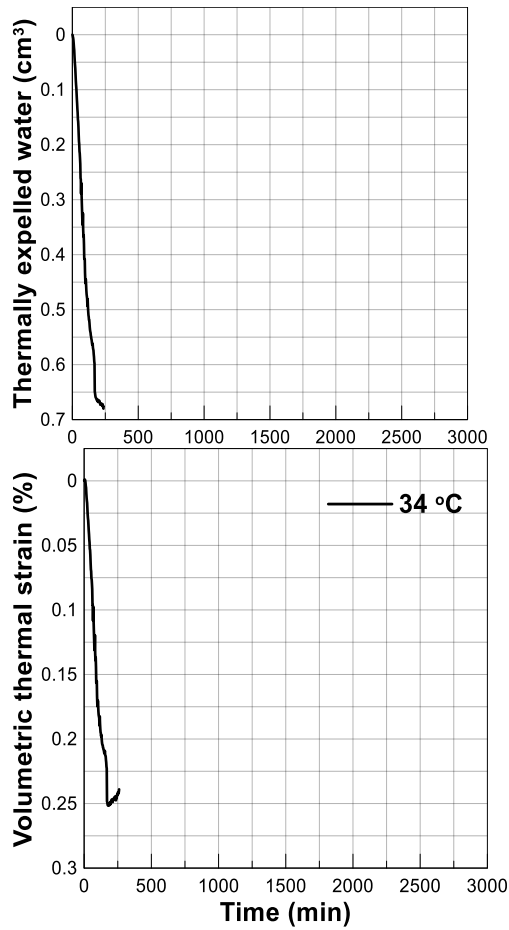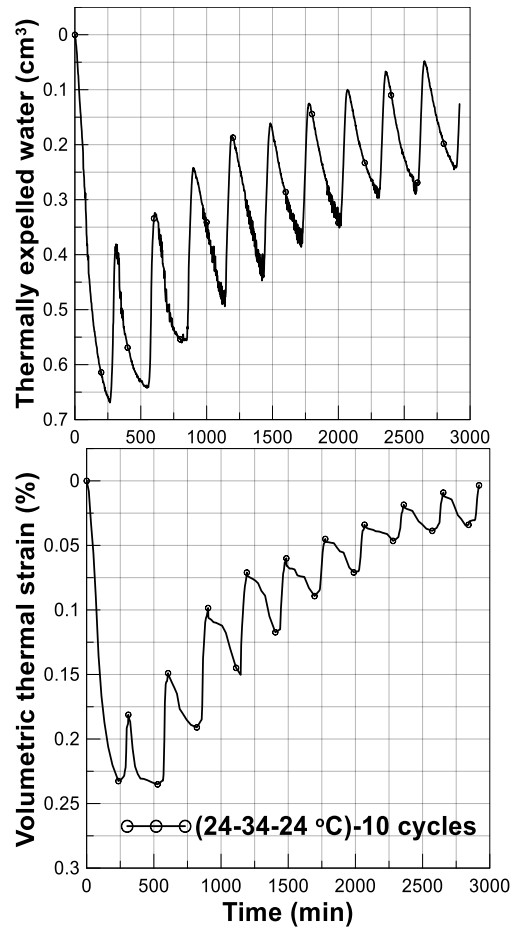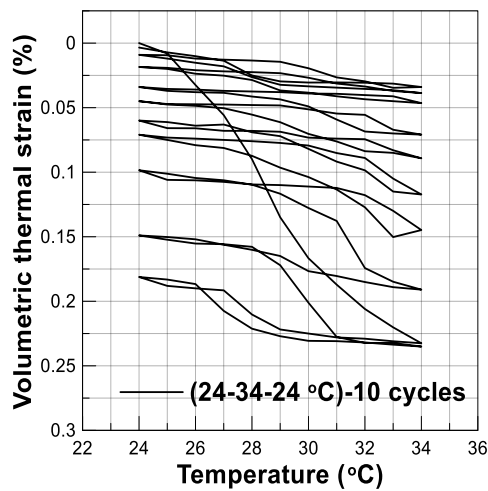
Figure 3-11- Thermal volume behavior of clays with OCR=2 (a) versus time (during non-cyclic heating), (b) versus time (during cyclic heating), and (c) versus temperature.
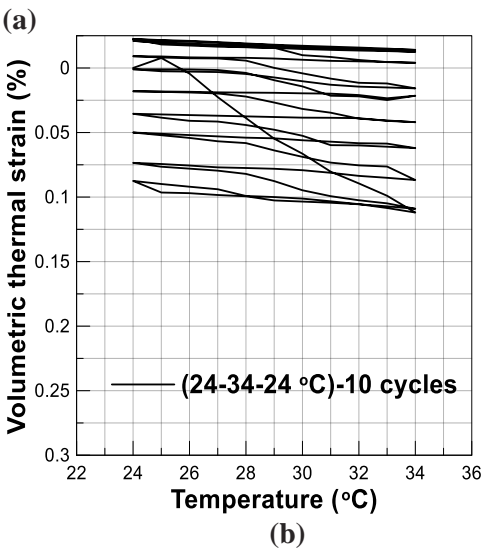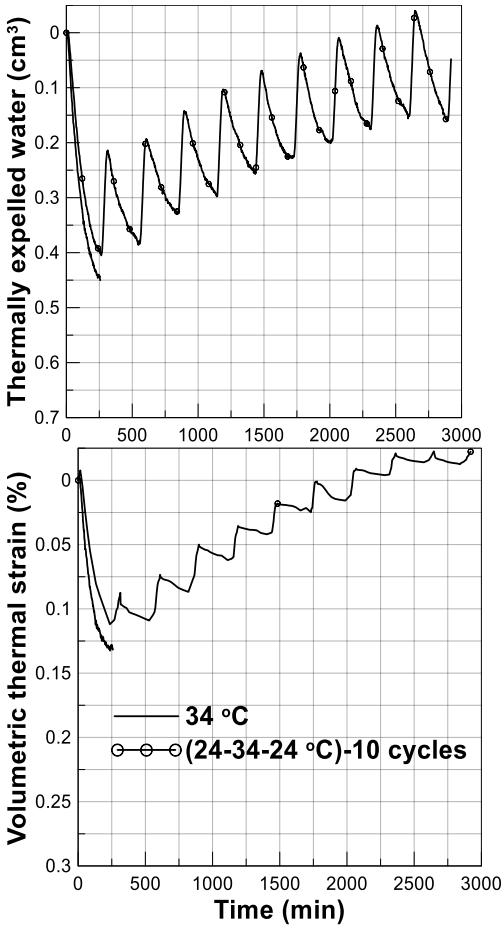
Figure 3-12-Thermal volume behavior of clays with OCR=5 (a) versus time, and (b) versus temperature.
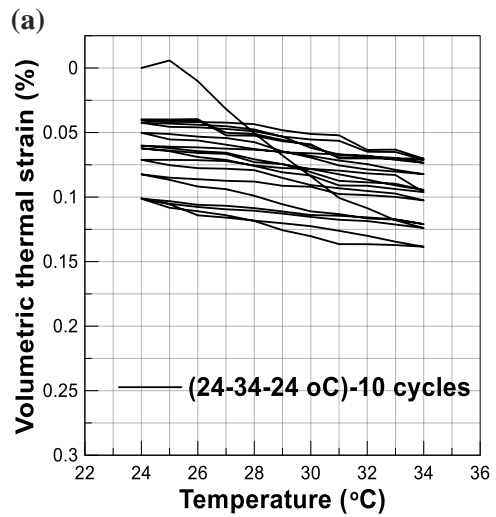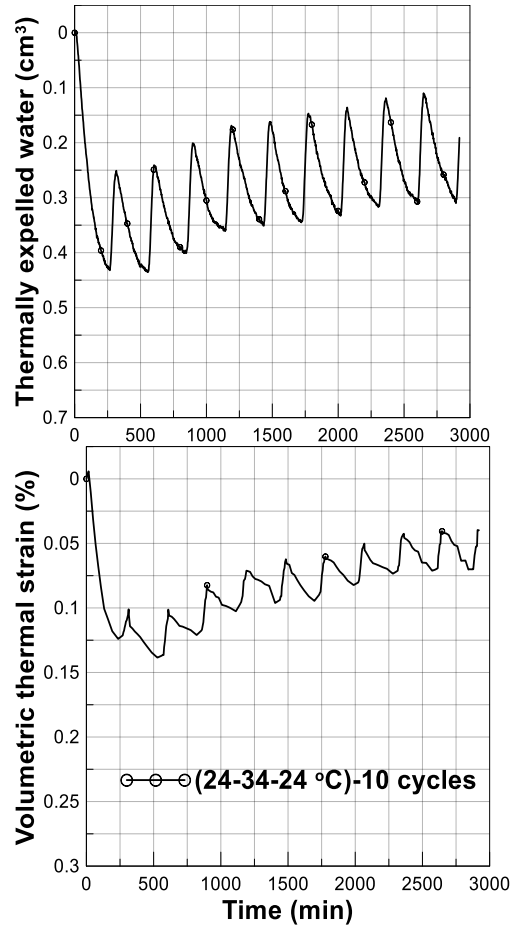
Figure 3-13-Thermal volume behavior of clays with OCR=9 (a) versus time, and (b) versus temperature.

89

Furthermore, as already mentioned above, the thermally induced changes in porosity of OC clays tends to decrease with OCR, as compared to the reference NC clay (at 100 kPa). The volumetric strains corresponding to the NC clays consolidated at 200 kPa and 300 kPa lie above those corresponding to the reference NC clay consolidated at 100 kPa, meaning that the heat-induced changes in porosity decreases with the stress state. This observation may be described on the basis of the initial lower porosity condition achieved by the clay at higher OCR and effective confining pressure, which can reduce the subsequent heat-induced volume changes as opposed to the reference NC clay (at 100 kPa) with relatively higher initial porosity.

In summary, Figures (3-8) -(3-14) indicate that thermally induced volumetric strains seldom exceed 0.25%, which means that in the range of applied temperatures, the effect of temperature on porosity is minor.
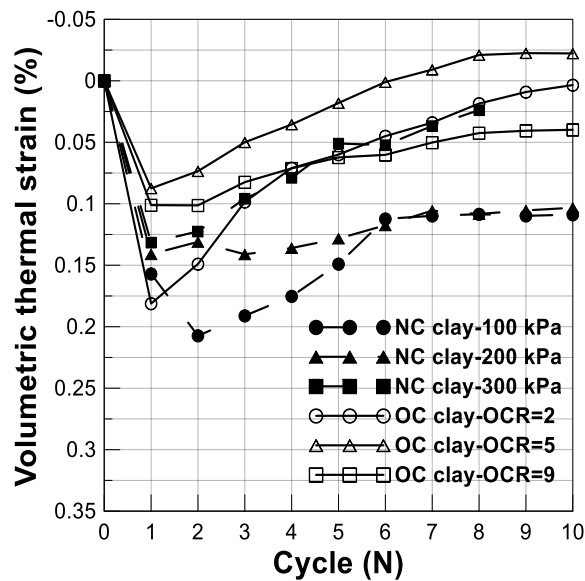
Figure 3-14- Volumetric thermal strain versus heat cycle number (for 10 heat cycles).

Effects of temperature on shear strength
The results of CD triaxial tests with different thermal loading conditions are discussed in this section. Figure 15 presents the triaxial test results for NC clay with an effective confining pressure
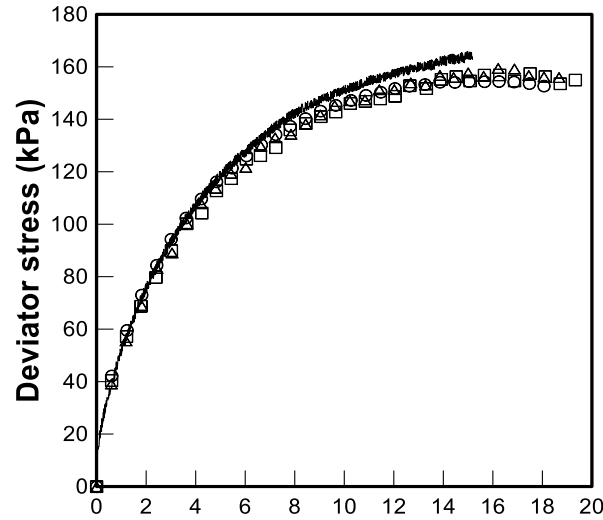
(a)
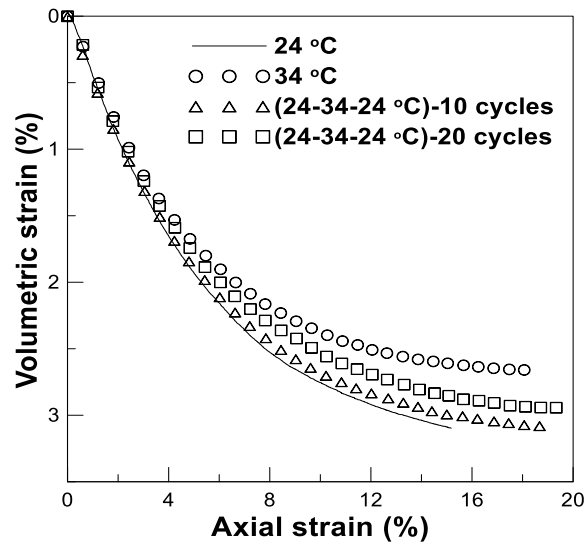
(b)

Figure 3-15-Effects of thermal loading on shearing behavior of NC specimen at 100 kPa.

of 100 kPa. The results indicate that specimen heated before shearing shows slightly lower shear strength as compared with that not heated. Additionally, it can be noted that the heated specimens have higher volume change during shearing phase, although the difference is less than 0.5%. Table 3-1 summarizes the results presented in Figure 3-15. It shows that thermal loading causes a 6% decrease in deviator stress (Tests No. 1-No. 4 in Table 3-1). Furthermore, applying cyclic thermal

loading doesn't make significant difference as compared with non-cyclic one (Tests No. 1-No. 4 in Table 3-1). Abuel Naga et al. (2007b) also observed an almost identical change in shear strength of clay under either elevated or cycling temperature, although they reported a thermal increment in shear strength.

The effect of temperature variations on the shearing response of isotropically consolidated specimens at 200 kPa and 300 kPa are shown in Figures 3-16 and 3-17. Unlike the shearing behavior observed at 100 kPa, heating specimen at higher confining pressures results in larger shear strength. Furthermore, thermal loading leads to lower volume change during shearing. According to Table 3-1, 10 heating/cooling cycles induce a deviator stress increase of 3.6% and 7% for specimens consolidated at 200 kPa and 300 kPa, respectively (Tests No.7 and No.10 in Table 3-1). As for non-cyclic heating, however, shear strength and temperature are almost independent (Tests No.6 and No.9 in Table 3-1).

In general, thermal loading can cause two different shearing trends in NC clays. NC clays isotropically reconsolidated at pressure identical to that applied during reconstitution (100 kPa), show thermal softening, while those reconsolidated at larger pressure (200 kPa and 300 kPa) exhibit thermal hardening. This signifies that the stress state (confining pressure) is an important factor affecting shearing response of NC clays subjected to thermo-mechanical loads. Similarly, the study by Abuel-Naga et al. (2006) [4] indicated that NC clays sheared in drained conditions at elevated temperatures (70°C and 90°C) have exhibited higher shear strength. Cekerevac and Laloui (2004) [12] have also reported that NC clay specimens (consolidated at 600 kPa) exhibited higher shear strength at higher temperatures. Hueckel1 and Baldi (1990) [21] concluded that elevated temperatures can slightly increase NC clay shear strength in CD tests. Trani et al. (2010) [39] observed an increase in both drained and undrained shear strength of NC Boom clay under

drained cyclic/non-cyclic heating. Abuel Naga et al. (2007b) indicated that shear strength of NC clay is improved as it is subjected to either elevated or cyclic temperatures. They observed that both elevated and cyclic temperatures resulted in similar increase in shear strength.
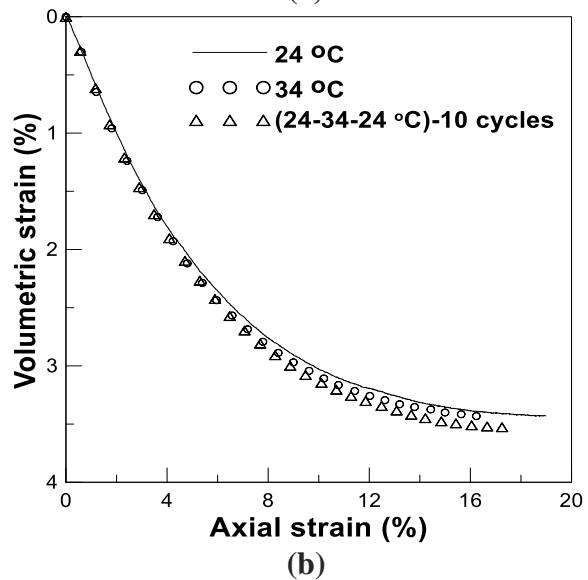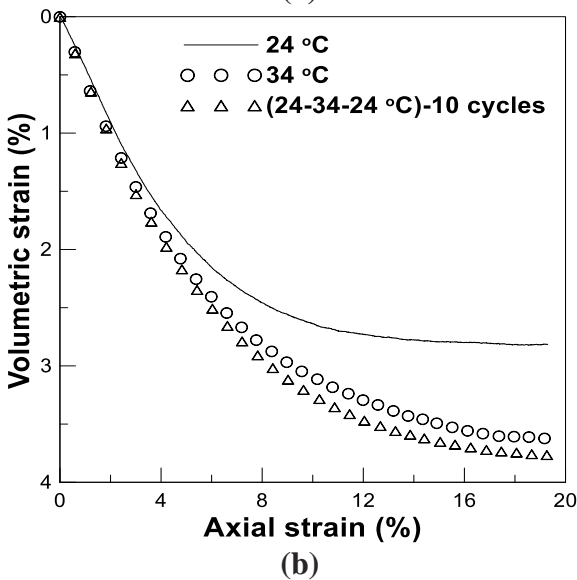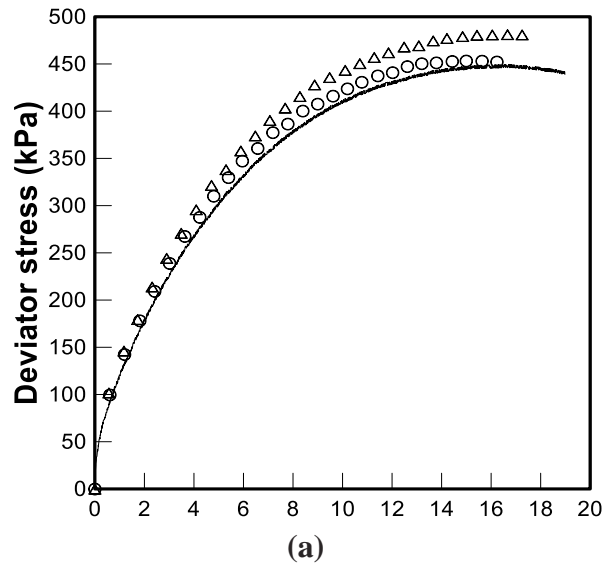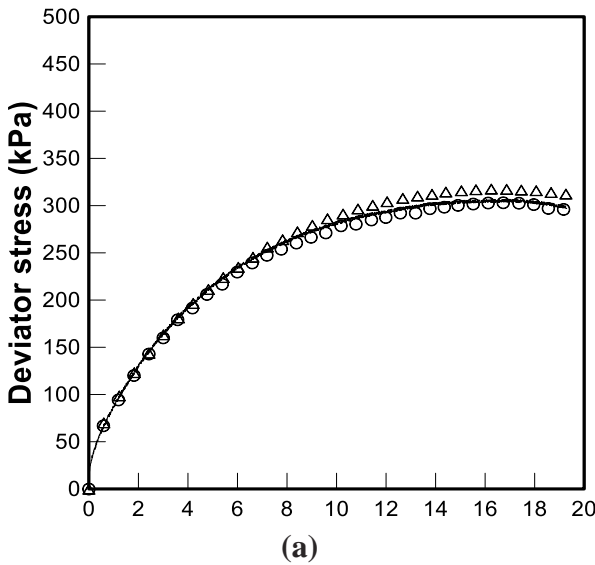
Figure 3-16- Effects of thermal loading on shearing behavior of NC specimen at 200 kPa.

Figure 3-17- Effects of thermal loading on shearing behavior of NC specimen at 300 kPa.

Several studies have investigated the thermal effects on shear strength of clay in undrained conditions (i.e. CU and UU tests). The results of CU tests carried out by Burghignoli et al. (2011)

[10] indicated that drained cyclic and non-cyclic temperature changes caused insignificant increase in NC clay shear strength. Abuel-Naga et al. (2006) [4] showed that both cyclic and non-cyclic heating in drained conditions induced an increase in undrained shear strength. Tanaka et al. (1997) [36] have also observed that clay specimens with higher temperatures exhibited higher undrained shear strength. Houston et al. (1985) [19] found an important increase in undrained shear strength of illitic and smectite-rich ocean sediments due to elevated temperatures (200°C), which was thought to be attributed to significant soil densification during thermal consolidation. Bruyn and Thimus (1996) [9], however, reported a decrease in undrained shear strength of NC clay because of undrained heating.

Figure 3-18 presents triaxial test results for lightly OC clays (OCR=2) subjected to thermal loading. The figure indicates a slight reduction in the peak deviator stress of approximately 4%. Both cyclic and non-cyclic thermal loadings produced nearly equal effects on shear strength (Tests No. 11-No. 13 in Table 3-1). Intermediate overconsolidated clays (OCR=5) and highly overconsolidated clays (OCR=9) exhibited the same trend, but with greater reduction in shear strength of approximately 9% and 14%, respectively, as indicated in Figures 3-19 and 3-20 (Tests No. 14-No. 19 in Table 3-1). It appears that the overconsolidation ratio (OCR) has a profound effect on clay behavior, in terms of shear strength, when subjected to thermal loading (Figures (3-18)-(3-20)). On the other hand, volume change of clay exhibited no clear trend with OCR at different thermal loading. Figure 3-21 illustrates the importance of stress history on shearing strength of clay under different thermo-mechanical loads.

Thermal loading caused a reduction in shear strength, although the degree of reduction is more pronounced at higher OCRs. Similar results were obtained by Hueckel and Baldi (1990) [21] for two clays with higher values of OCR (5 and 9) under drained heating and shearing. It was noted

that the drained shear strength reduced by 18% for clay with OCR=9. Hueckel et al. (1998) [24] also observed a 25% drop in drained shear strength of an intermediate OC clay at 120 °C. However, Cekerevac and Laloui (2004) [12] and Abuel Naga et al. (2007b) found that both cyclic and non-cyclic heating enhanced drained shear strength of OC clays.
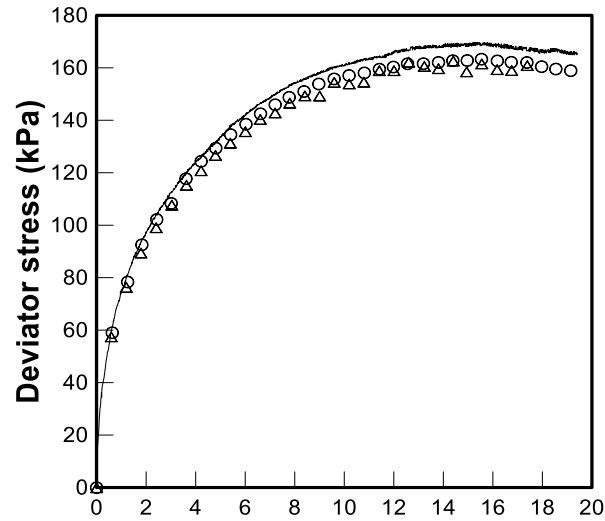
(a)
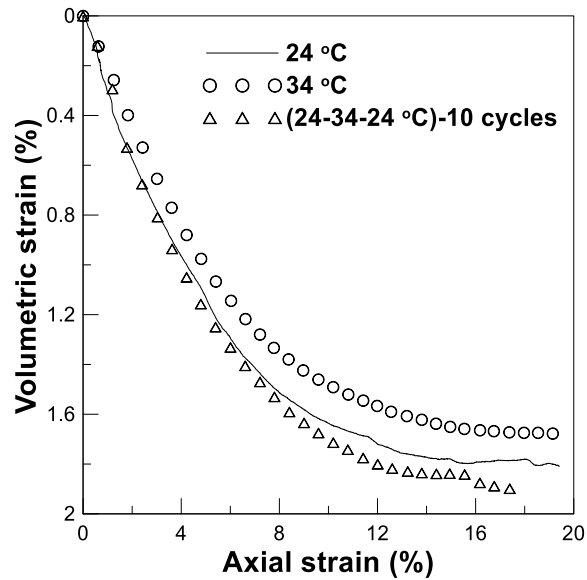
(b)

Figure 3-18- Effects of thermal loading on shearing behavior of lightly OC clay (OCR=2) at 100 kPa.
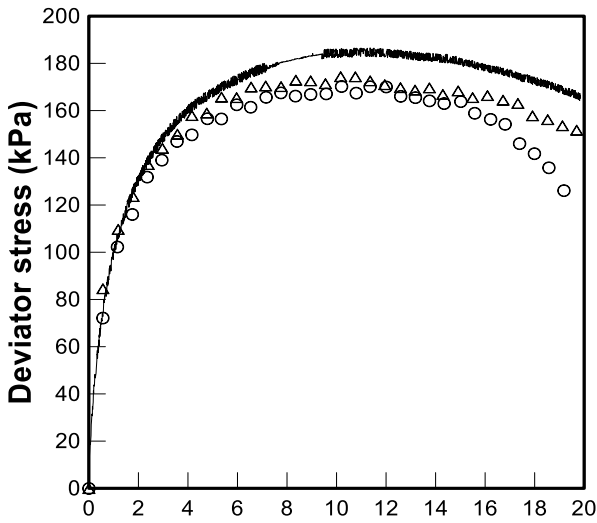
(a)
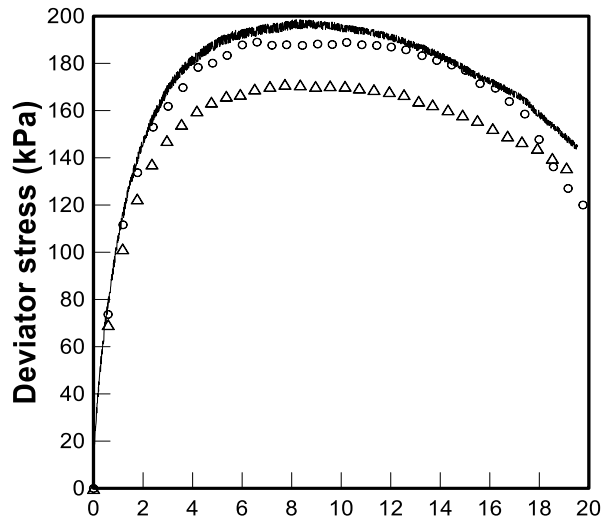
(a)
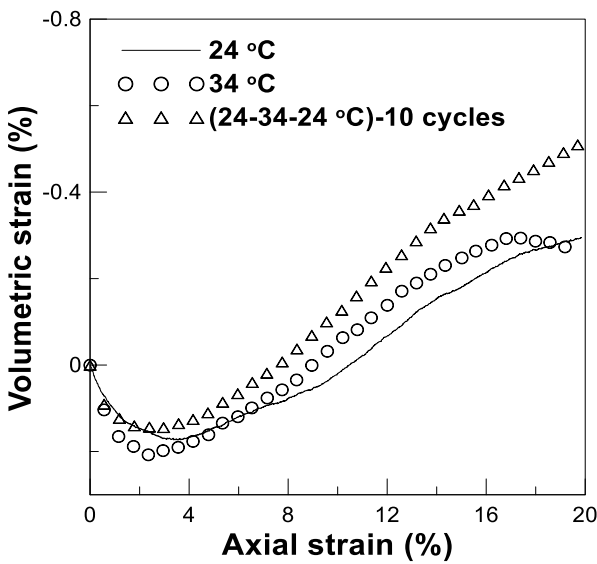
(b)
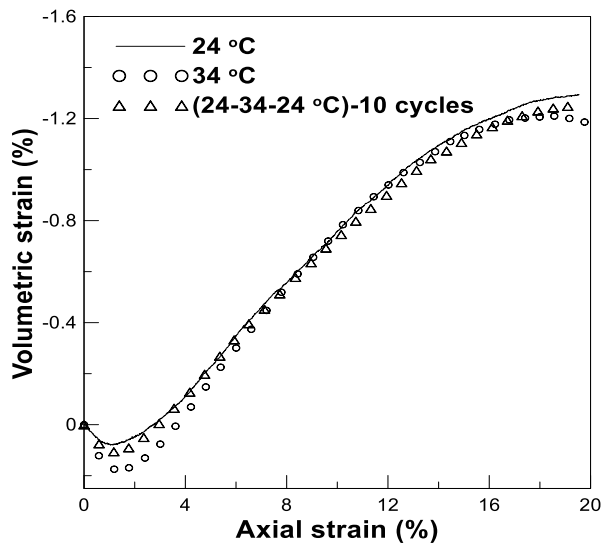
(b)

Figure 3-19- Effects of thermal loading on shearing behavior of intermediate OC clay (OCR=5) at 100 kPa.

Figure 3-20- Effects of thermal loading on shearing behavior of intermediate OC clay (OCR=9) at 100 kPa.

Figure (3-15) -(3-20) clearly illustrate the importance of stress state and history on describing the

effect of temperature variations on shearing strength of clays. Eventually, it can be concluded that

in the range of temperatures investigated, the shear strength of NC clays seems to be insignificantly

influenced by thermal loading, while thermal loading produces a developing decline in shear strength with OCR.
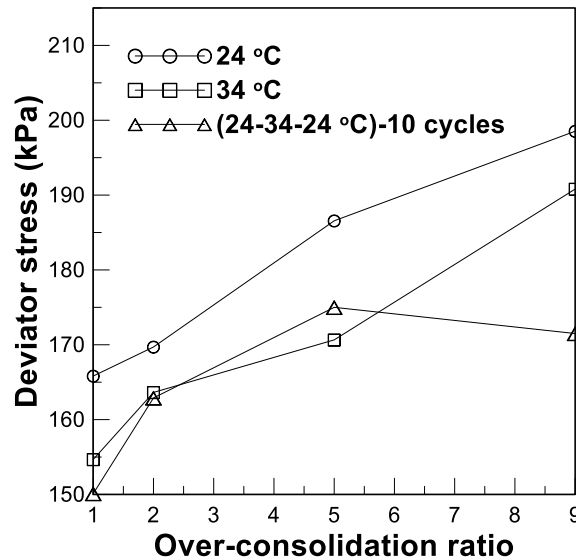
Figure 3-21- Importance of OCR on shear strength of clay subjected to heating.

Effects of temperature on friction angle at critical state
Figure 3-22 presents the effects of thermal loading on NC clay at critical state conditions. The figure shows that the slope of the critical state line, M, changes slightly with thermal loading (M=0.96±0.01). This change is deemed insignificant. This indicates that the critical state friction angle is independent of thermal loading for the range of temperatures used herein. This finding is consistent with the written literature (Cekerevac and Laloui (2004) [12]; Abuel-Naga1 et al. (2006 [4] and 2007b [3]); Trani et al. (2010) [39]; and Burghignoli et al. 2011 [10]).

Effects of temperature on elastic moduli
Figure 3-23 illustrates the effect of thermal loading on the drained elastic modulus of NC clay estimated from the stress–strain curves in Figures (3-15)-(3-17). The secant elastic modulus was determined for an axial strain of 0.5%. Figure 3-23 shows that the effects of thermal loading on

the secant elastic modulus are insignificant at lower confining pressures. While at higher confining

pressures both cyclic and non-cyclic thermal loading induced a significant increase in the secant

elastic module. For example, at a 300-kPa confining pressure, 10 cycles of heating/cooling caused

a 20% increase in the elastic modulus, whereas 8% increase was induced by monotonically

increasing the temperature to 34°C. These observations are consistent with those found in the

literature (Abuel-Naga et al. (2006 [4] and 2007b [3]); Trani et al. (2010) [39]; and Burghignoli et

al. (2011) [10]).
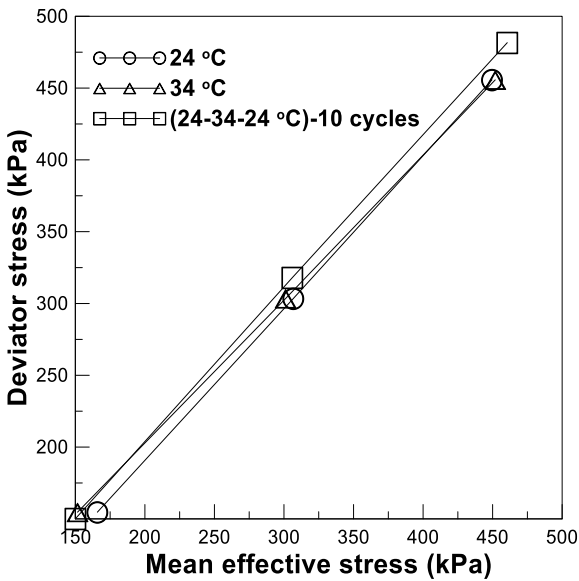
Figure 3-22- Effects of thermal loading on friction angle at critical state.
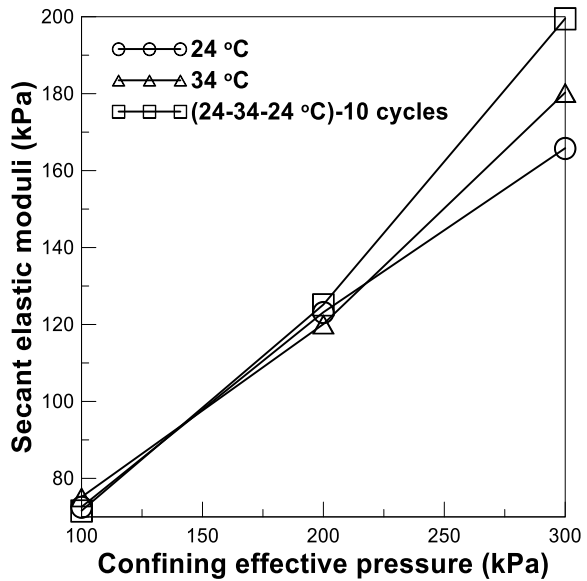
Figure 3-23- Effects of thermal loading on drained secant elastic module.

Effects of temperature on Mohr–Coulomb shear strength parameters
Figure 3-24 illustrates the effects of temperature variations on Mohr-Coulomb shear strength

parameters for NC Clay. Table 3-2 presents the relationship between thermal loading and soil

strength parameters (c' and ϕ') derived from Figure 3-24. The effective cohesion intercept

demonstrates a decrease due to thermal loading. Conversely, cyclic and non-cyclic thermal loading

caused approximately 3.7% and 8% increase in the internal friction angle, respectively. For

temperatures of 4-200° C, Houston et al. 1985 [19] also observed an increase in the friction angle (33° to 50°) with temperature. Bruyn and Thimus (1996) [9], however, reported that heating leads to an increase in clay cohesion, while internal friction angle decreases because of heating.
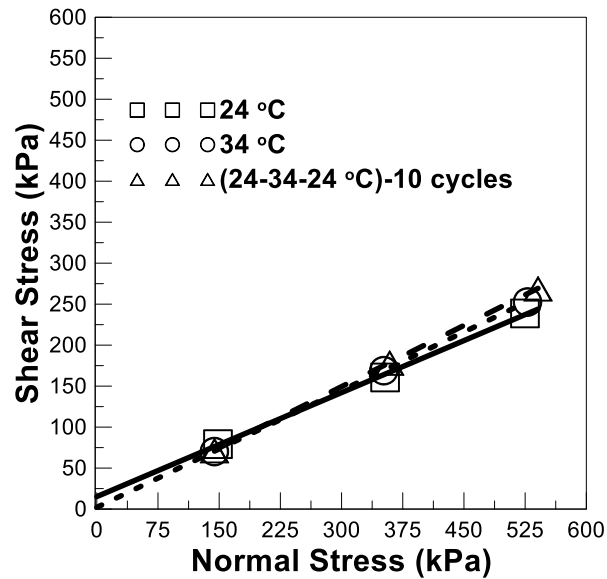
Figure 3-24- Effects of thermal loading on Mohr-Coulomb shear strength parameters (NC clays)

Table 3-2- Thermal loading influence on shear strength parameters of clay

Thermal loading	Cohesion, c'(kPa)	Friction angle, ϕ' (°)
24°C	12.01	24.5
34°C	2.08	25.43
(24°C-34°C)-10 cycles	≈ 0	26.47

3-5- Analysis of Test Results

Assuming α_s and α_w are constant in the range of temperature applied here, the following theoretical explanation, constructed based on Equation (3-4), is presented for thermal volume evolution of a clay specimen in triaxial cell during heating. It is already known that initial porosity for an OC clay is less than that for the corresponding NC clay resulting in lower permeability and initial moisture content. With equal temperature increment, it induces lower amount of $(\Delta V)_{wdr}$

99

and $(\alpha_w V_w \Delta T)$ for the OC clay compared with the corresponding NC clay, while $(\alpha_s V_s \Delta T)$ remains constant for both clays. Actually, different OCR ratios produce different $(\Delta V)_{wdr}$ and $(\alpha_w V_w \Delta T)$, while $(\alpha_s V_s \Delta T)$ doesn't change. Thus it may be suggested to represent Equation (3-4) using OCR-dependent coefficient, $(\Delta V)_{wdr} - (\alpha_w V_w \Delta T)$, and OCR-independent coefficient, $(\alpha_s V_s \Delta T)$: $(\Delta V)_{\Delta T} = ((\Delta V)_{wdr} - \alpha_w V_w \Delta T) - (\alpha_s V_s \Delta T)$. Regarding NC clays exhibiting thermally contractive behavior, the OCR-dependent coefficient is always greater than the other one during a temperature increment. For OC clays, however, it is difficult to determine a unique relationship between these two coefficients because of uncertainty in variation of the OCR-dependent one, as both $(\Delta V)_{wdr}$ and $(\alpha_w V_w \Delta T)$ tends to decrease with OCR. Despite that, at low OCR (similar to NC clays), the OCR-dependent coefficient seems to be greater than the other coefficient resulting in a contractive behavior during heating. At intermediate and high OCR's, however, the OCR-dependent coefficient is initially smaller with respect to other coefficient and tends to decrease with temperature prior to reach "transition temperature", resulting in a dilative response. After reaching the "transition temperature", it gradually grows with temperature leading to a transition from thermal dilation to a thermal contraction.

Alternatively, the volumetric response of clays to heating can be explained based on the mechanical secondary consolidation behavior following the most recent loading or unloading increment prior to heating (Coccia and McCartney 2016(a) [13] & (b) [14]; Towhata et al. 1993 [38]; Burghignoli et al. 2011 [10]). According to this alternative explanation, intermediate and heavily OC clays showing a mechanical secondary compression with negative rate will exhibit thermally dilative response to heating. While it is expected to observe a thermally contractive behavior for NC clays as they undergo a mechanical secondary compression with positive rate.

The thermally induced variations in the shear strength can be explained in terms of the changes in porosity (specimen volume change) and the effective stress during thermal loading. For instance, the absolute volumetric strain in NC clays due to the elevated and cyclic heating (Figures (3-8)-(3-10)) is less than 0.25%. This small volume changes may not importantly contribute to the total developed changes in the shear strength (up to 7%) shown in Figures (3-15)-(3-17). Therefore, the thermally induced variation in strength (increment at high pressure and decrease at low pressure) are possibly described with respect to the thermal changes in effective stress, which is believed to be associated with the thermal rearrangement of clay particles (fabric), as experimentally observed by Jaradat et al. (2017). In fact, the thermally induced change in microstructure possibly increases the inter-particle contact forces (effective stresses) in the clay specimens consolidated at high pressure causing an increase in the shear strength. While, it possibly decreases the inter-particle contact forces in the clay specimens consolidated at lower pressure resulting in thermal softening. Using a Microscopic study, Push and Guven (1990) [32] showed that heating generates a permanent microstructure rearrangement in Na-bentonite (in the form of denser grouping of stacks of the montmorillonite flakes) that mechanically strengthens the soil skeleton.

Similar analysis was performed by Trani et al. (2010) [39] to assess the contribution of the thermal consolidation and the thermal rearrangement of clay particles to the thermally induced strengthening of NC clay (PI=60%). They experimentally found that only 60% of the total induced strength increase is associated with the thermal consolidation and suggested that the remaining 40% increase is induced by the soil fabric change due to elevated temperature (90°C).

The above description can be reinterpreted on the basis of changes in the inter-particle forces, σ_{R-A}, through Equations (3-5) -(3-11). Any change in physical arrangement of clay particles will influence physico-chemical interaction σ_{R-A} through changing $\xi_\delta d\delta$, as mathematically shown in

Equation 3-11. In view of Lambe-Bolt's model, the possible thermal changes in σ_{R-A} (Equation 3-11) are not taken into account in estimating the effective stress, through Equation 3-9. As a result, the Lambe-Bolt's model seems inadequate in explaining the thermo-mechanical behavior of clays sheared in triaxial cell. This is probably because of the parallel arrangement of clay particles assumed in the model. Such arrangement may not be possible under isotropic pressure application in a triaxial testing environment. A flocculated arrangement is more likely to be generated under isotropic pressure. Thus, Sridharan and Rao's model is more appropriate to provide a theoretical description of this phenomenon. According to this model, the following theoretical interpretation can be presented for the shearing behavior of NC clays under thermal loading: The applied thermal loading restructures soil fabric (particle rearrangement) causing a decline in physico-chemical interaction, through Equation 3-11. Subsequently, the effective stress will increase, according to Equation 3-7, leading to an increment in the shearing strength of the clay particles.

Similar to NC clays, the small thermal volume changes in OC clays ($0 \% \leq |\varepsilon_{v-th}| \leq 0.25 \%$), couldn't be the primary reason for 3.6-14% reduction in the shear strength, Figure (3-18)-(3-20). Probably, the thermal rearrangement of the clay particles is the main factor determining the shearing response of OC clays under thermal loading. In view of Sridharan and Rao's model, in contrast to NC clays, the thermal rearrangement of OC clay particles generates an increment in physico-chemical forces (Equation 3-7) giving decay to the effective stresses and the shearing strength, through Equations 3-7 and 3-11.

Although the above interpretation allows us to qualitatively understand the observed clay shearing response to temperature, it has been derived from a theoretical basis which might be limited to

describe a real clay behavior. In this regard, a detailed microscopic study may be required to study the effect of temperature on the physico-chemical forces and the clay particles rearrangement.

3-6- Conclusion

This section investigated the influence of thermal loading on shearing strength of kaolin clay by performing a series of consolidated drained triaxial tests. An attempt has been made to explain the results in terms of thermally induced variations in initial porosity and effective stress. The main conclusions drawn can be described as follows:

1. An overall volume decrease was observed for both NC and OC clays during heating phase. However, the intermediate and heavily OC clays exhibited an initial expansion followed by contraction through the remainder of the thermal loading step. During cooling phase, both NC and OC clays showed dilative response.

2. Thermal volumetric strain is found insignificant in the range of temperature applied.

3. The shearing strength dependency on temperature is controlled by the stress state and history as well as the temperature history.

4. With respect to NC condition, clays reconsolidated at the pressure identical to that used during reconstitution, showed thermal softening due to both cyclic and non-cyclic thermal loading. Whereas, specimens subjected to thermal loading at higher confining effective stress experienced hardening. In this case, the induced increase in shear strength due to cyclic thermal loading is slightly greater.

5. All OC clays exhibited a reduction in strength due to heating. The strength reduction became more important as OCR increased.

6. In the range of temperatures investigated, the thermally induced volume changes were insignificant and therefore could not account for the change in shear strength. However, the temperature-induced changes in physico-chemical forces that may alter effective stresses, could be responsible for shear strength changes.

7. The friction angle at critical state was found to be nearly independent of thermal loading.

8. The Mohr-coulomb shear strength parameters were found to be slightly affected by temperature variation. The effective cohesion intercept decreased due to heat application, while the internal friction angle increased.

9. The dependence of secant elastic module on temperature was found to be mainly controlled by the magnitude of confining effective pressure. At low pressures, the secant elastic modulus was nearly independent of thermal loading, while significant increase was observed at higher confining pressures.

References:

[1] Abdelaziz, S., and Ozudogru T.Y. (2016). Non-uniform thermal strains and stresses in energy piles. *Environmental Geotechnics*, 3 (4), 237-252.

[2] Abuel-Naga, H. M., Bergado, D. T., and Bouazza, A. (2007). Thermally induced volume change and excess pore water pressure of soft Bangkok clay. *Engineering Geology*, 89, 144-154.

[3] Abuel-Naga, H. M., Bergado, D. T., and Lim, B. F. (2007b). Effect of temperature on shear strength and yielding behavior of soft Bangkok clay. *Soils Found.*, 47 (3), 423–436.

[4] Abuel-Naga, H. M., Bergado, D. T., Ramana, G. V., Grino, L., Rujivipat, P., and Thet, Y. (2006). Experimental evaluation of engineering behavior of soft Bangkok clay under elevated temperature. *Journal of Geotechnical and Geo-environmental Engineering-ASCE*, 132 (7), 902-910.

[5] Baldi, G., Hueckel, T., and Pellegrini, R. (1988). Thermal volume changes of the mineral–water system in low-porosity clay soils. *Canadian Geotechnical Journal*, 25, 807–825.

[6] Bing, Bai., Lanjie, G., and Song, H. (2014). Pore pressure and consolidation of saturated silty clay induced by progressively heating/cooling. *Mechanics of Materials*, 75, 84-94.

[7] Bourne-Webb, P.J., Amatya, B., Soga, K., Amis, T., Davidson, C., and Payne, P. (2009). Energy Pile Test at Lambeth College, London: Geotechnical and Thermodynamic Aspects of Pile Response to Heat Cycles. *Géotechnique*, 59 (3), 237–248.

[8] Brandl, H. (2000). Energy foundations and other thermo-active ground structures. *Geotechnique*, 56 (2), 81-122.

[9] Bruyn, D. D., and Thimus, J. F. (1996). The influence of temperature on mechanical characteristics of Boom clay: The results of an initial laboratory program. *Engineering Geology*, 41, 117-126.

[10] Burghignoli, A., Desideri, A., and Miliziano, S. (2011). A laboratory study on the thermo-mechanical behavior of clayey soils. *Canadian Geotechnical Journal*, 37, 764-780.

[11] Campanella, R.G., and Mitchell, J.K. (1968). Influence of temperature variations on soil behavior. *Journal of Geotechnical Engineering-Division-ASCE*, 94 (3), 709–734.

[12] Cekerevac, C., and Laloui, L. (2004). Experimental study of thermal effects on the mechanical behavior of clay. *International Journal for Numerical and Analytical Methods in Geomechanics*, 28, 209-228.

[13] Coccia, C.J.R., and McCartney, J.S. (2016a). Thermal volume change of poorly draining soils I: Critical assessment of volume change mechanisms. *Computers and Geotechnics*, 80, 26–40.

[14] Coccia, C.J.R., and McCartney, J.S. (2016b). Thermal volume change of poorly draining soils II: Model development and experimental validation. *Computers and Geotechnics*, 80 (2), 16-25.

[15] Darbari, z., Jaradat, K., and Abdelaziz, S. (2017). Heating–freezing effects on the pore size distribution of a kaolinite. *Environmental Earth Sciences*, 76 (20), 713-720.

[16] Demars, K.R., and Charles, R.D. (1982). Soil volume changes induced by temperature cycling. *Canadian Geotechnical Journal*, 19, 188–194.

[17] Delage, P., Sultan, N., and Cui, Y.J. (2000). On the thermal consolidation of Boom clay. *Canadian Geotechnical Journal*, 37, 343-354.

[18] Donna, A. D., and Laloui, L. (2015). Response of soil subjected to thermal cyclic loading: Experimental and constitutive study. *Engineering Geology*, 190, 65-76.

[19] Houston, S.L., Houston, W.N., and Williams, N.D. (1985). Thermomechanical behaviour of sea floor sediments., *Journal of Geotechnical* Engineering, ASCE, 111, 1249–1263.

[20] Hueckel, T. (1992b) On effective stress concept and deformation in clays subjected to environmental loads: discussion. *Canadian Geotechnical Journal*, 29, 1120-1125.

[21] Hueckel, T., and Baldi, G. (1990). Thermo-plasticity of saturated clays: experimental constitutive study. *Journal of Geotechnical Engineering-ASCE*, 116 (3), 197-212.

[22] Hueckel, T., Francios, B., and Laloui, L. (2009). Explaining thermal failure in saturated clays. *Ge´otechnique*, 59 (3), 197-212.

[23] Hueckel, T., and Pellegrini, R. (1989). Modeling of thermal failure of saturated clays. *Numerical models in geomechanics*, *NUMOG III*, 81–90.

[24] Hueckel, T., Pellegrini, R., and Del-Olomo, C. (1998). A constitutive study of thermo-elastoplasticity of deep carbonate clays. *Int. J. Numer. Anal. Meth. Geomech.*, 22, 549-574.

[25] Khalili, N., Uchaipichat, A., and Javadi, A.A. (2010). Skeletal thermal expansion coefficient and thermo-hydro-mechanical constitutive relations for saturated homogeneous porous media. *Mechanics of Material*, 42, 593–598.

[26] Laloui, L., and Cekerevac, C. (2003). Thermoplasticity of clays: anisotropic yield mechanism. *Computer and Geotechnics*, 30 (8), 649–660.

[27] Laloui, L., Olgun, C. G., Sutman, M., McCartney, J. S., Coccia, C. J., Abuel-Naga, H. M., and Bowers, G. A. (2014). Issues involved with thermoactive geotechnical systems: characterization of thermomechanical soil behavior and soil-structure interface behavior. *The Journal of the Deep Foundations Institute*, 8 (2), 108-120.

[28] Lambe, T.W. (1960). A mechanistic picture of strength in a clay. presented at Proceeding of ASCE Conference on Shear Strength of Cohesive Soils, Boulder, Colorado, 503-532.

[29] McCartney J.S., and Murphy, K.D. (2017). Investigation of potential dragdown/uplift effects on energy piles. *Geomechanics for Energy and the Environment*, 10, 21–28.

[30] Mimouni, T., and Laloui, L. (2015). Behavior of a group of energy. *Canadian Geotechnical Journal*, 52, 1913–1929.

[31] Noble, C.A. and Demirel, T. (1969). Effects of temperature on strength behavior of cohesive soil. presented at Int. Conf. effects of Temperature and Heating on Engineering Behavior of Soils, Highway Res. Board Publ., Washington, D.C., 103, 204-210.

[32] Push, R., and Guven, N. (1990). Electron microscopic examination of hydrothermally treated Bentonite clay. *Engineering Geology*, 28, 303-314.

[33] Salgado, R. (2007). The Engineering of Foundations, McGraw Hill Education.

[34] Sultan, N., Delage, P., and Cui, Y.J. (2002). Temperature effects on the volume change behavior of Boom clay. *Engineering Geology*, 64, 135–145.

[35] Stewart, M. A., and McCartney, J. S. (2014). Centrifuge modeling of soil-structure interaction in energy foundations. *ASCE Journal of Geotechnical and Geoenvironmental Engineering*, 140 (4), 1-11.

[36] Tanaka, N., Graham, J., and Crilly, T. (1997). Stress–strain behavior of reconstituted illitic clay at different temperatures. *Engineering Geology*, 47 (4), 339–350.

[37] Terzaghi, K. (1936). The shearing resistance of saturated soils and the angle between the planes of shear, presented at preceding of the 1st International Conference on Soil Mechanics, Harvard University, 1, 45-56.

[38] Towhata, I., Kuntiwattanaul, P., Seko, I., and Ohishi, K. (1993). Volume change of clays induced by heating as observed in consolidation tests, *Soils and Foundations*, 33, 170–183.

[39] Trani, L. D. O., Bergado, D. T., and Abuel-Naga, H. M. (2013). Thermo-mechanical behavior of normally consolidated soft Bangkok clay. *International Journal of Geotechnical Engineering*, 4, 31-44.

[40] Vega, A., and McCartney, J.S. (2015). Cyclic heating effects on thermal volume change of silt. *Environmental Geotechnics*, 2 (5), 257-268.

[41] Virdi, S.P.S., and Keedwell, M.J. (1988). Some observed effect of temperature variation on soil behavior. presented at International Conference on Rheology and Soil Mechanics, Coventry, 336–35.

[42] Yilmaz, G. (2011). The effects of temperature on the characteristics of kaolinite and bentonite. *Scientific Research and Essays*, 6 (9), 1928–1939.

[43] Yilmaz, I. (2009). Swell potential and shear strength estimation of clays. *Applied Clay Science*, 46, 376–384.

[44] Yazdani, S., Helwany, S., and Olgun, O. (2018a). Experimental evaluation of shear strength of Kaolin Clay under Cyclic and Non-Cyclic Thermal Loading. *Geotechnical Testing Journal*, https://doi.org/10.1520/GTJ20180020.

Chapter 4

Effect of Temperature on the Shear Strength of Pile-Clay Interface Under Constant Normal Load (CNL)-Direct Shear Test

4-1- Introduction

As mentioned in the second chapter, cyclic temperature variations in the pile and the surrounding soil is expected to occur due to energy pile operation that may affect the response of pile-soil interface. In fact, cyclic temperature variations generate repeated relative motions between the pile and the soil that may cause degradation of the frictional resistance at pile-soil interface (De Jong et al. 2003 and 2006). Furthermore, temperature variations can directly change the mechanical properties of the soil at interface. These two thermal influences create a complex interface behavior under thermo-mechanical loading that should be well understood to properly design an energy pile.

Due to its wide availability and relatively simple test setup the direct shear is used extensively to study the mechanical behavior of pile-soil interface. For energy pile application, however, a modified temperature-controlled direct shear test is required to examine the thermo-mechanical behavior of interface. The response of pile-soil interface has been investigated by some authors at both low and high temperatures using the modified temperature-controlled direct shear test (Cui et al. (2013) [1], Kawaguchi et al. (2013) [2], Jiankun et al.(2014) [3], Lv et al. (2013) [4], Xiao et al.(2014) [5], Di Donna et al. (2016) [6], and Yavari et al., 2016 [7]). In the following the results of studies concerning the interface behavior under thermo-mechanical conditions represented by an energy pile are briefly presented.

Xiao et al. (2014) [5] evaluated the effect of temperature on mechanical properties of compacted silty soil-concrete interface. They reported a 15% increase in shear strength of interface at 38 °C as compared with that at 4 °C. This thermal-strengthening behavior for soil-pile interface was also observed under cyclic temperature variations (26-38-26 °C). Di Donna et al. (2016) [6] presented

the experimental results on the response of both sand/clay-concrete interfaces at three different elevated temperatures (20 °C, 50 °C and 60 °C) using a modified direct shear apparatus. The study was carried out under different variables such as roughness, normal stiffness, constant normal load (CNL) and constant normal stiffness (CNS) conditions and cyclic and non-cyclic shearing. They observed insignificant changes in the response of sand-concrete interface with temperature variations under both CNL and CNS conditions, while an improvement in the shearing resistance of clay-concrete interface under the same conditions. It was concluded that shearing at higher temperatures resulted in higher interface adhesion and lower interface friction. In another recent study, shearing behavior of sand, clay and clay-concrete interface at three temperatures (5 °C, 20 °C, and 40 °C) was investigated using a similar direct shear apparatus under CNL condition (Yavari et al., 2016 [7]). The study concluded that the shearing response of the soil and the soil-concrete interface was nearly independent of elevated temperature.

The objective of this section is to experimentally investigate the clay-concrete interface response under various thermo-mechanical loadings, applicable to energy piles. The tests were carried out under CNL condition using a temperature-controlled direct shear apparatus modified to better reflect the cyclic movements at soil-pile interface. To better understand the influence of temperature variations on interface behavior, the results of the current study are presented together with those obtained in the third chapter. It should be noted that the test plan was designated for an energy pile operating in summer mode, where soil behaves as a heat sink. The annual average temperature was assumed to be 24 °C, which is common in tropical climate, and the induced temperature variations due to energy pile operation to be +10 °C. In the following sections, the test apparatus and results will be discussed in more details.

4-2- Soil-concrete interface behavior

There is a general agreement that the soil-solid interface is the narrow area formed at the contact between solid and soil where an intense localization of shear strains occurs. The effects of temperature on shearing behavior of soil-solid interface can essentially be examined by understanding of the basic mechanisms and influential factors controlling the shear strength of interface. Among the factors affecting interface behavior, surface roughness and the average grain size of soil are the most significant factors to influence interface failure mechanism (Potyondy (1961) [9], Acar et al. (1982) [10], Goh and Donald (1984) [11], Uesugi and Kishida (1986a) [12], Uesugi and Kishida (1986) [13], Kishida and Uesugi (1987) [14], Uesugi et al. (1988) [15], Uesugi et al. (1989), Uesugi et al. (1990),Tsubakihara and Kishida (1993) [18], Subba and Robinson (1996) [19], Porcino et al. (2003) [20], Lemos and Vaughan (2000) [21], Lings and Dietz (2005) [22], Hammoud and Boumekik (2006) [23], and Zhang and Zhang (2006) [24]).

Surface roughness is characterized by the surface's normal roughness, Rn (Uesugi and Kishida (1986a and b), Kishida and Uesugi (1987) [14], Uesugi et al. (1988, 1998, and 1990) [15-17], and Tsubakihara and Kishida (1993) [18]).The normal roughness, described by Equation 4-1, integrates the effect of surface roughness and soil particle size simultaneously:

$$R_n = \frac{R_{max}}{D_{50}} \qquad\qquad (4-1)$$

where, R_{max} is the vertical distance between highest peak and trough points over a length of L = D_{50}, and D_{50} is the mean particle size obtained from grain size distribution curve. With respect to normal roughness, the interface failure mechanism can be classified into three zones: smooth, intermediate and rough. In a smooth zone, interface failure is related to sliding soil particles at the solid surface. The lowest shearing resistance has been reported for this zone where changes in

interface shearing strength are negligible with reducing normalized roughness. With increasing R_n, the shearing behavior falls into the intermediate zone, in which interface failure is linked to mixed behavior of sliding at contact surface and shear deformation within the soil body. Unlike the smooth zone, a gradual increase in interface strength with roughness has been observed in the intermediate zone. At a critical normal roughness, the interface strength reaches its maximum value, which is usually upper-bounded by the strength of soil itself. For a normal roughness above the critical value, failure mechanism occurs only in the rough zone, where a shear band within the soil forms instead of sliding at the interface. For a critical normal roughness larger than a threshold value in the range of 0.06–0.3, it has been reported that the failure mechanism of soil-solid interface can occur in rough zone (Uesugi and Kishida (1986a and b) [12 & 13], Kishida and Uesugi (1987) [14], Uesugi et al. (1988, 1989, and 1990) [15-17], and Tsubakihara and Kishida (1993) [18]).

The interface roughness criterion described above is based on the results derived from shearing interfaces between various sands and solid materials. So far, however, no attempt has been made to propose a suitable criterion to present borders to different roughness at clay-solid interfaces. Clays and sands differ in many aspects, such as particles size and shape, quantity of surface forces acting between particles, and drainage rate. However, the shearing behavior presented by these materials in the vicinity of a solid surface is largely dependent on their particle shapes (Lemos and Vaughan, (2000) [21]; and Lupini et al., (1981) [25]). In fact, clay particles are normally "platy", while sand particles tend to be "spherical" or "angular". This, in turn, influences particle motion along the soil-solid interface and creates two different failure mechanisms at the interface. Interface shearing in sands is associated with particles rolling or translating within the shear zone; this is known as turbulent shearing, while interface shearing in clays involves particle orientation

within the shear zone because of the platy shape, which is known as sliding shearing (Lemos and Vaughan, (2000) [21]; and Lupini et al., (1981) [25]). Thus, values of critical roughness of the sand-solid interface available in the literature may not be applicable to clay-solid interface. Further research on clay-solid interface behavior is required.

4-3- Description of the modified direct shear test apparatus

The lower half of conventional direct shear box (100 mm ×100 mm × 40 mm) was used to house a concrete plate, whereas the upper half was used to house a clay specimen as shown in Figure 4-1. The left end of the concrete plate is affixed to the wall of the direct shear test apparatus. A lubrication layer is applied at the interface between the bottom of the concrete plate and the shear box to reduce friction and to facilitate the concrete plate lateral expansion and contraction relative to the shear box when heat cycles are applied. The unique design of the modified direct shear test apparatus allows the concrete specimen to approximately freely expand/contract along the interface (in both longitudinal and transversal directions) when it is subjected to cycles of heating/cooling thus simulating the interface behavior of an energy pile subjected to similar thermal loading conditions. This characteristic of the test setup makes it more suitable for investigating interface behavior of energy pile comparing with the one that induces interface shearing cycles by applying cyclical lateral loads on the upper half of the shear apparatus. However, the test setup may not perfectly reproduce mechanical conditions in the field since the pile-soil interface presents a CNS condition rather than CNL condition (Lehane et al. 1993 [8]).

The concrete plate was 150 mm long, 150 mm wide, and 25 mm thick. The concrete mixture ratio for fine sand, cement and water was 1:1:0.3. As a part of the heating/cooling system,

114

a 6.4 mm-diameter copper tube was installed inside the concrete plate (Figure 4-1(b)).

Heating/cooling fluid was circulated through the tube, via a heat pump, to control the interface

temperature. The clay-concrete contact area was 100 mm by 100 mm.
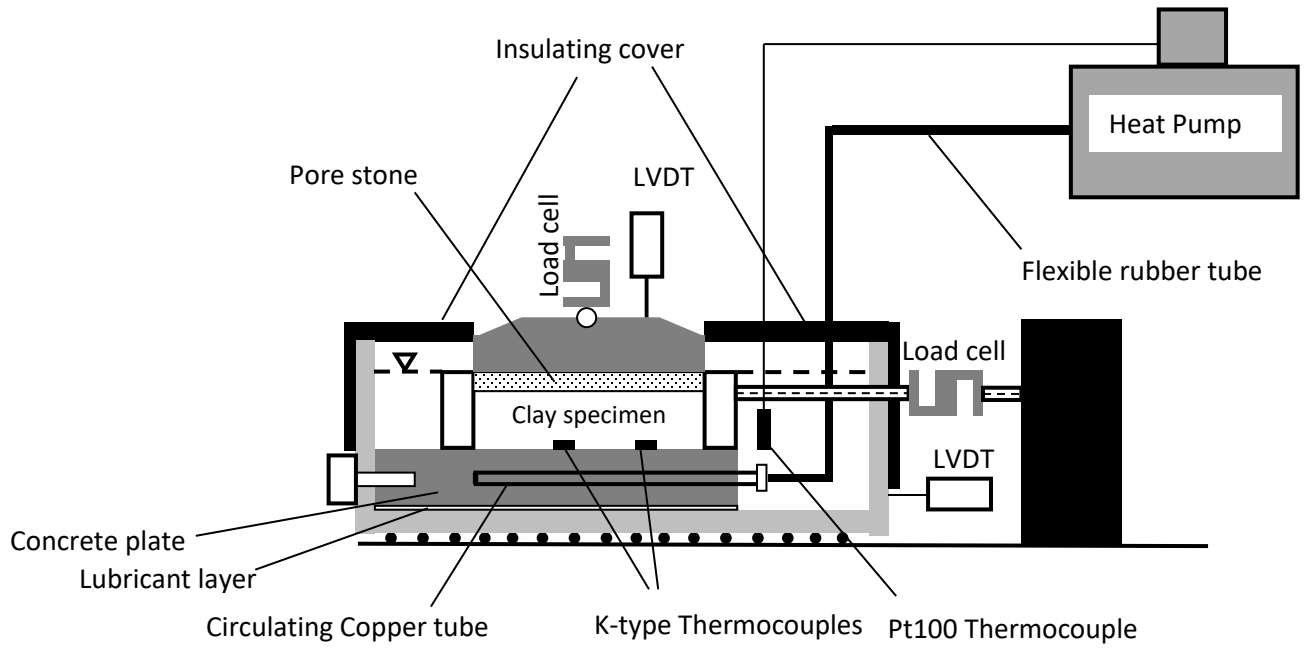
(a)
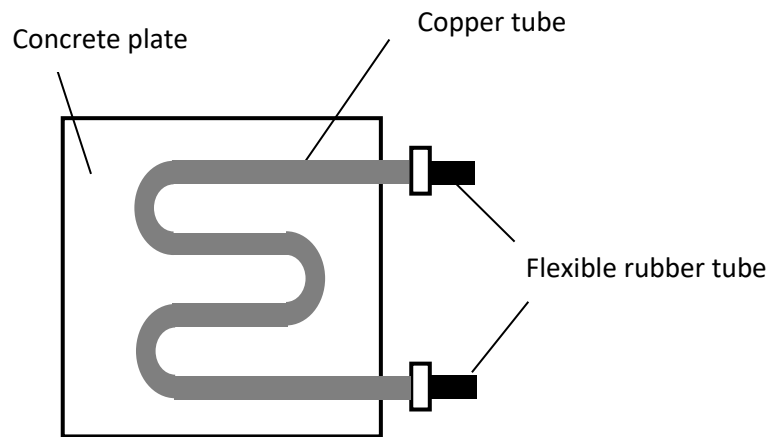
(b)

Figure 4-1-(a) Schematic view of modified direct shear apparatus (b) Layout of the heating/cooling tubing in the concrete plate.

Figure 4-2 shows a magnified image of concrete surface profile taken from laser photography. As shown in the figure, asperities have not been distributed uniformly along the surface, which makes it impossible to determine a representative R_{max}. As a result, normal roughness estimated using Equation (4-1) varies between 0.88 and 5.38, which is clearly beyond the range reported for critical roughness of sand-solid interface in the literature (0.06-0.3). This finding does not necessarily imply that the interface failure mechanism falls into the "rough zone", since clay and sand exhibit different shearing behavior at interfaces discussed previously. However, an attempt will be made in the following sections to assess whether interface shearing takes place in the clay body or at the concrete surface.

The clay specimen was a reconstituted kaolin HC-77 (CL) that is commercially available as powder, the same as that used in CD triaxial tests. Figure 4-3 shows the grain-size distribution of the kaolin used in this study.
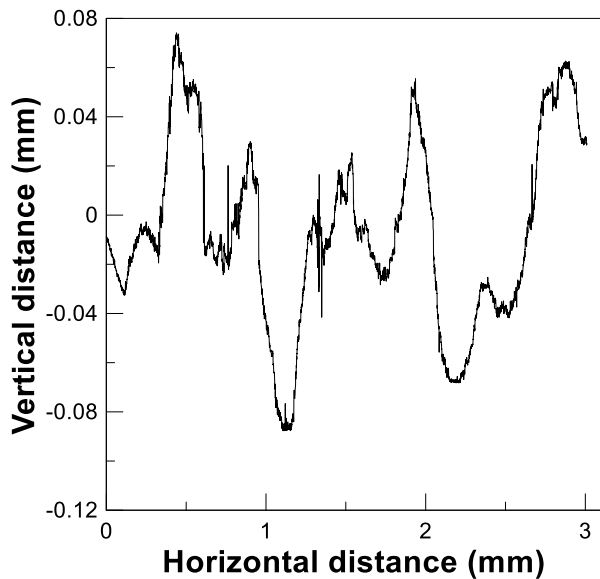
Figure 4-2- Typical profile of concrete interface (laser photography).
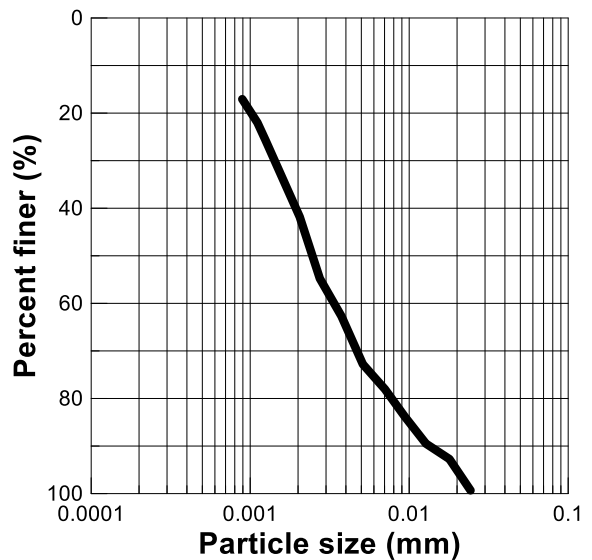
Figure 4-3- Particle size distribution of Kaolin HC-77.

Physical properties of clay are shown in Table 4-1. The clay specimen was prepared by mixing the kaolin powder with a water content of two times the liquid limit. The slurry was then normally consolidated in the direct shear box through several steps of loading up to 100 kPa. After consolidation, the clay specimen was carefully removed, trimmed off and placed on top of the concrete plate. The size of the clay specimen after consolidation was approximately 100 mm×100 mm×20 mm.

Table 4-1- Physical properties of kaolin clay

Parameter	Value
D_{50}	0.0026 mm
Plastic Limit (PL)	25 %
Liquid Limit (LL)	45 %
Plastic Index (PI)	20 %
Poisson's Ratio (v)	0.25
G_s	2.62

The heating/cooling system consisted of the heat pump described in the third chapter, thermocouples, and a data acquisition system. The interface thermal loading was applied by circulating heating/cooling fluid through the copper tube embedded in the concrete plate. The temperature at the interface surface was measured using two miniature size thermocouples placed on the concrete plate top surface. The total area occupied by these two thermocouples at contact area were about 0.4 cm2, which is clearly insignificant as compared with that of interface, 100 cm2. The water temperature in the basin, measured using the third thermocouple, was used to automatically control the heat pump. Several calibration tests were conducted prior to the actual tests to find a correlation between temperature of water and the interface. Figure 4-4 provides the results of a "calibration" test that illustrates the relationship among the reference temperature provided by the heat pump (heating/cooling fluid temperature), the interface temperature, and the temperature of the water in the basin, during the application of one heat cycle.

117
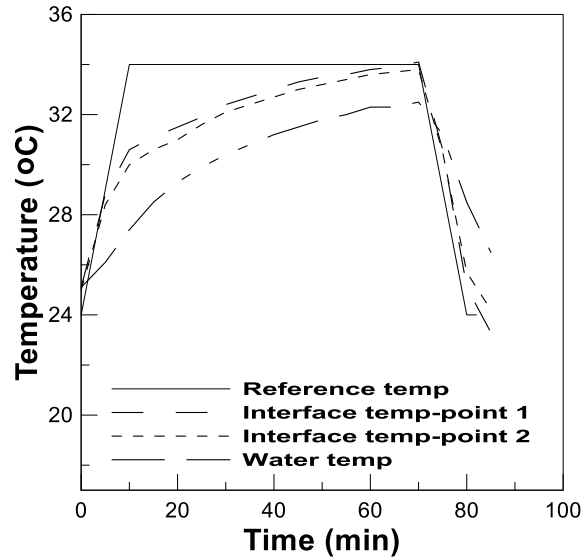
Figure 4-4- Results of thermal calibration test.

To minimize any potential impacts associated with temperature fluctuations on the output accuracy of displacement and force sensors, their temperature was kept constant during each test. To do so, the entire length of sensors was wrapped around by flexible rubber tubes through which a constant-temperature water (at room temperature) was continuously circulated, as shown in Figure 4-5. The water basin of the direct shear test apparatus was insulated to minimize heat loss in the system.

Figure 4-5- Actual modified direct shear test setup, external water bath and water circulation plastic tubes.

4-4-   Testing program:

The experimental testing procedure consisted of 4 steps:

Step 1- Preparation: once the clay specimen was pre-consolidated and trimmed off, it was placed on the concrete plate. As shown in Figure 4-1, the concrete plate was fixed at one end and free at its other end so that it can approximately freely expand/contract during thermal loading.

Step 2-Normal stress application: The modified direct shear test was performed at three normal pressures:150 kPa, 225 kPa and 300 kPa. These pressures correspond to lateral earth pressures on an energy pile at depths of 22 m, 33 m, and 44 m, respectively, considering a saturated unit weight of 19 kN/m^3 for the soil and a coefficient of lateral pressure of 0.74.

Step 3- Thermal loading: In this step the interface temperature was changed by applying both non-cyclic and cyclic thermal loading. The reference temperature variation shown in Figure 4-4 was repeated 10, 20 and 40 times to generate cyclic thermal loading, while non-cyclic thermal loading was applied by increasing interface temperature up to 34 °C. The temperature of 24 °C is assumed to be the average in situ temperature of the soil surrounding an energy pile, and 34 °C is assumed to be the maximum temperature induced at pile-soil interface during pile operation. Note that it was assumed that the energy pile operates in tropical climate, where the energy pile is used to provide cooling energy.

Figure 4-4 shows that the interface temperature took about 70 minutes to reach the desired 34 °C, whereas it took about 10 minutes to reduce the interface temperature to 24 °C. This step was not performed under controlled-drainage condition as pore water pressure (PWP) measurement was not possible at the interface. However, a heating rate of 3.33 °C/h has been recommended by several researchers (example: Laloui et al., (2014) [26]) that may be used as a threshold limit to

ensure drained heating condition. In this study the heating rate is higher than 3.33 °C/h in the first 10 minutes of each cycle, but for the rest of the cycle the interface was heated at a lower rate (almost 1 °C/h). Accordingly, some thermally induced PWP is expected at the interface, particularly in the first 10 minutes of each heating phase. At the end of the step, however, the concrete-clay interface was left for 210 minutes to ensure all thermally induced PWP are entirely dissipated and then the shearing phase was initiated. The time duration was chosen based on the calibration tests conducted on the same clay inside a triaxial cell (chapter 3), where the heat-induced excess PWP within a cylindrical clay specimen (having dimension of 5×10 cm) was continuously measured after subjecting to the same temperature rise of 10 °C. 210 minutes was estimated to be the required time for full dissipation of the induced PWP. It should be noted, however, that the time duration required for full dissipation of the heat-induced PWP within a specimen in the direct shear test is most likely to be much less than that estimated inside the triaxial test, due to its shorter drainage path (≈ 20 mm = specimen thickness) comparing to that inside the triaxial test (≈ 50 mm = half of the specimen hight).

Step 4- Shearing: After achieving the targeted temperature, the shear displacement was applied at a constant rate of 0.005 mm/min. This rate was chosen in accordance with ASTM D3080-98 to ensure that excess PWP is dissipated during shearing. Since this tests apparatus is considered a "small-scale" direct shear test the maximum shear displacement is limited to 10 mm. The contact area between soil and concrete remained constant during shearing since the concrete plate plane dimensions were greater than those of the clay specimen. The specimens subjected to cyclic thermal loading were sheared at 24 °C, while those subjected to non-cyclic thermal loading were sheared at 34 °C. At the end of each test, two samples were taken from the zone near the interface for moisture content measurement.

4-5-   Test results

To investigate the effects of stress state and stress history on thermo-mechanical behavior of interface, the tests were conducted under different normal stresses and different over-consolidation ratios. Some tests were carried out at least twice (3-4 times in some cases) to ensure that the results are repeatable. Test details are summarized in Table 4-2.

Table 4-2- Tests details performed in this study.

Test #	A (cm^2)	h (cm)	ω_0 (%)	ω_f (%)	OCR	σ_n (kPa)	Thermal loading	τ_{peak}(kPa)
1	103.2	1.94	36.12	28	1	150	24 °C	54.13
2	103.2	1.94	-	-	1	150	34 °C	54.1
3	103.2	1.94	-	-	1	150	(24-34-24 °C)-10 cycles	54.7
4	103.2	1.94	36	29	1	150	(24-34-24 °C)-20 cycles	56.6
5	103.2	1.94	36.2	28	1	150	(24-34-24 °C)-40 cycles	55.74
6	103.2	1.94	35.9	28.5	1	225	24 °C	67.92
7	103.2	1.94	-	-	1	225	34 °C	72.19
8	103.2	1.94	36	27	1	225	(24-34-24 °C)-10 cycles	79.38
9	103.2	1.94	35.9	27.6	1	300	24 °C	82.53
10	103.2	1.94	-	-	1	300	34 °C	90.3
11	103.2	1.94	35.6	28.5	1	300	(24-34-24 °C)-10 cycles	91.06
12	103.2	1.94	31.7	30	2	150	24 °C	54.8
13	103.2	1.94	-	-	2	150	34 °C	51.2
14	103.2	1.94	-	-	2	150	(24-34-24 °C)-10 cycles	49.3
15	103.2	1.94	30.5	29.6	5	150	24 °C	62.25
16	103.2	1.94	-	-	5	150	34 °C	60.6
17	103.2	1.94	-	-	5	150	(24-34-24 °C)-10 cycles	57.47

A: cross-sectional area of interface, h: clay specimen thickness, ω_0: initial moisture content, ω_f: moisture content after failure, σ_n: normal stress, τ_{peak}: peak shear strength of interface

Figure 4-6 shows the influences of heating on shearing behavior of clay-concrete interface sheared at normal stress of 150 kPa. It can be seen that the change in interface shear strength due to heating was minor. Looking at Table 4-3 summarizing the results in Figure 4-6, it appears that heat cycles slightly increased the peak shear stress (at small displacements) up to 5%, while non-cyclic heating (34° C) had no effects on it. The displacement at peak shear stress for interfaces subjected to thermal loading was smaller (≈5 mm) than that for interfaces sheared without experiencing

121

temperature variations (≈6 mm). Shear strength corresponding to large displacements slightly increased up to 6% due to heat cycles, while it decreased by 3.5% at elevated temperature (34 °C).
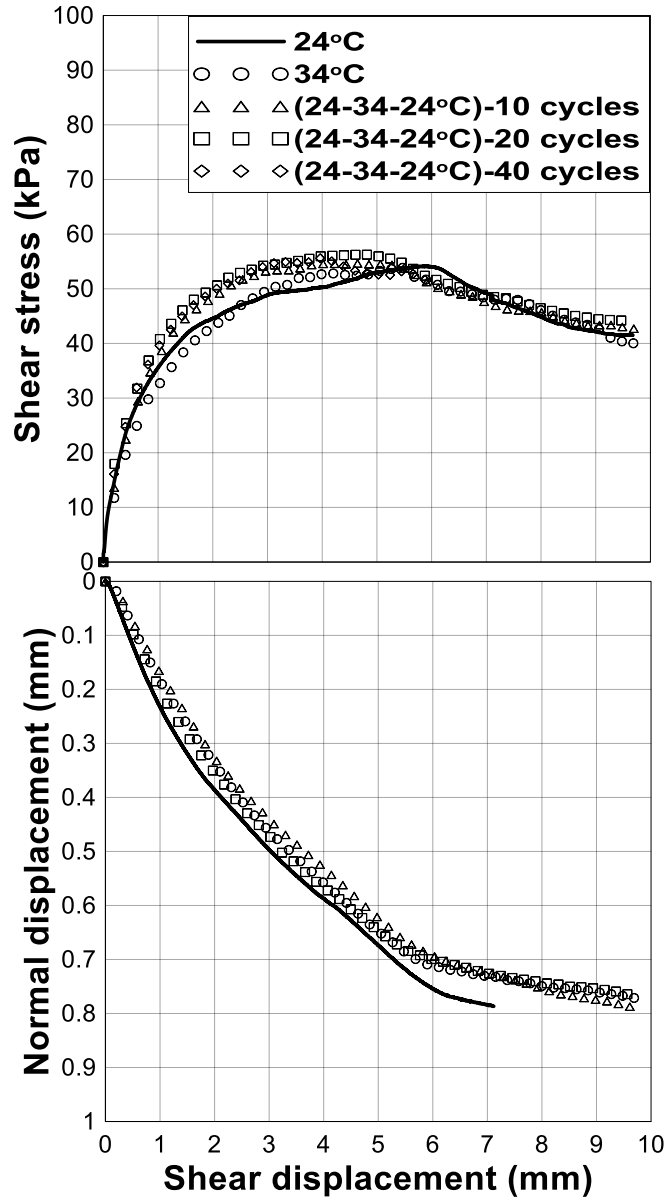
Figure 4-6- Shear strength of NC clay-concrete interface with different thermal loading at 150 kPa.

The effect of temperature on "residual" interface shear strength is not clear in this study because of the limit on maximum shear displacement of 10 mm. With respect to volumetric behavior,

122

heating decreased the contraction observed during the shearing. It is thought that the observed shearing/volumetric behavior is attributed to stiffening of NC clay occurring during heating.

Table 4-3- Effects of thermal loading on interface shear resistance at 150 kPa.

Thermal loading	Shear strength (kPa)	
	Small displacement	Large displacement
24 °C	54.13	41.56
34 °C	54.1	40.1
(24-34-24 °C)- 10 cycles	54.7	42.8
(24-34-24 °C)- 20 cycles	56.6	44.1
(24-34-24 °C)- 40 cycles	55.74	-

Figure 4-7 shows the effect of thermal loading on the interface shearing response at normal stresses of 225 kPa and 300 kPa. Table 4-4 illustrates that cyclic heating increased the peak strength (at small displacement) by 16% and 10% at 225 kPa and 300 kPa, respectively. However, elevated temperature (34 °C) increased the peak strength by approximately 6% and 9%, respectively. The thermal strengthening was also observed at large displacements, which is more important under heat cycles. On the other hand, the contraction occurring during shearing was lower for the interfaces subjected to heating.

Generally speaking, heating improves the shearing resistance of NC clay-concrete interface. This improvement, however, is more pronounced at high normal stresses. The results above are in agreement with the experimental tests carried out by Di Donna et al. (2016) [6]. They observed the shearing resistance of NC clay-concrete interface can be improved by 20-40% at elevated temperature. They also observed a thermally induced reduction in volumetric contraction during shearing.
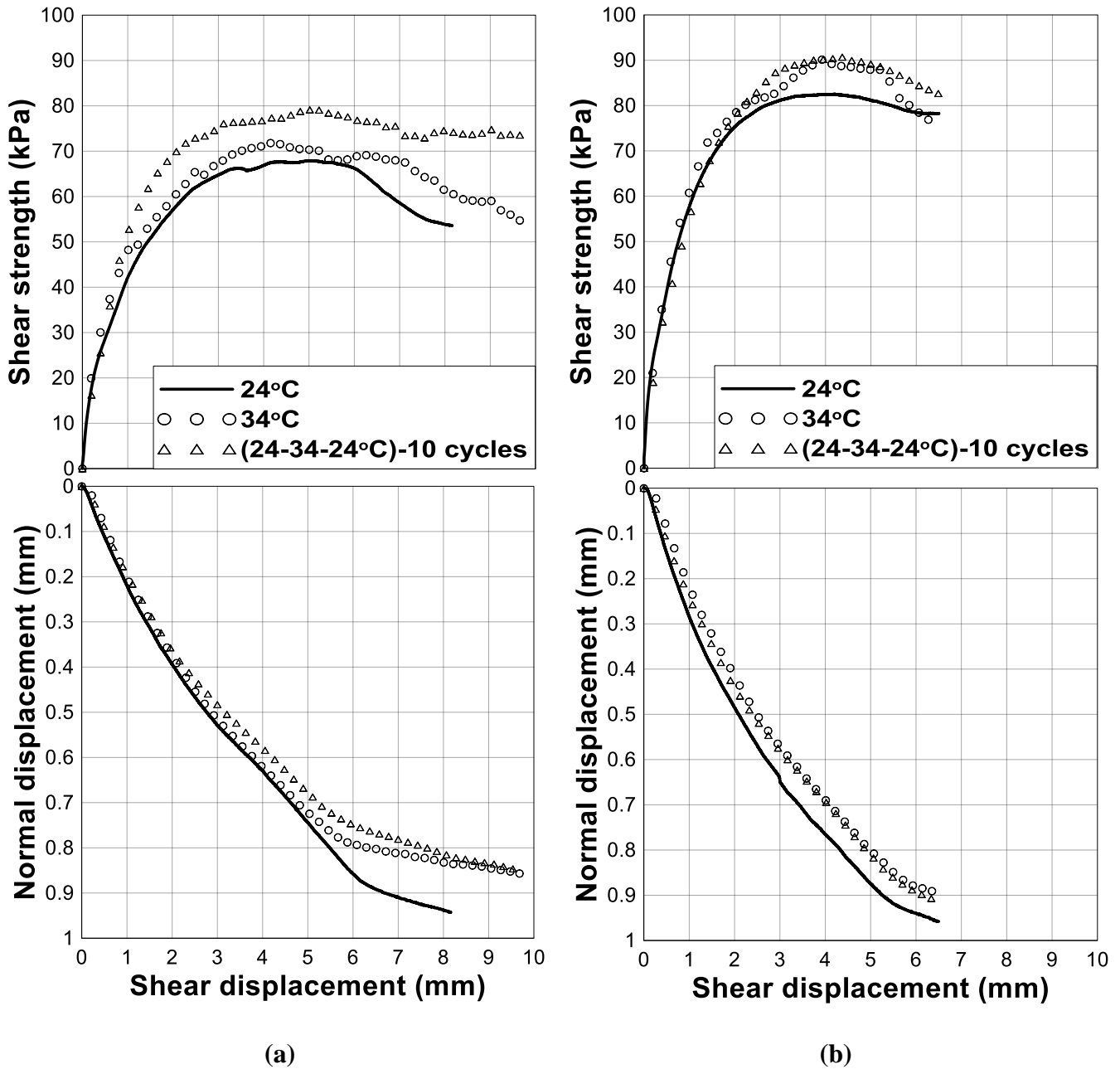
Figure 4-7- Shear strength of NC clay-concrete interface at (a) 225 kPa and (b) 300 kPa

The influence of the over consolidation ratio (OCR) on interface thermo-mechanical behavior is illustrated by Figure 4-8. Unlike the case of NC clay, both cyclic and non-cyclic thermal loading caused a reduction in peak strength (at small). Table 4-5, summarizing the results in Figure 4-8, shows 8-10% decline in the peak strength due to heat cycles, while 2-6% decrease due to elevated

temperature. Heating also caused thermal softening at large displacements, where the strength reduction due to heat cycles ($\approx$17%) was twice that ($\approx$8%) because of non-cyclic heating. Conversely, the volumetric behavior of interface during shearing seems thermally independent.

Table 4-4- Effects of thermal loading on interface shear resistance at 225 kPa and 300 kPa.

Thermal loading	$\sigma_n = 225\ kPa$		$\sigma_n = 300\ kPa$	
	Shear strength (kPa)		Shear strength (kPa)	
	Small displacement	Large displacement	Small displacement	Large displacement
24 °C	67.92	53.6	82.53	-
34 °C	72.19	54.1	90.3	-
(24-34-24 °C)- 10 cycles	79.38	73.3	91.06	-

From Figures (4-6)-(4-8), it can be concluded that the effect of heating on the interface resistance is governed by two main factors: interface normal stress and stress history of clay signified by OCR. Figure 4-9 illustrates the importance of these two factors in describing thermal change effects on interface strength. It should be noted that the data presented in Figure 4-9(b) was measured at normal stress of 150 kPa.

Table 4-5- Effects of thermal loading on interface shear resistance of OC clays.

Thermal loading	OCR = 2		OCR = 5	
	Shear strength (kPa)		Shear strength (kPa)	
	Small displacement	Large displacement	Small displacement	Large displacement
24 °C	54.8	49.8	62.25	50.5
34 °C	51.2	45.9	60.6	-
(24-34-24 °C)-10 cycles	49.3	41.5	57.47	42.2
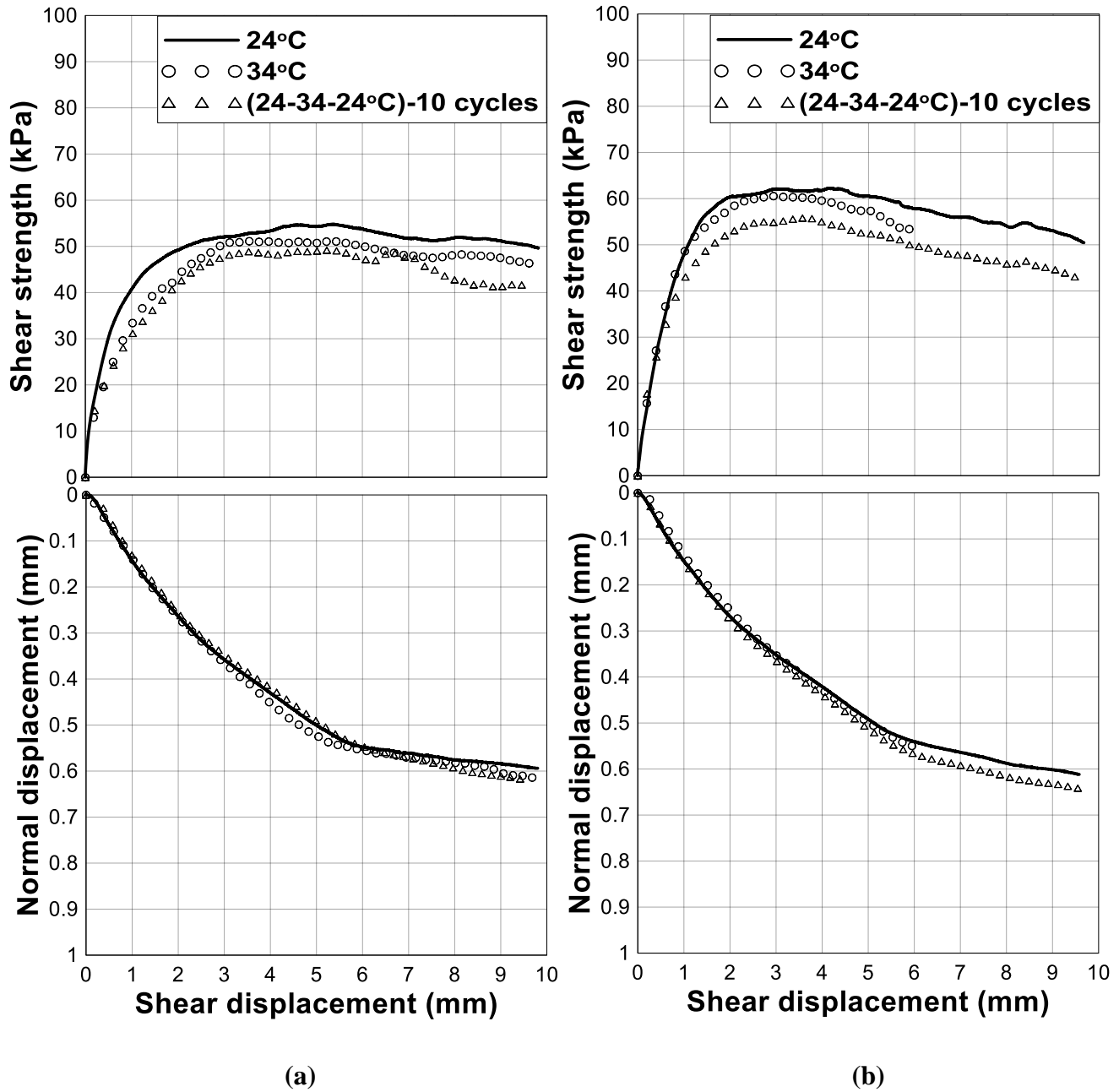
Figure 4-8- Shear strength of clay-concrete interface with different thermal loading at (a) OCR = 2 and (b) OCR = 5 at a normal stress of 150 kPa.

The relationship between shear strength of clay and heating is illustrated in Figure 4-10 illustrating the relationship between shear strength of clay and thermal loading path (obtained from Chapter 3) may help further understand the interface shearing response to heating.
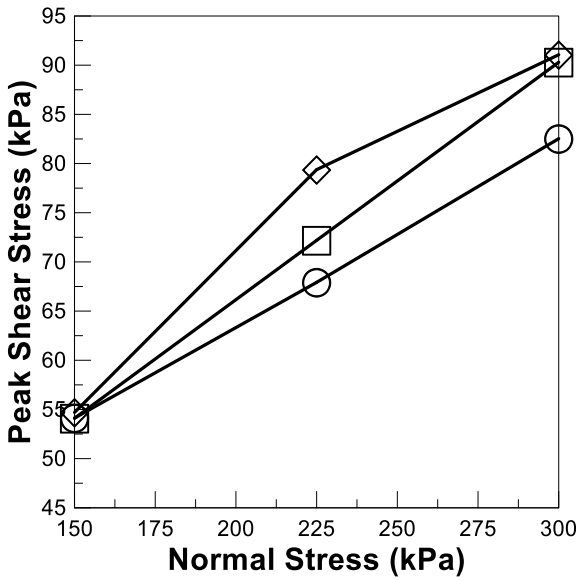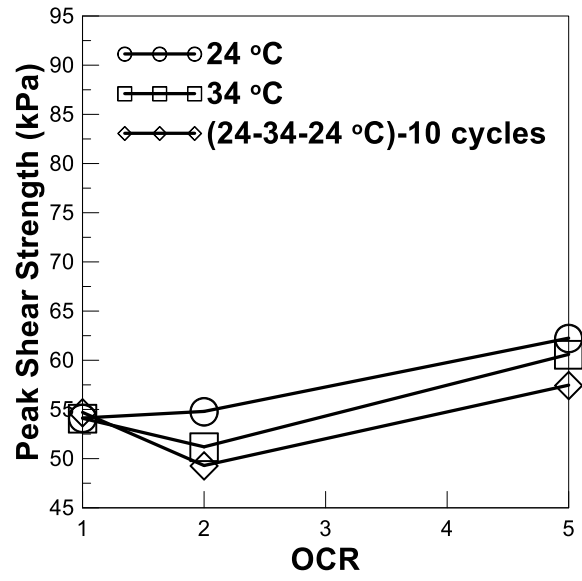
(a)   (b)

Figure 4-9- Effect of (a) interface normal stress, and (b) stress history of clay (OCR) on the thermo-mechanical response of interface.

Although the results shown in Figures (4-9) and (4-10) were obtained under different boundary conditions, it may be helpful to make a comparison between them.
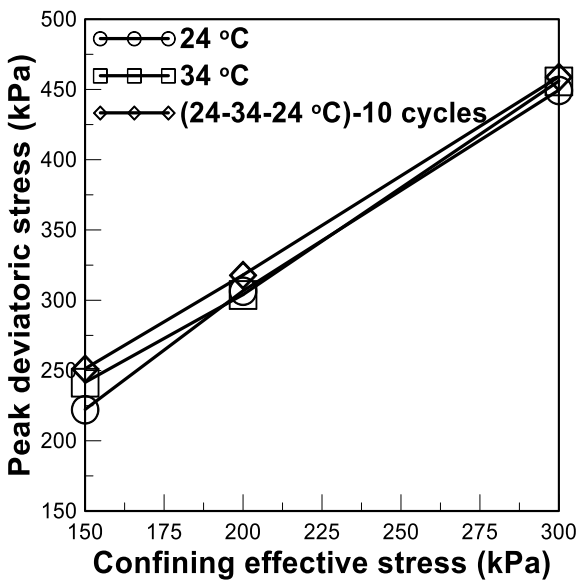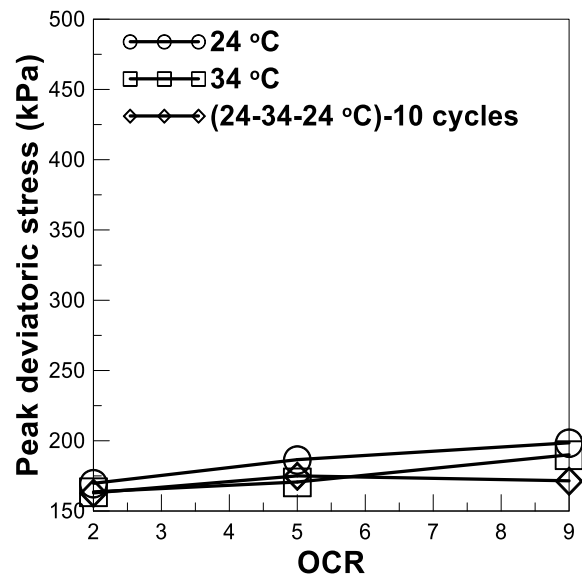
(a)   (b)

Figure 4-10- Effect of thermal loading on shear strength of clay in triaxial test (a) NC clay and (b) OC clay (at 100 kPa).

127

Under a qualitative point of view, there is an agreement between thermo-mechanical response demonstrated by the clay (in triaxial test) and clay-concrete interface (Figures 4-9). In fact, they both show OCR-dependent response to heating; NC clay and NC clay-concrete interface display thermal strengthening, while OC clay and OC clay-concrete interface show thermal softening. From a quantitative point of view, for instance, heat cycles induce 7.6% and 6% decrease in shearing resistance between intermediate OC clay and concrete (in direct shear test), and intermediate OC clay (OCR = 5, in triaxial test), respectively. As for NC clay, heat cycles cause an increase of ≈3% in shearing resistance of NC clay at 300 kPa, while an increase of ≈10% in corresponding interface resistance at normal stress of 300 kPa.

Figure 4-11(a) shows peak strength envelope for the NC clay-concrete interface at three different thermal loading. It can be seen that the peak friction angle increased as a result of thermal loading, while the interface adhesion slightly decreased. Figure 4-11 (b) compares the shear strength of NC clay, obtained from consolidated-drained (CD) compression triaxial and CD direct shear tests, and clay-concrete interface sheared at isothermal condition. The shear strength envelope for the triaxial test was estimated by plotting the best-fit tangent to three Mohr's circles at confining pressures of 100 kPa, 200 kPa and 300 kPa. The results indicate that the shear strength estimated by CD triaxial tests is greater than that measured by means of direct shear testing. The difference is more pronounced at higher normal stresses. This finding is in agreement with that reported by Castellanos and Brandon (2013) [27]. In their study, they performed an extensive comparison between effective shear strength obtained by triaxial tests and direct shear tests. They reported that the effective friction angle measured by the two devices can vary by 10-12° for clay. This is mainly attributed to the differences in stress/strain boundary conditions between the two testing methodologies. In addition, it is widely accepted that triaxial testing describes more closely the

soil's in situ and failure stress conditions than its counterpart, the direct shear testing. From Figure

4-11, it can also be seen that the clay (in both the triaxial cell and the direct shear box) exhibited

higher shear strength as compared with the clay-concrete interface.
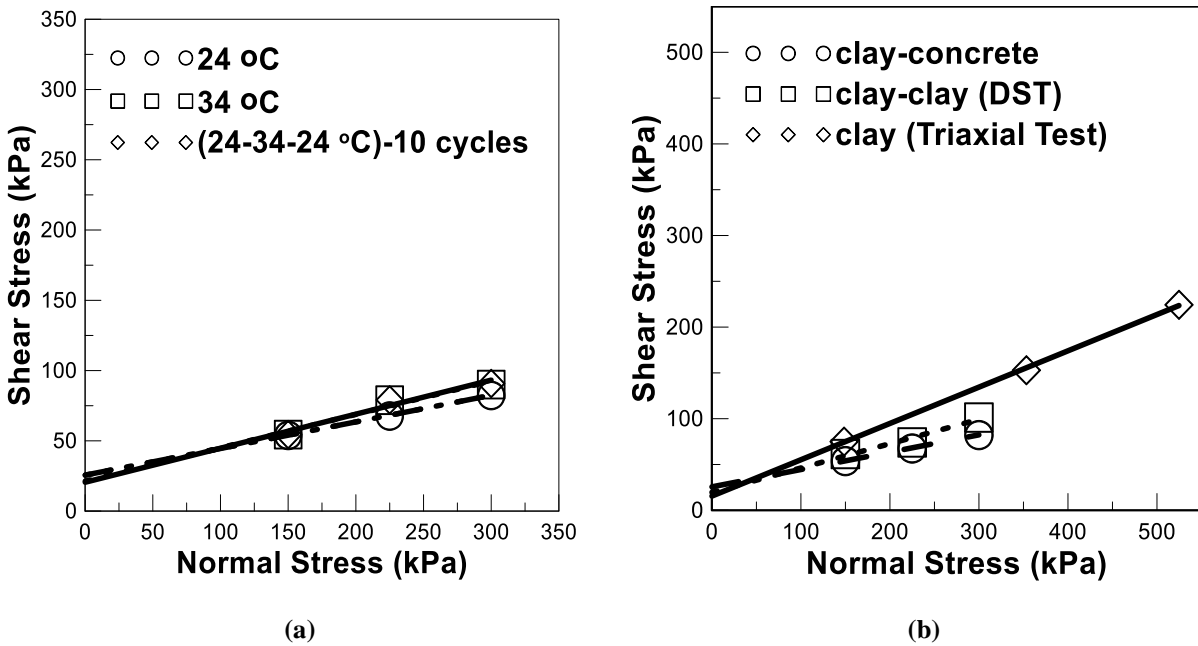
Figure 4-11- Shear strength envelope (a) Interface strength with thermal loading and (b) Interface strength (w/o thermal loading) in comparison with soil strength via direct shear and triaxial shear tests.

Table 4-6 summarizes the relationship between thermal loading and soil strength parameters (c'

and φ') and the clay-concrete interface strength parameters (c' and δ'). These parameters are

associated with the Mohr-Coulomb failure criterion:

$$\tau = c' + \sigma'_n \tan(\phi' \text{or } \delta') \qquad (4-2)$$

where, τ is the shear stress and σ'_n is the normal effective stress.

Table 4-6- Shear strength parameters of clay and clay-concrete interface.

| | Clay | | | | clay-concrete interface | |
| | CD triaxial test | | CD direct shear test | | | |
	c'(kPa)	ϕ' (°)	c' (kPa)	ϕ' (°)	c' (kPa)	δ' (°)
24 °C	12	24.5	20	15	25.59	10.72
34 °C	-	-	-	-	21.33	13.35
(24-34-24 °C)-10 cycles	-	-	-	-	20.51	13.63

From Table 4-5, the clay cohesion estimated in the direct shear device is much higher than that determined by the CD triaxial test at ambient temperature, while the measured friction angle is 63% lower than that obtained using the CD triaxial test. It also shows that the interface adhesion decreased by 17-20 % as temperature was increased from 24 C° to 34 C°. It is noted that the cyclic thermal loading has led to a slightly higher reduction in the interface adhesion as compared with the non-cyclic thermal loading. On the other hand, the thermal loading caused a significant increase in interface friction angle. The cyclic and non-cyclic thermal loading caused 27% and 25% increase in the interface friction angle, respectively. The ramifications of these findings on energy pile design can be very significant.

On the contrary, Di Donna et al. (2016) [6] found an increase in interface adhesion at elevated temperature, while a reduction in interface friction angle. In another study, however, elevated temperature was reported to both reduce and increase interface adhesion and friction angle depending on magnitude of temperature (Yavari et al., 2016 [7]). These controversial observations may be found dependent upon different thermo-mechanical response of the clays used in those tests.

4-6- Discussion

Interface shearing strength is characterized by two important parameters: effective normal stress acting on interface, and friction coefficient of interface. Therefore, a qualitative interpretation of

the thermally induced changes in shear resistance of interface could be presented in terms of thermally induced changes in these two parameters. As for the first parameter, any change in total normal stress during thermal loading is deemed insignificant, as all direct shear tests were performed under CNL condition. The induced excess pore water pressure during interface shearing is assumed to be zero since both heating and shearing phases were done in drained condition. As a result, changes in effective normal stress during interface shearing are negligible.

Thus, the influence of temperature variations on behavior of clay-concrete interface should be described with respect to the thermally induced changes in interface friction coefficient. According to Tsubakihara and Kishida 1993 [18], the total displacement along an interface (both medium and rough) consists of the shearing deformation of soil mass and the sliding displacement along the clay-concrete interface. The mobilized shearing resistance due to distortion of soil mass makes an important contribution to the total shearing resistance of interface (Uesugi et al. 1988 [14] and Tsubakihara and Kishida 1993 [18]). Accordingly, stiff clay-concrete interface is generally expected to present higher resistance to shear forces relative to soft clay-concrete interface, due to the presence of stronger clay near the interface.

In the same manner, the observed thermo-mechanical response of interface can be linked to the thermo-mechanical behavior of clay near the interface. Strictly speaking, the thermal strengthening presented by NC clay-concrete interface (Figure 4-9a) is due to the fact that the NC clay in the vicinity of interface (shear zone) has already subjected to thermal strengthening (Figure 4-10a). On the other hand, thermal softening behavior of OC clay-concrete interface (Figure 4-9b) is interpreted in terms of thermal softening of OC clay near the interface (Figure 4-10b).

With respect to shear strength parameters, NC clay-concrete interface exhibited greater friction angle (δ') at higher temperature, while its adhesion (c') decreased as heating occurred. The tests also indicated that thermal hardening of interface was insignificant at low normal stresses, while greater thermal hardening occurred at high normal stresses. In contrast, thermal loading resulted in a reduction in shear strength of OC clay-concrete interface. The observed reduction (softening) became more significant as OCR increased.

4-7-   Conclusion

In this section, a series of direct shear tests were carried out to study the effects of cyclic and non-cyclic heating on the clay-concrete interface shear strength. A modified direct shear apparatus capable of thermal loading application was developed. The following is a summary of important findings that may have significant effects on energy pile design:

1. The shearing behavior of clay-concrete interface under thermal loading is mainly controlled by the applied normal stresses and stress history of clay signified by OCR.
2. From a qualitative point of view, an agreement was found between thermo-mechanical response of clay (in triaxial test) and clay-concrete interface. In fact, the thermal strengthening/softening observed for NC/OC clay-concrete interface can be attributed to the thermal strengthening/softening response of NC/OC clay observed in Triaxial tests.
3. The peak friction angle of the NC clay-concrete interface increased, while the interface adhesion decreased, due to temperature increase.
4. Thermally induced hardening of NC clay-concrete interface was found to be minor at a low normal stress (150 kPa), while it was significant at higher normal stresses (225 kPa and

300 kPa). On the other hand, thermally induced softening of OC clay-concrete interface was observed as it was heated up either monotonically or cyclically.

References:

[1] Cui YH, Liu JK, Lv P. (2013). Research on the permafrost dynamic load direct shear apparatus. *Rock and Soil Mechanics*, 34(S2), 486–490.

[2] Kawaguchi T, Nakamura D, Yamashita S, Yamasaki S. (2013). Effects of Freeze-Thaw History on Deformation-Strength Properties and Permeability of Fine-Grained Soil. In: Proc., 18th Int. Conf. on Soil Mechanics and Geotechnical Engineering. Paris: 357-360.

[3] Jiankun L, Peng L, Yinghui C, Jingyu L. (2014). Experimental study on direct shear behavior of frozen soil–concrete interface. *Cold Regions Science and Techno*logy, 104-105, 1-6.

[4] Lv P, Liu JK, Cui YH. (2013). A study on dynamic shear strength of frozen soil–concrete contact interface. *Rock and Soil Mechanics*, 34(S2), 180–183.

[5] Xiao S, Suleiman MT, McCartney JS. (2014). Shear Behavior of Silty Soil and Soil-Structure Interface under Temperature Effects. In: *Geo-Congress GSP 234 © ASCE*.: 4105-4114.

[6] Di Donna A, Ferrari A, Laloui L. (2016). Experimental investigation of the soil concrete interface: physical mechanisms, cyclic mobilization and behavior at different temperatures. *Canadian Geotechnical Journal*. 43(4), 659-672.

[7] Yavari N, Tang AM, Pereira J-M, Hassen G.. (2016). Effect of temperature on the shear strength of soils and soil/structure interface. *Canadian geotechnical journal,* 53(7), 1186-1194.

[8] Lehane BM, Jardine RJ, Bond AJ, and Frank R. (1993). Mechanisms of shaft friction in sand from instrumented pile tests. *Journal of Geotechnical Engineering,* 119(1), 19–35.

[9] Potyondy JG. (1961). Skin friction between various soils and construction materials. *Geotechnique*. 11(4), 831– 853.

[10] Acar YB, Durgunoglu HT, Tumay MT. (1982). Interface properties of sand. *J. Geotechnical Engineering,* 108(4), 648– 654.

[11] Goh ATC, Donald IB. (1984). Investigation of soil-concrete interface behavior by simple shear apparatus. *Geomechanics-Interaction*, 84(2), 101-106.

[12] Uesugi M, Kishida H. (1986a). Influential factors of friction between steel and dry sands. *Soils and Foundations,* 26(2), 33–46.

[13] Uesugi M, Kishida H. (1986b). Frictional Resistance at Yield between Dry Sand and Mild Steel. *Soils and Foundations, Japanese Society of Soil Mechanics and Foundation Engineering*, 26(4), 139-149.

[14] Kishida H, Uesugi M. (1987). Tests of the interface between sand and steel in the simple shear apparatus. *Geotechnique*. 37, 45-52.

[15] Uesugi M, Kishida H, Tsubakihara Y. (1988). Behavior of sand particles in sand–steel friction. *Soils and Foundations*, 28(1), 107–118.

[16] Uesugi M, Kishida H, Tsubakihara Y. (1989). Friction between sand and steel under repeated loading. *Japanese Society of Soil Mechanics and Foundation Engineering*. 29(3), 127-137.

[17] Uesugi M, Kishida H, Uchikawa Y. (1990). Friction between dry sand and concrete under monotonic and repeated loading. *Soils and Foundations*, 30(1), 115–128.

[18] Tsubakihara, Y., Kishida, H. (1993). Frictional behavior between normally consolidated clay and steel by two direct shear type apparatuses. *Soils and Foundations,* 33(2), 1-13.

[19] Subba KS, Allam MM, Robinson RG. (1996). A note on the choice of interfacial friction angle. In: *Proc., the Institution of Civil Engineers - Geotechnical Engineering,* 119(2), 123-128.

[20] Porcino D, Fioravante V, Ghionna V, Pedroni S. (2003). Interface behavior of sands from constant normal stiffness direct shear tests. *Geotechnical Testing Journal,* 26(3), 289–301.

[21] Lemos LJL, Vaughan PR. (2000). Clay-interface shearing resistance. *Geotechnique*, 50(1), 55-64.

[22] Lings ML, Dietz MS. (2005). The peak strength of sand–steel interfaces and the role of dilation. *Soils and Foundations*. 45(6), 1–14.

[23] Hammoud F, Boumekik A. (2006). Experimental study of the behavior of interfacial shearing between cohesive soils and solid materials at large displacement. *Asian J. Civil Engineering (Building and Housing)*. 7(1), 63-80.

[24] Zhang G, Zhang JM. (2006). Monotonic and cyclic tests of interface between structure and gravelly soil. *Soils and Foundations Journal*, 46(4), 505–518.

[25] Lupini JF, Skinner AE, Vaughan PR. (1981). Drained Residual Strength of Cohesive Soils. *Geotechnique*, 31(2), 181–213.

[26] Laloui L, et al. (2014). Issues involved with thermoactive geotechnical systems: characterization of thermomechanical soil behavior and soil-structure interface behavior. *The Journal of the Deep Foundations Institute*. 8(2), 108-120.

[27] Castellanos BA, Brandon TL. (2013). A Comparison between the shear strength measured with direct shear and triaxial devices on undisturbed and remolded soils. In: *Proc. 18th Int. Conf. on Soil Mechanics and Geotechnical Engineering,* Paris: 317-320.

[28] Yazdani, S., Helwany, S., and Olgun, O. (2018b). Influence of Temperature on Soil-Pile Interface Shear Strength. *Geomechanics for Energy and the Environment,* 18, 69-78.

Chapter 5

Effect of Temperature on The Shear Strength of Pile-Clay Interface Under Constant Normal Stiffness (CNS)-Small Scale Pile Test

5-1- Introduction:

In addition to direct shear technique frequently used to assess the interface behavior under thermo-mechanical loading, different aspects of energy pile behavior, including serviceability and bearing capacity, have been investigated through either Finite Element (FE) analysis or physical modeling. Thermo-elastic FE analyses were used by Laloui and Nuth, (2006) [1] and Laloui et al. 2006 [2] to examine the variations of axial stress, strain and displacement in an energy pile during heating-cooling cycles. Full-scale thermal loading tests performed by several researchers also provide valuable insight into the energy pile response to thermal loads (Brandl 2006 [3], Laloui et al. 2006 [2], Bourne-Webb et al. 2009 [4], Laloui 2011 [5], Laloui and Nuth 2006 [1], Amatya et al. 2012 [6], Bouazza et al. 2011 [7], Wang et al. 2012 [8], and McCartney and Murphy 2012 [9]). On the other hand, laboratory-scale tests are also valuable tools for analyzing energy pile behavior as they can be repeated in carefully controlled conditions of soil stratigraphic, foundation geometry, end restraint boundaries and thermo-mechanical loadings.

A review of latest research findings on the thermo-mechanical behavior of energy piles using laboratory scale models are presented herein. Using centrifuge modeling technique, McCartney and Rosenberg (2011) [10] showed that bearing capacity of a concrete energy pile in compacted silt improves under heat cycles, possibly due to the greater lateral pressure induced by heating. In another centrifuge modeling experiment, Stewart et al. 2013 [11] reported that strain-stress relation in an end-restrained energy pile in unsaturated silt doesn't change significantly during heat cycles. Ng et al. 2014 [12] using similar testing apparatus found that floating energy piles in OC clay undergo a progressive thermally induced settlement at a reduced rate with heat cycles. Goode and McCartney (2015) [13] concluded that the bearing capacity improvement for energy piles in unsaturated silt is likely due to thermally-induced water flow that leads to an increase in effective

stress along the pile. Ghaaowd and McCartney (2018) [14] and Ghaaowd et al. (2018) [15] observed a significant increase in the pullout capacity of heated scale-model energy piles embedded in Normally-consolidated (NC) clay. They found that the pullout capacity for the energy piles subjected to temperature variations of 37 °C and 19 °C and pulled out at ambient temperature (≈ 26 °C) is approximately 95% and 40%, respectively, greater than that of unheated energy pile. On the other hand, 1-g laboratory pile test was also employed by the following researchers to examine the thermo-mechanical response of energy piles. Wang et al. 2011 [16] reported that the shaft resistance of a steel energy pile in sand decreases with heat cycles. Kalantidou et al. 2012 [17] and Yavari et al. 2014 [18] observed a nearly thermo-elastic settlement of energy pile under low mechanical loads, while an irreversible heat-induced settlement under higher mechanical loads (close to the estimated ultimate load).

The review of recent literature shows that attention was mainly focused toward the temperature effects on the serviceability and the ultimate bearing capacity. In this situation making quantitative/qualitative assessment of relative contribution of the shaft and the base resistances to the ultimate capacity would be difficult. Sometimes, however, it is of interest to explain the effects of temperature on the shaft and the base resistances separately.

This chapter describes the results of 5 pile load tests performed using 1-g laboratory scale models to understand the effects of temperature variations on energy pile's shaft resistance. The model concrete pile was embedded in a saturated clay in a way that allows the shaft resistance to be measured directly. As mentioned in the previous chapters, it was assumed that the energy pile operates in summer mode in which the ground is regarded as a heat sink. Accordingly, 24°C was assumed to be the average temperature at the shallow depths where the energy pile is installed, and 34°C was considered as the maximum temperature induced at the pile's surface during heat

exchange. A description of a simple thermo-mechanical model for energy piles is described below, followed by a description of the test setup and the results.

5-2- Thermo-mechanical behavior of energy piles

As mentioned in the second chapter restraints provided by the end boundary conditions and side shear resistance prevent the energy pile from expanding freely during heating. Consequently, some internal stresses will be created in the pile structure that may change the distribution of axial load (P) and mobilized side shear stress (q_s). in the Chapter 2 we discussed the effect of temperature variations on the pile settlement and axial load distribution. Here, the effect of heating and cooling on the mobilized side shear stress will schematically be explained. Figures 5-1 present a simplified framework, introduced by Amatya et al. 2012 [6] and Bourne-Webb et al. 2012 [19], for explaining this behavior under different ends constraints. Figure 5-1 and 5-2 illustrate the distribution of the axial load and side shear stress under individual effects of thermal and mechanical loadings, respectively. Figure 5-3 combines the mechanisms presented in Figures 5-1 and 5-2 to illustrate the response of an energy pile under combined thermo-mechanical loading. It can be noted that depending on the end constraints the compressive axial load and the side shear stress generated under combined thermo-mechanical loading are higher than those developed under the mechanical condition alone. Therefore, both the serviceability and the stability of an energy pile might be jeopardized owing to increases in the axial load and mobilized side shear stress, respectively.

$P \ (axial \ load): EA\varepsilon \ -q_s(mobilized \ shaft \ resistance)$

(a)   **(b)**
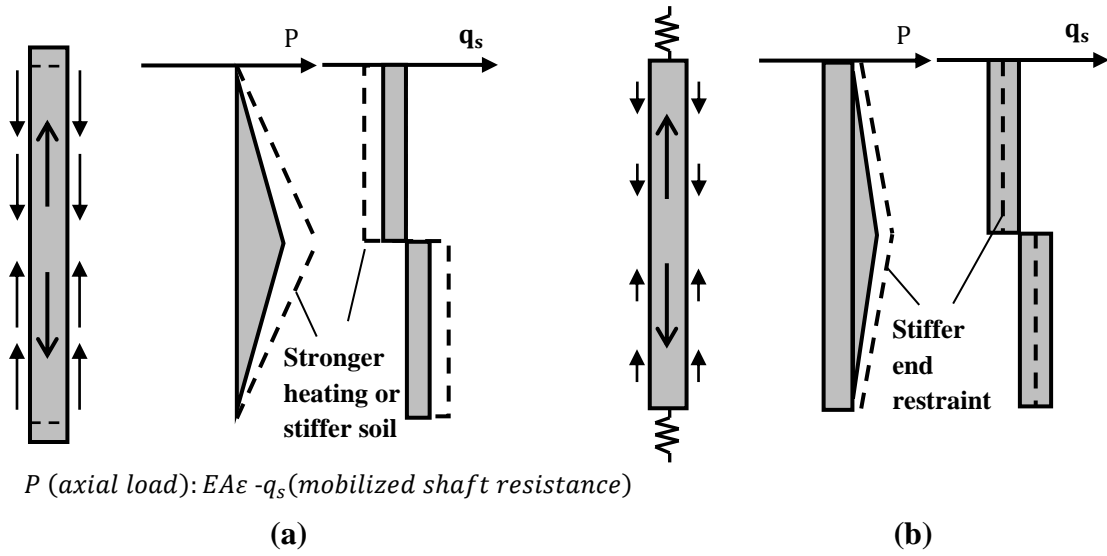
Figure 5-1- Effect of end-restraint on thermal response: **(a)** without end restraint **(b)** with end restraint (Bourne-Webb et al. 2012).
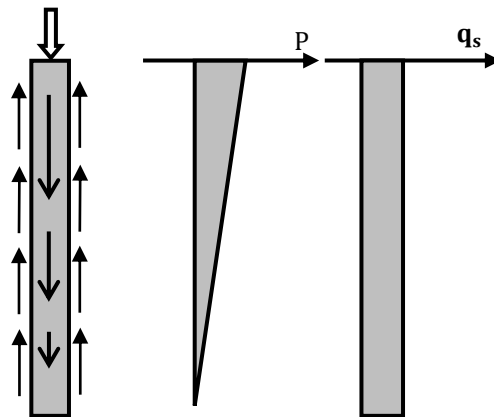
Figure 5-2- Axial load and side shear stress distribution under mechanical loading-without end restraint (Bourne-Webb et al. 2012).
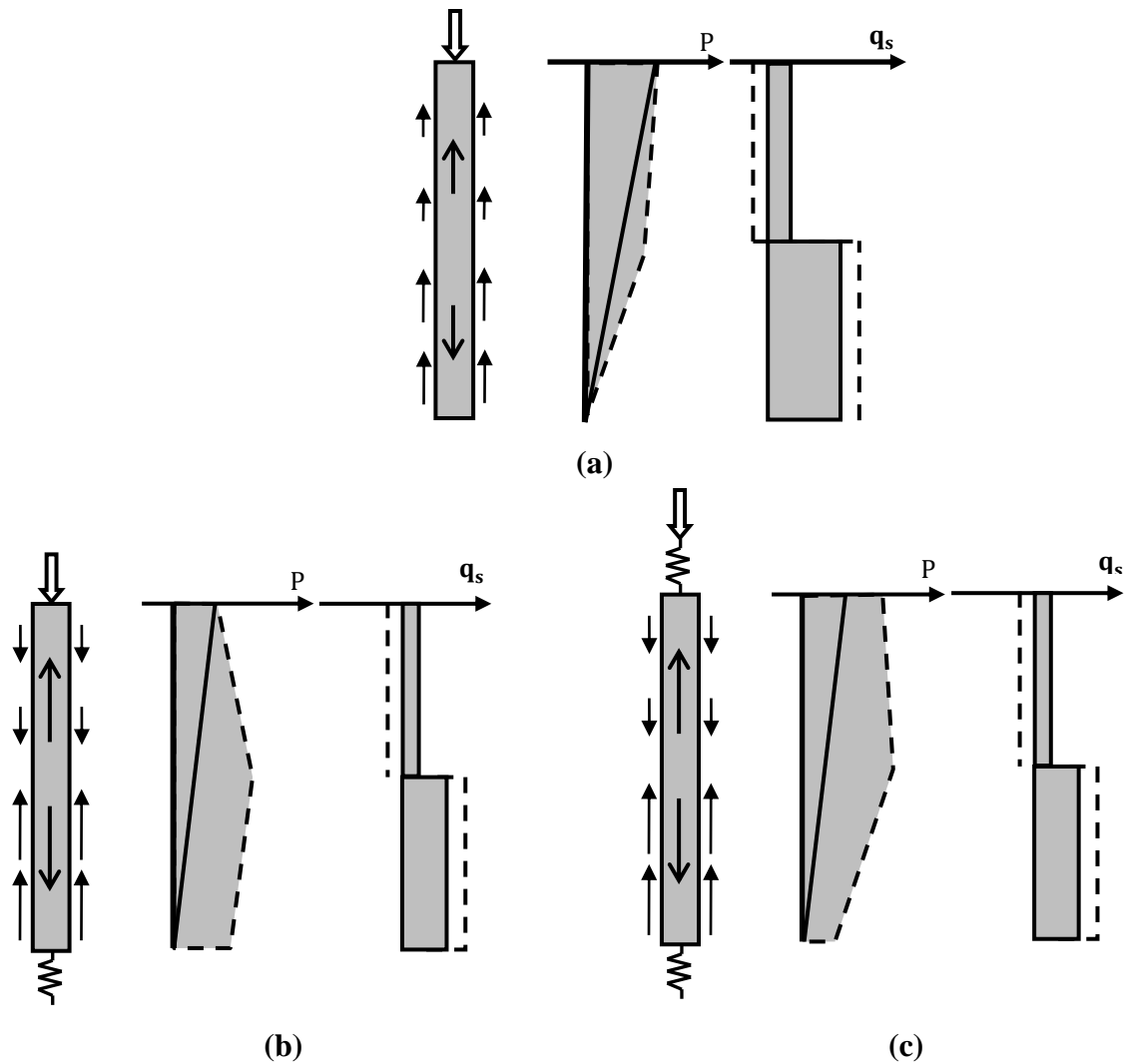
Figure 5-3-Mechanism of load transferring for energy piles subjected to thermo-mechanical loading: **(a)** Free end restrain **(b)** end restraint at toe **(c)** end restraint at two ends (Bourne-Webb et al. 2012).

5-3- Description of the laboratory-scale energy pile test

An instrumented laboratory test apparatus was developed, and tests were performed to examine the effects of heating/cooling cycles on the interaction between an energy pile subsection and soil. This test represents a portion (subsection) of a concrete energy pile, 19-mm in diameter, with an embedded length of 230-mm. The test was performed inside a cylindrical container ("calibration chamber") with 170-mm inner diameter that houses the pile subsection and the surrounding saturated clay.

It is desirable to isolate the frictional resistance of the pile from the tip resistance, since the objective of the test is to study the effects of heating/cooling cycles on the interface shear resistance. To do this, a circular opening with a diameter slightly greater than the diameter of the pile was made at the bottom of the soil container. The pile was allowed to slide freely through the cut. To simulate the in-situ stresses at a given depth, z, an equivalent vertical effective stress of 100 kPa (Figure 5-4) was applied at the top surface of the soil using a doughnut-shaped air bag with an outside diameter of 170-mm. The test procedure will be discussed in more detail in the following sections.
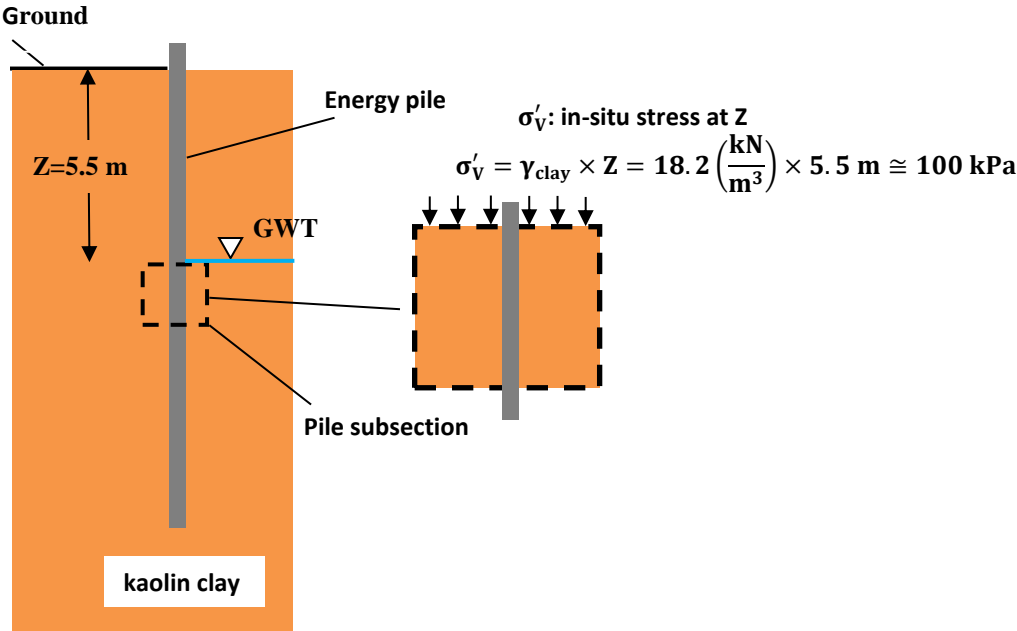
Figure 5-4- Pile subsection analysis under simplified condition.

5-4- Materials and test set up

Soil:

The same HC-77 kaolin clay was also used in this study. A slurry with a moisture content of twice the liquid limit of the kaolin was prepared and consolidated around the energy pile model using a uniform pressure of 100 kPa. More details about the clay pre-consolidation process are presented below.

Model pile:

The model energy pile was constructed using a hollow steel tube (shaft) coated with a thin layer of concrete (Figure 5-5(a) and (b)). The concrete mix ratio of 1:1:0.3 (fine sand: cement: water) was used. The shaft was a 19-mm stainless-steel tube threaded in the middle part (with a diameter of ≈ 15 mm), as shown in Figure 5-5(a). To cover the threaded part by concrete, the steel shaft was gradually pushed into a rigid plastic tube with an inner diameter equal to the steel shaft's outer diameter (19 mm). Once the plastic tube's end reached the threaded part, fresh concrete pouring was simultaneously employed to fill the existing space between the threaded part and the inner surface of the plastic tube till the whole space was filled by a thin layer of concrete. The surrounding plastic tube was removed after one week.

Due to the large frictional resistance between the threads and the concrete coating, no relative motion between them is expected under the thermo-mechanical loads applied herein. Therefore, the axial load at the pile head is assumed to be totally transferred by the frictional resistance mobilized between the external concrete surface and the surrounding clay.
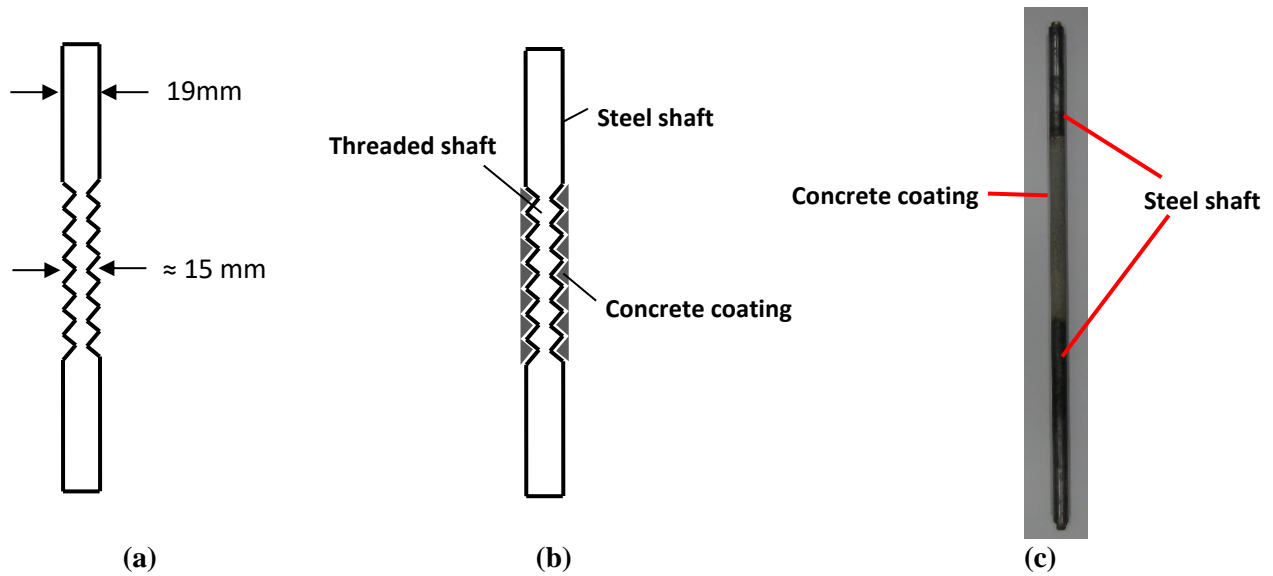
Figure 5-5- The model pile: (a) Schematic view of steel shaft (tube), (b) Schematic view of steel shaft and concrete coating, and (c) real steel/concrete shaft.

Test setup:

A schematic of the experimental setup and the instrumentation is shown in Figure 5-6. A loading machine was used for axial load application, during which the load-settlement response of the model pile was measured. The soil container was a low thermal conductivity rigid plastic cylinder with an inside diameter of 170 mm and a height of 300 mm (Figure 5-7). Its low thermal conductivity (0.1 W/ (m.K)) helped to minimize the conduction heat loss. The ratio of the container diameter (170 mm) to the pile diameter (19 mm) was chosen as 9 to minimize the scale effects on the shaft resistance. In the following sections possible scale effects on the shaft resistance and heat transfer (between the pile and surrounding clay) are described in detail. Inlet and outlet tubes were connected to the energy pile, as shown in Figure 5-6, to circulate the heat exchange fluid from a heat pump circulator.

To measure temperature distribution in the surrounding clay due to thermal loading, three miniature thermocouples were installed at distances of 1D, 2D and 3D (D is the pile diameter) from the pile surface as indicated in Figure 5-6. All thermocouples were inserted at the middle of

144

the pile length and were connected to a data logger. Figure 5-8 shows how the thermocouples were installed in the chamber. They were mounted on the 3 copper tube (with diameter of 3 mm) crossing the base of the container, before the main chamber and the clay slurry were placed.
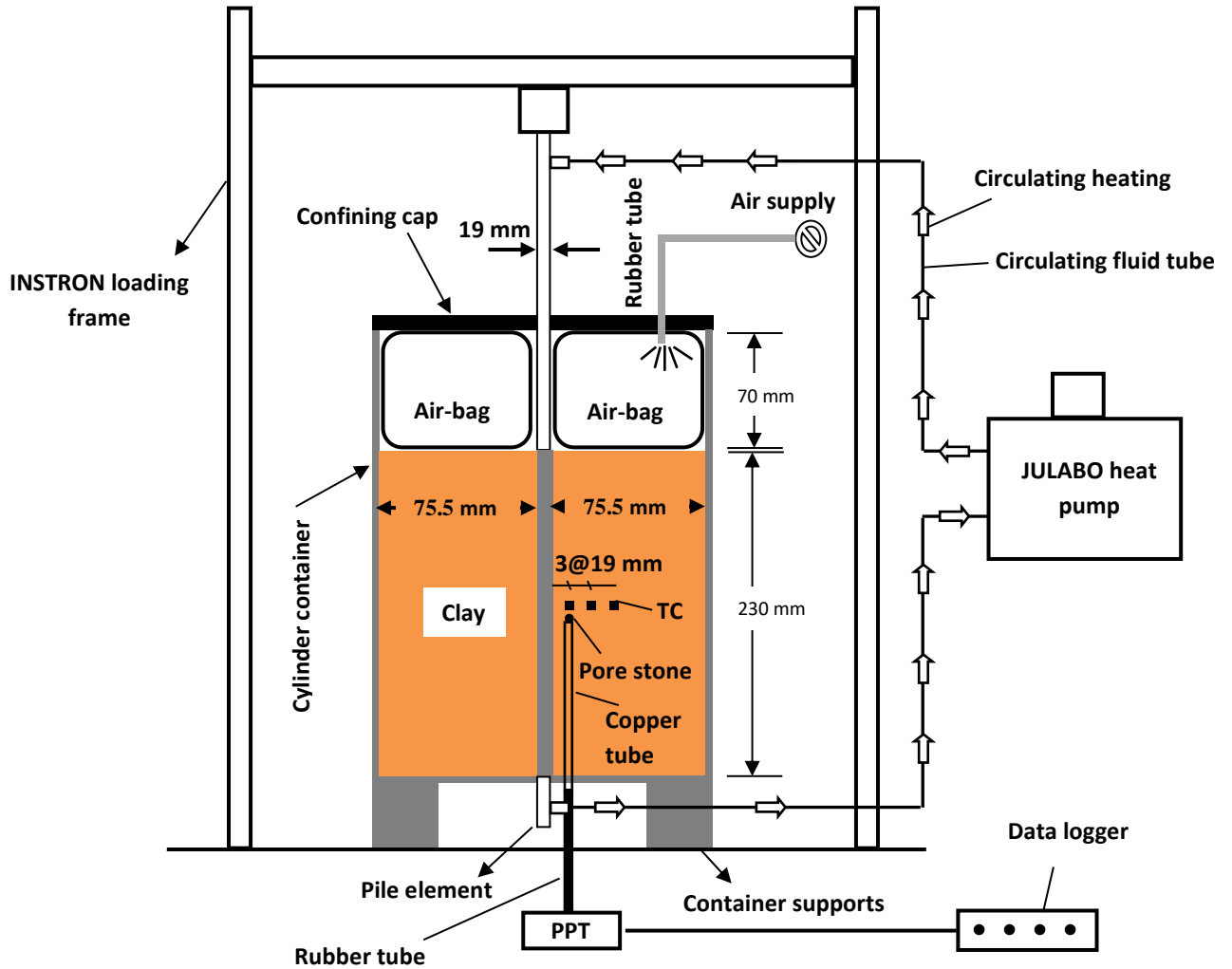
PPT: Pore Pressure Transducer
TC: Thermocouple

Figure 5-6- Schematic view of the experimental setup.

To minimize disturbance, only one point located at a distance of 1D away from the pile surface was chosen to measure the thermally induced pore water pressure (PWP) within the clay. However, no pore pressure transducer was directly placed in the clay to avoid any potential disturbances in

load transferring due to its size effect. Instead, a system to measure the PWP similar to that used in a triaxial cell was used in this setup. For this purpose, a brass pore stone having a cylindrical geometry (with ≈ 2.0 mm diameter and 5.0 mm height) was attached to the top of a copper tube (of outer/inner diameter 3.0 mm/1.5 mm) crossing the base and connected to an external pore pressure transducer through a flexible rubber tube, as shown in Figure 7. The whole measuring system was installed before pouring the kaolin slurry in the container, that as a result, the water drained through the pore stone during the slurry consolidation (Figure 9) could flow in the tubes and made them fully saturated, which is necessary to accurately measure excess PWP.

(a)   (b)
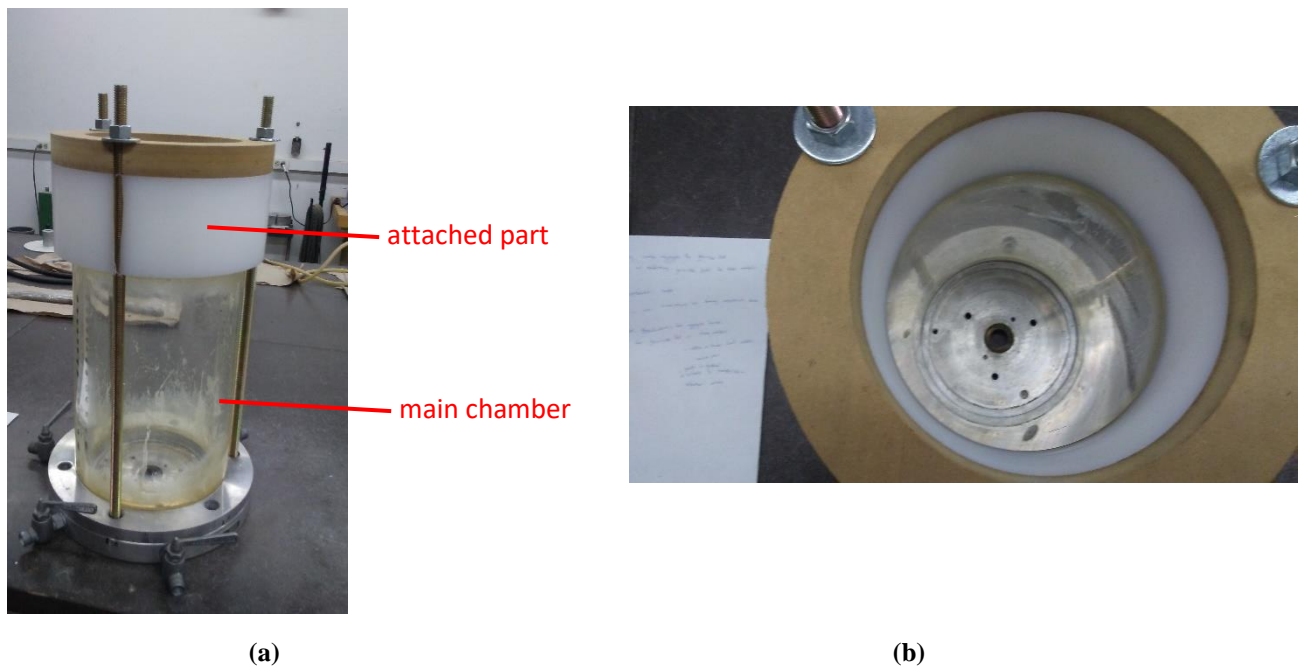
Figure 5-7- Soil container: (a) side view, and (b) plan view.

(a) **(b)**
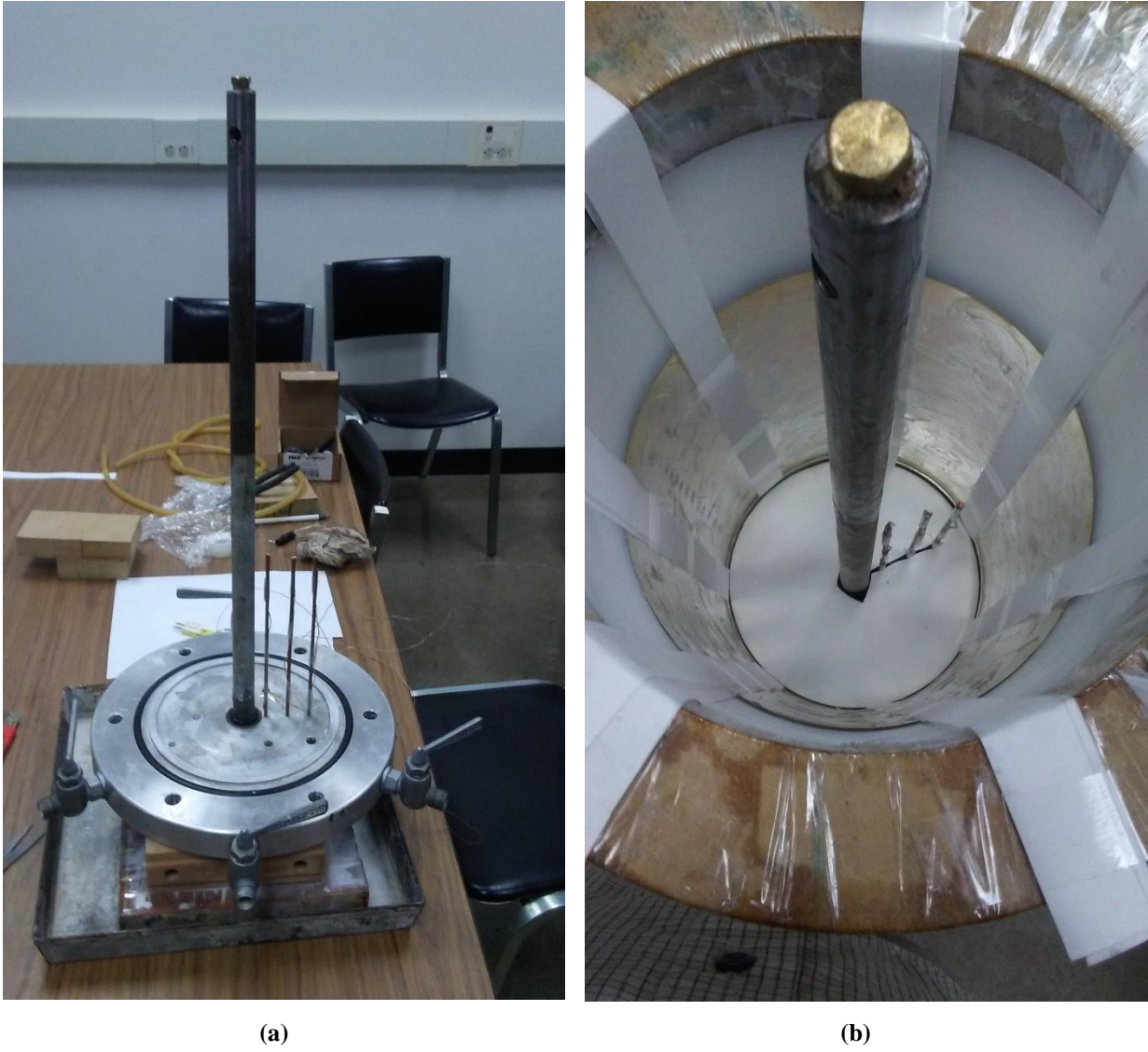
Figure 5-8- Thermocouple installation: (a) before and (b) after chamber installation.

5-5- Experimental procedures

The following is the step-by-step procedure adopted in all the tests. Figure 5-9 illustrates the procedure and corresponding pile surface temperature and surcharge load. For simplicity, the variation of surcharge load with time is assumed to be linear in the first step, as shown in Figure 5-9. As will be shown later, however, it is not completely linear. It should be noted that the tests were carried out in a temperature-controlled room at 24°C +/−0.5°C.

Step 1- Soil preparation

Step 2- Surcharge load application

Step 3- Thermal load application

Step 4- Pile load application
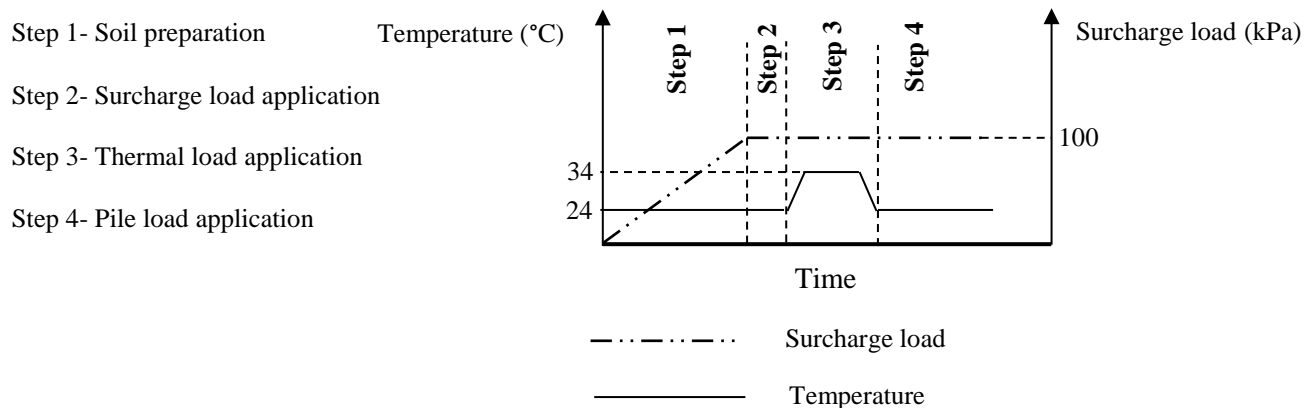
Figure 5-9- Experimental procedure.

Step 1- Soil Preparation:

Each test began with consolidating the clay slurry around the pile including applying load increment (ΔP) until the total consolidation pressure (P) reached 100 kPa. Each load increment (ΔP = 2.5 kPa, 2.5 kPa, 5 kPa, 10 kPa, 20 kPa, 40 kPa and 20 kPa) was maintained until the consolidation settlement rate under the applied pressure was insignificant. Figure 5-10 shows the relationship between the applied pressure, the corresponding consolidation settlement and time. Since the slurry consolidation involved significant settlement ($\approx$ 18 cm), a cylindrical extension was attached to the main container at the beginning of this step, as shown in Figure 5-7(a) and 5-11, and then was filled with the slurry. Drainage took place vertically through perforations in the top loading plate and the container base. Additionally, a series of uniformly spaced strips of filter paper were placed vertically on the inner wall of the container to facilitate radial consolidation. This effectively reduced the initially estimated consolidation time from 24 days to 13 days. Lubricant was also placed over the inner walls of the container to reduce friction between the clay and the container. The figure indicates that the total time duration required for slurry consolidation was 283 hours corresponding to a settlement of 180 mm.
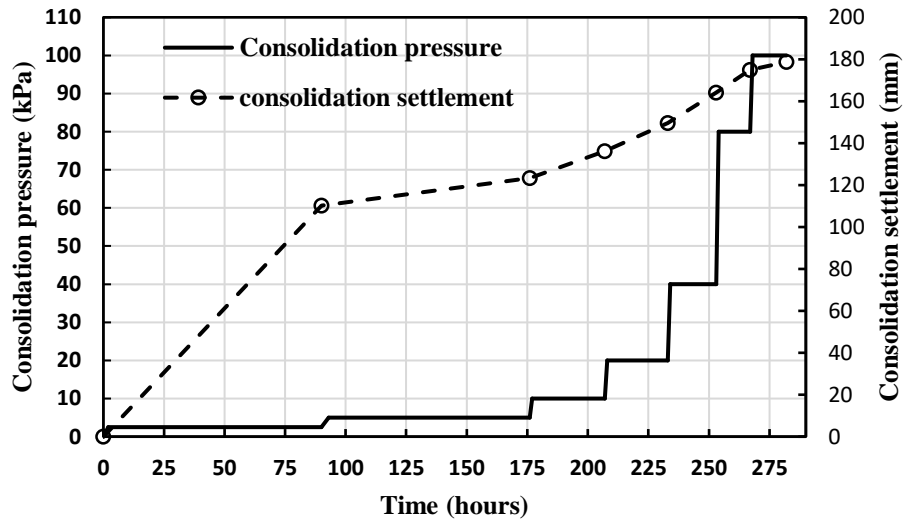
(a)
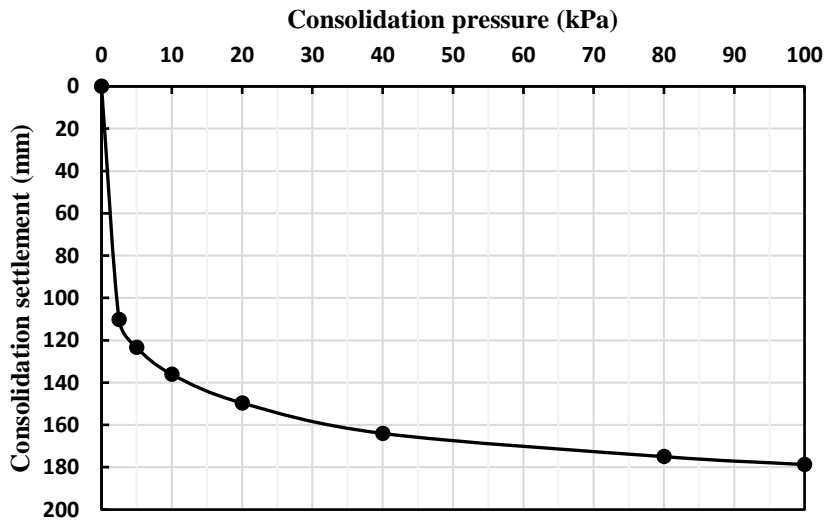
(b)

Figure 5-10- Consolidation process: (a) applied pressure and corresponding consolidation settlement versus time, and (b) consolidation settlement versus applied pressure.

The pile tip rests upon a rigid plate to avoid vertical movement due to the slurry consolidation, as shown in Figure 5-11.
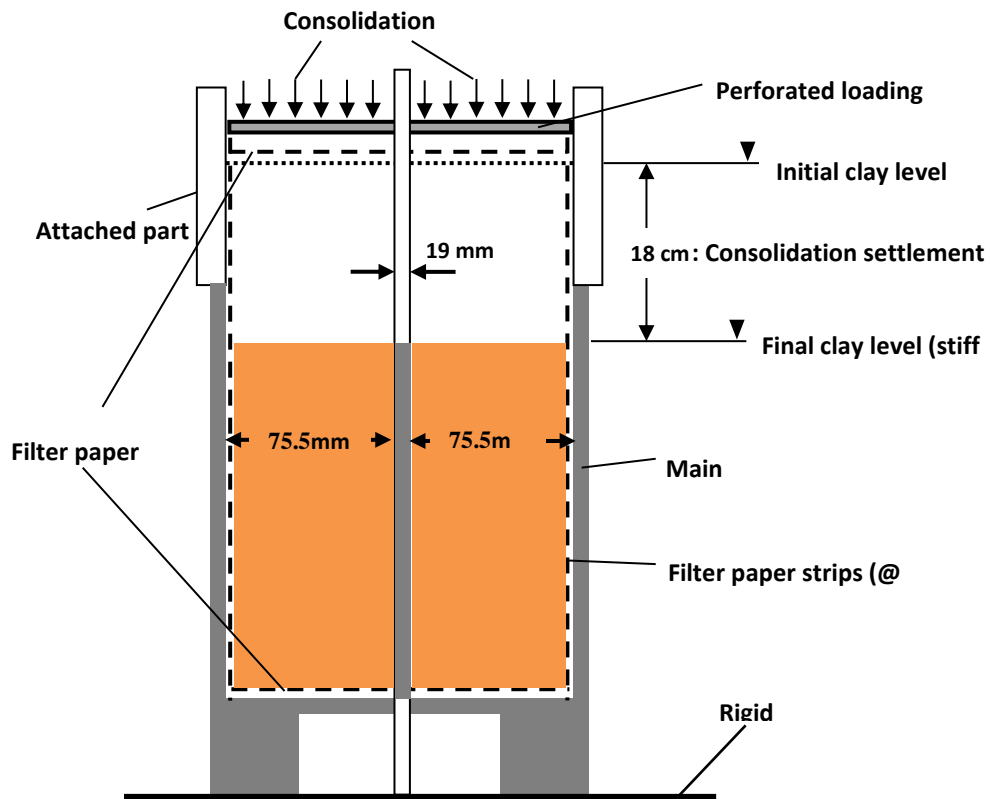
(a)
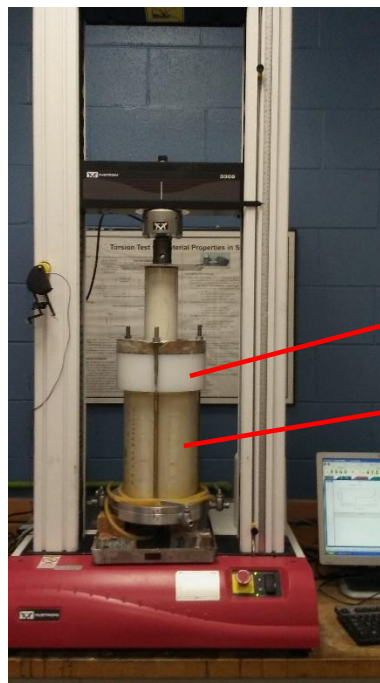
(b)

Figure 5-11- Assemblage of components utilized in the consolidation process: (a) Schematic view, and (b) actual.

Step 2-Surcharge load application:

Upon completion of primary consolidation, the cylindrical extension was removed, and an airbag was placed at the top of the clay. Air pressure was used to apply a constant and uniform 100-kPa pressure via the airbag. The applied pressure was kept for 17 hours to ensure complete dissipation of excess PWP. It should be noted that the PWP dissipation was confirmed by the measured PWP within the clay. The pile was also restricted from vertical movement during this stage by the presence of the rigid base at the pile tip.

Step 3-Thermal load application:

In this step the pile and the surrounding clay were subjected to non-cyclic and cyclic temperature variations by circulating temperature-controlled fluid inside the energy pile. The fluid circulation occurred through the two holes drilled at the top and bottom of the pile, as shown in Figure 5-6. The energy pile was constrained at the bottom end and free at the top so that it can expand and contract freely during thermal loading. This restraint condition may be applicable to an energy pile supporting a light building and resting on a stiff soil layer. One heating/cooling cycle (24-38-24 °C) consisted of increasing the fluid temperature from ≈24 °C (room temperature) to 38 °C (in 15 minutes), keeping the fluid at constant temperature of 38 °C (for 210 minutes), reducing temperature back to 24 °C (in 10 minutes), and finally keeping it constant for 50 minutes. The above thermal cycle was so chosen that the resulting temperature at the interface varied between 24 °C and 34 °C (24-34-24 °C). To do so, several calibration tests (prior to actual tests), in which both the fluid and the pile-clay interface temperature was measured simultaneously, were performed. The interface temperature was measured by mounting a thermocouple on the pile's surface. Figure 5-12 illustrates the results of the calibration tests during one heat cycle. As shown, the heating/cooling phases of each thermal cycle continued until the pile-clay interface reached a

steady state temperature (ΔT = ± 0.02 °C/min), without any control of the interface PWP distribution. On the other hand, non-cyclic heating consisted of heating the fluid from 24°C to 38°C (in 15 minutes) and keeping it at constant temperature of 38°C (for 210 minutes).
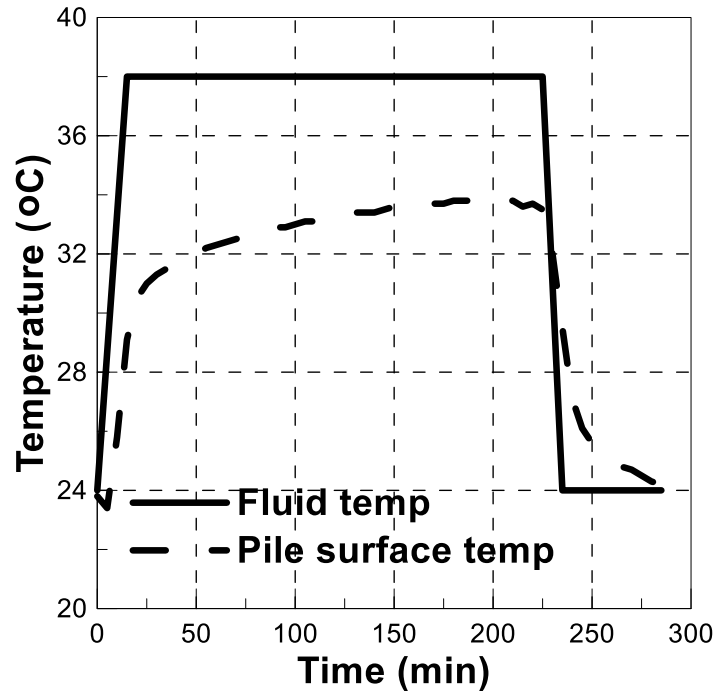
Figure 5-12- Variations of the fluid and the pile surface temperature.

In the actual tests, where no thermocouple was attached to the interface to avoid any possible disturbance in the side shear load transfer, it was assumed that the interface undergoes the same temperature variation under one heating/cooling cycle (as that one shown in Figure 5-12). This assumption is reasonable since both the actual and the calibration tests were carried out under the same thermo-mechanical conditions.

At the end of this step, the test set-up was left about 2 hours to ensure that the measured excess PWP in the clay stabilized before the shearing phase was initiated. The thermally induced PWP usually stabilized at negative value of ≈ -1 kPa, which can be called the thermally induced

permanent excess PWP. It should be noted that the induced excess PWP at the interface was not monitored during actual tests to prevent any potential disturbance in the mobilized shaft resistance.

Step 4-Pile load application:

Following the thermal loading step, the energy pile was subjected to a gradually increasing axial load. A constant strain rate of 0.25 mm/min was applied to the pile in accordance with ASTM D1143–81, until the pile head settlement reached 20 mm. The ultimate shaft resistance was then determined from the load-settlement curve.

5-6- Results

Five identical pile load tests were performed under different thermal loading conditions. Table 1 presents a summary of test conditions and results. In the following the induced temperature variations and excess PWP within the surrounding clay as well as the interface shearing resistance of the pile will be presented.

Table 5-1- Summary of pile load test results

Test	Thermal loading	R (mm/min)	T (°C)	P (N)	S (mm)	P-10%D (N)	RS (N)
1	24 °C	0.25	24 °C	55.4	1.9	55.4	50.5
2	34 °C	0.25	34 °C	108.7	2.1	107	81.6
3	(24 -34 -24 °C)-10 cycles	0.25	24 °C	82.46	1.65	81.47	51.6
4	(24 -34 -24 °C)-20 cycles	0.25	24 °C	78	1.96	76.9	57
5	(24 -34 -24 °C)-40 cycles	0.25	24 °C	82	1.6	79.25	49.4

R: rate of loading, **T**: temperature at which the pile is axially loaded, **P**: peak value of load-settlement curve, **S**: settlement corresponding to peak value of pile load, **P-10%D**: pile load value corresponding to settlement of 10%D (pile diameter), and **RS**: residual value of load-settlement curve

Temperature variations:

Figure 5-13 shows the measured temperature changes within the clay at the middle of the embedded pile length at two radial distances from the pile's surface (1D and 3D). The temperature

153

variations recorded at distance of 2D are not presented here because of some concerns about their validity. Unlike the interface temperature shown in Figure 5-12, the clay temperature didn't reach a steady-state condition during thermal loading. The surrounding clay also showed slightly lower temperature rise during the heating period compared to the interface temperature. A peak temperature of about 33 °C and 32 °C was measured during heating at distances of 1D and 3D, respectively. It is apparently a low radial temperature gradient implying that a large zone of the clay was radially influenced by the temperature variation imposed at the pile surface. This could be attributed to the large volume of heat exchange fluid (with respect to the pile volume) flowing inside the pile (that leads to large heat fluxes at the pile surface), and poor thermal conduction properties of the boundaries ($\approx$ 4D away from the pile). However, these thermal boundary conditions may not be representative for actual in-situ condition, where heat flux leaving the pile surface is possibly lower and the presence of material with very low thermal conductivity at a boundary 4D from the pile is unlikely. Therefore, the operation of real energy piles would cause the soil temperature to decrease more rapidly with increasing radial distance. Furthermore, the induced change in soil temperature around the energy pile is likely to be less due to lower values of heat flux along the pile surface.

It should be noted that transfer of heat within saturated soils generally occurs by conduction (through soil particles and quiescent pore fluid) and convection (through pore fluid flow). Convection, however, was assumed to be insignificant for the saturated clay used herein due to its low hydraulic conductivity ($k \approx 1.3 \times 10^{-9}$ m/s). The impact of thermocouples on the heat transfer within the clay was also expected to be minimal due to their very small dimensions (≈ 0.5 mm).
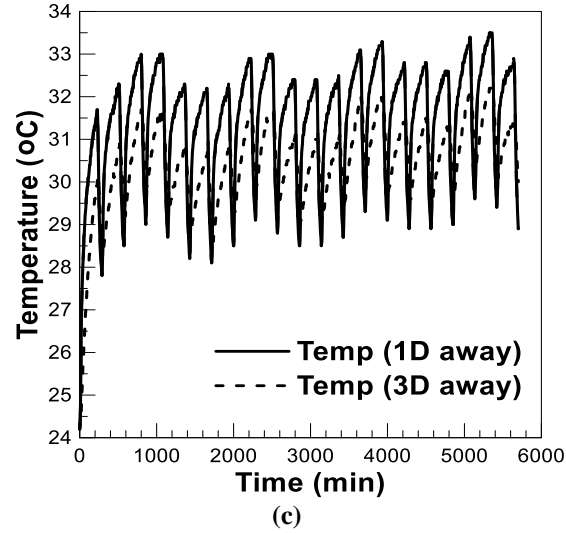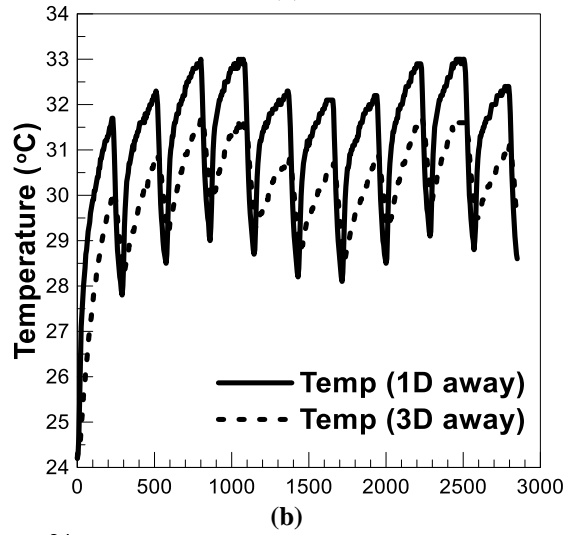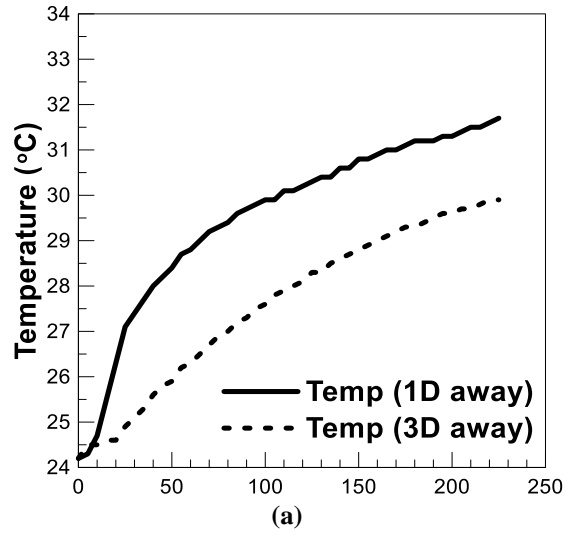
Figure 5-13- Variations of temperature within the clay (a) non-cyclic, (b) 10 cycles and (c) 20 cycles.

Thermally-induced excess pore water pressure:

The measured variation of thermally-induced PWP at distance of 1D is illustrated in Figure 5-14. As for non-cyclic heating, thermally induced PWP rose initially up to 2.6 kPa and was then fully dissipated by the end of heating period (PWP≈0). Regarding heat cycles, a rise/drop in PWP can be noted during heating/cooling phases. For instance, in the first heat cycle, a PWP increment of ≈ 3.5 kPa was observed because of temperature rise that generated a peak value of ≈ 3.5 kPa, followed by a gradual PWP decrease down to zero in the rest of heating phase. Upon cooling phase, a PWP drop of ≈ 5.5 kPa occurred leading to a total PWP value of ≈ -5.5 kPa. In the subsequent cycles, PWP raised by ≈ 6-7 kPa during heating phases resulting a negative value for PWP ($-0.5 \text{ kPa} < \text{PWP} < -1 \text{ kPa}$) at the end of each phase (except for the second cycle, where PWP is slightly larger than zero). During cooling phases, a decrease of ≈ 6.5 kPa can be noted in PWP in the subsequent cycles.

The smaller induced PWP rise in the first cycle (≈ 3.5 kPa) comparing to that in the subsequent cycles (≈ 6.5-7 kPa) could be linked to the temperature-induced clay contraction (thermal consolidation) occurring during the heat cycles. In fact, the majority of thermal consolidation occurs in the first cycle, while it is expected to be smaller in the subsequent heat cycles, as shown by Campanella and Mitchell 1968 [20] and Yazdani et al. 2018a [21]. This volumetric behavior of clay during thermal cycling is similar to its compression/swelling response to isotropic loading/unloading cycles (Campanella and Mitchell 1968 [20]). Thus, a lower porosity and permeability condition is achieved by the clay at the end of the first cycle. Upon temperature rise in the second cycle, higher heat-induced excess PWP is anticipated to develop in the clay (because of its lower porosity/permeability) relative to that in the first cycle. In the following cycles, however, an equivalent PWP increase is likely to occur as the thermal evolution of porosity tends
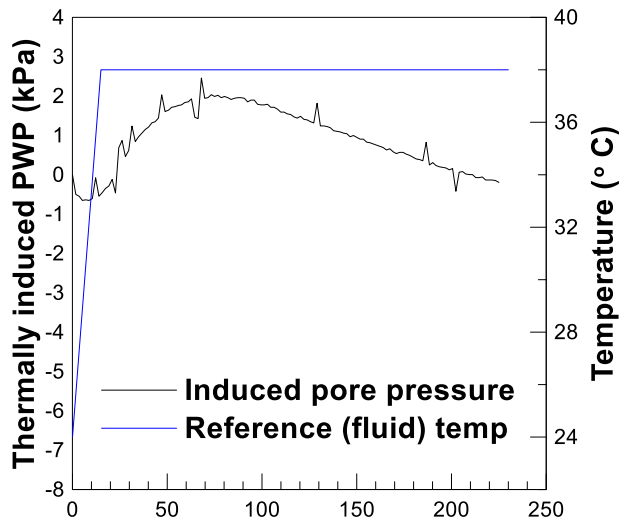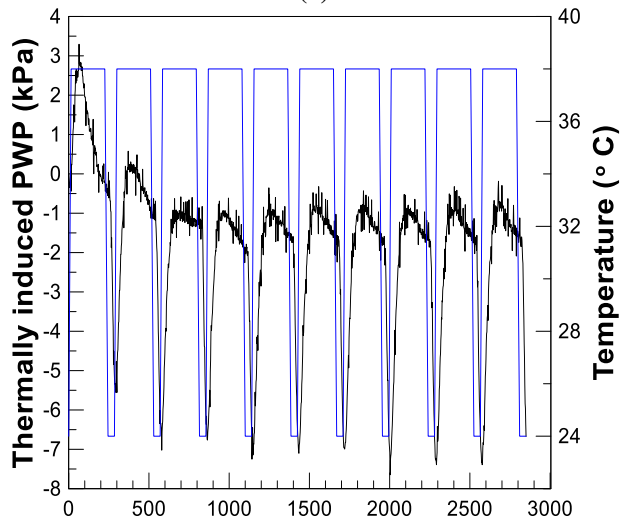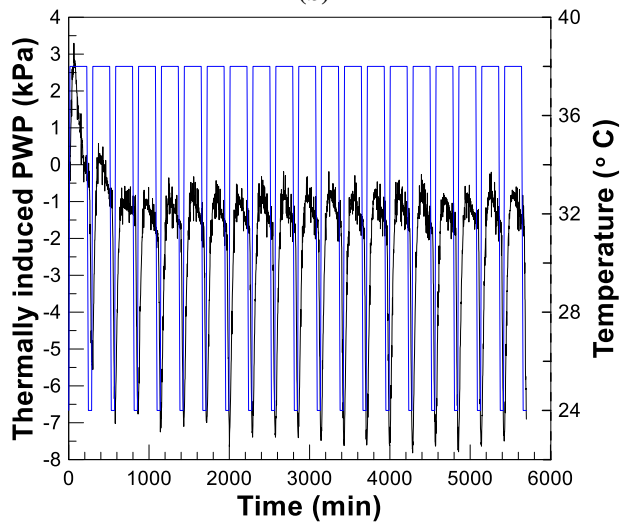
Figure 5-14- Thermally-induced pore water pressure in clay (1D from the pile surface-at the middle of pile length) (a) non-cyclic, (b) 10 cycles and (c) 20 cycles.

to be small (and equal), which is comparable to the clay volumetric behavior during isotropic loading/unloading cycles.

Figure 5-15 illustrates the thermal evolution of PWP during 10 heat cycles (shown in Figure 5-14b), with respect to temperature (Figure 5-15a) and heat cycle number (Figure 5-15b). The induced PWP shown in Figure 14b corresponds to the end of each cycle. From Figure 5-15a, it can be observed that except for the initial part of the first cycle, where some positive PWP was induced, the temperature variations mainly caused negative cumulative PWP throughout the thermal loading step. Figure 5-15b indicates that the induced PWP reached a stabilized value of ≈ -7 kPa at the end of the second cycle. The negative PWP is possibly related to the applied fast cooling, where the induced excess PWP was not allowed to fully dissipate. It should be noted that the magnitude of thermally induced PWP are mainly determined by the heating/cooling rate and the permeability/compressibility of the clay (Fuentes et al. (2016) [22]).

As mentioned earlier, PWP's variations at the pile surface were not measured to avoid possible disturbances in load transfer at the interface. It is anticipated, however, that relatively higher fluctuations in PWP may develop at the pile's surface as temperature variations are greater in this zone, which is evident in Figures 5-12 and 5-13. From Figure 5-12, it can be seen that the temperature variations at the pile's surface is $^{+}_{-}10\,℃$ during heating/cooling phases, while it is evaluated to be $^{+}_{-}5\,℃$ within the clay as shown in Figure 5-13.
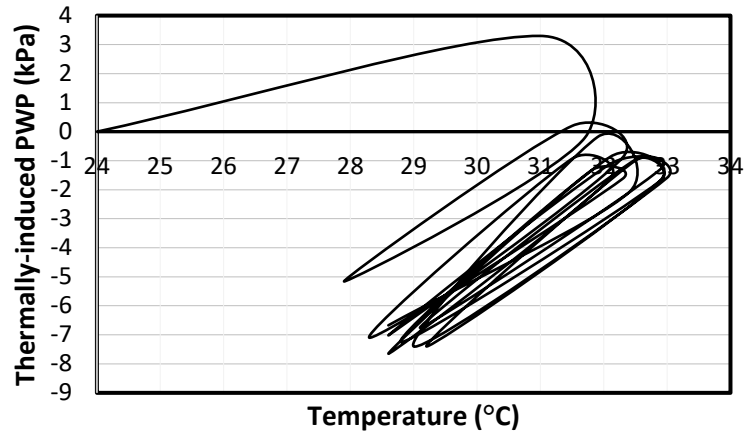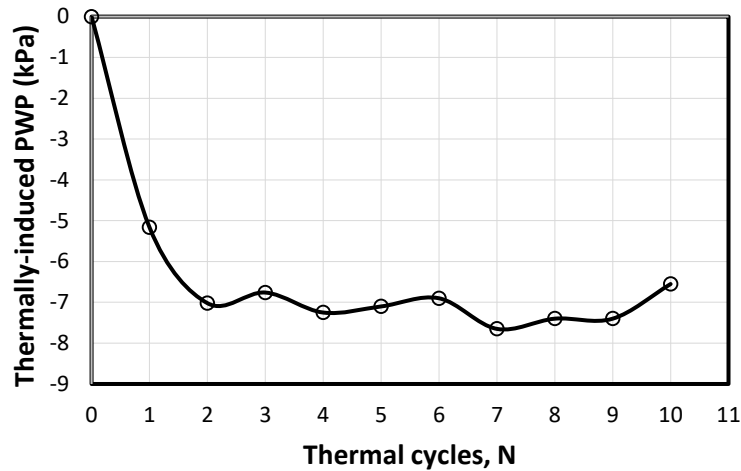
Figure 5-15- Thermally-induced PWP against (a) temperature, and (b) thermal cycles (temperature variation for a thermal cycle: 24-34-24 °C).

Load-settlement behavior:

Figure 5-16 shows the measured load-settlement curves for the pile under different thermal loading conditions. The peak value of the curves was used as the pile's axial resistance or the shaft resistance. A summary of the pile's shaft resistance obtained from Figure 5-16 has been presented in Table 5-1. The results indicate that the shaft resistance exhibited by the pile subjected to 10, 20 and 40 heat cycles was 48%, 44% and 48% larger than that of the reference pile, which was not

subjected to thermal loading, while non-cyclic heating caused 96% increase in the shaft resistance. Assuming negligible effect on the tip resistance, the finding above indicates that heating can improve the ultimate axial capacity. Therefore, the negative impacts of the heat-induced rise in axial load in the pile (Figures 5-1 to 5-3) may be fully compensated by the thermally improved ultimate axial capacity. However, additional studies measuring the heat-induced changes in both the pile axial capacity and pile axial load are required to validate such a conclusion.

Although cyclic and non-cyclic thermal loadings caused different shaft resistance, it can be noted from Figure 5-16 that the shaft resistance is nearly independent of the number of heating cycles as practically the same resistance rise was observed for different numbers of heat cycles. In addition, although the interface temperature was not measured during the actual tests, it is expected based on the calibration test results (Figure 5-12) that the pile loading occurred at an interface temperature of 24 °C after it was cyclically heated. That may explain their moderate shaft resistance that falls approximately in the middle between the shaft resistance of the control pile tested at a constant 24° C (without cycling) and the pile tested at a constant 34° C (without cycling). The results shown in Figure 5-16 are in good agreement with previous studies showing that pile temperature rise improves the ultimate frictional resistance mobilized between energy piles and clay (Di Donna et al. 2016 [23]), and sand (Wang et al. 2015 [24]). However, using a parametric study, Fuentes et al. 2016 [22] showed that the short-term shaft resistance of energy piles, in low permeability ($k \leq 1 \times 10^{-11}$ m/s) and low compressibility ($k_s \geq 20$ GPa) clays, can substantially reduce because of the large heat-induced excess PWP and the resulting low effective contact pressure at the interface.
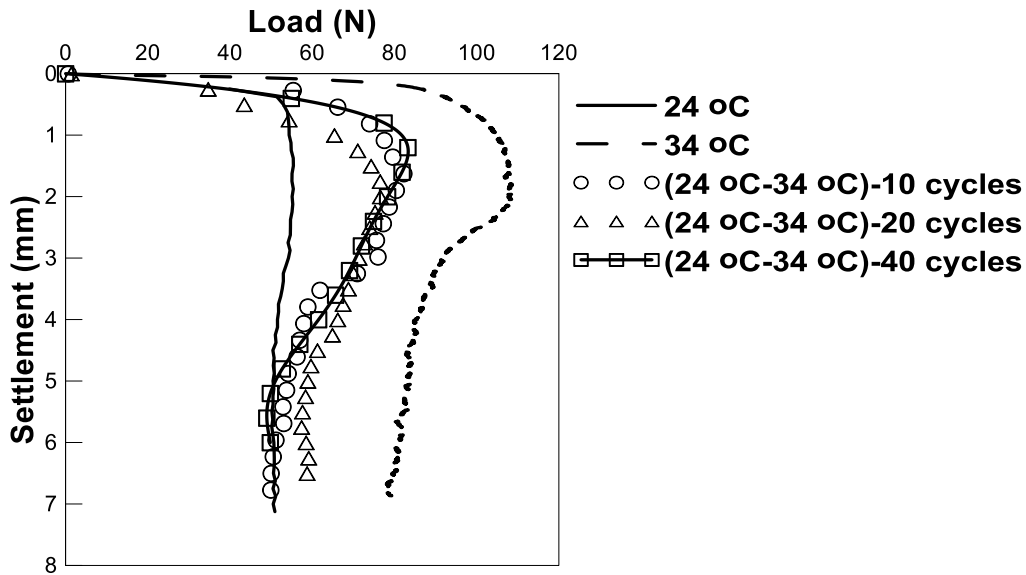
Figure 5-16- Load-settlement curves for the model energy pile under different thermal loading paths.

The pile's ultimate load capacity (=shaft resistance for the piles tested herein) may be assessed using settlement-based criteria, where the ultimate load is defined as the load corresponding to 10% relative displacement (ω_r), which is equal to the ratio of the pile head settlement (ω) to the pile diameter (D):

$$\omega_r = \frac{\omega}{D} \qquad\qquad (5-1)$$

Table 1 shows the estimated shaft resistance based on the 10% relative settlement criterion, which are the loads corresponding to the settlement of 1.9 mm (D=19 mm). It can be noted from Table 5-1 that the settlement at which the peak of the load-settlement curve occurred was almost equal to 10% of pile diameter. This indicates that the two criteria (the settlement-based and peak value criteria) can be used interchangeably for estimating the shaft resistance of the model energy pile. Figure 5-17 shows a comparison of the two criteria.

161
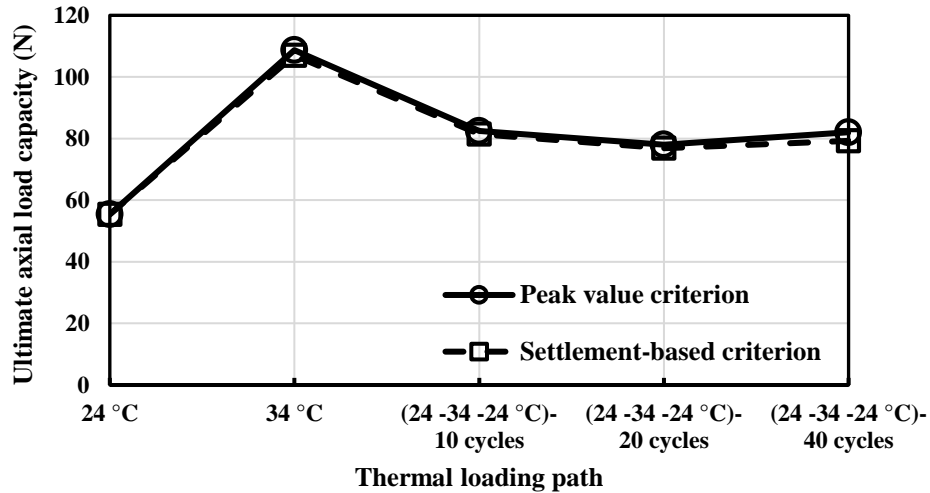
Figure 5-17- Ultimate axial load capacity (shaft resistance in this study) estimated using two different criteria (data from Table 5-1).

Lastly, two important factors that may impact the load-settlement curves are considered. The first factor is the negative skin friction that may develop at the interface in steps 1 and 2 due to downward movement of the surrounding clay relative to the pile. It may underestimate the total shaft capacity evaluated in Figure 5-16. However, the negative skin friction induced during the step 1 is expected to disappear completely at the end of the step due to unloading. In step 2, where the clay previously reconstituted at 100 kPa is vertically reconsolidated at the same pressure, limited negative friction is likely to mobilize. It can be explained by this fact that further consolidation settlement is not expected to occur due to surcharge applied (100 kPa) as the clay is formerly fully consolidated under 100 kPa (Abdrabbo and Ali 2015 [25], and El-Mossallamy et al. 2013 [26]). Therefore, it can be assumed that the total force acting down is only equal to the shearing resistance mobilized during the fourth step (pile loading) and the influence of negative friction is insignificant.

The second factor is the size of the sensors installed in the clay that may disturb the side shear stresses. However, their impact on the measured shaft resistance is actually negligible due to their

small size and relatively large distances from the pile's surface. In fact, the interface shearing behavior is determined by a shear zone formed near the pile surface, where strain localization or large relative motion of soil particles occur (Uesugi et al. 1988 [27]). The thickness of the shear zone along the pile-sand interface is generally $5D_{50}$ (D_{50}: the average diameter of sand particles) that may be used to approximately determine the shear zone's thickness formed along the pile-clay interface ($\approx 5 \times 0.0025$ mm$=0.0125$ mm). Therefore, considering the distance of embedded sensors from the pile surface ($\geq 1D_{pile}=19$ mm) any important disturbance in the shear zone, approximately formed at 0.0125 mm from the pile surface, and the mobilized shear resistance is unlikely.

Initial stiffness of shaft resistance:

Table 5-2 shows that heating increased the initial stiffness of shaft resistance, which is defined as the initial slope of the load-settlement curves in Figure 5-16. The table indicates that the initial stiffness increased as the temperature increased from 24 to 34° C (without thermal cycling). The thermal cycles also caused a significant increase in the initial stiffness. This was a moderate increase falling between the increase caused by non-cyclic heating (loading at 34 ˚C) and the reference test carried out at 24 ˚C as shown in Table 5-2.

Table 5-2- Effects of heating on the initial shaft resistance stiffness

Thermal loading	Initial stiffness (N/mm)
24 °C	159.5
34 °C	565.7
(24 °C-34 °C)-10 cycles	380.5
(24 °C-34 °C)-20 cycles	326.3
(24 °C-34 °C)-40 cycles	368.4

5-7- Discussion

Any possible explanation for the pile response to temperature variations (observed in Figure 15) should be discussed in terms of the thermally-induced changes in the shaft resistance. In addition to total stress analysis (α method) the unit shaft resistance can be calculated using effective stress analysis, Equation (2) and (3) (Salgado 2006 [28]).

$$q_{us} = \sigma_h' \tan \delta \qquad\qquad (5-2)$$

$$\sigma_h' = K\sigma_V' \qquad\qquad (5-3)$$

Where, δ is friction angle of pile-soil interface, σ_h' is lateral effective stress, K is lateral earth pressure coefficient at pile-clay interface, and σ_V' is vertical effective stress. δ is generally influenced by the pile surface roughness, the soil particle size and the soil strength properties. According to Equation (5-2), the increase in the long-term shaft resistance observed in Figure 5-16 can be attributed to: (1) the thermal enhancement of the pile-clay interface friction angle δ, and/or (2) the increase of effective stress at the interface. Results of a recent experimental study performed by the authors using a temperature controlled direct shear test indicate that thermal loading causes a moderate increase in the interface shear strength as shown in Figure 5-18 (Yazdani et al. 2018b [29]). The figure indicates that thermal loading causes approximately 10% increase in the interface shear strength that will positively contribute to the shaft resistance.
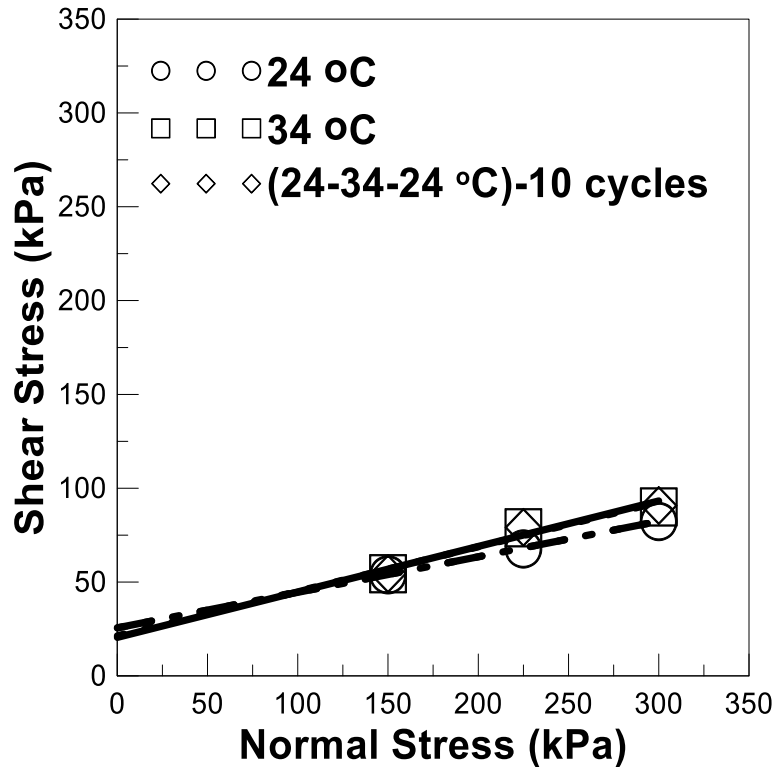
Figure 5-18- Interface strength of clay-concrete interface estimated by modified temperature controlled direct shear test device (Yazdani et al. 2018b [28]).

On the other hand, although the induced negative PWP in the clay reaches a stable condition before the pile loading step, the induced negative PWP at the pile's surface may not be fully dissipated even after the pile loading has initiated, due to potentially larger magnitude than that in the clay (Figure 5-14 and 15). Consequently, an increase in effective stresses at the pile-clay interface occurs that causes a positive contribution to the shaft resistance. This can be illustrated through a numerical example. Using Jaky's equation 1948 [30] ($K_0 = 1 - \sin\phi'$), K_0 is estimated as 0.59 for the clay (ϕ' is estimated as 24.5° from CD triaxial tests (Yazdani et al. (2018a) [31]). Assuming that the stress state at the pile-clay interface is at rest condition during pile loading, the effective lateral pressure on the pile is estimated to be 59 kPa ($\sigma'_v = 100$ kPa) before heat cycles are applied. If the negative PWP developed at the pile's surface is approximately equal to that generated in the

clay at 1D ($\approx$ -8 kPa, Figure 5-14), then greater lateral effective stress will act on the pile's surface after it has been subjected to heat cycles [$\sigma_h' \approx 59 \text{ kPa} - (-8 \text{ kPa}) = 67 \text{ kPa}$], assuming that the total contact pressure remains constant. This causes 14% increase in the shaft resistance according to Equation (5-2). As mentioned earlier, greater negative PWP is, however, likely to develop at the pile-clay interface because of the greater temperature fluctuations, thus producing greater rise in the lateral effective stress and the shaft resistance.

It may be argued that the contact pressure can also increase due to radial restriction on the thermal expansion of the clay by the container boundaries, thus resulting in an increase in the total shaft resistance. It is generally known, however, that saturated NC clays show a contractive response during heating, which contrasts with the classical expansive behavior of other porous material subjected to heating. In fact, although both clay particles and pore water undergo thermal expansion, the excess PWP induced due to discrepancy in their thermal expansion coefficients produces reduction in porosity if drainage is allowed, thus causing a decrease in volume (Baldi et al. 1988 [31]; Campanella and Mitchell 1968 [20]; Burghignoli et al. 2011 [32]). In the present study, since drainage was permitted through some holes in the container's base a contractive behavior is expected to occur. Nevertheless, under the assumption that a pure expansive behavior is presented by the saturated clay, the total estimated radial expansion with a 10 °C temperature rise is ≈ 0.1 mm (considering $\alpha_{kaolin} = 3.5 \times 10^{-5} \frac{1}{C°}$, $\alpha_{pore\ water} = 2.1 \times 10^{-4} \frac{1}{C°}$ and a uniform porosity (n) of 0.48 in the clay), which is clearly negligible.

Another possible explanation for the rise in the shaft resistance could be associated with the thermal radial expansion of the pile. In fact, it causes radial deformation in the surrounding clay generating further stiffening in the radial direction, or/and increased lateral pressure at the interface if the pile expansion is constrained by a hard clay. Both scenarios may result in larger frictional

resistance at the interface. However, the following simple analysis would conclude that the thermal radial expansion of the pile has negligible effect on the shaft resistance, obviously due to its ignorable magnitudes. For simplicity, it is assumed that the thermal expansion behavior is controlled by the thermal properties of the steel shaft, as the cross-sectional area of the concrete coating is less than 20% of the whole solid part of the tube (Figure 5-5). Considering $\alpha_{steel} = 15 \times 10^{-6} \frac{1}{C°}$, the radial expansion of the model pile due to temperature rise of 10 °C is estimated to be 0.001425 mm ($= 15 \times 10^{-6} \frac{1}{C°} \times 10°C \times 19/2$ mm), which is equal to a radial strain of 0.015%. Obviously, this thermal deformation cannot produce important stiffening within the clay. On the other hand, the lateral pressure is not expected to increase since the surrounding clay is characterized as a soft clay due to its low undrained compressive strength (24 kPa). A similar analysis can be applied to a real concrete energy pile having solid circular cross section: Considering $\alpha_{concrete} = 10 \times 10^{-6} \frac{1}{C°}$ and $D_{pile} = 1 \, m$, the heat-induced radial deformation in the pile due to temperature rise of 10°C is estimated to be 0.005 cm that is unlikely to affect the shaft resistance existing at the interface. With respect to heat-induced axial deformation, both the tube (in this study) and the solid cylinder (a real energy pile) also demonstrate similar behavior. In other words, a heat-induced relative axial motion between their outer surface and the surrounding clay is expected due to presenting different thermal expansion coefficients compared to clay. It, in turn, may cause interface strength degradation in both cases.

In summary, the increased shaft resistance shown in Figure 5-16 may be explained through increases in the interface friction angle and the effective lateral stress due to thermally induced negative PWP. Further research is needed to better quantify the thermo-mechanical behavior of shaft resistance, perhaps by placing several miniature pore pressure transducers at the soil-pile interface to measure thermally-induced PWPs.

5-8- Conclusions:

In this study, the effect of thermal loading on the shaft resistance of a concrete energy pile embedded in soft Kaolin clay was investigated via a lab scale model. The model energy pile was a subsection of a concrete energy pile allowed to move freely without end bearing. Five pile load tests were performed in undrained conditions after the piles were subjected to various types of thermal loading with temperatures ranging from 24°C to 34°C. The testing approach and the results offer a good insight into the changes in the shaft resistance due to thermal loading, although there are some limitations related to the effects of scaling and boundary conditions. These limitations are primarily due to the fact that in-situ stress/strain condition cannot be perfectly re-produced in the lab. Based on the observed results, the following conclusions can be made:

- Heating phase of the first thermal cycle resulted in generation of excess PWP in the surrounding clay. In the subsequent cycles, however, PWP stayed below zero even during heating periods and relatively large negative pore pressure was developed during cooling periods. As for non-cyclic heating, PWP increased in the beginning of the heating period and then gradually decreased approaching zero at the end of the heating period.

- Significant increase in the shaft resistance was caused by thermal loading. The increase was more pronounced when the pile was loaded at a constant temperature of 34°C (w/o cycling).

- Effective stress analysis (β method) was employed to explain test results. Thermally-induced improvements of interface friction angle (δ) and effective lateral stress (σ_h') are potentially responsible for the shaft resistance enhancement.

- The results showed a clear increase in the initial stiffness of shaft resistance with temperature increase.

168

Acknowledgment

The data presented in this chapter is based on the recent work, titled "Investigation of thermal loading effects on the shaft resistance of energy pile using laboratory scale model", published at the Journal of Geotechnical and Geo-environmental Engineering [33].

References:

[1] Laloui, L., and Nuth, M. (2006). Numerical Modeling of Some Features of Heat Exchanger Pile. *ASCE Geotechnical Special Publication: Foundation analysis and design-Innovative methods*, 189-194.

[2] Laloui, L., Nuth, M., and Vulliet, L. (2006). Experimental and numerical investigations of the behavior of a heat exchanger pile. *International Journal for Numerical and Analytical Methods in Geomechanics*, 30(8), 763–81.

[3] Brandl, H. (2006). Energy foundations and other thermo-active ground structures. *Geotechnique*, 56(2), 81-122.

[4] Bourne-Webb, P.J., Amatya, B., Soga, K., Amis, T., Davidson, C., and Payne, P. (2009). Energy Pile Test at Lambeth College, London: Geotechnical and Thermodynamic Aspects of Pile Response to Heat Cycles. *Géotechnique*, 59(3), 237–48.

[5] Laloui, L. (2011). In-situ testing of heat exchanger pile. *Proceeding of the GeoFrontiers 2011*, Dallas, Texas, CD-ROM.

[6] Amatya, B. L., Soga, K., Bourne-Webb, P. J., Amis, T., and Laloui, L. (2012). Thermo-mechanical behavior of energy piles. *Geotechnique*, 62(6), 503–519.

[7] Bouazza, A., Singh, R. M., Wang, B., Barry-Macaulay, D., Haberfield, C., Chapman, G., Baycan, S., and Carden, Y. (2011). Harnessing on site renewable energy through pile foundations. *Australian Geomechanics Journal*, 46(4), 79–90.

[8] Wang, B., Bouazza, A., Haberfield, C. (2011). Preliminary observations from laboratory scale model geothermal pile subjected to thermo-mechanical loading. *Geo-Frontiers 2011 advances in geotechnical engineering*, 430-439.

[9] McCartney, J. S., and Murphy, K. D. (2012). Strain distributions in full scale energy foundations. *DFI J.*, 6(2), 28–36.

[10] McCartney, J. S., and Rosenberg, J. E. (2011). Impact of heat exchange on side shear in thermos-active foundations. *GeoFrontiers 2011 (GSP 211)*. J.Han and D.E. Alzamora, eds. ASCE, Reston VA. 488-498.

[11] Stewart, M. A., and McCartney, J. S. (2014). Centrifuge modeling of soil-structure interaction in energy foundations. *ASCE Journal of Geotechnical and Geoenvironmental Engineering*, 140(4), 1-11.

[12] Ng, C.W.W., Shi, C., Gunawan, A., and Laloui, L. (2014). Centrifuge modeling of energy piles subjected to heating and cooling cycles in clay. *Geotechnique Letters*, 4, 310–316.

[13] Goode, J.C., III and McCartney, J.S. (2015). Centrifuge modeling of boundary restraint effects in energy foundations. *Journal of Geotechnical and Geoenvironmental Engineering,* 141(8), 04015034. DOI: 10.1061/(ASCE)GT.1943-5606.0001333.

[14] Ghaaowd, I. and McCartney, J.S. (2018). Centrifuge modeling of temperature effects on the pullout capacity of energy piles in clay. *DFI 43rd Annual Conference on Deep Foundations*, Anaheim, CA., Oct 24-27. 1-7.

[15] Ghaaowd, I., McCartney, J.S., Huang, X., Saboya, F., and Tibana, S. (2018). Issues with centrifuge modeling of energy piles in soft clays. *Proceedings of the 9th International Conference on Physical Modeling in Geotechnics: Physical Modelling in Geotechnics*. A. McNamara et al., eds. Taylor & Francis Group, London, 1365-1370.

[16] Wang, B., et al. (2012). Field and laboratory investigation of a heat exchanger pile. *Proc., GeoCongress 2012 (GSP 225)*, R. D. Hryciw, A. Athanasopoulos-Zekkos, and N. Yesiller, eds., ASCE, Reston, VA, 4396–4405.

[17] Kalantidou, A., Tang, AM., Pereira, J.M., and Hassen, G. (2012). Preliminary study on the mechanical behavior of heat exchanger pile in physical model. *Geotechnique*, 62(11), 1047–1051.

[18] Yavari, N., Tang, A. Minh., Pereira, J.M., Hassen, Ghazi. (2014). Experimental study on the mechanical behavior of a heat exchanger pile using physical modeling. *Acta Geotechnica*, 9, 385–398.

[19] Bourne-Webb, P. J., Amatya, B. L., and Soga, K. (2012). A framework for understanding energy pile behavior. *Proceedings of the Institution of Civil Engineers*, 166, 170-177.

[20] Campanella, R.G., and Mitchell, J.K. (1968). Influence of temperature variations on soil behavior, *Journal of Geotechnical Engineering-Division-ASCE*, 94(3), 709–734.

[21] Yazdani, S., Helwany, S., and Olgun, O. (2018a). Experimental evaluation of shear strength of Kaolin Clay under Cyclic and Non-Cyclic Thermal Loading. *Geotechnical Testing Journal*, https://doi.org/10.1520/GTJ20180020.

[22] Fuentes, R., Pinyol, N., and Alonso, E. (2016). Effect of temperature induced excess porewater pressures on the shaft bearing capacity of geothermal piles. *Geomechanics for Energy and the Environment,* 8, 30-37.

[23] Di Donna, A., Ferrari, A., Laloui, L. (2016). Experimental investigation of the soil concrete interface: physical mechanisms, cyclic mobilization and behavior at different temperatures. *Canadian Geotechnical Journal,* 43(4), 659-672.

[24] Wang, B., Bouazza, A., Singh, R.M., Haberfield, C., Barry-Macaulay, D., Baycan, S. (2015). Posttemperature effects on shaft capacity of a full-scale geothermal energy pile. *J Geotech Geoenviron Eng*., 141(4), 1–12.

[25] Abdrabbo, F. M., and Ali, N. A. (2015). Behaviour of single pile in consolidating soil. *Alexandria Engineering Journal*, 54, 481–495.

[26] El-Mossallamy, Y.M., Hefny, A.M., Demerdash, M.A., and Morsy, M.S. (2013). Numerical analysis of negative skin friction on piles in soft clay. *HBRC Journal*, 9, 68–76.

[27] Uesugi, M., Kishida, H., and Tsubakihara, Y., (1988). Behavior of sand particles in sand–steel friction. *Soils and Foundations*, 28(1), 107–118.

[28] Salgado R. (2007). The Engineering of Foundations. McGraw. Hill.

[29] Yazdani, S., Helwany, S., and Olgun, O. (2018b). Influence of Temperature on Soil-Pile Interface Shear Strength. *Geomechanics for Energy and the Environment,* 18, 69-78.

[30] Jaky, J. (1948). Pressure in silos. *2nd ICSMFE*, London, 1, 103-107.

[31] Baldi, G., Hueckel, T., and Pellegrini, R. (1988). Thermal volume changes of the mineral–water system in low-porosity clay soils, *Canadian Geotechnical Journal*, 25, 807–825.

[32] Burghignoli, A., Desideri, A., and Miliziano, S. (2011). A laboratory study on the thermo-mechanical behavior of clayey soils, *Canadian Geotechnical Journal*, 37, 764-780.

[33] Yazdani, S., Helwany, S., and Olgun, O. (2019). Investigation of thermal loading effects on the shaft resistance of energy pile using laboratory scale model. *Journal of Geotechnical and Geoenvironmental Engineering*, 10.1061/(ASCE)GT.1943-5606.0002088

Chapter 6

Mechanisms Contributing to the Improved

Shaft Resistance Observed in Chapters 4 and

5

6-1-   Introduction

This section aims to will provide a qualitative/quantitative explanation of the observed increase in the unit shaft resistance observed in chapters 4 and 5. The outcomes of chapters 3-5 will be qualitatively/quantitatively synthesized and discussed using different analysis approach (than that used in each individual chapter) to better understand the mechanisms contributing to the enhanced unit shaft resistance.

The key assumption underlying this study is that the thermo-mechanical behavior of clay under consolidated drained (CD) condition, found in chapter 3, describes the thermo-mechanical behavior of clay in the vicinity of interface. This assumption is reasonable as all the tests (chapters 3-5) were conducted at similar mechanical/thermal conditions using the same clay specimen. Throughout this section, long-term shaft resistance refers to the interface strength at steady-state condition, under which the induced pore water pressure (PWP) and temperature at the pile-soil interface (due to energy pile operation) is entirely dissipated (or stabilized). Short-term shaft resistance, on the other hand, refers to the interface strength at transient state, under which the heat-induced PWP and temperature at the pile-soil interface is not fully dissipated.

Before analyzing the data from previous chapters, findings from available literature about the temperature influences on the soil strength and shaft resistance will again be presented.

Using a modified direct shear test device with capability of thermal loading application, Xiao et al. (2014) reported that silt demonstrates a thermal-strengthening response due heat application [1]. On the other hand, Yavari et al. (2016) found that the effect of temperature on shearing strength of clay/sand is minor [2]. Based on the results of direct shear tests performed under constant normal load (CNL) condition, Maghsoodi et al. (2018) showed that NC clay cohesion increases with temperature, while the effects of temperature on internal friction angle was found to be minor [21].

174

Yazdani et al. (2018a) indicated that cyclic heating-cooling and elevated temperature increase peak drained shear strength of NC clay, while the drained shear strength of OC clay decreases with temperature [41].

Temperature controlled direct shear test device has also been used to assess thermo-mechanical behavior of interface. For instance, Xiao et al. (2014) [1] showed that compacted silty soil-concrete interface presents thermal strengthening (up to 15%). Di Donna et al. (2016) [5] observed an increase in shear strength of clay-concrete interface at elevated temperatures (20°C, 50°C and 60°C), while a temperature-independent shearing behavior for sand-concrete interface was noted. Yavari et al. (2016) [2] reported that shearing response of soil-concrete interface is nearly independent of elevated temperature (5°C, 20°C, and 40°C). Maghsoodi et al. (2018) [3] showed that NC clay-concrete interface sheared under both constant normal load (CNL) and constant normal stiffness (CNS) conditions shows higher shear strength at elevated temperature, possibly due to thermal consolidation of clay. Yazdani et al. (2019) reported that NC clay-conerete interface shows thermal strengthening, while OC clay-concrete interface shows thermal softening [6].

Centrifuge modeling test able to apply thermal loading is another effective approach that has been used for characterizing base/shaft resistance at non-isothermal condition. For instance, McCartney and Rosenberg (2011) [7] showed that heat cycles can improve the total loading and shaft capacities of energy piles in compacted silt, possibly due to the greater lateral pressure generated on pile surface. Under different restrained boundary condition, Goode III and McCartney (2015) showed that ultimate bearing capacity of centrifuge-scale semi-floating energy piles in unsaturated silt increases at elevated tempretures, while the temperature effects on ultimate bearng capacity are minor for those embedded in dry sand [8]. They, however, observed that ultimate bearing capacity of end-bearing piles presents temperature independency. Ng et al. (2015) reported that

both shaft and base resistances of centrifuge model pile in saturated sand are improved at elevated temperature [9]. Significant temperature-induced increase in pull-out capacity of centrifuge model pile (in NC clay) was observed by Ghaaowd and McCartney (2018) [10].

1-g laboratory pile test has also been employed by some researchers to study the temperature effects on soil-concrete interface. Wang et al. (2011) [11] reported that the pile shaft resistance (in silica sand) tends to insignificantly decrease because of temperature increase (up to 40°C). Wang et al. (2016) indicated that shaft resistance of energy piles can be influenced by heat exchange operation as the contact pressure at interface increases/decreases, respectively, during heating and cooling [12]. Yazdani et al. (2019) reported that NC clay-concrete interface significantly increases under both cyclic and non-cyclic heating [43].

Furthermore, the results of a series of borehole shear test conduced by Murphy and McCartney (2014) indicated that concrete-clay interface sheared at elevated temperatures shows greater strength comparing to that sheared at isothermal condition [9]. The results of full-scale tests on energy piles (in sand and silt) shows that heating improves ultimate bearing capacity ([14] & [15]). The findings of the above-mentioned small/full scale tests on thermal behavior of soil-concrete interface reveal that heating causes interface strengthening. Note that most of the studies reviewed above reported that the interface shearing (or pile loading) occurred after steay state temperature and PWP distribution was achieved at the interface, meaning that the measured interface strength was equivalent to the loang-term shaft resistance, as mentioned previously. Since the mentioned studies This strengthening is clearer in soils with low permeability such as saturated/unsaturated clay and silt. It has been reported that the induced strengthening is likely attributed to one or a combination of the following mechanisms: heat- induced increase in contact stress at the interface, thermal stiffening (consolidation) of the surrounding saturated soil or moisture migration away

from the interface in the case of presense of unsaturated soils around the pile. However, the existing literature lacks quantitative assessment of contribution of these mechanisms to the heat-induced interface strengthening.

6-2-   Background

As mentioned in previous chapters, the limit unit shaft resistance q_s at isothermal condition is proportional to the drained friction angle available at pile-clay interface δ and the effective normal stress acting σ'_h, which can mathematically be presented in the following equation:

$$q_s = \sigma'_h \, tan(\delta) \qquad\qquad (6-1)$$

δ is dependent on varying parameters including pile surface roughness, particle size/shape and strength/deformability characteristics of the surrounding clay [16]. When pile-clay interface is heated, it is very unlikely that geometrical properties mentioned above (i.e. the roughness and particle size/shape) are impacted under the low temperature variations typically induced at an energy pile interface. Therefore, the heat-induced change in clay strength/deformability characteristics is possibly responsible for causing any variation in interface friction angle ($\Delta\delta_{th}$) during heat application. It can be described with direct temperature effects on clay microscopic structure and/or its indirect effects through thermal consolidation occurring within the clay mass. Shaft friction degradation may also occur due to the heat-induced cyclic displacement along interface, similar to that observed by several researchers for the piles cyclically loaded ([17-22]). This is primarily attributed to the fact that soils (particularly sands) near pile surface tend to show a contractive behavior under cyclic shearing, causing a progressive decrease in the effective normal stress acting at interface, thus reducing the interface frictional resistance. This degradation

phenomenon has mainly been observed for the interface between sandy soils and different construction material ([17-22]), while the response of clay-concrete interface under cyclic shearing has not been investigated well. Nevertheless, a progressive volume decrease in clay is also expected due to this phenomenon that will cause a reduction in confining lateral pressure, an increment in pore water pressure (PWP) at interface (due to progressive contraction in clay), as well as shaft friction degradation. However, shaft degradation is less significant at clay-concrete interface since clays volumetric reduction toward cyclic shearing forces is generally lower than that in sandy soils. Furthermore, depending on the amount of contraction accumulated at the end of heat cycles, the "post-heat cycling" interface strength can be altered, that should be taken into account in energy pile design.

σ_h' can also vary due to the heat-induced excess PWP, which is strongly dependent on the rate of heating/cooling as well as clay permeability [23]. The induced excess PWP is due to differential expansion between clay particles and pore water [24]. If drainage is allowed (even at a slow rate), the excess PWP generated during heating will dissipate with time, leading to a thermal consolidation in clay. Conversely, when an interface is cooled down to the initial temperature, development of a negative PWP (suction) primarily occurs in clay followed by restoration if there is enough time. The earlier case can lead to a reduction in σ_h' and shaft resistance, while the latter can enhance both.

The above complicated interaction between the mechanical stresses-PWP-mechanical properties available at interface, limit unit shaft resistance and heating/cooling cycles can be expressed in the following mathematical form;

$$q_s = (\sigma_{h0}' + \Delta\sigma_{h-th}')\tan(\delta + \Delta\delta_{th}) \qquad (6-2a)$$

$$\Delta\sigma_{h-th}' = \Delta\sigma_{h-th} - \Delta u_{th} \qquad (6-2b)$$

Where, σ'_{h0} is effective lateral stress before heat application, and $\Delta\sigma'_{h-th}$ and $\Delta\delta_{th}$ are heat-induced changes in lateral effective stress and interface friction angle, respectively, with a sign, either positive or negative. $\Delta\sigma_{h-th}$ and Δu_{th} are the thermally induced changes in total lateral stress and excess PWP, respectively.

6-3- Analysis and discussion of the laboratory test results

In the current section the results from chapter 3 are briefly presented first. It allows for observing the heat-induced changes in shear strength of clay, and the subsequent effects on the friction angle at interface (δ), as discussed previously. Afterward, the results from chapters 4 and 5 indicating a heat-induced strengthening of clay-concrete interface, are briefly reviewd, and integrated with the results of chapter 3 followed by an effective analysis and discussion to provide more complete understanding of interface response at non-isothermal condition.

Temperature controlled CD triaxial test results

Figure 6-1 shows that the NC clay specimens subjected to heating presents higher shearing strength. Furthermore, the increase of strength due to heat cycles is higher than that because of non-cyclic heating ($\approx 13\%$ against $\approx 8\%$). However, there is no clear trend between the stress state and thermal strengthening. While the observed growth in peak stress varies between 7% and 13% for the heated specimens at 150 kPa and 300 kPa, it is about 3% at 200 kPa.
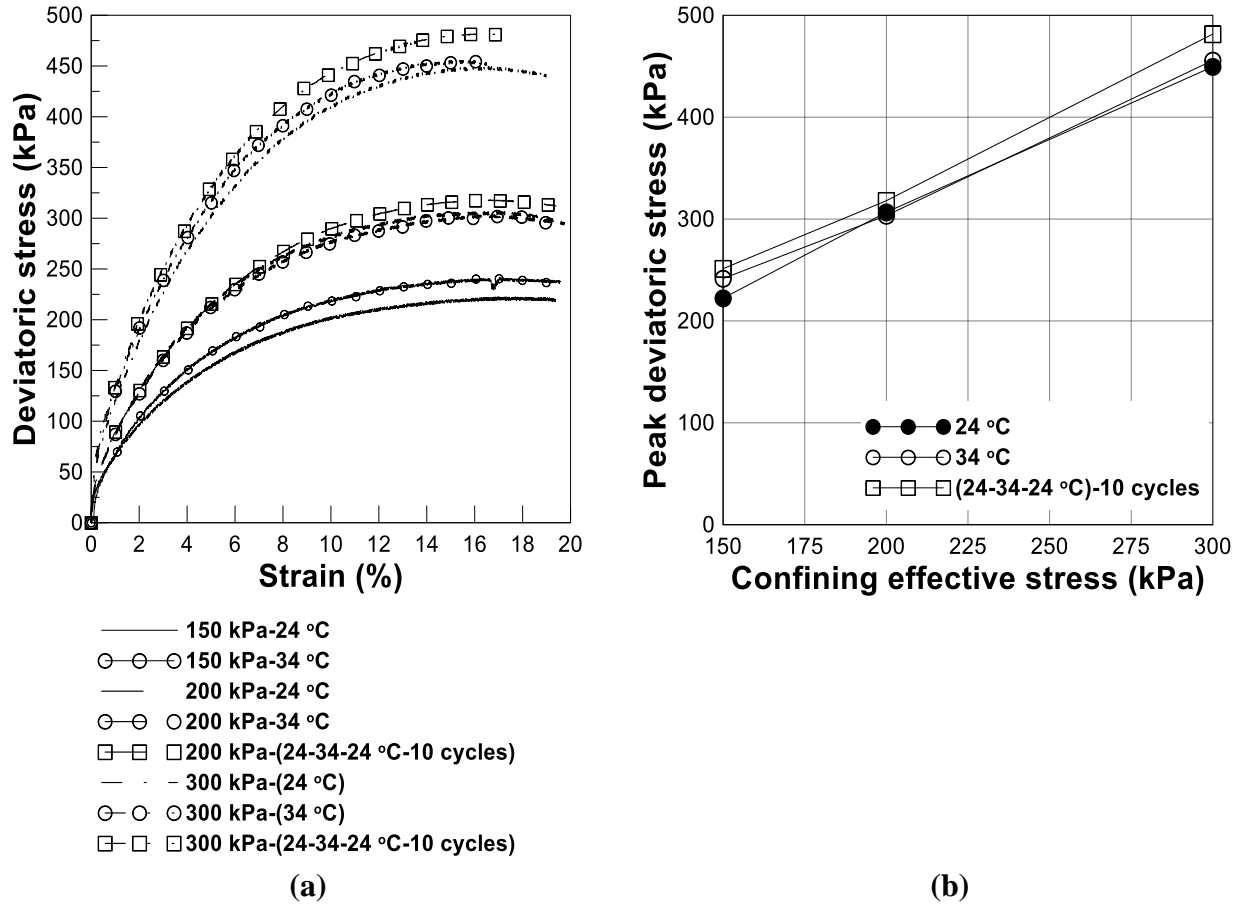
Figure 6-1- Shearing response of NC clay under different thermal loading: (a) $\Delta\sigma_d - \varepsilon(\%)$, and (b) corresponding $(\Delta\sigma_d)_{peak} - P_0'$ (P_0' : initial effective confining pressure).

Unlike NC clays, OC clays exhibit a thermal weakining which is more important to the specimens with higher OCR (Figure 3). Figure 3b indicates that the induced decrease of strength due to heat cycles is about 14% and 4% for the heavily (OCR=9) and lightly (OCR=2) OC clays, respectively. Similar thermal softening behavior has also been reported for OC clays in the literature [2, 3, 15, 32]. Based on the above observation, it appears that the thermo-mechanical response of clay is critically OCR-dependent: while the NC clay specimen demonstrates a thermal strengthening behavior, the peak deviatoric stress of OC clay decreases with temperature. It was suggested by Yazdani et al. (2018a) [4] that the clay shearing response to heating is possibly related to the heat-

induced change of effective stress, which is associated with the thermal rearrangement of clay

particles (fabric) during thermal consolidation, as also observed by Darbari et al. (2017) [25].

(a)   (b)
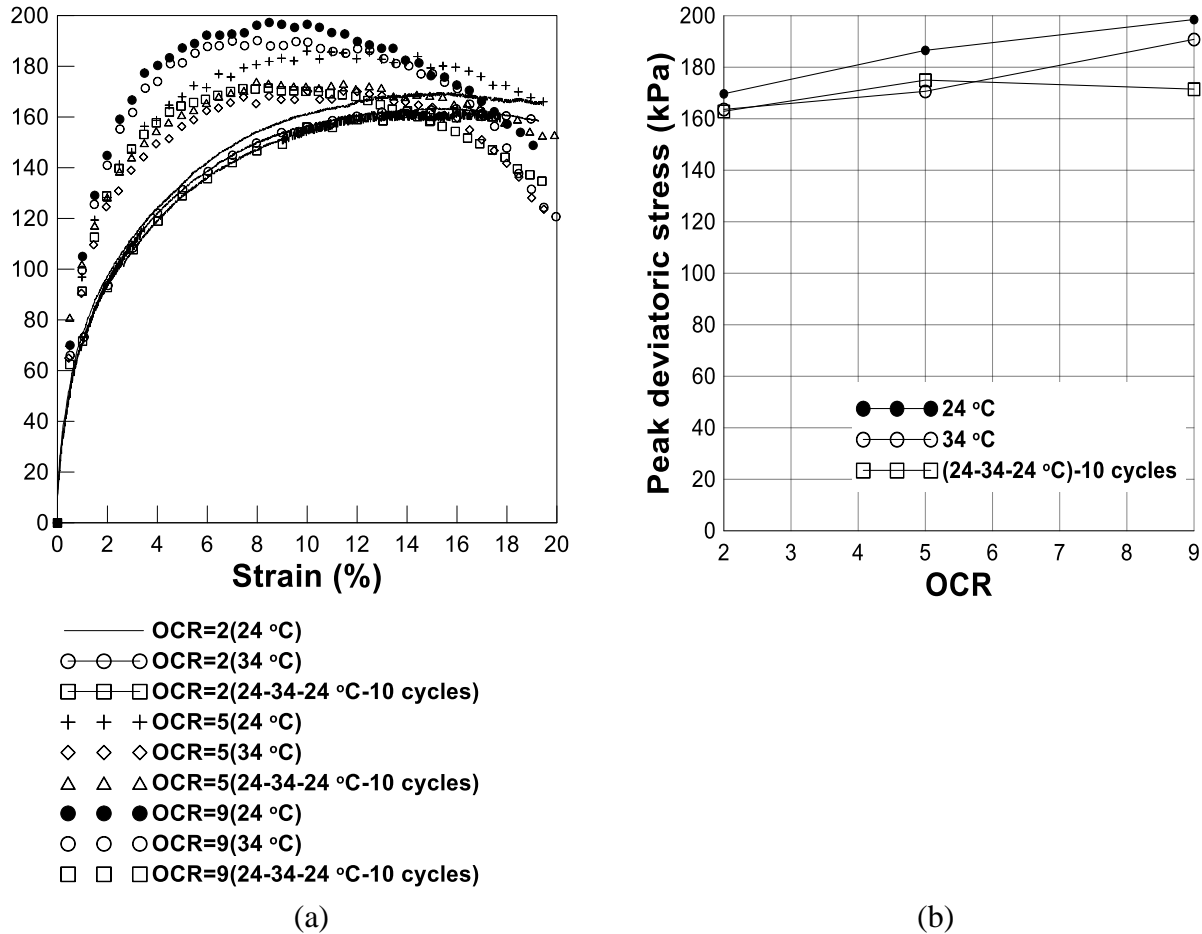
Figure 6-2- Shearing response of OC clay under different thermal loading: (a) $\Delta\sigma_d - \epsilon(\%)$ (at initial confining pressure of 100 kPa), and (b) corresponding $(\Delta\sigma_d)_{peak} - OCR$.

Temperature-controlled direct shear test results

Figure 6-3 shows that heat application caused an increase in the shear strength of NC clay-concrete

interface, which is consistent with the results of previous studies carried out under CNL condition

[1-3]. On the other hand, cyclic/non-cyclic heating caused a reduction in the peak shear strength

of OC clay-concrete interface, which is not necessarily inconsistent with the the results of previous

studies (frequently reporting a heat strengthening of interface), due to this fact that the published

literature does not contain information related to temperature effects on the shearing strength of OC clay-concrete interface.

The following analysis is made to determine the contributing fators to the heat strengthening of NC clay-concrete interface, which has also been observed by other researchers, and the heat weakening of OC clay-concrete interface observed in [4]. The analysis consists of integration the output from [4] (Figure 6-3) and [6] (Figures 6-1 and 6-2), and analyzing them using Equation 6-2. It should be mentioned that Equations (6-1) and (6-2) defining the limit unit shaft resistance of pile (q_s) is also applicable to the limit unit interface frictional resistance (τ_s) developing in direct shear test since σ'_h and δ can interchangeably illustrate the effective normal stress (σ'_n) and interface friction angle between the concrete slab and clay specimen (in direct shear apparatus). The observed interface response to heating is largely explained therefore, by possible heat-induced changes in effective normal stress σ'_n, and interface friction angle δ, which is explained as follows: Since the tests were conducted under CNL condition, any possible changes in the total normal stress during both the temperature variation and shearing steps is expected to be zero, which mathematically means $\Delta\sigma_{h-th} = 0$. Similarly, the heat-induced PWP change is most likely to be zero ($\Delta u_{th} = 0$), as the interface temperature variation was applied under drained condition. This is in turn concluded that the temperature-induced change in effective normal stress throughout the test is zero ($\Delta\sigma'_{h-th} = 0$). Note that the shearing occurred under drained condition. Therefore, according to Equation (6-2), it is suggested that the heat-induced change in strength of interface under CNL condition is linked to $\Delta\delta_{th}$. As mentioned earlier, $\Delta\delta_{th}$ is directly proportional to the heat-induced changes in internal friction angle of soil ($\Delta\phi_{th}$).
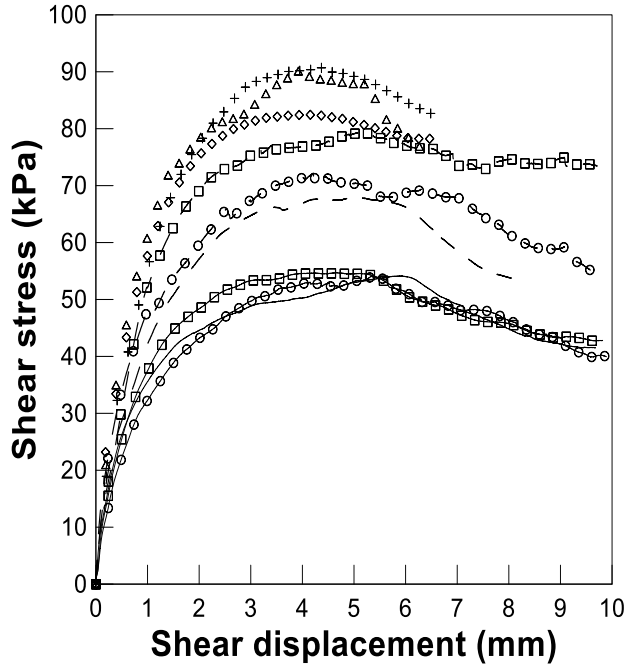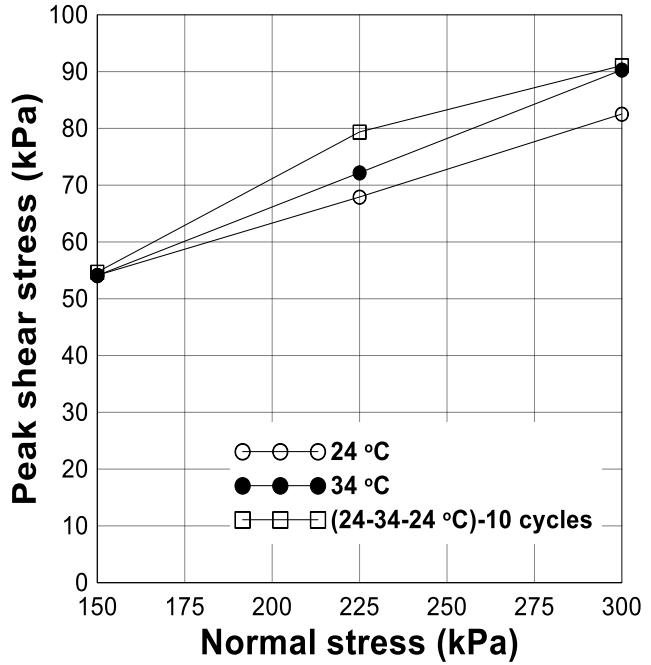
Figure 6-3- Shear stress versus tangential displacement (NC clay-interface): (a) shear stress-displacement, (b) Max shear stress-Normal stress ([6]).

The above analysis can be better explained as follows:

The frictional resistance developing between clay and concrete slightly before the peak strength, is primarily offered by a thin layer of clay (near the interface), which undergoes a uniform shear deformation during interface shearing [26 and 27]. It is followed by a relative displacement (sliding) at interface and a gradual reduction in the mobilized frictional resistance as shearing continues [26 and 27]. Accordingly, the strength/stiffness of clay in the vicinity of interface makes

an important contribution to the total frictional resistance offered by interface, that thus suggesting $\Delta\delta_{th}$ and overall change in frictional resistance (under CNL condition) are closely related to $\Delta\phi_{th}$. The above qualitative explanation can be further expanded by examining the data presented in Figure 6-4, where a comparison has been made between the peak friction coefficient estimated for the interface ($\tan\delta_p$) and clay (in triaxial test) ($\tan\phi_p$) under different temperature variations. $\tan\delta_p$ and $\tan\phi_p$ are defined as the maximum shear stress normalized by the corresponding effective normal stress at the interface or the failure plane (in triaxial condition), respectively. It can be seen that temperature effects on $\tan\delta_p$ is similar to that estimated for the clay sheared in triaxial condition ($\tan\phi_p$). While heating produces higher friction coefficient for the NC clay and NC clay-concrete interface, a heat-induced decrease in the friction coefficient can be noted for the OC clay and OC clay-concrete interface.

Table 6-1 summarizes the results in Figure 6-4. With respect to the NC case, $\tan\phi_p$ ($\tan\delta_p$) rises from 0.47 (0.3), at ambient temperature, up to 0.48 (0.325) and 0.5 (0.33) under non-cyclic and cyclic heating, respectively. As for the OC case, for instance OCR=2, $\tan\phi_p$ ($\tan\delta_p$) drops from 0.52 (0.37), at ambient temperature, down to 0.5 (0.34) and 0.5 (0.33) under non-cyclic and cyclic heating, respectively. Table 6-1 also presents the corresponding relative changes in friction coefficient of clay and interface (in the parenthesis) with respect to isothermal condition (at 24 °C). It can be seen that the they are upper-bonded by 7% and 11% for the clay and interface, respectively.
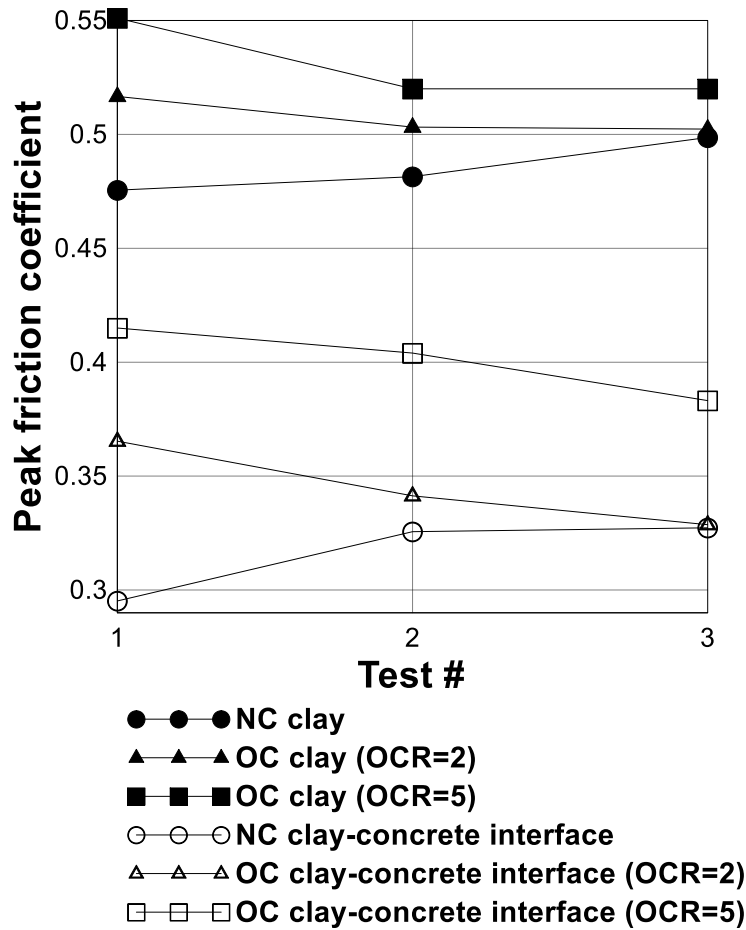
Figure 6-4- Peak friction coefficient versus temperature variation (Test1: 24 °C, Test2: 34 °C, and Test3: (24-34-24 °C)-10 cycles).

The variation of interface friction coefficient at residual condition (at large displacement), $\tan\delta_r$, is also ploted versus thermal loading path in Figure 6-5. It does not show the residual friction coefficient for clay specimen (in triaxial test), as it was not attained in the range of applied displacement.

Table 6-1- Summary of test results (peak friction coefficient) in Figure 6-4.

Stress history	OCR=1 (NC)			OCR=2			OCR=5		
	$tan\delta$	$tan\phi$	$\frac{tan\delta}{tan\phi}$	$tan\delta$	$tan\phi$	$\frac{tan\delta}{tan\phi}$	$tan\delta$	$tan\phi$	$\frac{tan\delta}{tan\phi}$
24 °C	0.3	0.47	0.64	0.37	0.52	0.71	0.415	0.55	0.75
34 °C	0.32 (8.3%)	0.48 (2.1%)	0.67	0.34 (-8.1 %)	0.5 (-3.85%)	0.68	0.4 (-3.6%)	0.52 (-5.4%)	0.77
(24-34-24)-10 cycles	0.33 (10%)	0.5 (6.4%)	0.66	0.33 (-10.8%)	0.5 (-3.85%)	0.66	0.38 (-8.43%)	0.52 (-5.4%)	0.72

Note: $tan\delta$ is estimated form direct shear tests on clay-concrete interface, while $tan\phi$ is measured through CD triaxial tests.
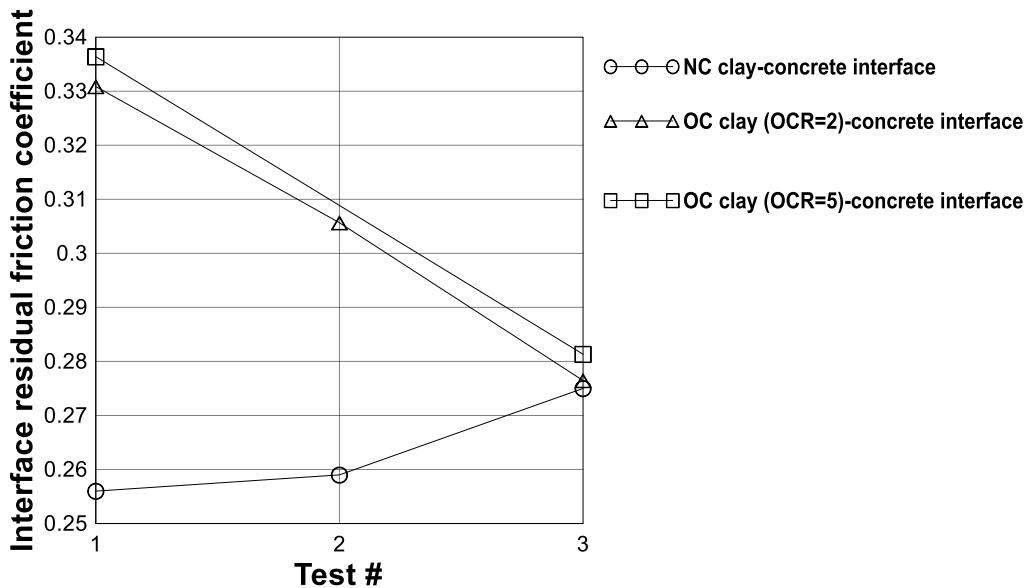
Figure 6-5- Residual friction coefficient versus temperature variation (Test1: 24 °C, Test2: 34 °C, and Test3: (24-34-24 °C)-10 cycles).

Therefore, it is not possible to make general suggestion similar to that previously made for the peak shear strength. However, it can be noted that the residual friction coefficient also shows similar OCR-dependent response to heating; While heat strengthening of NC clay-concrete interface is observed at large displacement, the residual strength of OC clay-concrete interface presents heat weakening.

Another contributing factor to heat strengthening of interface observed under CNL condition could be clay stiffening due to cumulative interface contraction (clay contraction) developed during the heat-induced cyclic shear. This phenomenon has been observed for the sand-concrete interface cyclically sheared under CNL condition, where the "post-cyclic" interface strength increases because of sand densification induced during cyclic shearing [28, 29]. To assess the contribution of this phenomenon to the increase in interface resistance observed in Figures 6-3 to 6-5, the vertical deformation of clay (near the interface) taking place during 10 cycles of heating/cooling is shown in Figure 7. Note that each heating/cooling cycle is equivalent to (24-34-24 °C), as previously mentioned. Furthermore, the vertical deformation shown in Figure 7 corresponds to the end of each heat cycle when the interface was cooled back down to 24 °C.
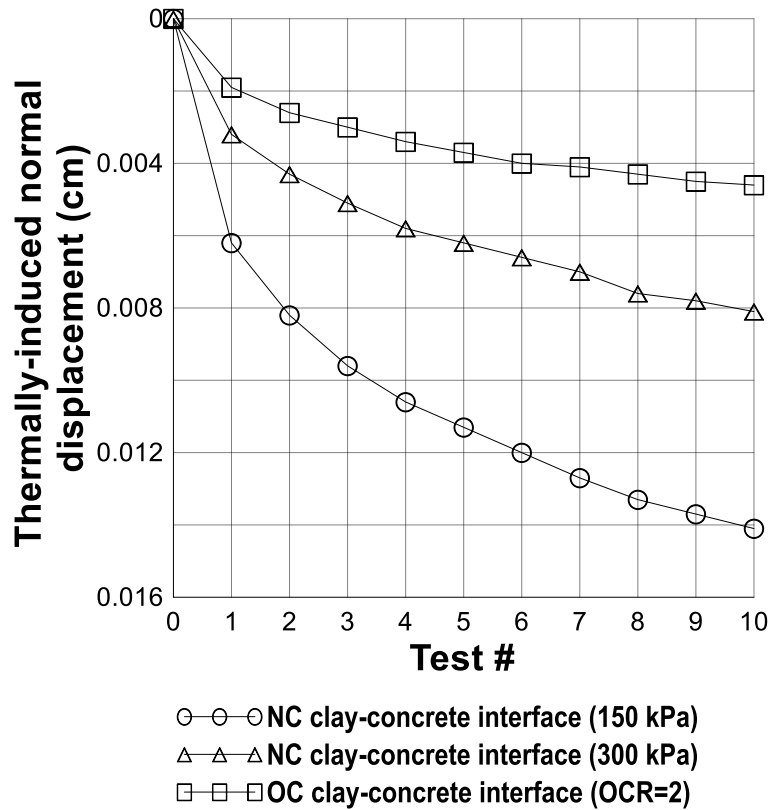
Figure 6-6- Temperature-induced normal displacement at clay-concrete interface (during 10 heat cycles).

It can be seen that the overall change in vertical displacement (during heat application) is insignificant. It varies between 0.0046 cm (at the OC clay-concrete interface) and 0.014 cm (at the NC clay concrete interface at $\sigma_n = 150$ kPa), which corresponds to volumetric strains equal to 0.22% and 0.7%, respectively. As for the NC clay-concrete interface at $\sigma_n = 300$ kPa, the total vertical deformation lies between the values of two other cases. Owing to very small volume change of interface shown in Figure 6-6, it is concluded that the long-term resistance of clay-concrete interface exhibits an independency toward the cyclic tangential displacement induced by cyclic temperature variation. This phenomenon is actually expected due to the very small amplitude of cyclic tangential displacement, which is estimated to be 0.00225 cm (considering $\alpha_{concrete} = 1.5 \times 10^{-5} \frac{1}{C°}$, $L_{concrete} = 15 \ cm$, and $\Delta T = 10 \ °C$).

At the end of this section, the following conclusion can be drawn about the the increased strength of interface under CNL condition, absorved in chapter 4 and previous studies [1-3]: (1) Heat strengthening of NC clay is the key contributing factor to the heat strengthening of NC clay-concrete interface. Likewise, heat weaking of OC clay appears to mainly contribute to the weaking of OC clay-concrete interface. (2) The contribution of both cummulitative clay contraction (due to heat-induced cyclic shearing) and clay thermal consolidation was found to be blunted.

Temperature controlled 1g lab-scale pile test results
Figure 6-7 illustrates the load-settlement response of the pile after applying different thermal loading. It is evident that heating has significant effects on the shaft resistance of the pile. The pile tested at elevated temperature of 34 °C showed an increase of 100% in the shaft resistance relative to the pile sheared at isothermal condition, while the piles subjected to cyclic heating showed almost similar increase of 50%. Similar heat-induced increase in the shaft resistance (up to 95%) was also reported by othere reserachers using small-scale tests (for example: [8-10]).

A similar analysis, by integrating the data from chapter 5 with data from chapters 3 and 4, will be made to investigate the contributing factors to the heat-induced increase of skin friction observed in small-scale tests [7, 8, 10, 12 & 13]. The analysis may also help better characterize the heat-induced improvement of shaft resistance absorved in full-scale tests [14 and 15] since both small- and full-scale tests are generally performed under CNS condition. In fact, the available literature reporting on thermo-mechanical behavior of interface can be divided into studies performed under CNS condition (i.e. small/full scale tests and DST carried out under CNS condition) and those performed under CNL condition (i.e. DST carried out under CNL condition). Although the results of both studies indicate an improvement of interface strength due to heat application, they show different amount of improvement, mainly due to different stiffness boundatry conditions employed in those studies.
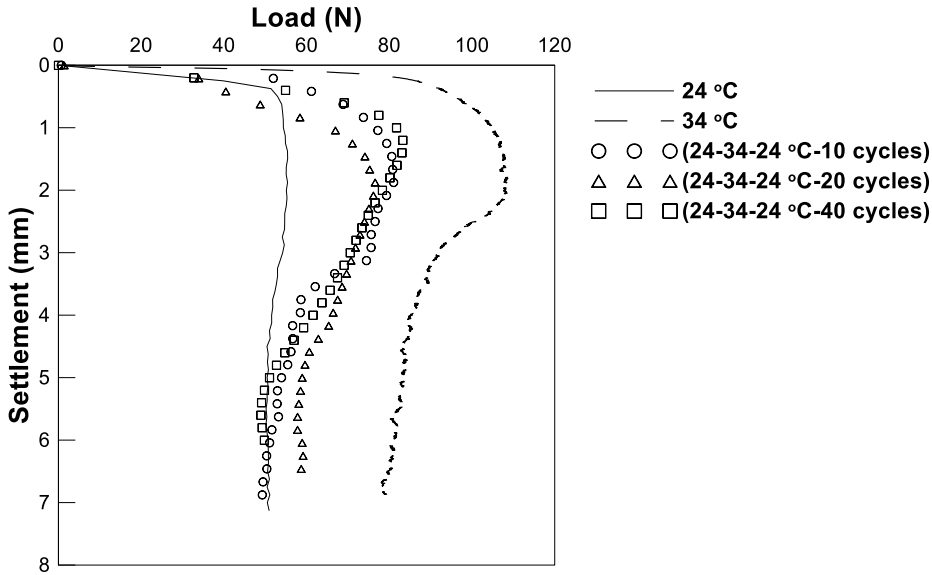
(a)
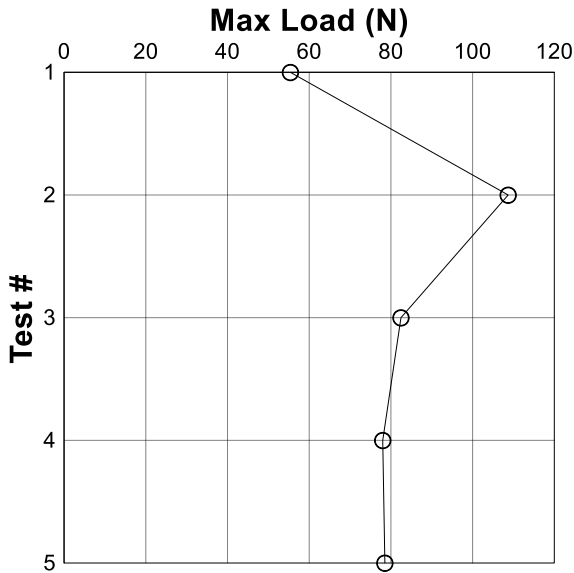
(b)

Figure 6-7- (a) load-settlement curves for the model under different thermal loading and (b) corresponding maximum pile load (Test1: 24 °C, Test2: 34 °C, and Test3: (24-34-24 °C)-10 cycles, Test4: (24-34-24 °C)-20 cycles and Test5: (24-34-24 °C)-40 cycles).

Therefore, before discussing the results in Figure 6-7, it would be interesting to quantitively compare the outcomes of the direct shear test (done in CNL condition) and 1g small-scale test (done in CNs condition) at both isothermal and non-isothermal conditions. Assuming that the effective normal stress acting round the pile shaft σ'_h is 57 kPa (considering $\sigma'_h = K_0\sigma'_v$, in which

$K_0 = 1 - \sin\phi'_{clay}$, $\phi'_{clay} = 25°$ (Figure 5) and $\sigma'_v = 100$ kPa), the interface friction coefficient tan

δ (= (Pile axial load)÷(lateral effective load on pile surface)) at isothermal condition is estimated

to be 0.16, which is 50% lower than that (0.3) measured using direct shear test (Table 6-1). It is

apparently because the pile surface is smoother than the concrete surface used in direct shear test,

as shown in Figure 6-8.

(a)   (b)
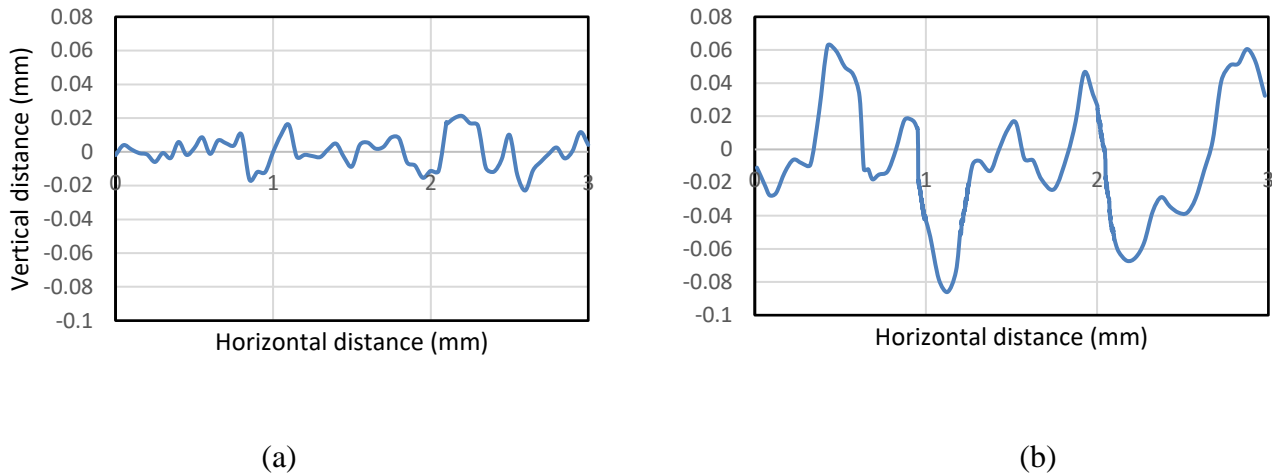
Figure 6-8- Roughness profile of interface (laser photography): (a) pile surface, and (b) concrete slab.

According to the method of Arithmetic mean deviation (Equation (6-3)), which is commonly used

for characterizing the clay-solid interface roughness [30 31], average roughness is estimated to be

4.48 µm and 28.8 µm for the pile surface and the concrete slab (used in direct shear test),

respectively.

$$R = \frac{1}{n}\sum_{i=1}^{n}|y_i| \qquad\qquad (6-3)$$

(a)

(b)
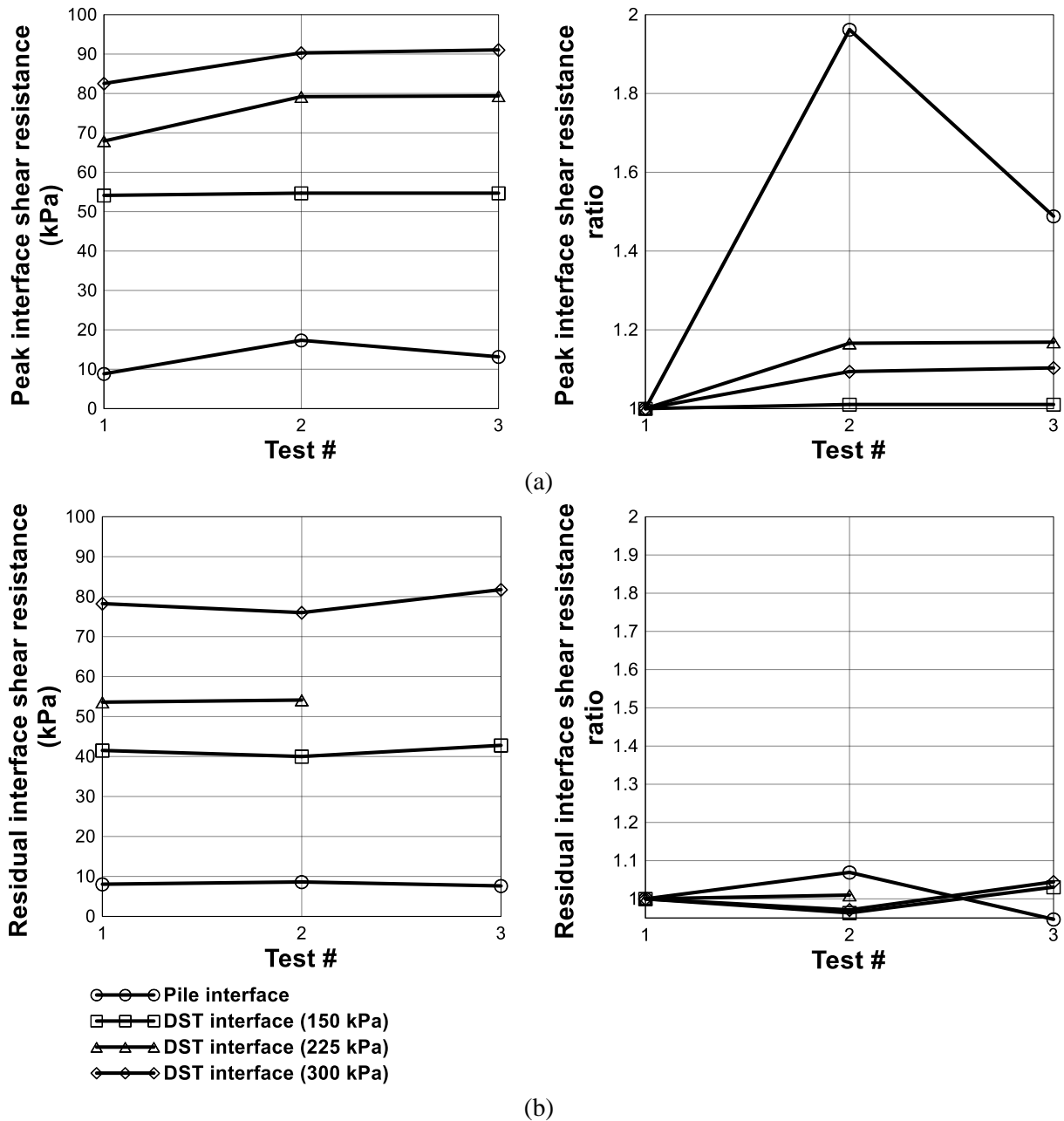
Figure 6-9- Quantitative comparison between interface shear strength obtained by the direct shear test and small-scale pile: (a) peak interface shear strength, and (b) residual interface shear strength (Test1: 24 °C, Test2: 34 °C, and Test3: (24-34-24 °C)-10 cycles).

Where, R is the interface relative roughness, n is the number of sampling point and y is the height of asperities at the sampling points.

At non-isothermal condition, however, the "tan δ based" comparison of interface resistance may not be applicable since the lateral stress is unlikely to remain constant (57 kPa) during heat application. Instead, the peak and residual shear strength of interface and their corresponding ratios at non-isothermal and isothermal conditions (τ_{p-T}/τ_{p-T0} or τ_{r-T}/τ_{r-T0}), for both testing approaches, are compared in Figure 10. Note that τ_{p-T} and τ_{p-T0} are the peak interface strength at non-isothermal and isothermal conditions, respectively, while τ_{r-T} and τ_{r-T0} are the residual interface strength at non-isothermal and isothermal conditions, respectively. Besides the smoother surface, lower lateral pressure generated at the pile-clay interface (≈ a fraction of the over-burden pressure, 100 kPa) is the other important reason for the observed lower interface resistance (Figure 6-9a). Note that interface shearing in direct shear test took place under 150 kPa, 225 kPa and 300 kPa.

From the above analysis it is found that less significant improvements are achieved when shearing occurs in direct shear box (under CNL condition). In fact, the peak shear strength ratio estimated from the direct shear test is upper-bonded by 1.2, while that calculated from the 1g small-scale test results is upper-bonded by 2. As mentioned earlier, different stiffness boundary conditions available at the interface are possibly responsible for the above behavior. It will be explained with more details in the following section. With respect to the ratio of residual strength under CNS condition, no clear trend can be seen towards the temperature variations. Furthermore, at both conditions, the residual shear resistance is affected less significantly as opposed to the peak shear resistance.

Now the heat strengthening interface observed in 1g lab-scale test is analyzed and discussed. Let us rewrite the limit unit shaft resistance presented in Equation (6-2a) in a way that help examine the results of small-scale pile test:

$$\frac{q_{s-T}}{q_{s-T_0}} = \frac{\sigma'_{h-T} tan\delta_T}{\sigma'_{h-T_0} tan\delta_{T_0}} = \left(\frac{\sigma'_{h-T}}{\sigma'_{h-T_0}}\right)\left(\frac{tan\delta_T}{tan\delta_{T_0}}\right) \qquad\qquad (6-4)$$

The equation shows the ratio of the limit unit shaft resistance developed at the pile-clay interface, where T and T_0 denote the non-isothermal and isothermal conditions, respectively. Unlike the direct shear test, the ratios of effective lateral stress $\left(\frac{\sigma'_{h-T}}{\sigma'_{h-T_0}}\right)$ and friction coefficient $\left(\frac{tan\delta_T}{tan\delta_{T_0}}\right)$ were not directly measured in lab-scale test. However, $\left(\frac{tan\delta_T}{tan\delta_{T_0}}\right)$ may be approximated by that previously estimated for NC clay-concrete interface in direct shear test (Table 6-1). In fact, friction coefficient ratio in 1g small-scale test is expected to be upperbonded by the corresponding values measured by the direct shear test, due to this fact that the concrete surface used in direct shear test is rougher than the surface od pile model, as shown in Figure 6-8. Note that both tests were conducted under similar themo-mechanical conditions and soil properties, except that different surface roughness and stiffness boundary conditions used in them. Furthermore, it is widely accepted that the interface friction coefficient is independent of stiffness boundary condition (i.e. CNL or CNS).
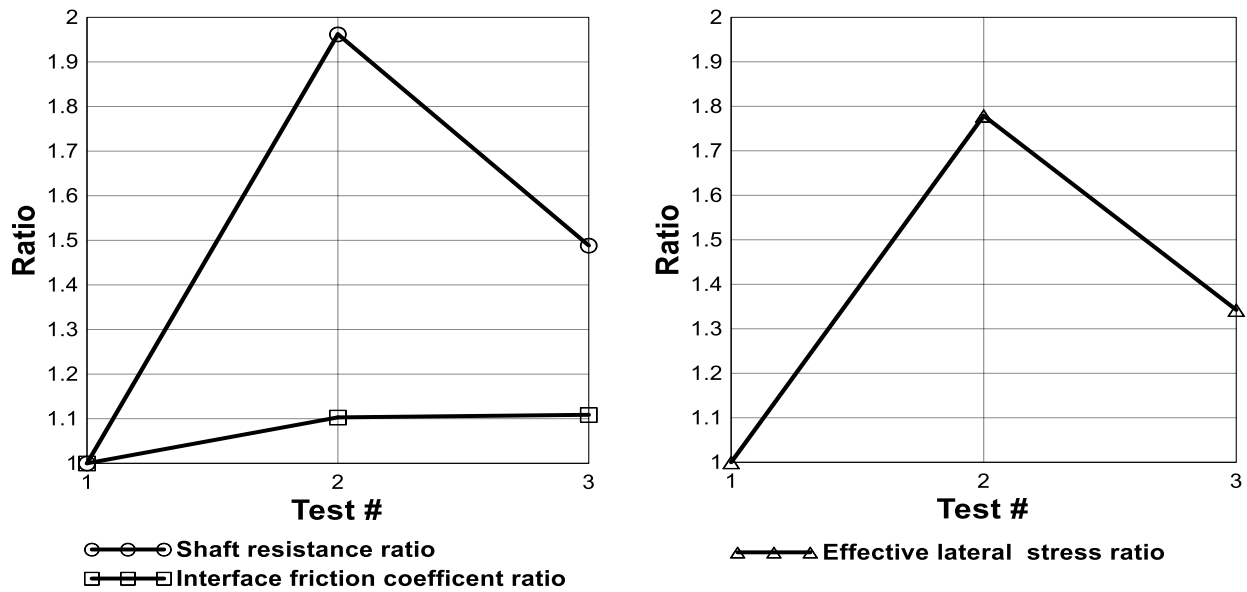
(a)   (b)

Figure 6-10- Heat induced variation of (a) the limit unit shaft resistance and friction coefficient ratios, and (b)

effective lateral stress ratios with temperature (Test1: 24 °C, Test2: 34 °C, and Test3: (24-34-24 °C)-10 cycles).

In order to continue the analysis, it is assumed that $\left(\frac{\tan\delta_T}{\tan\delta_{T_0}}\right)$ is equal to that estimated using the

direct shear test, as shown in Table 1 (i.e. 1.083 at 34 °C and 1.1 for 10 heating cycles). Figure 6-

10a shows $\left(\frac{q_{s-T}}{q_{s-T_0}}\right)$ together with the $\left(\frac{\tan\delta_T}{\tan\delta_{T_0}}\right)$ (approximated from DST results). Using the data in

Figure 6-10a and Equation 6-4, the corresponding $\left(\frac{\sigma'_{h-T}}{\sigma'_{h-T_0}}\right)$ at the interface can be calculated, as

shown in Figure 6-10b. According to Table 6-2, which summarizes the results in Figure 6-10, the

increased effective lateral stress is the primary reason for the improvement of the pile shaft

resistance.

Table 6-2- Summary of the pile test results presented in Figure 11.

	$\dfrac{q_{s-T}}{q_{s-T_0}}$	$\dfrac{\tan\delta_T}{\tan\delta_{T_0}}$	$\dfrac{\sigma'_{h-T}}{\sigma'_{h-T_0}}$
24 °C	1	1	1
34 °C	1.96	1.083	1.81
(24-34-24)-10 cycles	1.49	1.1	1.35

Note: $\frac{\tan\delta_T}{\tan\delta_{T_0}}$ is estimated from DST.

To accurately interpret this finding, it is required to understand both heat-induced changes of total lateral stress ($\Delta\sigma_{h-th}$) and PWP (Δu_{th}). During heating period, excess PWP develops in the clay around the pile followed by a thermal consolidation. The amount of consolidation settlement primarily depends upon on Δu_{th} initially generated in the clay, which is a function of clay permeability and rate of drainage ([23]). Unlike the insignificant thermal consolidation observed in the clay tested in direct shear box (Figure 6-6), it should be more important in the pile test due to the longer drainage path and poor drainage occurring at the boundaries. Therefore, the following qualitative interpretation can be presented for the results in Figure 6-10: The thermal consolidation occurring in the clay causes time-dependent deformation within the clay in all direction. The lateral deformation toward the pile surface, however, is not allowed as it is constrained by the pile that thus increases the normal effective stresses on the pile surface. In other words, as thermal consolidation continues the effective lateral stress on the pile surface gradually increases beyond its initial value σ'_{h-T_0}, while the initially induced PWP gets gradually dissipated.

According to the above explanation, the pile is loaded at 34 °C (test 2) (upon the completion of heat application), is expected to experience an effective lateral stress larger than σ'_{h-T_0} leading to larger shaft resistance. With respect to the tests performed under cyclic heating, however, the cooling phase of each cycle (back to 24 °C) reverses the trend explained during the heating phase. In other words, the thermal expansion of clay during heating phase is followed by lateral

contraction during cooling phase inducing a reduction in the horizontal stress ($\Delta\sigma'_{h-th} < 0$). This in turn causes a cyclic variation in the sign of $\Delta\sigma'_{h-th}$ during heating/cooling phases of each cycle. However, the cumulative $\Delta\sigma'_{h-th}$ is expected to be positive at the end of each cycle, due to the plastic deformation occurring during heating phase of each heat cycle. Moreover, negative PWP (suction) is expected to develop during cooling phase resulting in an increase in the effective lateral stress ($\Delta\sigma'_{h-th} > 0$). As for Test 3, where the model pile is loaded after applying 10 cycles of heating/cooling, the effective lateral stress would be greater than σ'_{h-T_0}, but smaller than that in Test 6-1 due to contraction occurring in each cooling phase.

According to the above analysis, the following conclusion can be drawn about the the increased strength of interface under CNS condition: (1) The heat strengthening of shaft resistance is primarily attributed to heat-induced increase of effective lateral stress at pile surface. (2) The contribution of effective lateral stress is larger when energy pile is loaded at elevated temperature as compared to when the pile is loaded after applying cyclic heating. (3) The shaft resistance improvement may also be partially attributed to heat strengthening of clay near the pile surface.

As mentioned previously, the results discussed above can essentially be used for exploring the long-term shaft resistance as in all the test series interface shearing occurs after completion of thermal loading (second step), where full stabilization of temperature and PWP at the interface was attained. Practically, this situation could occur in 24 hours continuous operating mode, where the transient change of temperature and PWP observed in the beginning of energy pile operation is followed by a steady state condition in which full stabilization of temperature and PWP is achieved at the interface and maintained till the end of operation. Using full-scale experimental tests, Faizal et al. (2016) [32] observed that the time required to reach temperature/PWP steady state within the pile and surrounding soil (in continuous mode of operation) was less than 72 hours.

In intermittent operating mode, stabilization of temperature and PWP could also reach after complete cessation of energy pile operation, as reported by Faizal et al. (2016) [32]. Note that working under intermittent mode generates PWP/temperature transient state at the interface, whereby they cyclically vary with operating time (Faizal et al. (2016) [32]).

It was shown that the improvement of long-term shaft resistance frequently observed in the published literature is interpreted on the basis of the heat induced alteration of (i) the effective lateral stress σ'_h and (ii) the interface friction angle δ. Furthermore, the interpretation of shaft resistance improvement should be made based on the stiffness boundary conditions (i.e. CNS or CNL conditions) under which a test is carried out. Consideration must also be made to the effects of boundary restrictions in lab-scale tests, where the heat transfer process, pore pressure gradient and thus the thermal consolidation and the resulting changes in effective lateral stresses might be influenced.

In terms of the short-term predictions of shaft resistance, the same parameters should also be taken into account. Practically, the short-term shaft resistance corresponds to the shear strength of pile-soil interface available when energy piles operate intermittently. In fact, at short-term period, when heat exchange process continuously takes place at the interface, Δu_{th} is expected to grow at a fast rate (particularly in the beginning of heating periods), as shown by Fuentes et al. (2016) [32], while the degree of thermal consolidation is expected to be low. Correspondingly, the overall change in σ'_h tends to be negative ($\Delta\sigma'_{h-th} < 0$) that can potentially reduce the shaft resistance during heat application. Note that in the above statement it was assumed that the thermally-induced change of total lateral stress is zero ($\Delta\sigma_{h-th} = 0$). Under assumption that the total lateral stress remains constant during operation of an energy pile, Fuentes et al. (2016) [32] reported that the loss of

short-term shaft capacity is significant when an energy pile is surrounded by a clay with low permeability (k < 1E-11 m/s) and high compressibility (k_s > 20000 MPa).

6-4-   Conclusion

This study aims to quantitively/qualitatively determine the contributing factors to the increased interface strength of energy piles reported in the existing literature. The results of three separate experimental studies of thermo-mechanical behavior of clay and clay-concrete interface are integrated and analyzed. Based on this analysis the following conclusions can be made:

(1) The heat-induced improvement of shaft resistance can generally be explained on the basis of the heat-induced increase of lateral effective stress $\Delta\sigma'_{h-th}$, and interface friction angle $\Delta\delta_{th}$.

(2) The enhanced interface strength observed in the tests performed under constant normal load (CNL) condition, like those employing CNL direct shear tests, is exclusively related to the clay strengthening (or $\Delta\delta_{th}$).

(3) The thermally enhanced shaft resistance presented by the interface sheared under CNS condition, such as when a small/full scale test is done, is primarily attributed to $\Delta\sigma'_{h-th}$. $\Delta\delta_{th}$ also makes a partial contribution to the thermal strengthening of shaft. As for the pile loaded at elevated temperature (34 °C), the heat-induced rise in shaft resistance, effective lateral stress and interface friction coefficient are estimated to be 96%, 81% and 8%, respectively, While, they are 49%, 35% and 10%, respectively, for the piles loaded after subjected to heat cycles.

(4) The shaft resistance of energy piles in clay at the short-term period possibly decreases due to insufficient time for drainage of the generated excess PWP. Further research, however, is needed.

(5) Both short/long term shaft resistance will be better understood by future laboratory works using more realistic boundary condition and direct measurement of the effective lateral stress and PWP at the interface.

Acknowledgment

References:

[1] Xiao, S., Suleiman, MT., and McCartney, J.S. (2014). Shear Behavior of Silty Soil and Soil-Structure Interface under Temperature Effects. In Proceedings of Geo-Congress (GSP 234), 4105-4114.

[2] Yavari, N., Tang, AM., Pereira, JM., and Hassen, G. (2016). Effect of temperature on the shear strength of soils and soil/structure interface. *Canadian geotechnical journal* 53(7), 1186-1194.

[3] Maghsoodi, S., Cuisinier, O., and Masrouri, F. (2018). Thermal effects on the mechanical behavior of the soil-structure interface. *Canadian geotechnical journal*.

[4] Yazdani, S., Helwany, S., and Olgun, O. (2018a). Experimental evaluation of shear strength of Kaolin Clay under Cyclic and Non-Cyclic Thermal Loading. *Geotechnical Testing Journal*, https://doi.org/10.1520/GTJ20180020.

[5] Di Donna, A., Ferrari, A., and Laloui, L. (2016). Experimental investigation of the soil concrete interface: physical mechanisms, cyclic mobilization and behavior at different temperatures. *Canadian Geotechnical Journal*, 43(4), 659-672.

[6] Yazdani, S., Helwany, S., and Olgun, O. (2018b). Influence of Temperature on Soil-Pile Interface Shear Strength. *Geomechanics for Energy and the Environment*, 18, 69-78.

[7] McCartney, J.S., and Rosenberg, J.E. (2011). Impact of heat exchange on side shear in thermo-active foundations. *Geo-Frontiers 2011 Advances in Geotechnical Engineering*, 488-498.

[8] Goode III, J.C., and McCartney, J.S. (2015). Centrifuge modeling of boundary restraint effects in energy foundations. *ASCE J. Geotech. Geoenviron. Eng*, 141(8), https://doi.org/10.1061/(ASCE)GT.1943-5606.0001333.

[9] Murphy, K.D., and McCartney, J.S. (2014). Thermal Borehole Shear Device. *ASTM geotechnical testing journal*, 37(6), 1040-1055.

[10] Ghaaowd, I., and McCartney, J.S. (2018). Centrifuge modeling of temperature effects on the pullout capacity of energy piles in clay. DFI 43rd Annual Conference on Deep Foundations, Anaheim, CA., Oct 24-27. 1-7.

[11] Wang, B., Bouazza, A., and Haberfield, C. (2011). Preliminary observations from laboratory scale model geothermal pile subjected to thermo-mechanical loading. *Geo-Frontiers 2011 advances in geotechnical engineering*, pp. 430-439.

[12] Wang, C.-L., Liu, H.-L., Kong, G.-Q., Ng, C.W.W., Wu, D. (2016). Model tests of energy piles with and without a vertical load, *Environ. Geotech.*, 3 (4), 203-213.

[13] Yazdani, S., Helwany, S., and Olgun, O. (2019). Investigation of thermal loading effects on the shaft resistance of energy pile using laboratory scale model. *Journal of Geotechnical and Geoenvironmental Engineering*, 10.1061/(ASCE)GT.1943-5606.0002088

[14] Szymkiewicz, F., Burlon, S., Guirado, F., Minatchy, C., and Vinceslas, G. (2015). Experimental study of heating-cooling cycles on the bearing capacity of CFA piles in sandy soils. in: Proc. XVI ECSMFE: *Geotechnical Engineering for Infrastructure and Development*, Edinburgh, 2647-2652.

[15] Wang et al. (2014). Posttemperature Effects on Shaft Capacity of a Full-Scale Geothermal Energy Pile. *J. Geotech. Geoenviron. Eng.,* 141(4). DOI: 10.1061/(ASCE)GT.1943-5606.0001266.

[16] Lemos, LJL., and Vaughan, PR. (2004). Clay-interface shearing resistance. *Geotechnique*, 50(1): 55-64.

[17] Di Donna, A., Ferrari, A., and Laloui, L. (2016). Experimental investigation of the soil concrete interface: physical mechanisms, cyclic mobilization and behavior at different temperatures. *Canadian Geotechnical Journal*, 43(4): 659-672.

[18] Mortara, G., Mangiola, A., and Ghionna, V. (2007). Cyclic shear stress degradation and post-cyclic behavior from sand-steel interface direct shear tests. *Canadian Geotechnical Journal*, 44(7), 739-752.

[19] Tabucanon, TJ., Airey, DW., Poulos, HG. (1995). Pile skin friction in sands from constant normal stiffness tests. *Geotechnical Testing Journal,* 18(3), 350-364.

[20] Uesugi, M., Kishida, H., and Tsubakihara. Y. (1989). Friction between sand and steel under repeated loading. *Japanese Society of Soil Mechanics and Foundation Engineering,* 29(3), 127-137.

[21] Uesugi, M., Kishida, H., and Uchikawa, Y. (1990). Friction between dry sand and concrete under monotonic and repeated loading. *Soils and Foundations,* 30(1), 115–128.

[22] Zhang, G., and Zhang, JM. (2006). Monotonic and cyclic tests of interface between structure and gravelly soil. *Soils and Foundations Journal,* 46(4), 505–518.

[23] Fuentes, R., Pinyol, N., and Alonso, E. (2016). Effect of temperature induced excess porewater pressures on the shaft bearing capacity of geothermal piles. *Geomechanics for Energy and the Environment*, 8, 30–37.

[24] Campanella, RG., and Mitchell, JK. (1968). Influence of temperature variations on soil behavior. *Journal of Geotechnical Engineering-ASCE*, 94(3), 709–734.

[25] Demars, KR., and Charles, RD. (1982). Soil volume changes induced by temperature cycling. *Canadian Geotechnical Journal*, 19(2), 188–194.

[26] Goh, ATC., and Donald, IB. (1984). Investigation of soil-concrete interface behavior by simple shear apparatus. *Geomechanics-Interaction*, 84(2): 101-106.

[27] Tsubakihara, Y., and Kishida, H. (1993). Frictional behavior between normally consolidated clay and steel by two direct shear type apparatuses. *Soils and Foundations,* 33(2), 1-13.

202

[28] Mortara, G., Mangiola, A., and Ghionna, VN. (2007). Cyclic shear stress degradation and post-cyclic behavior from sand–steel interface direct shear tests. *Canadian Geotechnical Journal*, 44 (7), 739-752.

[29] Tabucanon, TJ., Airey, DW., and Poulos, HG. (1995). Pile skin friction in sands from constant normal stiffness tests. *Geotechnical Testing Journal,* 18(3), 350-364.

[30] Hammoud, F., and Boumekik, A. (2006). Experimental study of the behavior of interfacial shearing between cohesive soils and solid materials at large displacement. *Asian Journal of Civil Engineering (Building and Housing)*, 7(1), 63-80.

[31] Lemos, LJL., and Vaughan, PR. (2000). Clay-interface shear resistance. *Geotechnique,* 50(1), 55-64.

[32] Darbari, z., Jaradat, K., and Abdelaziz, S., (2017). Heating–freezing effects on the pore size distribution of a kaolinite, *Environmental Earth Sciences*, 76 (20), 713-720.

[33] Faizal, M., Bouazza, A., & Singh, R.M. (2016). An experimental investigation of the influence of intermittent and continuous operating modes on the thermal behavior of a full-scale geothermal energy pile. Geomechan. *Energy. Environ*, 8, 8-29.

[34] Yazdani, S., Helwany, S., and Olgun, O. (2019). Experimental Study of Potential Mechanisms Contributing to Thermally Enhanced Shaft Resistance of Energy Piles in Clay", submitted at *Canadian Geotechnical Journal* for publication.

Chapter 7

Numerical Analysis-Coupled Thermo-Hydro-Mechanical Analysis

7-1- Introduction:

In this chapter the capability of thermo-hydro-mechanical (THM) numerical models to assess thermo-mechanical behavior of clays and pile-clay interfaces is analyzed. To do so, a 3D Finite Element (FE) program, ABAQUS, was utilized to reproduce the experimental results discussed in chapters 3-6.

Different types of analysis can be performed by ABAQUS that can be listed as follows [1]: (1) Static/dynamic stress analysis, (2) Steady state transport analysis, (3) Heat transfer and thermal-stress analysis, (4) Electromagnetic analysis, (5) Coupled pore fluid flow and stress analysis, (6) Mass diffusion analysis, (7) Acoustic and shock analysis, and (7) Abaqus/Aqua analysis.

A porous medium such as soil can be modeled in Abaqus/Standard by the conventional approach that considers the medium as a material consisting of solid phase (particles) and pores, which can be filled by (wetting) fluid or/and gas. and adopts an effective stress principle to describe its behavior. Abaqus assumed the wetting liquid to be relatively incompressible, while the gas to be relatively compressible. Coupled pore fluid flow and stress analysis (or "SOILS" analysis) is employed to simulate the behavior of porous medium. In fact, it is capable of doing stress/strain analysis, modeling partially/fully saturated fluid flow through porous media (such as soil), calculating both total stress and pore pressure and thus total/effective stress, modeling heat transfers due to conduction in the soil particles and the pore fluid, and convection due to the pore fluid flow (by using coupled temperature–pore pressure displacement elements). The analysis can also be performed under steady/transient conditions and through both linear and non-linear solutions, which makes it a suitable analysis type for modeling the coupling between hydraulic, thermal and mechanical phases in some applications like energy pile embedded in soils.

7-2- Formulation of thermo-hydro-mechanical response of porous media [2]

Stress/strain analysis of porous medium

Mechanical stress/strain analysis of porous medium is performed by determining the discretized equilibrium in a porous medium. The principle of virtual work is used to write equilibrium equations for the volume (V) under consideration at time t:

$$\int_V \sigma : \delta\varepsilon \, dV = \int_S \bar{t}.\delta v \, ds + \int_V \bar{f}.\delta v \, dV \qquad (7-1)$$

Where δv is a virtual velocity field, $\delta\varepsilon$ is the virtual rate of deformation (or virtual strain), σ is the true (Cauchy) stress, $\bar{t}$ are surface tractions per unit area, and $\bar{f}$ are body forces per unit volume, which includes both the unit weight of wetting fluid and solid particles. σ is the total stress at a point, which is equal to the sum of normal stress between particles contact (effective stress), σ_e, and an average pressure in the wetting fluid, u_w, and gas u_a, which can be expressed as:

$$\sigma = \sigma_e + (S.u_w + (1-S)u_a) \qquad (7-2)$$

The above equation is known as effective stress principle in which S is the degree of saturation of the medium. Tensile stresses are also assumed to be positive. In most cases, however, the pressure of gas is very small and ignored in the above equation:

$$\sigma = \sigma_e + (S.u_w) \qquad (7-3)$$

Equation (7-3) is substituted into Equation (7-1) and as we can see later, the term $S.u_w$ will be used to couple the equilibrium equation and fluid flow equation.

$$\int_V (\sigma_e + S.u_w) : \delta\varepsilon \, dV = \int_S \bar{t}.\delta v \, ds + \int_V \bar{f}.\delta v \, dV \qquad (7-4)$$

or

$$\int_V \sigma_e : \delta\varepsilon \, dV + \int_V S.u_w : \delta\varepsilon \, dV = \int_S \bar{t}.\delta v \, ds + \int_V \bar{f}.\delta v \, dV$$

Abaqus uses Finite Element (FE) method to solve equilibrium equation (Equation (7-1)), where the equilibrium is approximated as a finite set of equations by introducing interpolation functions. For instance, the virtual velocity δv (an independent variable) field is interpolated as follow:

$$\delta v = N^n \delta v^n \qquad\qquad (7-5)$$

Where N^n is interpolation function defined as function of coordinates of element points. Thus, the virtual rate of deformation (strain) can therefore be interpolated by:

$$\delta\varepsilon = \frac{\partial N^n}{\partial X} \delta v^n = \beta^n \, \delta v^n \qquad\qquad (7-6)$$

where X is coordinates of element points. Note δv^n are prescribed nodal values (independent variable defined at the element coordinates), while interpolation functions N^n is function of element coordinates X. Equation (7-4) can then be discretized as follow:

$$\int_V \sigma_e : \beta^n \, \delta v^n \, dV + \int_V S.u_w : \beta^n \, \delta v^n \, dV = \int_S \bar{t}.N^n \delta v^n \, ds + \int_V \bar{f}.N^n \delta v^n \, dV \qquad (7-7)$$

or

$$\int_V \beta^n : \sigma_e \, dV + \int_V \beta^n : S.u_w \, dV = \int_S N^n : \bar{t}. \, ds + \int_V N^n : \bar{f} \, dV \quad \text{if} \quad \delta v^n \neq 0$$

The left-hand side equation is known as internal force array:

Internal (mechanical) force array: $I_m^n = \int_V \beta^n : (\sigma_e + S.u_w)\, dV$

The second term, $\int_V \beta^n : S.u_w\, dV$, is coupling between fluid flow and equilibrium. The equation on the right-hand side is referred to as external force:

External (mechanical) force array: $P_m^n = \int_S N^n : \bar{t}.\, ds + \int_V N^n : \bar{f}\, dV$

Therefore equation (7-7) can be expressed as a balance of internal and external forces as follow:

$$f = I_m^n - P_m^n = 0 \tag{7-8}$$

The above equation is actually a system of nonlinear equations that is solved by Newton's method where the Jacobian matrix of the system with respect to the nodal coordinates X^n and the nodal fluid pressure u_w:

$$df = \frac{\partial f}{\partial X^n} dX^n + \frac{\partial f}{\partial u_w^{\,n}} du_w^{\,n} \tag{7-9}$$

The derivative of I_m^n can be expressed as follows:

$$dI^n = \frac{\partial I_m^n}{\partial X^n} dX^n + \frac{\partial I_m^n}{\partial u_w^{\,n}} du_w^{\,n} \tag{7-10}$$

where:

$$\frac{\partial I_m^n}{\partial X^n} dX^n = \left(\int_V \left(\frac{\partial \beta^n}{\partial X^n} : \sigma_e + \frac{\partial \beta^n}{\partial X^n} : (S.u_w) + \frac{\partial \sigma_e}{\partial X^n} : \beta^n + \frac{\partial (Su_w)}{\partial X^n} : \beta^n \right) dV \right) : dX^n$$

$$\frac{\partial I_m^n}{\partial u_w^{\,n}} du_w^{\,n} = \int_V \left(\frac{\partial (Su_w)}{\partial u_w^{\,n}} : \beta^n \right) dV : du_w^{\,n} \qquad \left(\text{note: } \frac{\partial \beta}{\partial u_w^{\,n}} = 0 \text{ and } \frac{\partial \sigma_e}{\partial u_w^{\,n}} = 0 \right)$$

The derivative of P_m^n can be expressed as follows:

$$dP_m^n = \frac{\partial P_m^n}{\partial X^n} dX^n + \frac{\partial P_m^n}{\partial u_w{}^n} du_w{}^n \qquad (7-11)$$

$$\frac{\partial P_m^n}{\partial X^n} dX^n = \left(\int_S \frac{\partial N^n}{\partial X^n} : \bar{t} \cdot ds + \int_V \frac{\partial N^n}{\partial X^n} : \bar{f} \, dV \right) : dX^n$$

$$\frac{\partial P_m^n}{\partial u_w{}^n} du_w{}^n = 0$$

In the above equation the $(\frac{\partial I_m^n}{\partial X^n} + \frac{\partial P_m^n}{\partial X^n})$ is the stiffness matrix and the $\frac{\partial I_m^n}{\partial u_w{}^n}$ is the coupling matrix:

$[K_m]$: stiffeness matrix $=$

$$\int_V \left(d\beta^n : \sigma_e + d\beta^n : (S.u_w) + \frac{\partial \sigma_e}{\partial X^n} : \beta^n + \frac{\partial (Su_w)}{\partial X^n} : \beta^n + \int_V \frac{\partial N^n}{\partial X^n} : \bar{f} \right) dV + \int_S \frac{\partial N^n}{\partial X^n} : \bar{t} \cdot ds$$

$$[K_{m-f}] : \text{coupling matrix} : \int_V \left(\frac{\partial (Su_w)}{\partial u_w{}^n} : \beta^n \right) dV \qquad (7-12)$$

Note that P_m^n is the prescribed surface and volumetric forces that its contribution to the Jacobian is generally neglected. Thus the "virtual work" equation can be represented in the following matrix form:

$$[K_m]\{dX^n\} + [K_{m-f}]\{du_w{}^n\} = \{I_m^n - P_m^n\} \qquad (7-13)$$

Constitutive response of porous medium

Abaqus assumes that the constitutive response of soil (as a porous medium) consists of (1) conventional constitutive theory for the soil skeleton, (2) constitutive theory for individual soil grains and (3) constitutive theory for the pore fluid.

Constitutive theory for the soil skeleton relates the effective stress array at a point to its corresponding strain array. It is a function of strain history and soil temperature:

$$\partial\sigma_e = D : (\partial\varepsilon - \alpha_s dT) \qquad (7-14)$$

Where D is the material constitutive matrix, α_s is the soil (linear/volumetric) thermal expansion coefficient and T is temperature.

Partially/fully saturated fluid flow through porous media

Continuity equations (mass conservation) are used in Abaqus to model fluid flow through porous medium. Continuity equation indicates that the rate at which mass is flowing in/out of a control volume is equal to the rate of change of mass within it. Consider a control volume in porous medium with total volume of V and surface $\bar{S}$, the continuity equation can be written as follow:

$$\int_V \frac{d}{dt}(\rho_w Sn)dV + \int_{\bar{S}} \rho_w Sn\bar{n}.v_w d\bar{S} = 0 \qquad (7-15)$$

The first term is the rate of change of fluid mass inside the control volume and the second term is the rate of the liquid mass crossing the surface $d\bar{S}$. Where v_w is the seepage velocity (or the average velocity of the wetting liquid relative to the solid phase) and $\bar{n}$ is the outward normal to $\bar{S}$ and n is the porosity of the medium. Note that S is degree of saturation, while $\bar{S}$ is surface of the control volume. Using the divergence theorem, equation (7-15) can be re-written as follow:

$$\int_V \frac{d}{dt}(\rho_w Sn)dV + \int_V \frac{\partial}{\partial X}(\rho_w Snv_w)dV = 0 \qquad (7-16)$$

Note that dV is the current volume (at time t) of the control volume, that can be expressed as function of the reference volume (dV_0) and volumetric strain (ε_V):

$$dV = (1 - \varepsilon_V)dV_0$$

According to Darcy's law, the volumetric flow rate of the wetting liquid through a unit area of the medium, Snv_w is proportional to the gradient of the piezometric head ($\phi = z + \frac{u_w}{\rho_w g}$), as follow:

$$Snv_w = -\left(\frac{\rho_w g}{\mu}\right) K \cdot \frac{\partial \phi}{\partial X} \tag{7-17}$$

Where, K is the conventional permeability of porous medium, μ is the dynamic viscosity and g is the gravitational acceleration. By substituting Equation (7-17) into Equation (7-16), the continuity equation can be re-written as follows:

$$\int_V \frac{d}{dt}(\rho_w Sn)dV - \int_V \frac{\partial}{\partial X}\left(\frac{(\rho_w)^2 g}{\mu}\right) K \cdot \frac{\partial}{\partial X}\left(z + \frac{u_w}{\rho_w g}\right) dV = 0 \tag{7-18}$$

In practice, however, $\frac{\partial z}{\partial X}$ is ignored due to its small values. Therefore, Equation (7-18) can be re-written as:

$$\int_V \frac{d}{dt}(\rho_w Sn)dV - \int_V \left(\frac{\rho_w}{\mu}\right) K \cdot \frac{\partial^2 u_w}{\partial X^2} dV = 0 \tag{7-19}$$

The first term can be re-written as follows:

$$\int_V \frac{d}{dt}(\rho_w Sn)dV = \rho_w \int_V \frac{d}{dt}(S\varepsilon_v + \frac{nu_w}{k_w} - (Sn\varepsilon_T^f + (1-n)\varepsilon_T^s)dV \tag{7-20}$$

Where ε_v is the volumetric and strain in soil skeleton, and ε_T^f and ε_T^s are thermal volumetric strain of pore fluid and solid, respectively. Therefore, Equation (7-19) can be re-written as follows:

$$\int_V \frac{d}{dt}(S\varepsilon_v - \frac{nu_w}{k_w} - \varepsilon_T)dV = \int_V \left(\frac{1}{\mu}\right)K \cdot \frac{\partial^2 u_w}{\partial X^2} dV \qquad (7-21)$$

Where, $\varepsilon_T = Sn\varepsilon_T^f + (1-n)\varepsilon_T^s$, $\varepsilon_T^f = \alpha_f \Delta T$ and $\varepsilon_T^s = \alpha_s \Delta T$.

α_f and α_s are volumetric thermal expansion coefficient of pore fluid and solid particles, respectively.

Finite element method is used, by attaching the mesh to the solid phase, to solve the above equation. The main variable is the pore fluid pressure u_w interpolated over the elements as a function u_w at the element's nodes.

$$u_w = N^n u_w^n \qquad (7-22)$$

Abaqus uses back-ward Euler method to approximate the derivative with respect to time. Thus, equation (7-22) is re-written as follows:

$$\int_V \left(\left(\frac{K}{\mu}\right)\frac{\partial^2 u_w}{\partial X^2}\right)_{t+\Delta t}dV - \frac{1}{\Delta t}[\int_V ((\rho_w S\varepsilon_v)_{t+\Delta t} - (\rho_w S\varepsilon_v)_t)dV$$

$$- \int_V \left(\left(\left(\frac{n}{k_w}\right)u_w\right)_{t+\Delta t} - \left(\left(\frac{n}{k_w}\right)u_w\right)_t\right)dV - \int_V \frac{d}{dt}((\varepsilon_T)_{t+\Delta t} - (\varepsilon_T)_t)dV] = 0 \qquad (7-23)$$

The weak form of the above equation is:

$$\int_V \omega((\frac{K}{\mu})\frac{\partial^2 u_w}{\partial X^2})_{t+\Delta t}dV - \frac{1}{\Delta t}[\int_V \omega((\rho_w S\varepsilon_v)_{t+\Delta t} - (\rho_w S\varepsilon_v)_t)dV - \int_V \omega\left((\frac{n}{k_w})u_w\right)_{t+\Delta t}$$

$$- \left((\frac{n}{k_w})u_w\right)_t)dV - \int_V \omega((\varepsilon_T)_{t+\Delta t} - (\varepsilon_T)_t)dV] = 0 \qquad (7-24)$$

ω is an arbitrary and continuous function. Using Galerkin method:

$$\omega = N^n \qquad (7-25)$$

Applying integration by part[4] on Equation (20) (i.e. the first term):

$$\int_S (\frac{K}{\mu})\omega\bar{n}.(\frac{\partial u_w}{\partial X})_{t+\Delta t}dS - \int_V (\frac{K}{\mu})\frac{\partial \omega}{\partial X}.(\frac{\partial u_w}{\partial X})_{t+\Delta t}dV - \frac{1}{\Delta t}[\int_V \omega((\rho_w S\varepsilon_v)_{t+\Delta t}$$

$$- (\rho_w S\varepsilon_v)_t)dV - \int_V \omega\left((\frac{n}{k_w})u_w\right)_{t+\Delta t} - \left((\frac{n}{k_w})u_w\right)_t)dV - \int_V \omega((\varepsilon_T)_{t+\Delta t} - (\varepsilon_T)_t)dV]$$

$$= 0 \qquad (7-26)$$

By substituting equation (7-25) into equation (7-26) the above equation can be rearranged as follows:

$$\int_V (\frac{K}{\mu})\frac{\partial N^n}{\partial X}.(\frac{\partial u_w}{\partial X})_{t+\Delta t}dV - \frac{1}{\Delta t}\int_V N^n\left((\frac{n}{k_w})u_w\right)_{t+\Delta t}dV + \frac{1}{\Delta t}\int_V N^n((\rho_w S\varepsilon_v)_{t+\Delta t}dV$$

$$= \int_S (\frac{K}{\mu})N^n\bar{n}.(\frac{\partial u_w}{\partial X})_{t+\Delta t}dS + \frac{1}{\Delta t}\int_V N^n\left((\frac{n}{k_w})u_w\right)_t dV - \frac{1}{\Delta t}\int_V N^n((\rho_w S\varepsilon_v)_t dV$$

---

[4] $\int_V v\nabla u \, dV = \int_S vu\bar{n} \, dS - \int_V u\nabla v \, dV$ ---- V and S are the element volume and the corresponding surface. $\bar{n}$ is the outward unit surface normal to S.

$$+ \frac{1}{\Delta t} \int_V N^n((\varepsilon_T)_{t+\Delta t} - (\varepsilon_T)_t) dV \qquad (7-27)$$

ε_v (volumetric strain) is equal to $(\varepsilon_x + \varepsilon_y + \varepsilon_z)$. In matrix form, therefore, ε_v is written as follows:

$$\varepsilon_v = m{:}\varepsilon , \qquad m = [1\ 1\ 1\ 0\ 0\ 0] \qquad (7-28)$$

$$\int_V \left(\frac{K}{\mu}\right) \frac{\partial N^n}{\partial X} \cdot \left(\frac{\partial u_w}{\partial X}\right)_{t+\Delta t} dV - \frac{1}{\Delta t} \int_V N^n \left(\left(\frac{n}{k_w}\right) u_w\right)_{t+\Delta t} dV + \frac{1}{\Delta t} \int_V N^n (\rho_w S m \varepsilon)_{t+\Delta t} dV$$

$$- \frac{1}{\Delta t} \int_V N^n \left(\left(\frac{n}{k_w}\right) u_w\right)_t dV + \frac{1}{\Delta t} \int_V N^n ((\rho_w S m \varepsilon)_t dV = \int_S \left(\frac{K}{\mu}\right) N^n \bar{n} \cdot \left(\frac{\partial u_w}{\partial X}\right)_{t+\Delta t} dS$$

$$+ \frac{1}{\Delta t} \int_V N^n((\varepsilon_T)_{t+\Delta t} - (\varepsilon_T)_t) dV \qquad (7-29)$$

Note $\varepsilon_T = \alpha_f \Delta T$, where α_f is the volumetric thermal expansion coefficient.

Let us represent equation (7-28) as follows:

$$f = I_f^n - P_f^n = 0$$

I_f^n is the left-hand side equation (integration over volume) (independent variables are X^n and u_w^n), while P^n is prescribed parameters (known parameter). Therefore, the Jacobian of (f) is:

$$df = dI_f^n = \frac{\partial I^n}{\partial X^n} dX^n + \frac{\partial I^n}{\partial u_w^n} du_w^n \qquad (7-30)$$

$$\frac{\partial I_f^n}{\partial X^n} dX^n = \int_V \frac{\partial}{\partial X^n} \left[\left(\frac{K}{\mu}\right) \frac{\partial N^n}{\partial X} \cdot \left(\frac{\partial u_w}{\partial X}\right)_{t+\Delta t} dV - \frac{1}{\Delta t} \int_V N^n \left(\left(\frac{n}{k_w}\right) u_w\right)_{t+\Delta t} dV$$

$$+ \frac{1}{\Delta t} \int_V N^n ((\rho_w S m \varepsilon)_{t+\Delta t}] dV dX^n$$

$$\frac{\partial I_f^n}{\partial u_w^n} du_w^n = \int_V \frac{\partial}{\partial u_w^n} \left[\left(\frac{K}{\mu}\right) \frac{\partial N^n}{\partial X} \cdot \left(\frac{\partial u_w}{\partial X}\right)_{t+\Delta t} dV - \frac{1}{\Delta t} \int_V N^n \left(\left(\frac{n}{k_w}\right) u_w\right)_{t+\Delta t} dV$$

$$+ \frac{1}{\Delta t} \int_V N^n ((\rho_w S m \varepsilon)_{t+\Delta t}] dV du_w^n$$

Note that the variation of integral at time (t) is zero. In the above equation the $\frac{\partial I_f^n}{\partial u_w^n}$ is the (hydraulic) stiffness matrix and the $\frac{\partial I_f^n}{\partial X^n}$ is the coupling matrix:

$\frac{\partial I_f^n}{\partial u_w^n}$: (hydraulic) stiffness matrix : $[K_f]$

$$\int_V \frac{\partial}{\partial u_w^n} \left(\left(\left(\frac{K}{\mu}\right) \frac{\partial N^n}{\partial X} \cdot \left(\frac{\partial u_w}{\partial X}\right)_{t+\Delta t} - \frac{1}{\Delta t} \int_V N^n \left(\left(\frac{n}{k_w}\right) u_w\right)_{t+\Delta t} + \frac{1}{\Delta t} \int_V N^n ((\rho_w S m \varepsilon)_{t+\Delta t}] \right) dV \right)$$

$\frac{\partial I_f^n}{\partial X^n}$: coupling matrix: $[K_{f-m}]$

$$\int_V \frac{\partial}{\partial X^n} \left(\left(\left(\frac{K}{\mu}\right) \frac{\partial N^n}{\partial X} \cdot \left(\frac{\partial u_w}{\partial X}\right)_{t+\Delta t} - \frac{1}{\Delta t} \int_V N^n \left(\left(\frac{n}{k_w}\right) u_w\right)_{t+\Delta t} + \frac{1}{\Delta t} \int_V N^n ((\rho_w S m \varepsilon)_{t+\Delta t}] \right) dV \right)$$

Thus, the continuity equation can be re-written in matrix form as follows:

$$[K_f]\{dX^n\} + [K_{f-m}]\{du_w^n\} = [I_f^n - P_f^n] \tag{7-31}$$

Heat transfer through porous media

The Abaqus is able to analyze heat transfer through a porous medium by modeling solid body heat conduction, convection and radiation. Heat conduction is modeled by solving basic energy balance equation which is:

$$\int_V \rho \dot{U} dV = \int_S q \, dS + \int_V r \, dV \qquad (7-32)$$

Where V is the volume of the control volume, S is the surface area, ρ is the density of the material, $\dot{U}$ is the time rate of the internal energy, q is the heat flux per unit area flowing into the body, and r is the heat supplied internally into the body per unit volume. It is assumed that thermal response is not influenced by mechanical/hydraulic responses.

The term on the left-hand side of the above equation can also be written in the following form:

$$\int_V \rho \dot{U} dV = \int_V \rho \frac{\partial(c_V T)}{\partial t} dV \qquad (7-33)$$

Where, c_V is the heat capacity. On the other hand, the heat flux per unit area q, is assumed to be governed by the Fourier law,

$$q = -\lambda \frac{\partial T}{\partial X} \qquad (7-34)$$

Where λ is the conductivity matrix, which is typically a function of temperature, T is temperature, and X is position. The conductivity can be fully anisotropic, orthotropic, or isotropic.

By substituting Equations (7-32) and (7-33) into Equation (7-34) the following equation is resulted:

$$\int_V \frac{\partial(\rho c_V T)}{\partial t} dV = \int_S -\lambda \frac{\partial T}{\partial X} dS + \int_V r\, dV \qquad (7-35)$$

By applying the divergence theorem, the following equation is resulted:

$$\int_V \frac{\partial(\rho c_V T)}{\partial t} dV = \int_V \frac{\partial}{\partial X}(-\lambda \frac{\partial T}{\partial X}) dV + \int_V r\, dV \qquad (7-36)$$

The weak form of the above equation is:

$$\int_V \omega \frac{\partial(\rho c_V T)}{\partial t} dV = \int_V \omega \frac{\partial}{\partial X}(-\lambda \frac{\partial T}{\partial X}) dV + \int_V \omega r\, dV \qquad (7-37)$$

By applying integration by part on the equation (i.e. the first term on the right-hand side):

$$\int_V \omega \frac{\partial(\rho c_V T)}{\partial t} dV = \int_V \frac{\partial \omega}{\partial X} \cdot (-\lambda \frac{\partial T}{\partial X}) dV - \int_S \omega \bar{n} \cdot \left(-\lambda \frac{\partial T}{\partial X}\right) dS + \int_V \omega r\, dV \qquad (7-38)$$

Note that $T = N^n T^n$ and $\omega = N^n$ (Standard Galerkin approach).

Back-ward Euler method is used to approximate the derivative with respect to time.

$$\frac{1}{\Delta t}[\int_V (N^n)^T (\rho c_V T)_{t+\Delta t} dV - \int_V (N^n)^T (\rho c_V T)_t dV] + \int_V \left(\frac{\partial N^n}{\partial X}\right)^T \cdot \left(-\lambda \frac{\partial T}{\partial X}\right)_{t+\Delta t} dV =$$

$$\int_S N^n \bar{n} \cdot \left(\lambda \frac{\partial T}{\partial X}\right) dS + \int_V N^n r\, dV \qquad (7-39)$$

Which can be rearranged as follows (by ignoring $\int_V N^n r\, dV$ which is very common in energy pile application):

$$\frac{1}{\Delta t}\int_V (N^n)^T (\rho c_V T)_{t+\Delta t} dV - \int_V \left(\frac{\partial N^n}{\partial X}\right)^T \cdot \left(\lambda \frac{\partial T}{\partial X}\right)_{t+\Delta t} dV$$

$$= \int_S N^n \bar{n} \cdot \left(\lambda \frac{\partial T}{\partial X}\right) dS + \frac{1}{\Delta t}\int_V (N^n)^T (\rho c_V T)_t dV \qquad (7-40)$$

The above equation can be represented as follows:

$$f = I_T^n - P_T^n = 0$$

I_T^n is the left-hand side equation (integration over volume) is variable with respect to T, while P_T^n is prescribed parameters (known parameter). Note that the first term on the left side is the prescribed heat flux. Therefore, the Jacobian of (f) is:

$$df = dI_T^n = \frac{\partial I^n}{\partial T} dT^n$$

$$\frac{\partial I^n}{\partial T} dT^n = [\int_V \frac{\partial}{\partial T}(\frac{1}{\Delta t}(N^n)^T(\rho c_V T)_{t+\Delta t})dV - \int_V \frac{\partial}{\partial T}((\frac{\partial N^n}{\partial X})^T \cdot (\lambda \frac{\partial T}{\partial X})_{t+\Delta t})dV] \, dT^n \quad (7-41)$$

In the above equation:

$$[K_{hc}] = \text{Heat storage matrix} = \int_V \frac{\partial}{\partial T}(\frac{1}{\Delta t}(N^n)^T(\rho c_V T)_{t+\Delta t})dV$$

$$[K_{hs}] = \text{Heat conductance matrix} = \int_V \frac{\partial}{\partial T}((\frac{\partial N^n}{\partial X})^T \cdot (\lambda \frac{\partial T}{\partial X})_{t+\Delta t})dV$$

Thus, the energy balance equation can be re-written in matrix form as follows:

$$[K_{hc}]\{dT^n\} + [K_{hs}]\{dT^n\} = [I_T^n - P_T^n] \qquad (7-42)$$

Fully coupled thermo-hydro-mechanical analysis in porous media

Since it is assumed that heat transfer in porous media is independent of mechanical/hydraulic behavior, a THM analysis is performed by first solving the pure heat transfer problem (equation

(7-42)), then reading the temperature solution into a stress and fluid flow analyses as a predefined field. The virtual work and continuity equations (matrix form) can be solved together. Thus, the following equation should be solved for a fully coupled THM analysis:

$$[K_{hc}]\{dT^n\} + [K_{hs}]\{dT^n\} = [I_T^n - P_T^n] \tag{7-43}$$

$$\begin{bmatrix} K_m & K_{m-f} \\ K_{f-m} & K_f \end{bmatrix} \begin{Bmatrix} dX^n \\ du_w^n \end{Bmatrix} = \begin{Bmatrix} I_m^n - P_m^n \\ I_f^n - P_f^n \end{Bmatrix} \tag{7-44}$$

7-3- Numerical simulation of experimental test results

Triaxial test results:

The analyses aim to reproduce the results of the CD triaxial tests presented in chapter 3. Figure 7-1 shows the geometry of the FE clay specimen model which is the same as the actual specimen presented in chapter 3 (i.e. the diameter and height are 5 cm and 10 cm, respectively). Due to axisymmetric geometry, only half of the specimen was modeled in this simulation. The FE mesh contains 12992 elements and 14877 nodes. The 8-node trilinear displacement, pore pressure, and temperature element, C3D8PT, was used for modeling thermo-hydro-mechanical (THM) response of the clay specimen. The element, available only for axisymmetric and three-dimensional problems, has pore pressure degree of freedom, displacement degree of freedom 1-3 and temperature degree of freedom. Furthermore, the element uses linear- interpolation for the geometry and displacements, pore pressure and temperature (Abaqus Analysis User's Manual).
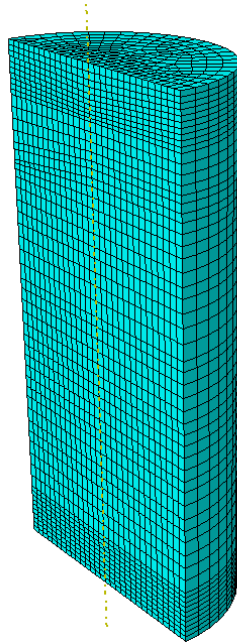
Figure 7-1- Geometry of FE model of clay specimen used in Triaxial tests (chapter 3).

The initial temperature of the soil and the initial pore water pressure are 24 °C and zero, respectively. The initial effective stress is isotropic stress determined by the applied isotropic (cell) pressure, as discussed in detail in the following sections. The clay was assumed to be fully saturated and gravity was neglected.

Assuming a perfectly rough contact between the clay and pore stone, the base of the model was fully restrained (i.e. pinned boundary), while the top surface was only fixed in horizontal direction. The displacement perpendicular to the plane of symmetry was restrained (i.e., roller boundary), while the outer side was free to move. Fluid flow is allowed through the top surface (i.e. pore pressure is zero), while other sides of the model are impermeable. As for thermal boundary condition, heat flow is allowed through all boundaries.

The elastic deformation of the soil was modeled using porous elastic model, while the plastic response was modeled with modified cam-clay plasticity. According to porous elastic model the elastic volumetric strain ε_v^{el} is linked to effective isotropic pressure P $(= -\frac{1}{3} \text{ trace } (\sigma))$ as follows:

$$\varepsilon_v^{el} = 1 - \frac{\kappa}{1+e_0} \text{ Ln} \left(\frac{P}{P_0}\right) \tag{7-45}$$

Where κ is a material parameter, and e_0 and P_0 are the initial void ratio and effective isotropic pressure (Figure 7-2).
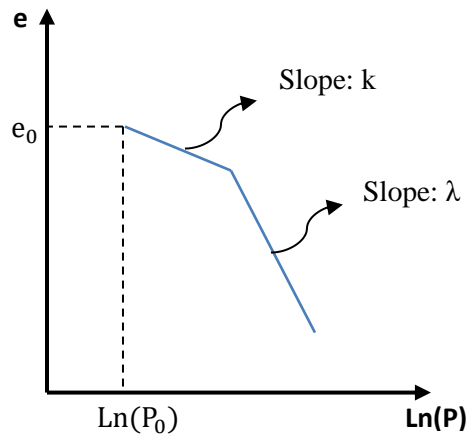
Figure 7-2- Porous elastic model [3].

Assuming that the tensile strength of clay is zero, the general modified Cam-clay yield function used by Abaqus can be written as ([3]):

$$\frac{1}{\beta^2} \left(\frac{P}{a} - 1\right)^2 + \left(\frac{q}{Ma}\right)^2 - 1 = 0 \tag{7-46}$$

Where;

P : effective isotropic stress $= -\dfrac{1}{3}\,\text{trace}(\sigma)$

q : equivalent shear stress $= \sqrt{(\dfrac{3}{2}\,S{:}\,S)}$

S : deviatoric stress $= (\sigma + PI)$

M: the slope of the critical state line in P-q plane (Figure 7-3)

a: is a measure of yield surface size which is usually equal to $\dfrac{P_c}{2}$ (Figure 7-3)

β: constant used to modify the shape of the yield surface on the wet side of critical state ($P \leq P_c$)

(Figure 7-3)
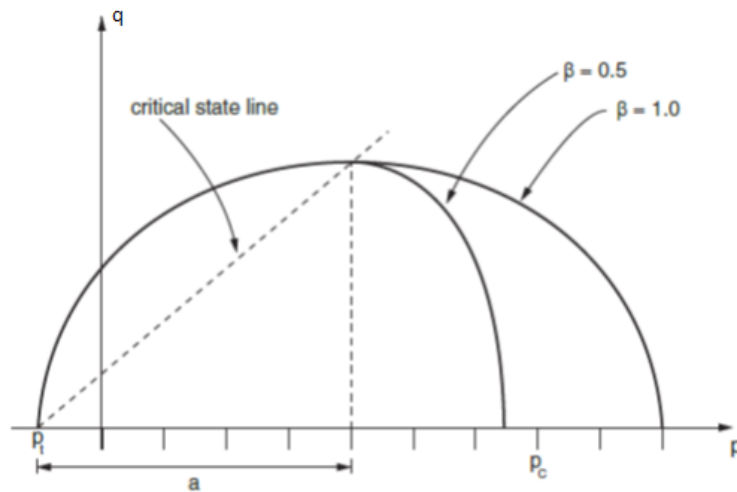
Figure 7-3- Cam-clay yield surface in p-q plane ([3]).

Note that P_c is the consolidation pressure at any time, which can be written as:

$$P_c = P_{c0}\,\exp\!\left(\left(\dfrac{1 + e_0}{\lambda - \kappa}\right)\varepsilon_v^{pl}\right) \tag{7 $-$ 47}$$

Where ε_v^{pl} is a plastic portion of the volumetric strain, and P_{c0} is the effective pre-consolidation pressure. Mechanical/hydraulic/thermal properties of clay are presented in Table 7-1. It was assumed that the clay is fully saturated and heat transfer only occurs through conduction mechanism. The mechanical properties are calibrated based on the experimental tests presented in chapter 3. In fact, the data from consolidation phase at isothermal condition (under three confining pressures) was used to estimate κ and λ. M and its relationship with temperature were calibrated based on the results obtained from shearing phase (i.e. $q - p$ plane) under isothermal/non-isothermal conditions. Back analysis of deviatoric stress-axial strain at isothermal condition ($q - \varepsilon$) was used to determine β. Hydraulic permeability was assumed to linearly vary with porosity, as shown in Table 7-1.

Table 7-1- Soil properties used in numerical simulation.

Physical properties	
dry unit weight γ_{dry}	$1360\ ^{kg}/_{m^3}$
initial porosity n	0.462
Mechanical properties	
a	75 kPa (for P_{C0} = 150 kPa)
	100 kPa (for P_{C0} = 200 kPa)
	150 kPa (for P_{C0} = 300 kPa)
compression index λ	0.085
recompression index κ	0.014
slope of critical state line M	1 at 24 °C
	1.014 at 34 °C
	1.0485 for heat cycle (24-34-24 °C)
Poisson's ratio	0.25
Hydraulic properties	
permeability coefficient k (*)	1.257×10^{-9} m/s (at n=0.48)
	1.1×10^{-9} m/s (at n=0.46)
	1.01×10^{-9} m/s (at n=0.45)
Thermal properties	
specific heat capacity c	$1450\ ^{j}/_{kg.\,C°}$ (for P_{C0} = 150 kPa)
	$1439\ ^{j}/_{kg.\,C°}$ (for P_{C0} = 200 kPa)
	$1420\ ^{j}/_{kg.\,C°}$ (for P_{C0} = 300 kPa)
thermal conductivity coefficient λ	$2.037\ ^{W}/_{m.\,C°}$ (for P_{C0} = 150 kPa)
	$2.07\ ^{W}/_{m.\,C°}$ (for P_{C0} = 200 kPa)
	$2.12\ ^{W}/_{m.\,C°}$ (for P_{C0} = 300 kPa)
Clay thermal expansion coefficient α_{clay}	3.5×10^{-5} 1/C°
water thermal expansion coefficient α_{water}	$2.1\ \times 10^{-4}$ 1/C°

(*) $k = 1.49\ e^{2.03}\ \times 10^{-9}\ \frac{m}{s}$, where e is void ratio [4].

(**) $c = \rho_w c_w n + \rho_s c_{ws}(1 - n)$, where w and s denote water and soil, respectively [5].

(***) $\lambda = \lambda_w^n . \lambda_s^{(1-n)}$, where w and s denote water and soil particles, respectively [6].

Furthermore, all properties were assumed to be temperature independent, except for M. As previously observed in chapter 3, the experimental results indicated that M increases due to heat application. Accordingly, to consider the temperature dependence of M the following values were

considered for M under different thermal loading path; M = 1.0 at isothermal condition (24 °C), M

= 1.014 at elevated temperature (34 °C), and M = 1.0485 under cyclic heating.

Like the experimental analysis (chapter 3), the numerical analysis is run in three steps: isotropic

consolidation (initial geostatic equilibrium), thermal loading and drained shearing. In the first step

(isotropic consolidation) an initial geostatic analysis was considered where the confining pressure

(150 kPa, 200 kPa and 300 kPa) was applied to the outer side and the top surface and the initial

stress was given through initial condition. The initial stress components are essentially equal to

the outer geostatic pressure (confining pressure). In geostatic analysis step, Abaqus checks whether

the equilibrium is satisfied between the current confining pressure and the given initial stresses. If

it is not, the hardening parameter "a" is modified to create an equilibrium between them.

In the second step, similar thermal loading paths were considered. Transient soil consolidation

analysis was applied used an automated time stepping. Variable surface temperature (like those

shown in chapter 3) were applied to the outer surface and the top surface to simulate thermal

loading. To simulate drained heating, drainage was allowed through the top surface, similar to

experimental tests.

In the third step, drained shearing, the top surface was moved downward (with a rate of 0.005

mm/min) by 20% of the initial specimen height. A transient soil consolidation analysis with

drainage through the top surface was also considered for this step. Drainage occurred through the

top surface. Although there was some excess pore pressure generated in the beginning of loading,

drainage condition was satisfied during the rest of loading. It should be noted that the geometric

nonlinearity due to 20% soil compression was ignored in the current analysis. The accuracy of the

time integration for the second and third steps using transient soil consolidation analysis was

controlled by maximum allowable values for pore pressure and temperature. Figures 7-4, 7-5 and 7-6 compares the shearing response of NC clay (under different thermo-mechanical loading) estimated using numerical and experimental analyses.

(a)

(b)
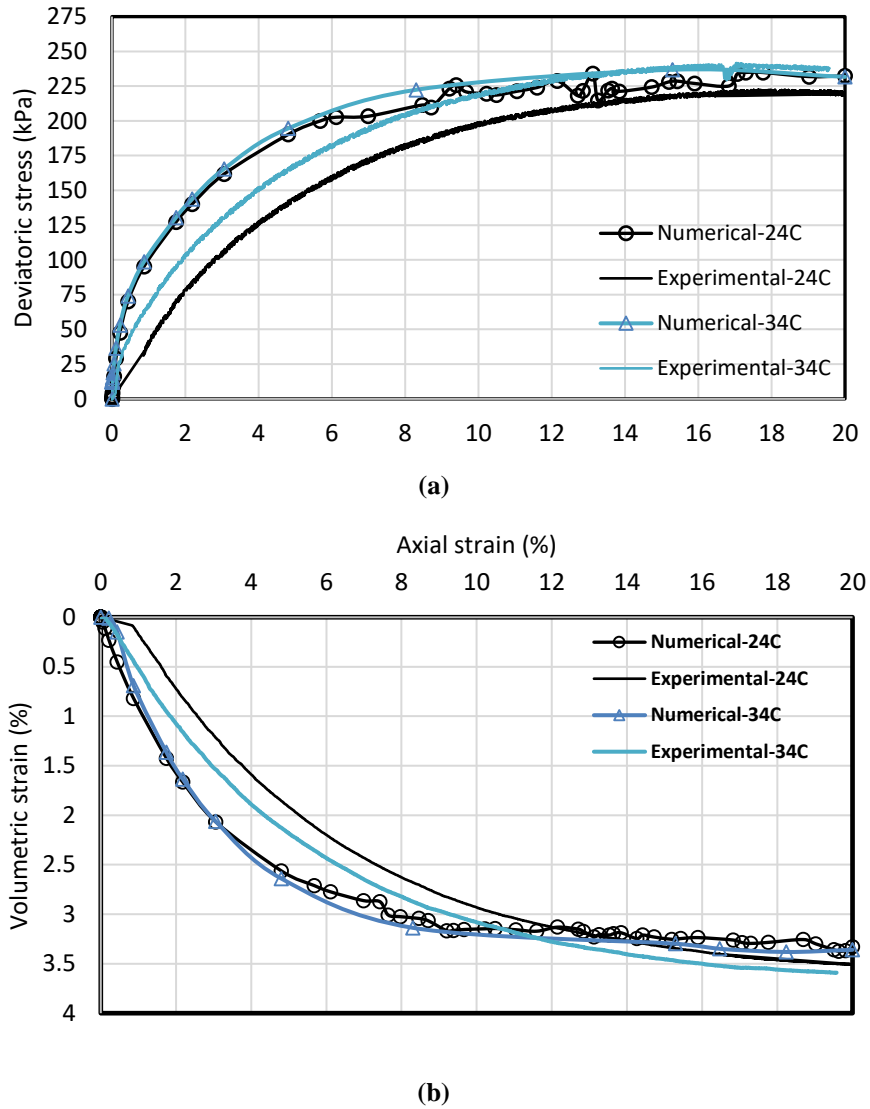
Figure 7-4- Triaxial test results (under confining pressure of 150 kPa): **(a)** deviatoric stress-axial strain curve, and **(b)** volumetric strain-axial strain.
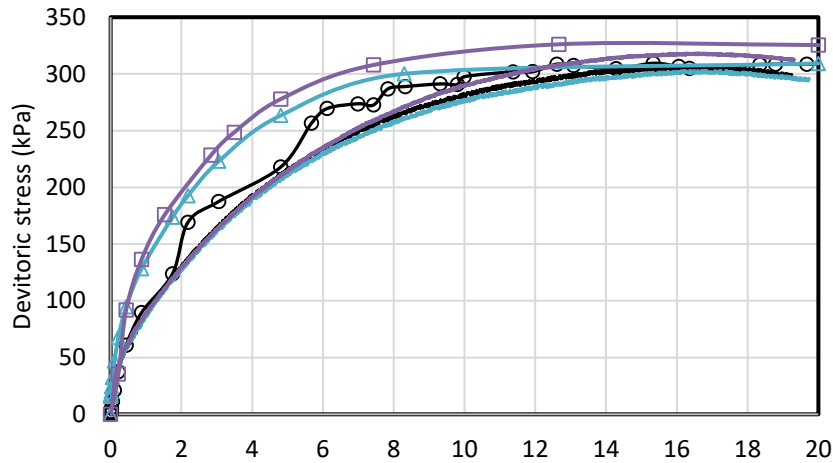
(a)
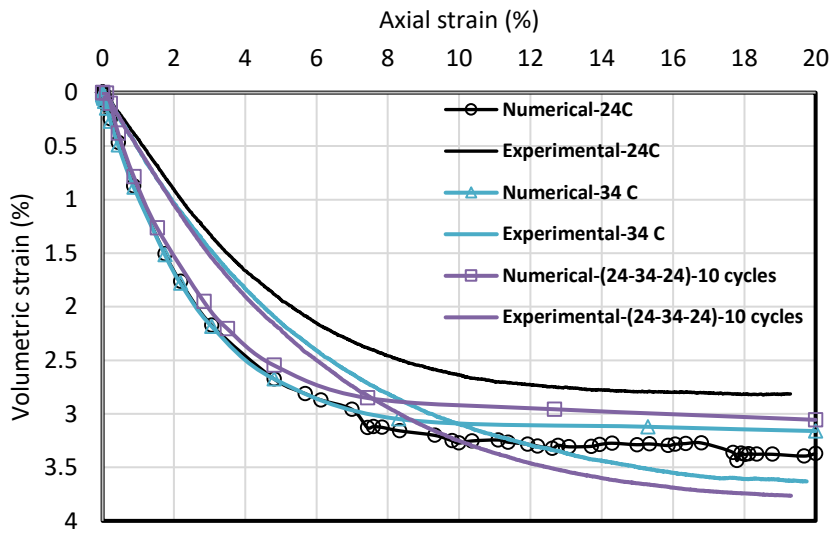
(b)

Figure 7-5- Triaxial test results (under confining pressure of 200 kPa): **(a)** deviatoric stress-axial strain curve, and **(b)** volumetric strain-axial strain.

Generally, a good agreement between numerical and experimental results is observed. The "deviatoric stress-axial strain" responses were predicted relatively well, although with some loss of accuracy at strains smaller than 10%. In fact, the shear stress was overestimated at lower axial strain, where the clay strength was estimated to be (up to) 14% higher than that physically measured. This discrepancy may be attributed to uncertainty in clay properties calibration or/and

temperature-independent constitutive model used for clay. However, the predicted shear strength at larger axial strains, where critical state is approached, agreed more reasonably with that estimated by experimental analysis.

Similar discussion can be made for volumetric response of clay.

(a)

(b)

Figure 7-6- Triaxial test results (under confining pressure of 200 kPa): **(a)** deviatoric stress-axial strain curve, and **(b)** volumetric strain-axial strain.
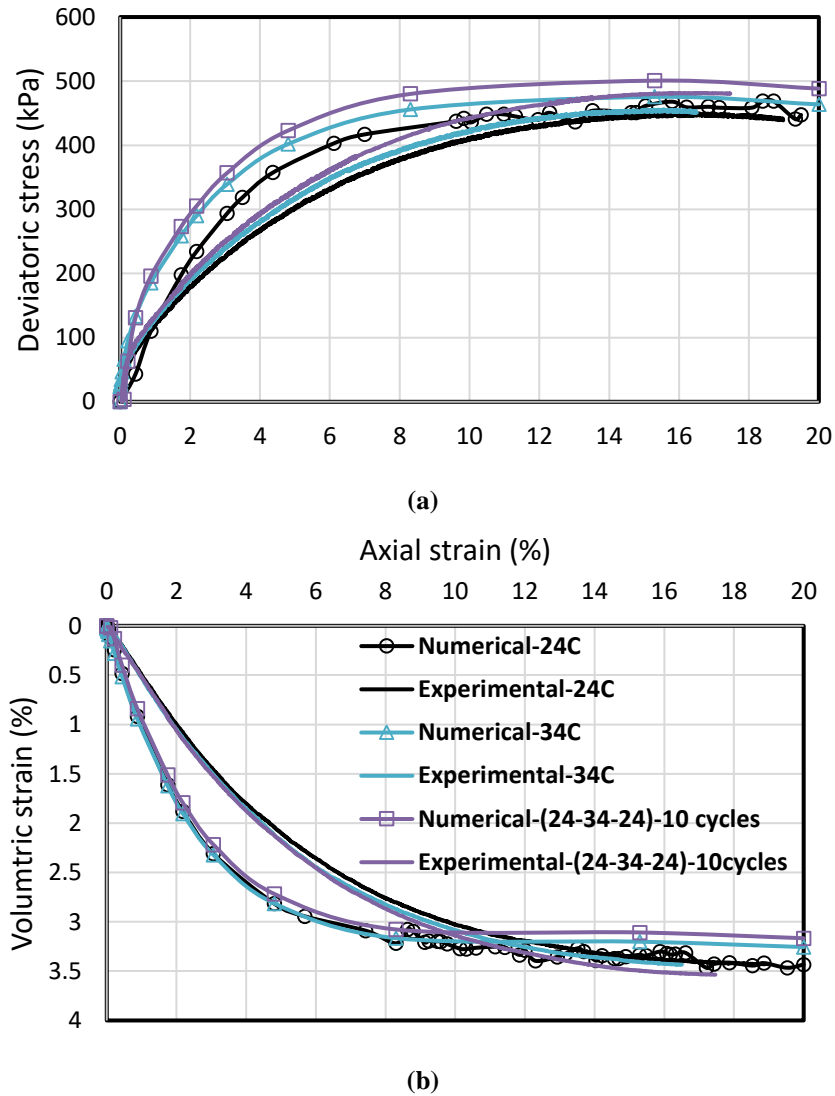
Figure 7-7 shows well agreement between the simulations and experimental results, for the peak value of shear strength. The calculated error is lower than 5% which is negligible.

(a)   (b)
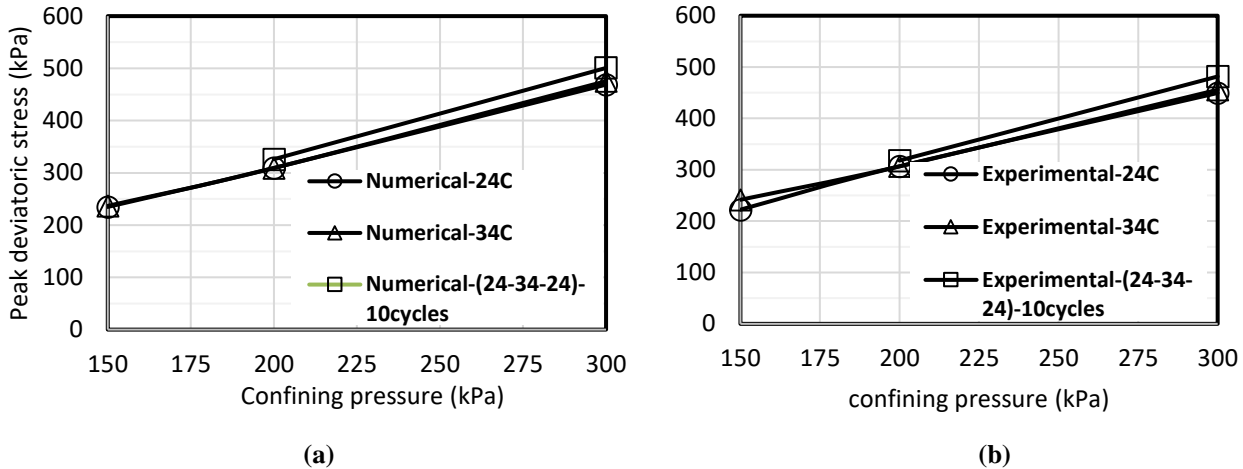
Figure 7-7- Peak deviatoric stress versus confining pressure: (a) results from numerical analysis, and (b) results from experimental analysis.

Small scale pile test results

The analyses aim to reproduce the results of the small-scale pile tests presented in chapter 5. Figure 7-8 shows the geometry of the model pile and surrounding clay. The dimension of the model is the same as that used in experimental tests presented in chapter 5 (i.e. The overall diameter of the model including the pile and surrounding clay has a diameter of 170 mm, and a length of 230 mm. the pile diameter is 19 mm.). Like CD triaxial simulation, only half of the specimen was modeled in this simulation due to axisymmetric geometry. A finer mesh was used around the pile surface to model shear stress/strain localization in the shear band. Furthermore, mesh sensitivity analysis was initially conducted to ensure the selected discretization is acceptable. The FE mesh contains 15600 elements and 17794 nodes (for clay part) and 1800 elements and 2883 nodes. The C3D8PT and C3D8T (8-node trilinear displacement, and temperature element) were used for modeling the pile body and the surrounding clay, respectively.
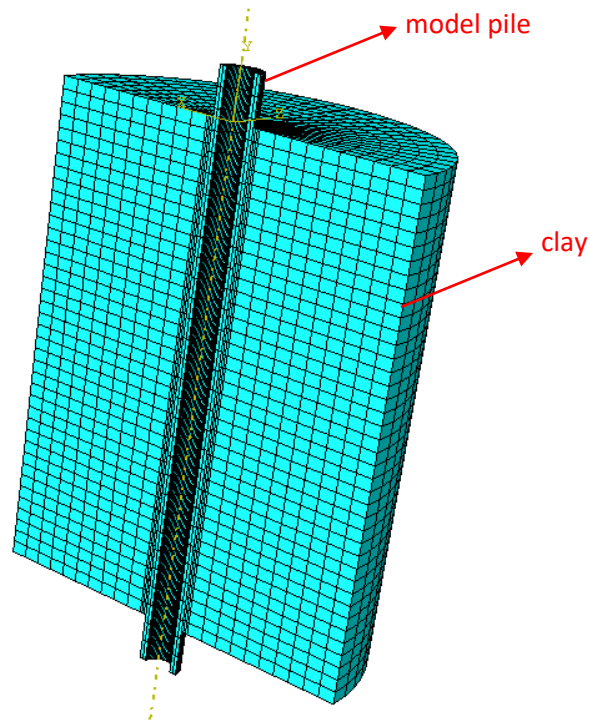
Figure 7-8- Geometry of FE model of the model pile and surrounding clay (chapter 5).

The initial temperature of the pile and surrounding soil is 24 °C. The initial pore water pressure in the surrounding clay is zero, while the pile body was assumed to be impervious (meaning that fluid flow does not occur in the pile). The initial effective stress in the pile and surrounding soil, due to overburden pressure (100 kPa), was calculated considering at-rest lateral coefficient K_0 equal to 0.9. It should be noted that the accurate determination of K_0 was difficult due to the specific clay specimen preparation method used in this study. As shown in chapter 5, the clay was reconstituted by consolidating clay (in a cylindrical container with small volume and rigid walls) from a slurry state. Therefore, in the early stages (under low pressure), during which the clay behaves like a fluid or is very soft, where the internal friction angle of clay is very small, an isotropic stress state is very likely to develop, and K_0 is expected to approach 1.0, according to Jaky's equation. However, at larger consolidation load, when the clay specimen becomes relatively stiff, an anisotropic stress

state develops causing larger internal friction angle and K_0 essentially smaller than 1.0. According to this fact and the "load-settlement" obtained under isothermal condition K_0 was taken as 0.9. The surrounding clay was assumed to be fully saturated and gravity was neglected.

Assuming that the clay can slide freely with respect to inner sides of the wall and the base, the normal displacement to the plane of symmetry, outer side and bottom of the model was restrained (i.e., roller boundary), while the top surface was free to move. Fluid flow is allowed through a portion of the bottom surface (a circle having a diameter of 3.0 cm at the center of the base), while other sides of the model are impermeable. As for thermal boundary condition, heat flow was only allowed through the top and bottom faces.

The elastic and plastic responses of the surrounding clay were modeled with porous elastic and modified cam-clay model, respectively. The properties presented in Table 7-1 were also used to model the THM response of clay. The pile was modelled as a thermo-elastic material. Table 7-2 presents the mechanical and thermal properties of the pile. The properties were determined assuming that the pile is made entirely of steel.

Table 7-2- Mechanical/thermal properties of the pile

Physical properties	
unit weight γ_{pile}	$7800 \ ^{kg}/_{m^3}$
Mechanical properties	
Modulus of elasticity E_{pile}	200 GPa
Poisson's ratio ν_{pile}	0.3
Thermal properties	
specific heat capacity c_{pile}	$500 \ ^{j}/_{kg. \, C^\circ}$
thermal conductivity coefficient λ_{pile}	$40 \ ^{W}/_{m. \, C^\circ}$
thermal expansion coefficient α_{pile}	$15 \times 10^{-5} \ 1/C^\circ$

Coulomb friction model was used to simulate the pile-soil contact (interaction) in tangential direction. According to Coulomb model, the following relationship is defined between the maximum shear stress τ and normal stress σ_n across the interface:

$$\tau_{max} = \mu \cdot \sigma_n$$

$$\mu = \tan(\delta)$$

μ is known as friction coefficient and δ is the interface friction angle. Once the shear stress at the contacting points reach τ_{max}, they start sliding relative to each other (sliding state). By default, there is no relative motion between contacting points when the shear stress is less than τ_{max} indicating that the shear stiffness of interface is infinity (sticking state). However, penalty method can be used to define a finite value for the shear stiffness based on which some relative motion is permitted before τ_{max} is reached. Friction coefficient μ was estimated to be 0.049. The value was obtained by dividing the unit shaft resistance (at isothermal condition) by the estimated normal pressure ($K_0\sigma_v = 0.9 \times 100 \text{ kPa} = 90 \text{ kPa}$).

As for contact pressure-overclosure relationship, "hard" contact relationship was used, based on which any contact pressure can be transmitted once the surfaces are in contact. The contact pressure reduces to zero when contacting surfaces separate. Conductive heat transfer was considered between the pile and surrounding soil using the following equation:

$$q = \lambda_{interface} (T_{pile} - T_{soil})$$

where, $\lambda_{interface}$ is thermal conductive coefficient of the interface, T_{pile} and T_{soil} are the temperature of pile surface and soil surface at a contact point. $\lambda_{interface}$ is assumed to be the same as that of pile, $40 \text{ }^W/_{m. C^\circ}$.

Simulations were done in three steps: initial geostatic equilibrium (under overburden pressure $\sigma_v = 100$ kPa), thermal loading and pile loading. In the first step an initial geostatic analysis was used to establish an equilibrium with overburden pressure (applied to the top surface) and initial stresses (with uniform vertical component of 100 kPa and lateral coefficient of 0.9).

In the second step, uniform temperature variations (i.e. 24 °C (isothermal condition), 34 °C (elevated temperature), and (24-34-24 °C)- 10 cycles, 20 cycles and 40 cycles) were applied to the pile inner surface (across the plane of symmetry). Transient soil consolidation analysis was applied used an automated time stepping.

Undrained pile loading step (the third step) was modeled by downward movement (by 20 mm) of the top surface (with a rate of 0.25 mm/min). A transient soil consolidation analysis with drainage through a portion of the bottom surface was considered.

Figures 7-9 compares the load-settlement response of the small-scale pile estimated using numerical and experimental analyses. It can be seen that the pile response to the axial load was correctly predicted under isothermal condition and cyclic heating. The predicted pile response, however, does not reproduce the peak observed in experimental results. It is mainly because of this fact that the interface was assumed to be elastic perfectly plastic (Coulomb friction model). For this case, Abaqus predicts the max pile load with and error of less than 6%. Under elevated temperature (34 °C), however, there is discrepancy between the results, where a lower shaft resistance is predicted by Abaqus.
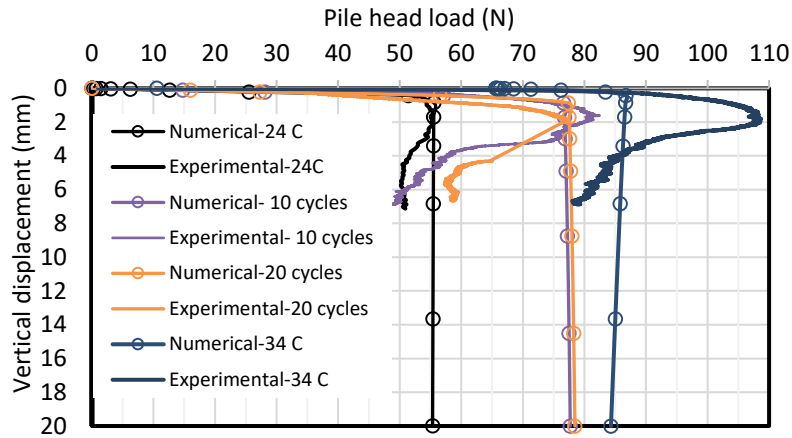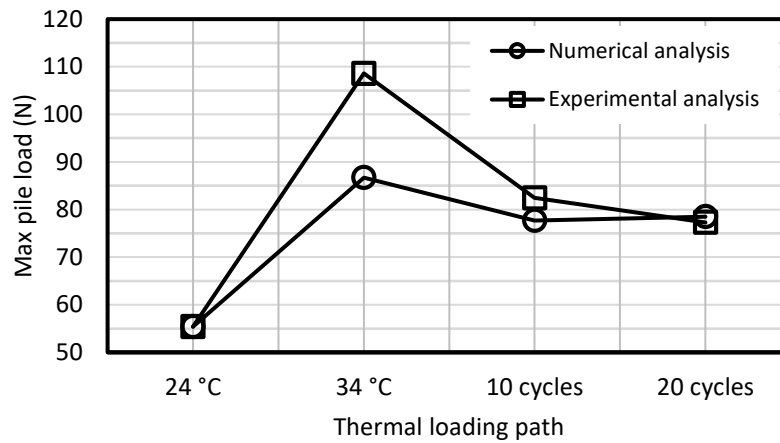
Figure 7-9- Simulated and measured pile load-settlement curve: (a) load-displacement curve, and (b) max pile load-thermal loading path.

Figure 7-10 illustrates the variation of temperature-induced excess PWP, total lateral pressure and effective lateral pressure at the pile-clay interface versus heat cycles. Note that the data corresponding to the end of each cycle was only plotted. These data could be very informative as they were not directly measured in the laboratory tests. In fact, they can help understand the contributing factors to the observed shaft resistance improvement. According to the figure, the heat induced excess PWP increases due to the first heat cycle, followed by a progressive decrease at a reduced rate with heat cycles. In fact, it is nearly unchanged since the heat cycle number 7,

where the induced PWP is ≈ -10 kPa. This behavior was also observed for the measured PWP in the soil 1D away from the pile surface (chapter 5). The total lateral pressure also shows same trend toward heat cycles, where it stabilized at ≈ 54 kPa since the cycle number 7. As for the lateral effective pressure, it rose by ≈ 41% in the first 3 heat cycles. in the following cycles, however, the lateral effective pressure stabilized at a value of ≈ 63 kPa.

(a)

(b)
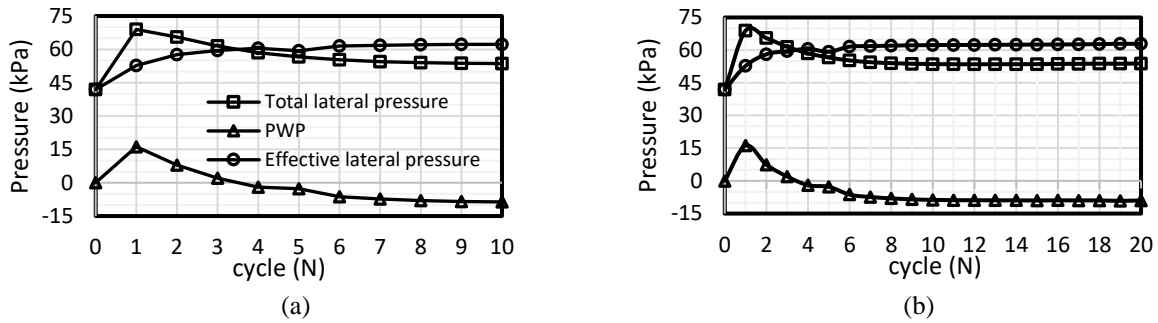
Figure 7-10- Variation of Total/effective lateral pressure and heat induced excess PWP with heat cycles: (a) 10 heat cycles, and (b) 20 heat cycles.

Figure 7-11 shows the ratio of the effective lateral stress ($\frac{\sigma_{n-T}}{\sigma_{n-T_0}}$) at the beginning of pile loading step (at the end of last heat cycle). Note that σ_{n-T} and σ_{n-T_0} are the effective lateral stress at non-isothermal and isothermal conditions, respectively. The ratio approximated by experimental tests is less than that predicted by numerical simulations (i.e. 1.35 against 1.48 for 10 heat cycles, and 1.36 against 1.49 for 20 heat cycles). This discrepancy may be caused by the assumption made in the analysis of experimental results in which the interface friction angle (measured in small pile test) was assumed to be the same as that one obtained in direct shear test. As mentioned in chapter 6, the friction angle at the pile-clay interface is expected to be lower than that at the concrete-clay interface in direct shear test. However, both simulation and experimental results indicate increase in lateral effective pressure mostly contribute to the shaft enhancement.
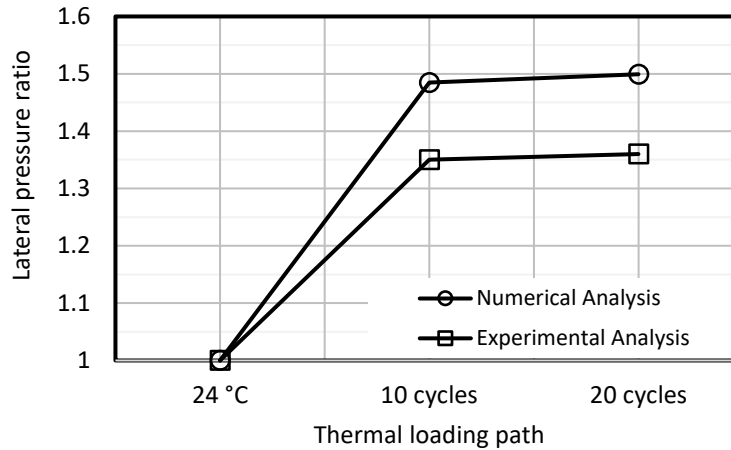
Figure 7-11- Ratio of the effective lateral pressure at non-isothermal and isothermal conditions (numerical versus experimental analysis).

7-4- Conclusion

The following conclusions can be drawn from the results in this chapter:

- Generally, there is good agreement between the results measured and simulated. THM analysis can effectively be used to describe the thermo-mechanical response of energy piles in clays.

- Both measured and simulated results indicate that a negative PWP gradually develops in the clay (around the piles) with heat cycles. The negative PWP partially contributes to the increased shaft resistance.

- Both approaches suggest that the increased shaft resistance is mainly related to the heat-induced increase in the effective lateral stress.

References:

[1] ABAQUS 2016, Analysis User's Guide Volume II: Analysis, Section 6.1.1: Solving Analysis Problems: Overview.

[2] ABAQUS 2016, Analysis User's Guide Volume II: Analysis, Section 6.8: Coupled pore fluid flow and stress analysis.

[3] ABAQUS 2016, Analysis Theory Guide Volume II: Analysis, Section 4.4.3: Critical State Model.

[4] Al-Tabbaa, A. & Wood, D. M. (1987). Some measurements of the permeability of kaolin. *Geˊotechnique*, 37 (4), 499–514.

[5] Ng, C.W.W., Shi, C., Gunawan, A., & Laloui, L. (2014). Centrifuge modelling of energy piles subjected to heating and cooling cycles in clay. *Geotech. Lett*, 4 (4), 310-316.

[6] Johansen, O. (1975). Thermal conductivity of soils. PhD thesis, Trondheim, Norway (CRREL Draft Translation 637, 1977). ADA 044002.

CURRICULUM VITAE

Saeed Yazdani

Education

University of Wisconsin at Milwaukee	*2014-2019*

- PhD Student
- Teaching and Research Assistant –Geotechnical Engineering

Purdue University, West Lafayette, Indiana	*2013- 2014*

- PhD. Student in Civil Engineering

Tarbiat Modares University, Tehran, Iran

- M.S. in Civil Engineering
- Research: Study of Hydro-Mechanical effects on Arch Dam

Shahid Chamran University, Ahvaz, Iran

- B.S. in Civil Engineering

Teaching Experience

Instructor- Foundation Engineering	*Fall 2018-Present*
*Teaching Assistant-*Strength of Material	*Fall 2017-Spring 2018*
Soil Mechanics Lab Instructor	*Fall 2014-Spring 2017*
*Teaching Assistant-*Strength of Material	*Summer 2016*
*Teaching Assistant-*Statics	*Summer 2016*
*Teaching Assistant-*Reinforced Concrete Structure	*Spring 2007*

Journal Publications

Yazdani, S., Yazdani, M., Assadi-Langroudi, A., Ghadr, S., and Abbas, A.A. 2019. *Integrated FE-DE Solution for Flow through Jointed Rocks*. in revision at Soil and Foundation.

Yazdani S., Helwany, S., Olgun, O. 2019. *Laboratory study of the Long-Term shaft resistance of Energy Piles in Saturated clay.* in press at Canadian Geotechnical Journal.

Yazdani, S., Helwany, S., and Olgun, O. 2019. *Investigation of thermal loading effects on the shaft resistance of energy pile using laboratory scale model*. Journal of Geotechnical and Geoenvironmental Engineering, 10.1061/(ASCE)GT.1943-5606.0002088.

Yazdani, S., Helwany, S., and Olgun, O. 2018. *Influence of Temperature on Soil-Pile Interface Shear Strength*. Geomechanics for Energy and the Environment. 18, 69-78.

Yazdani, S., Helwany, S., and Olgun, O. 2018. *Experimental evaluation of shear strength of Kaolin Clay under Cyclic and Non-Cyclic Thermal Loading*. Geotechnical Testing Journal, https://doi.org/10.1520/GTJ20180020.

Journal Publications (Continued)

Yazdani S., Yazdani M., and Ahmadi M. (2010). *Importance of Joint Geometric Parameters on Concrete Arch Dams' Safety Evaluation*. Journal of Technical & Engineering of Tarbiat Modares University, 11, pp.27-39, 2011.

Yazdani S., and Yazdani M. (2010). *2D Numerical Study of the Stability of Concrete Arch Dams with Special focus on the Role of Rock Joints and the Internal Flowing Water*. Journal of Iranian Association of Engineering Geology, 3(1&2), pp. 71-82.

Yazdani S., Yazdani M., and Ahmadi M. (2010). *Safety Evaluation of Abutment of Concrete Arch Dams Based on Hydromechanical Analysis.* Journal of Technical & Engineering of Sharif University of Technology, 26(2), pp. 69-78.

Yazdani S., Yazdani M., and Ahmadi M. (2008) *Study of Joint Geometric Parameters Influences on Hydraulic Abutment Behavior of Concrete Arch Dams.* Journal of Hydraulic, 3, pp. 33-44.

Conference Publications

Yazdani M., **Yazdani S.**, and Ahmadi M. (2007). *Evaluation of Hydromechanical Behavior of Jointed Rock Mass on Stability of Concrete Arch Dam Abutments*. 11th International Rock Mechanics congress, Lisbon, Portugal.

Yazdani M., **Yazdani S.**, (2007). Importance of Joints Geometrics Parameters on Concrete Arch Dam safety Evaluation. 60th Canadian Geotechnical conference & 8th Joint CGS/IAH-CNC Groundwater Conference, Ottawa, Canada.

Yazdani M., **Yazdani S.**, and Ahmadi M. (2007). *Evaluation of Concrete Arch Dam Safety Using Distinct Element Method*. 3th National Iranian Conference on Civil Engineering, Tabriz, Iran.

Research Experience

"Study of the long-term shaft resistance of energy piles in saturated clays", **University of Wisconsin at Milwaukee.**	*August 2014-Jun 2019*
"An analytical solution of stress-displacement distribution at the crack tip in pore-elastic media due to fluid flow", **Purdue University**.	*Sep 2013-Sep 2014*
"*Study of Foundation and Abutment Behavior of Concrete Arch Dams with Emphasis on Discontinuities Roles (with accompanying a Stability Case study on "SEIMAREH Concrete Arch Dam " in Iran)*", with participation of the **Iranian Ministry of Energy** and **C.E Department of Tarbiat Modares University,** Tehran, Iran.	*Sep 2008-May 2011*
"Evaluation of Hydro-mechanical Behavior on Stability of Jointed Rock Mass of Concrete Arch Dam Abutments", Master thesis, **Tarbiat Modares University**, Tehran, Iran.	*Sep 2004-Apr 2007*

Awards

CEAS Dean's Scholarship ($ 4000.0)	*Spring 2019*
Honorable Mention-2018 UWM Student Research Poster Competition	*Spring 2018*
CEAS Dean's Scholarship	*Spring 2018*
CEAS Dean's Scholarship	*Spring 2017*
CEAS Dean's Scholarship	*Fall 2016*
CEAS Dean's Scholarship	*Spring 2015*
CEAS Dean's Scholarship	*Fall 2014*

Research Interest

- Numerical/Experimental Thermo-Hydro-Mechanical Analyses in Porous Media
- Experimental tests in soil mechanics test
- Soil-Solid Interaction Analysis
- Foundation Engineering
- Geotechnical Earthquake Engineering
- Soil Mechanics and Soil Improvement
- Performance-Based-Design in Geomechanics
- Unsaturated soil mechanics and Geo-Environmental Engineering

References

- **Professor Sam Helwany**. Professor,
  Civil and Environmental Engineering Department-Geotechnical Program,
  University of Wisconsin-Milwaukee, USA- E-mail: helwany@uwm.edu
- **Professor Mahmoud Yazdani**. Assistant Professor,
  Civil and Environmental Engineering Department,
  Tarbiat Modares University, Iran- E-mail: myazdani@modares.ac.ir